Application of Steady and Unsteady Detonation Waves to Propulsion

Thesis by

Eric Wintenberger

In Partial Fulfillment of the Requirements

for the Degree of

Doctor of Philosophy

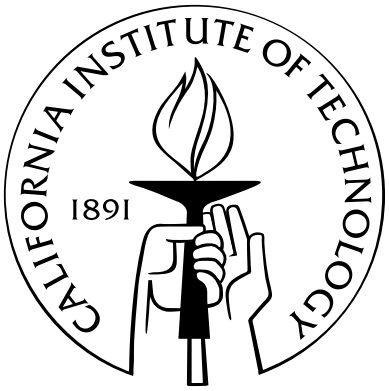

California Institute of Technology

Pasadena, California

2004

(Defended February 6, 2004)

Acknowledgements

I would like to thank my advisor, Professor Joe Shepherd, for his great insight, enthusiasm, and support in the course of my graduate studies. He was at the origin of many of the ideas developed in this work and many problems I faced in the course of this work were solved following discussions with him. Professor Hans Hornung deserves my thanks for many helpful discussions and suggestions, and also for teaching me how to use Amrita. I gratefully acknowledge the help of the other members of my doctoral committee, Professors Melany Hunt and Fred Culick, and Dr. James Polk.

The current and past members of the Explosion Dynamics Laboratory at Caltech have all contributed to this work through helpful discussions, suggestions, and comments. Many thanks to Eric Schultz, Julian Lee, Joanna Austin, Marco Arienti, Scott Jackson, Marcia Cooper, Tony Chao, Dan Lieberman, and Florian Pintgen.

I would like to thank Dr. Matei Radulescu for pointing out the issue of the influence of non-equilibrium flow on detonation tube impulse. Suzy Dake's administrative and organizational assistance was greatly appreciated.

Additionally, I would like to thank my skiing and climbing partners for balancing my graduate student life with extreme adventures!

Finally, this work would never have been completed without the love, support, and understanding of my parents and my lovely wife, Virginie.

This research was sponsored by a Multidisciplinary University Research Initiative from the Office of Naval Research "*Multidisciplinary Study of Pulse Detonation Engine*," by General Electric, and by a Department of Navy Grant "*Pulse Detonation Engines: Initiation, Propagation, and Performance*."

Abstract

The present work investigates the applications of steady and unsteady detonation waves to air-breathing propulsion systems. The efficiency of ideal detonation-based propulsion systems is first investigated based on thermodynamics. We reformulate the Hugoniot analysis of steady combustion waves for a fixed initial stagnation state to conclude that steady detonation waves are less desirable than deflagrations for propulsion. However, a thermostatic approach shows that unsteady detonations have the potential for generating more work than constant-pressure combustion. The subsequent work focuses on specific engine concepts. A flow path analysis of ideal steady detonation engines is conducted and shows that their performance is limited and poorer than that of the ideal ramjet or turbojet engines. The limitations associated with the use of a steady detonation in the combustor are drastic and such engines do not appear to be practical. This leads us to focus on unsteady detonation engines, i.e., pulse detonation engines. The unsteady generation of thrust in the simple configuration of a detonation tube is first analyzed using gas dynamics. We develop one of the first models to quickly and reliably estimate the impulse of a pulse detonation tube. The impulse is found to scale directly with the mass of explosive in the tube and the square root of the energy release per unit mass of the mixture. Impulse values for typical fuel-oxidizer mixtures are found to be on the order of 160 s for hydrocarbon-oxygen mixtures and 120 s for fuel-air mixtures at standard conditions. These results are then used as a basis to develop the first complete system-level performance analysis of a supersonic, single-tube, air-breathing pulse detonation engine. We show that hydrogen- and JP10-fueled pulse detonation engines generate thrust up to a Mach number of 4, and that the specific impulse decreases quasi-linearly with

increasing flight Mach number. Finally, we find that the performance of our pulse detonation engine exceeds that of the ramjet below a Mach number of 1.35.

Contents

Acknowledgements iv

Abstract vi

List of Figures xxiv

List of Tables xxvi

Nomenclature 1

1 Introduction 1

1.1 Detonations . . . 1

1.1.1 Chapman-Jouguet theory . . . 1

1.1.1.1 Properties of the upper CJ point . . . 4

1.1.1.2 Detonation in a perfect gas . . . 6

1.1.2 ZND model . . . 7

1.1.3 Cellular structure of the detonation front . . . 10

1.1.4 Flow field behind a detonation wave in a tube . . . 13

1.2 Steady-flow air-breathing propulsion . . . 15

1.2.1 Thrust and efficiencies . . . 17

1.2.2 Ramjet . . . 22

1.2.3 Turbojet . . . 25

1.2.4 Thermodynamic cycle analysis . . . 27

1.2.4.1 General cycle analysis . . . 28

1.2.4.2 Cycle analysis for propulsion systems . . . 31

1.3 Unsteady-flow air-breathing propulsion 34
1.3.1 Flow path analysis 35
1.3.2 Thermodynamic cycle analysis 36
1.3.3 Selection of the combustion mode 41
1.3.4 Pulsejet 42
1.3.5 Pulse detonation engine 47
1.4 Thesis outline 51

2 Thermodynamic Analysis of Combustion Processes for Propulsion Systems 53

2.1 Entropy variation along the Hugoniot 54
2.2 The role of irreversibility in steady-flow propulsion 56
2.2.1 Irreversible entropy rise and thermal efficiency 61
2.2.2 The stagnation Hugoniot 62
2.3 Detonation applications in unsteady flow: the Fickett-Jacobs cycle . . 67
2.3.1 Basic FJ cycle 67
2.3.2 Thermal efficiency 73
2.3.3 FJ cycle with precompression 80
2.4 Detonation and constant-volume combustion 84
2.4.1 Comparison of FJ cycle with Brayton and Humphrey cycles . 84
2.4.2 Entropy generated by a detonation 87
2.4.3 Kinetic energy in detonations 92
2.4.4 Performance comparison for a straight detonation tube 95
2.5 Blowdown model 97
2.5.1 Constant-volume combustion engine 98
2.5.2 Constant-volume blowdown of a combustion chamber 100
2.5.3 Performance calculation 101
2.5.4 Hydrogen and JP10 fueled CV engines 104
2.6 Conclusions 106

3 Steady Detonation Engines **109**

3.1 Introduction . . . 109

3.2 Stabilized normal detonations . . . 112

3.2.1 Detonation stabilization condition . . . 114

3.2.2 General limitations . . . 115

3.2.3 Steady detonation stability . . . 119

3.2.4 Detonation-related limitations . . . 122

3.2.4.1 Limitations on detonation chamber diameter . . . 126

3.2.4.2 Limitations on detonation chamber length . . . 127

3.2.4.3 Near-detonability limit effects . . . 128

3.2.4.4 Application to hydrogen-air and JP10-air stabilized detonations . . . 129

3.3 Detonation ramjet . . . 131

3.3.1 Performance analysis . . . 131

3.3.2 Performance comparison . . . 134

3.3.3 Dramjet limitations . . . 139

3.4 Detonation turbojet . . . 142

3.5 Thermodynamic cycle analysis . . . 146

3.6 Conclusions . . . 151

4 Single-Cycle Pulse Detonation Tube Performance Modeling **153**

4.1 Introduction . . . 153

4.2 Flow field associated with an ideal detonation in a tube . . . 157

4.2.1 Ideal detonation and Taylor wave . . . 158

4.2.2 Interaction of the detonation with the open end . . . 158

4.2.3 Waves and space-time diagram . . . 161

4.2.4 A numerical simulation example . . . 161

4.3 Impulse model . . . 167

4.3.1 Determination of the impulse . . . 168

4.3.2 Determination of α . . . 171

4.3.3 Determination of β . . . 173
4.3.4 Determination of P_3 and c_3 . . . 174
4.4 Validation of the model . . . 178
4.4.1 Comparisons with single-cycle experiments . . . 178
4.4.2 Comparisons with multi-cycle experiments . . . 182
4.4.3 Comparisons with numerical simulations . . . 186
4.5 Impulse scaling relationships . . . 187
4.5.1 Dependence of impulse on energy content . . . 188
4.5.2 Dependence of impulse on initial pressure . . . 191
4.5.3 Dependence of impulse on initial temperature . . . 191
4.5.4 Mixture-based specific impulse . . . 191
4.6 Impulse predictions – Parametric studies . . . 193
4.6.1 Impulse per unit volume . . . 194
4.6.2 Mixture-based specific impulse . . . 197
4.6.3 Fuel-based specific impulse . . . 200
4.6.4 Influence of initial temperature . . . 200
4.7 Conclusions . . . 204

5 Air-Breathing Pulse Detonation Engine Performance Modeling 206
5.1 Introduction . . . 206
5.2 Single-tube air-breathing PDE . . . 208
5.3 Control volume analysis . . . 210
5.3.1 Mass conservation . . . 210
5.3.2 Momentum conservation . . . 211
5.3.3 Energy conservation . . . 212
5.3.4 Thrust calculation . . . 213
5.4 Detonation tube dynamics . . . 214
5.4.1 Detonation/blowdown process . . . 215
5.4.2 Purging/filling process . . . 217
5.5 Modeling of the filling process . . . 220

5.5.1 Plenum/detonation tube coupling . . . 220
5.5.1.1 Subsonic flow at the valve plane . . . 222
5.5.1.2 Sonic flow at the valve plane . . . 224
5.5.1.3 Average plenum conditions . . . 225
5.5.2 Comparison with numerical simulations of the filling process . 228
5.6 Flow fluctuations in the engine . . . 231
5.6.1 Unsteady flow in the plenum . . . 231
5.6.2 Inlet response to flow fluctuations . . . 234
5.7 PDE performance calculation . . . 236
5.7.1 PDE thrust equation . . . 237
5.7.2 Specific impulse and effect of purging time . . . 239
5.7.3 Detonation tube impulse . . . 242
5.7.3.1 Detonation tube impulse model . . . 242
5.7.3.2 Comparison with numerical simulations of detonation process . . . 244
5.8 Application to hydrogen- and JP10-fueled PDEs . . . 246
5.8.1 Input parameters . . . 246
5.8.2 Hydrogen-fueled PDE . . . 247
5.8.2.1 Conditions inside the engine . . . 247
5.8.2.2 Performance variation with flight Mach number . . . 249
5.8.2.3 Performance variation with altitude . . . 251
5.8.2.4 Performance variation with purge coefficient . . . 252
5.8.3 JP10-fueled PDE . . . 253
5.8.3.1 Performance parameters . . . 253
5.8.3.2 Issues associated with the use of JP10 . . . 254
5.8.4 Uncertainty analysis . . . 255
5.8.5 Comparison with the ideal ramjet . . . 256
5.9 Conclusions . . . 258

6 Conclusions **260**

Bibliography **280**

A Steady detonation engine performance computation **281**

A.1 Formulas for steady detonation engine performance 281

A.2 Realistic thermodynamic cycle 282

B Influence of non-equilibrium flow on detonation tube impulse **285**

C Impulse model prediction tables **288**

D Iterative method for air-breathing PDE performance model **301**

List of Figures

1.1 Control volume used in the Chapman-Jouguet theory. 2
1.2 Hugoniot curve with energy release and shock Hugoniot. 3
1.3 ZND profile for a detonation in a stoichiometric hydrogen-air mixture at 1 atm and 300 K initial conditions. The detailed mechanism of Konnov (1998) is used. The leading shock front is located at $x = 0$. Left: pressure and temperature profiles. Right: species concentration profiles. 9
1.4 Pattern left on a sooted foil by a detonation propagating in $2H_2$-O_2-17Ar at 20 kPa and 295 K initial conditions (from Austin, 2003). 10
1.5 Cellular structure of the detonation front. The triple point tracks form a cellular pattern, defining the cell width λ. 11
1.6 Shadowgraph of detonation front in $2H_2$-O_2-12Ar mixture at 20 kPa initial mixture and 295 K initial temperature (from Austin, 2003). . . . 12
1.7 Space-time diagram of the flow field behind a propagating detonation wave in a closed tube. State 1 is the initial reactant state, state 2 is the CJ state, while state 3 is the state of the products behind the Taylor wave. 13
1.8 Profile of pressure, temperature, density, and flow velocity behind an ideal detonation wave modeled using the one-γ model. $\gamma = 1.2$, $q/RT_1 = 40$. 16
1.9 Control volume Ω used for the calculation of thrust produced by a general steady-flow propulsion system. 17

1.10 Total temperature at the exit plane of a constant-pressure combustor as a function of equivalence ratio for propane-air mixtures. Initial stagnation conditions at the combustor inlet are 400 K and 2 bar. 20
1.11 Schematic representation of a ramjet. The pressure and temperature profiles through the engine are shown. 22
1.12 Specific thrust (left) and thrust-specific fuel consumption (right) of the ideal ramjet for various values of T_{max}. $q_f = 45$ MJ/kg, $T_0 = 223$ K. . . 23
1.13 Schematic of a turbojet engine, including the variation of pressure and temperature across the engine. 25
1.14 Specific thrust of the ideal turbojet as a function of flight Mach number for varying compression ratios. $T_{max} = 1700$ K, $q_f = 45$ MJ/kg, $T_0 = 223$ K. 27
1.15 Arbitrary thermodynamic cycle ending with constant-pressure process. 28
1.16 Brayton cycle plotted in the pressure-specific volume plane (left) and the temperature-entropy plane (right). $q_f = 45$ MJ/kg, $f = 0.05$, $\gamma = 1.4$, $T_0 = 223$ K, $P_4/P_0 = 8$. 33
1.17 Steady- and unsteady-flow expansion from the same initial state. $\gamma = 1.4$. 38
1.18 Schematic of a valved pulsejet (from Foa, 1959). 43
1.19 Specific impulse of ideal and standard pulsejet without backflow, calculated using the entropy method (Foa (1959, 1960)). $\gamma = 1.4$, $q_f = 45$ MJ/kg, $f = 0.035$, $T_0 = 278$ K, $n = -1$. 45
1.20 Schematic of a ducted pulsejet with tail shrouding. 46
1.21 Pulse detonation engine cycle. 48

2.1 Solutions of the conservation equations for the Hugoniot for M_2 as a function of M_1 (left) and Hugoniot curve in the pressure-specific volume plane (right) for a perfect gas with $\gamma = 1.4$ and $q_c/C_pT_1 = 4$. 54
2.2 Variation of the total entropy rise along the Hugoniot. $\gamma = 1.4$, $q_c/C_pT_1 = 4$. 55

2.3 Mollier diagram used to calculate minimum entropy component. Solid lines are isobars for reactants and dotted lines are isobars for products. 58

2.4 Reversible and irreversible components of the entropy rise along the Hugoniot, $\gamma = 1.4$, $q_c/C_pT_1 = 4$. 60

2.5 Ideal steady engine in flight showing the location of the combustion wave. 61

2.6 Solutions of the conservation equations for the stagnation Hugoniot for M_2 as a function of M_1 (left) and stagnation Hugoniot curve in the pressure-specific volume plane (right) for a perfect gas with $\gamma = 1.4$ and $q_c/C_pT_1 = 0.8$. 63

2.7 Total entropy rise along the stagnation Hugoniot. The minimum component of the entropy rise is fixed along the stagnation Hugoniot and is shown as the straight line. The total entropy variation is due to the irreversible component only. $\gamma = 1.4$, $q_c/C_pT_{t1} = 0.8$. 65

2.8 Thermal efficiency of an ideal engine flying at $M_0 = 5$ as a function of the combustion mode selected, $\gamma = 1.4$, $q_c/C_pT_{t1} = 0.8$. 66

2.9 Piston cylinder arrangement used to implement Fickett-Jacobs cycle. . 68

2.10 Physical steps that make up the Fickett-Jacobs cycle. a) Detonation moving to right with simultaneous application of external work to move piston on left at velocity u_p. b) Instantaneous acceleration of piston on right when detonation has consumed all the material. c) Conversion of mechanical motion to external work to bring detonation products to rest. d) Expansion of products back to atmospheric pressure. e) Extraction of energy as heat at constant pressure to return detonation products to initial temperature. f) Conversion of products to reactants at constant temperature and pressure. The flows of work and heat corresponding to the various steps are shown. 69

2.11 Pressure-specific volume diagram showing the sequence of states and connecting paths that make up the FJ cycle for a stoichiometric propane-air mixture at 300 K and 1 bar initial conditions. 71

2.12 FJ cycle thermal efficiency as a function of CJ Mach number for the one-γ model of detonation for two values of γ representative of fuel-oxygen ($\gamma = 1.1$) and fuel-air ($\gamma = 1.2$) detonations. 74

2.13 FJ cycle thermal efficiency as a function of CJ Mach number for the two-γ model of detonation with $\gamma_1 = 1.4$. 76

2.14 FJ cycle thermal efficiency for stoichiometric hydrogen, ethylene, propane, and JP10 mixtures with oxygen and air as a function of initial pressure at 300 K (left) and initial temperature at 1 bar (right). 76

2.15 Left: FJ cycle thermal efficiency as a function of equivalence ratio at 300 K and 1 bar initial conditions for hydrogen, ethylene, propane and JP10. Right: FJ cycle thermal efficiency as a function of nitrogen dilution for stoichiometric fuel-oxygen mixtures at 300 K and 1 bar initial conditions for hydrogen, ethylene, propane and JP10. 77

2.16 Pressure-specific volume diagram showing the sequence of states and connecting paths that make up the FJ cycle with precompression ($\pi_c = 5$) for a stoichiometric propane-air mixture at 300 K and 1 bar initial conditions. 81

2.17 Left: FJ cycle thermal efficiency as a function of the compression ratio π_c for the one-γ model of detonation using different values of the non-dimensional heat release. Right: temperature-entropy diagram for FJ cycle without and with precompression ($\pi_c = 20$) using the one-γ model of detonation. $q_c/RT_1 = 40$, $\gamma = 1.2$. 82

2.18 FJ cycle thermal efficiency as a function of the compression ratio π_c for hydrogen, ethylene, propane, and JP10 with oxygen and air at initial conditions of 1 bar and 300 K. 83

2.19 Pressure-specific volume diagram comparing the FJ, Humphrey, and Brayton cycles with precompression ($\pi_c = 5$) for a stoichiometric propane-air mixture at 300 K and 1 bar initial conditions. 85

2.20 Thermal efficiency as a function of compression ratio (left) and combustion pressure ratio (right) for FJ, Humphrey and Brayton cycles for a stoichiometric propane-air mixture at 300 K and 1 bar initial conditions. 86

2.21 Entropy rise generated by CP combustion, CV combustion, and detonation. $\gamma = 1.2$. 89

2.22 Numerical simulation of detonation propagation and reflection in a closed duct. $q/RT_1 = 40$, $\gamma = 1.2$. Left: distance-time diagram (horizontal axis is distance, vertical axis is time). Right: average entropy rise in the duct and pressure at the left end of the duct as a function of time. 91

2.23 Ratio of kinetic energy to total energy release as a function of the adiabatic exponent for a detonation wave propagating in a closed tube. $q_c/RT_1 = 40$. Note that the dashed portion is non-physical for ideal gases but is often used in modeling high explosives. 94

2.24 Non-dimensionalized pressure at the closed end of the tube and impulse for CV combustion and detonation as a function of time. $q_c/RT_1 = 40$, $P_R = 1$, $\gamma = 1.2$. 96

2.25 Non-dimensionalized impulse for CV combustion and detonation as a function of energy release q_c/RT_1 with $P_R = 1$ (left) and pressure ratio P_R with $q_c/RT_1 = 40$ (right). $\gamma = 1.2$. 97

2.26 Schematic of constant-volume combustion engine. 99

2.27 CV combustion engine cycle. 1) Combustion chamber contains reactants between closed inlet and outlet valves. 2) Instantaneous CV combustion of reactants. 3) Outlet valve opens and CV blowdown of combustion products begins. 4) When chamber pressure equals inlet pressure, inlet valve opens and air flows in. Residual combustion products are exhausted through CP blowdown. Once the chamber is filled with air, both valves close and fuel is instantaneously injected and mixed with air. 99

2.28 Fuel-based specific impulse of stoichiometric hydrogen and JP10 fueled CV engines compared with the ideal ramjet at 10,000 m altitude. . . . 104

3.1 Standing detonation generated by the isentropic expansion of an airflow from a reservoir of total temperature T_{t0}, with fuel injection downstream of the nozzle throat. 114

3.2 Allowable domain for the generation of a stabilized detonation in hydrogen-air as a function of the reservoir total temperature T_{t0} and the fuel-air mass ratio f. $q_f = 120.9$ MJ/kg for hydrogen. 118

3.3 Cell width λ as a function of initial pressure P_4 for stoichiometric hydrogen-air at 297 K and JP10-air at 373 K. The lines correspond to cell width predictions using calculated reaction zone lengths (Shepherd, 1986, Kee et al., 1989) for hydrogen and ignition time correlation (Davidson et al., 2000) for JP10. The symbols correspond to experimental data of Stamps and Tieszen (1991) and Austin and Shepherd (2003). 124

3.4 Cell width λ as a function of equivalence ratio for hydrogen-air at 297 K and JP10-air at 373 K and 1 bar. The lines correspond to cell width predictions using calculated reaction zone lengths (Shepherd, 1986, Kee et al., 1989) for hydrogen and ignition time correlation (Davidson et al., 2000) for JP10. The symbols correspond to experimental data of Ciccarelli et al. (1994), Guirao et al. (1982), and Austin and Shepherd (2003). 125

3.5 Cell width λ as a function of initial temperature T_4 for stoichiometric hydrogen- and JP10-air mixtures at 1 bar. The lines correspond to cell width predictions using calculated reaction zone lengths (Shepherd, 1986, Kee et al., 1989) for hydrogen and ignition time correlation (Davidson et al., 2000) for JP10. The symbols correspond to experimental data of Stamps and Tieszen (1991). 126

3.6 Schematic representation of a detonation ramjet (or dramjet). The pressure and temperature profiles through the engine are shown. 132

3.7 Specific thrust of ramjet and dramjet. $T_0 = 223$ K, $P_0 = 0.261$ atm, $q_f = 45$ MJ/kg, $T_{max} = 2500$ K. The limits for effective detonation stabilization are shown for hydrogen and JP10. 134

3.8 Total pressure ratio across a CJ detonation wave, a normal shock, and the reaction zone using the one-γ model. $\gamma = 1.4$. 136
3.9 Variation of the CJ Mach number and the total pressure ratio across the detonation wave with flight Mach number for the dramjet. $T_0 = 223$ K, $P_0 = 0.261$ atm, $q_f = 45$ MJ/kg, $T_{max} = 2500$ K. 137
3.10 Thrust-specific fuel consumption (left) and efficiencies (right) of ramjet and dramjet. $T_0 = 223$ K, $P_0 = 0.261$ atm, $q_f = 45$ MJ/kg, $T_{max} = 2500$ K. 138
3.11 Fuel-air mass ratio f (left) and cell width λ (right) versus flight Mach number M_0 for a dramjet operating with hydrogen and JP10. $T_0 = 223$ K, $P_0 = 0.261$ atm, $T_{max} = 2500$ K, $\gamma = 1.4$. 141
3.12 Schematic of a detonation turbojet, including the variation of pressure and temperature across the engine. 142
3.13 Specific thrust of turbojet and turbodet engines. $\pi_c = 30$, $T_0 = 223$ K, $P_0 = 0.261$ atm, $q_f = 45$ MJ/kg, $T_{max} = 1700$ K. 143
3.14 Thrust-specific fuel consumption (left) and efficiencies (right) of turbojet and turbodet engines. The efficiency curves for the turbodet are those extending only from $M_0 = 1.75$ to 3. $\pi_c = 30$, $T_0 = 223$ K, $P_0 = 0.261$ atm, $q_f = 45$ MJ/kg, $T_{max} = 1700$ K. 144
3.15 Influence of compression ratio π_c on the specific thrust of the turbodet. $T_0 = 223$ K, $P_0 = 0.261$ atm, $q_f = 45$ MJ/kg, $T_{max} = 1700$ K. 145
3.16 Cell width λ versus flight Mach number M_0 for a turbodet operating with hydrogen and JP10. $\pi_c = 30$, $T_0 = 223$ K, $P_0 = 0.261$ atm, $T_{max} = 1700$ K. 146
3.17 Ideal thermodynamic cycle of the ramjet and the dramjet in the (P,V) and (T,s) planes. $T_0 = 223$ K, $P_0 = 0.261$ atm, $M_0 = 5.4$, $T_{max} = 2500$ K. Primes denote states corresponding to the dramjet case. 147
3.18 Ideal thermodynamic cycle of the turbojet and the turbodet in the (P,V) and (T,s) planes. $T_0 = 223$ K, $P_0 = 0.261$ atm, $M_0 = 2$, $T_{max} = 1700$ K. Primes denote states corresponding to the dramjet case. 148

3.19 Altitude-Mach number diagram for a hydrogen-fueled dramjet. $\phi = 0.4$. The various limitations associated with net thrust production, cell sizes, hydrogen-air auto-ignition, and a very optimistic maximum temperature condition are given. 149

4.1 Pulse detonation engine cycle: a) The detonation is initiated at the thrust surface. b) The detonation, followed by the Taylor wave, propagates to the open end of the tube at a velocity U_{CJ}. c) An expansion wave is reflected at the mixture-air interface and immediately interacts with the Taylor wave while the products start to exhaust from the tube. d) The first characteristic of the reflected expansion reaches the thrust surface and decreases the pressure at the thrust surface. 154

4.2 Pressure-velocity diagram used to compute wave interactions at the tube open end for fuel-oxygen mixtures. 160

4.3 Pressure-velocity diagram used to compute wave interactions at the tube open end for fuel-air mixtures. 160

4.4 Space-time diagram for detonation wave propagation and interaction with the tube open end. 162

4.5 Numerical schlieren images of the exhaust process. 163

4.6 Pressure along the tube centerline from numerical simulation. P_1 is the initial pressure inside and outside the tube. 164

4.7 Velocity along the tube centerline from numerical simulation. c_1 is the initial sound speed inside and outside the tube. 165

4.8 Non-dimensionalized thrust surface pressure and impulse per unit volume as a function of non-dimensionalized time for the numerical simulation. 167

4.9 Control volumes a) typically used in rocket engine analysis b) used in our analysis. 168

4.10 Sample pressure recorded at the thrust surface (Cooper et al., 2002) for a mixture of stoichiometric ethylene-oxygen at 1 bar and 300 K initial conditions. 169
4.11 Idealized model of the thrust surface pressure history. 170
4.12 Logarithm of pressure (left) and temperature (right) versus logarithm of specific volume along the CJ equilibrium and frozen isentropes for ethylene-oxygen and -air mixtures. 176
4.13 Model predictions versus experimental data (Cooper et al., 2002) for the impulse per unit volume. Filled symbols represent data for unobstructed tubes, whereas open symbols show data for cases in which obstacles were used. Lines corresponding to +15% and -15% deviation from the model values are also shown. * symbols denote high-pressure (higher than 0.8 bar), zero-dilution cases. 180
4.14 Comparison of specific impulse between model predictions and experimental data for hydrogen-air (Schauer et al., 2001) with varying equivalence ratio and stoichiometric hydrogen-oxygen (Cooper et al., 2002). Nominal initial conditions are $P_1 = 1$ bar, $T_1 = 300$ K. Lines corresponding to +15% and -15% deviation from the model values are also shown. 183
4.15 Comparison of specific impulse between model predictions and experimental data (Cooper et al., 2002, Schauer et al., 2001) for propane-air with varying equivalence ratio. Nominal initial conditions are $P_1 = 1$ bar, $T_1 = 300$ K. Lines corresponding to +15% and -15% deviation from the model values are also shown. 184
4.16 Thrust prediction for a 50.8 mm diameter by 914.4 mm long hydrogen-air PDE operated at 16 Hz. Comparison with experimental data of Schauer et al. (2001). Nominal initial conditions are $P_1 = 1$ bar, $T_1 = 300$ K. Lines corresponding to +15% and -15% deviation from the model values are also shown. 185

4.17 Specific impulse scaling with energy content. Model predictions (Eq. 4.8) versus effective specific energy content q for hydrogen, acetylene, ethylene, propane, and JP10 with air and oxygen including 0, 20%, 40%, and 60% nitrogen dilution at $P_1 = 1$ bar and $T_1 = 300$ K. 193
4.18 Variation of impulse per unit volume with initial pressure. Nominal initial conditions are $T_1 = 300$ K, stoichiometric fuel-oxygen ratio. . . . 195
4.19 Variation of impulse per unit volume with equivalence ratio. Nominal initial conditions are $P_1 = 1$ bar, $T_1 = 300$ K. 196
4.20 Variation of impulse per unit volume with nitrogen dilution. Nominal initial conditions are $P_1 = 1$ bar, $T_1 = 300$ K, stoichiometric fuel-oxygen ratio. 197
4.21 Variation of mixture-based specific impulse with initial pressure. Nominal initial conditions are $T_1 = 300$ K, stoichiometric fuel-oxygen ratio. 198
4.22 Variation of mixture-based specific impulse with equivalence ratio. Nominal initial conditions are $P_1 = 1$ bar, $T_1 = 300$ K. 199
4.23 Variation of mixture-based specific impulse with nitrogen dilution. Nominal initial conditions are $P_1 = 1$ bar, $T_1 = 300$ K, stoichiometric fuel-oxygen ratio. 199
4.24 Variation of fuel-based specific impulse with initial pressure. Nominal initial conditions are $T_1 = 300$ K, stoichiometric fuel-oxygen ratio. . . . 201
4.25 Variation of fuel-based specific impulse with equivalence ratio. Nominal initial conditions are $P_1 = 1$ bar, $T_1 = 300$ K. 201
4.26 Variation of fuel-based specific impulse with nitrogen dilution. Nominal initial conditions are $P_1 = 1$ bar, $T_1 = 300$ K, stoichiometric fuel-oxygen ratio. 202
4.27 Variation of impulse per unit volume with initial temperature for different values of the stagnation pressure. 203
4.28 Variation of mixture-based specific impulse with initial temperature for different values of the stagnation pressure. 203

5.1 Schematic representation of a single-tube PDE. 209
5.2 Control volume considered for analysis of single-tube PDE. 212
5.3 PDE cycle schematic for a detonation tube. a) The detonation is initiated at the closed end of the tube and b) propagates towards the open end. c) It diffracts outside as a decaying shock and a reflected expansion wave propagates to the closed end, starting the blowdown process. d) At the end of the blowdown process, the tube contains burned products at rest. e) The purging/filling process is triggered by the opening of the valve, sending a shock wave in the burned gases, followed by the air-products contact surface. f) A slug of air is injected before the reactants for purging. g) The purging air is pushed out of the tube by the reactants. h) The reactants eventually fill the tube completely and the valve is closed. 216
5.4 Numerical schlieren images of the filling process. $P_R = 8$, $T_f/T_0 = 7.69$, $\gamma = 1.4$. 218
5.5 Control volume V_C considered for analysis of flow in the plenum. . . . 221
5.6 Flow configuration used to model the filling process in the case of subsonic flow at the valve plane. 223
5.7 Flow configuration used to model the filling process in the case of sonic flow at the valve plane. 225
5.8 Ratio of the average pressure in the plenum to the total pressure downstream of the inlet (left) and ratio of the open time to the close time (right) as a function of the flight Mach number. $P_0 = 0.265$ bar, $T_0 = 223$ K, $A_0 = 0.004$ m^2, $A_2 = 0.04$ m^2, $A_V = 0.006$ m^2. 227
5.9 Comparison of model predictions and numerical simulations with Amrita (Quirk, 1998) for the velocity at the valve plane, the average filling velocity, and the pressure at the valve plane. $T_f/T_0 = 7.69$, $\gamma = 1.4$. . . 228

5.10 Pressure and velocity profiles along the centerline from the numerical simulations with Amrita (Quirk, 1998). The valve is located at an axial distance of 100 and the detonation tube exit is located at 200. The dashed line shows the value of the model prediction. $P_R = 8$, $T_f/T_0 = 7.69$, $\gamma = 1.4$. 231

5.11 Evolution of flow properties in the plenum. $A_0 = 0.004$ m^2, $A_2 = 0.04$ m^2, $A_V = 0.006$ m^2, $V_C = 0.02$ m^3, $\dot{m}_0 = 0.9915$ kg/s, $\overline{P_C} = 1.885$ bar, $\overline{T_C} = 401.4$ K, $t_{close} = 0.01$ s, $t_{open} = 0.007865$ s. 233

5.12 Modeling of pressure and flow velocity at the valve plane during a cycle. 237

5.13 Control volume used to calculate ramjet performance. 240

5.14 Numerical schlieren image of the initial configuration for the numerical simulations of the detonation process with moving flow. The Taylor wave is visible behind the detonation front at the tube exit. 244

5.15 Non-dimensional detonation tube impulse as a function of the filling Mach number. Comparison of model predictions based on Eq. 5.60 and results of numerical simulations with Amrita (Quirk, 1998). $q/RT_i = 40$, $\gamma = 1.2$. 245

5.16 Filling velocity and velocity at the valve plane (left) and cycle frequency (right) as a function of flight Mach number for single-tube PDE operating with stoichiometric hydrogen-air. $Z = 10,000$ m, $A_0 = 0.004$ m^2, $A_2 = 0.04$ m^2, $A_V = 0.006$ m^2, $t_{close} = 0.005$ s. 248

5.17 Left: inlet stagnation pressure, plenum pressure, pressure at the valve plane, and filling pressure non-dimensionalized with freestream total pressure as a function of flight Mach number. Right: freestream stagnation temperature, temperature at the valve plane and filling temperature as a function of flight Mach number. Stoichiometric hydrogen-air, $Z = 10,000$ m, $A_0 = 0.004$ m^2, $A_2 = 0.04$ m^2, $A_V = 0.006$ m^2. 249

5.18 Specific impulse of a single-tube PDE operating with stoichiometric hydrogen-air as a function of flight Mach number at sea level and at an altitude of 10,000 m. $A_0 = 0.004$ m^2, $A_2 = 0.04$ m^2, $A_V = 0.006$ m^2, $\pi = 0$. Data from multi-cycle numerical simulations by Wu et al. (2003) for $M_0 = 2.1$ at 9,300 m altitude are shown. Experimental data from Schauer et al. (2001) and our single-cycle impulse model predictions are also given as a reference for the static case. The uncertainty region for the specific impulse at 10,000 m is the shaded area. 250

5.19 Various terms in specific impulse equation as a function of flight Mach number for hydrogen-fueled PDE. $Z = 10,000$ m, $A_0 = 0.004$ m^2, $A_2 = 0.04$ m^2, $A_V = 0.006$ m^2, $\pi = 0$. 251

5.20 Left: specific impulse of a single-tube PDE operating with stoichiometric hydrogen-air as a function of flight Mach number varying the purge coefficient. Right: variation of specific impulse of a single-tube hydrogen-fueled PDE flying at $M_0 = 2$ with purge coefficient. $Z = 10,000$ m, $A_0 = 0.004$ m^2, $A_2 = 0.04$ m^2, $A_V = 0.006$ m^2. 253

5.21 Specific impulse of a single-tube air-breathing PDE compared to the ramjet operating with stoichiometric hydrogen-air and JP10-air. $Z = 10,000$ m, $A_0 = 0.004$ m^2, $A_2 = 0.04$ m^2, $A_V = 0.006$ m^2, $\pi = 0$. Data from multi-cycle numerical simulations by Wu et al. (2003) for $M_0 = 2.1$ at 9,300 m altitude are shown. Experimental data from Schauer et al. (2001) and Wintenberger et al. (2002), referred to as CIT, and our impulse model predictions are also given as a reference for the static case. 257

B.1 Influence of non-equilibrium flow in the Taylor wave on the plateau pressure P_3 and the specific impulse for stoichiometric ethylene-oxygen mixtures diluted with nitrogen at 1 bar and 300 K initial conditions. . 286

List of Tables

1.1 CJ detonation velocity and pressure for a range of mixtures at 1 bar and 300 K initial conditions. 5

3.1 Boiling point and auto-ignition temperature of various fuels. *Lide (2001), †Kuchta (1985), ‡Zabetakis (1965), ϒCRC (1983) 119

3.2 CJ parameters and minimum detonation chamber length and diameter for a range of initial conditions for hydrogen- and JP10-air. The minimum dimensions are based on the proposed criteria using the computed reaction zone lengths for hydrogen-air (Shepherd, 1986, Kee et al., 1989) and the ignition time correlation for JP10-air of Davidson et al. (2000). 130

4.1 Frozen and equilibrium values of γ evaluated at the CJ point for stoichiometric ethylene-oxygen and ethylene-air at 1 bar and 300 K initial conditions compared with results from fitting the isentrope based on the polytropic relationship using pressure and specific volume or temperature and specific volume. 177

4.2 Comparison of the model predictions for the mixture-based specific impulse. 181

4.3 Detonation CJ parameters and computed impulse for selected stoichiometric mixtures at 1 bar initial pressure and 300 K initial temperature. 189

5.1 Uncertainty on some of the model parameters compared to the results of the numerical simulations of the filling and detonation processes. . . 256

C.1 Impulse model predictions for C_2H_4-O_2 mixtures 289

C.2 Impulse model predictions for C_3H_8-O_2 mixtures 290
C.3 Impulse model predictions for C_2H_2-O_2 mixtures 291
C.4 Impulse model predictions for H_2-O_2 mixtures 292
C.5 Impulse model predictions for Jet A-O_2 mixtures 293
C.6 Impulse model predictions for JP10-O_2 mixtures 294
C.7 Impulse model predictions for C_2H_4-air mixtures 295
C.8 Impulse model predictions for C_3H_8-air mixtures 296
C.9 Impulse model predictions for C_2H_2-air mixtures 297
C.10 Impulse model predictions for H_2-air mixtures 298
C.11 Impulse model predictions for Jet A-air mixtures 299
C.12 Impulse model predictions for JP10-air mixtures 300

Nomenclature

A	cross-sectional area
$\mathcal{A}$	constant of proportionality
A_e	exit area
A_V	valve cross-sectional area
A_0	effective inlet capture area
A_2	plenum cross-sectional area
$\hat{C}^-$	first reflected characteristic to reach the thrust surface
$C^\pm$	characteristics, left and right-facing families
C_p	specific heat at constant pressure
C_v	specific heat at constant volume
c	speed of sound
d	detonation tube diameter
E	total energy
E_C	total energy in plenum
e	internal energy per unit mass
F	thrust
$\mathbf{F}$	force vector
f	fuel-air mass ratio
f_{st}	fuel-air mass ratio for stoichiometric conditions
g	Earth's gravitational acceleration
$\mathcal{H}$	non-dimensional heat release parameter for one-γ model of detonation
h	enthalpy per unit mass
h_i^0	enthalpy of formation per unit mass of species i

h_t	total enthalpy per unit mass
h_{tf}	total enthalpy per unit mass of fuel
I	impulse
I_{CV}	impulse generated by constant-volume blowdown
I_{CP}	impulse generated by constant-pressure blowdown
I_{dt}	detonation tube impulse
I_{SPF}	fuel-based specific impulse
I_{SPFdt}	detonation tube fuel-based specific impulse
I_V	impulse per unit volume
J^-	Riemann invariant on a left-facing characteristic
K	proportionality coefficient
k	number of combustion chambers
L	detonation chamber length
L_E	engine size
$\mathcal{L}$	critical length scale for DDT
M	Mach number
M_{CJ}	Chapman-Jouguet Mach number
M_{fill}	filling Mach number
M_S	shock wave Mach number
$\mathcal{M}$	mass
$\mathcal{M}_f$	initial mass of fuel within detonation tube
$\dot{m}$	air mass flow rate
$\dot{m}_{CC}$	average mass flow rate through a single combustion chamber
$\dot{m}_f$	fuel mass flow rate
$\dot{m}_s$	mass flow rate through side surfaces of control volume
N	mixture number of moles
N_i	number of moles of species i
n	polytropic exponent
$\mathbf{n}$	surface normal vector
P	static pressure

P_R	pressure ratio
P_t	total pressure
Q	heat exchange
P_0	environment pressure
$\mathcal{Q}$	non-dimensional energy release parameter
q	effective energy release per unit mass of mixture
q_c	heat of combustion per unit mass of mixture
q_f	heat of combustion per unit mass of fuel
q_{in}	heat per unit mass input into the system in the equivalent heat addition model
q_{out}	heat per unit mass removed from the system during a cycle
q_{net}	net amount of heat per unit mass received by the system during a cycle
R	perfect gas constant
$\mathcal{R}$	universal gas constant
s	entropy per unit mass
$\overline{s_i}$	partial molar entropy of species i
$\overline{s}_i^0$	standard entropy of species i
T	static temperature
T_c	condensation temperature
T_{ign}	auto-ignition temperature of mixture
T_{max}	maximum temperature at combustor outlet
T_t	total temperature
$TSFC$	thrust specific fuel consumption
t	time
t'	non-dimensional time $= c_3 t/L$
t_b	characteristic time of blowdown process
t_{close}	valve close-up time
t_{CV}	duration of constant-volume blowdown
t_{fill}	filling time
t_{open}	valve open time
t_{purge}	purging time

t_1	time taken by the detonation wave to reach the open end of the tube
t_2	time taken by the first reflected characteristic to reach the thrust surface
t_3	time associated with pressure decay period
t^*	time at which the first reflected characteristic exits the Taylor wave
U_{CJ}	Chapman-Jouguet detonation velocity
U_{fill}	filling velocity
u	flow velocity
$\mathbf{u}$	velocity vector
u'	flow velocity in wave reference frame
u_p	piston velocity
v	specific volume
V_C	plenum volume
V_{dt}	detonation tube volume
W	work
$\dot{w}$	power per unit mass
w	work per unit mass
w_{ij}	work per unit mass done by the system between states i and j
w_{net}	net work per unit mass done by the system during a cycle
X_{O_2}	oxygen mole fraction
x	position coordinate
Y_F	fuel mass fraction
Y_i	mass fraction of species i
Z	altitude
α	non-dimensional parameter corresponding to time taken by first reflected characteristic to reach thrust surface
β	non-dimensional parameter corresponding to pressure decay period
Γ_{CV}	non-dimensional integral for CV blowdown impulse calculation
γ	ratio of specific heats or polytropic exponent
γ_b	detonation products γ
Δ	reaction zone length

$\Delta_f h^0$	enthalpy of formation per unit mass
ΔP	pressure differential $= P - P_0$
ΔP_3	pressure differential at the thrust surface
Δs_{irr}	irreversible component of entropy rise
Δs_{min}	minimum component of entropy rise
Δs_{rev}	reversible component of entropy rise
ϵ_c	compressor adiabatic efficiency
ϵ_d	inlet diffuser adiabatic efficiency
ϵ_n	exit nozzle adiabatic efficiency
ϵ_{n1}	compressor-combustor nozzle adiabatic efficiency for turbodet
ϵ_{n2}	combustor-turbine nozzle adiabatic efficiency for turbodet
ϵ_t	turbine adiabatic efficiency
η	similarity variable $= ct/L$
η_{FJ}	thermal efficiency of FJ cycle
η_H	thermal efficiency of Humphrey cycle
η_p	propulsive efficiency
η_{th}	thermal efficiency
η_ν	efficiency of non-uniformity
η_0	overall efficiency
λ	cell width
ξ	non-dimensional time $= 1 + t/t_b$
Π	non-dimensional pressure
π	purging coefficient
π_c	compression ratio
ρ	density
Σ	engine control surface
$\dot{\sigma}$	thermicity
τ	cycle time
τ_{ign}	ignition time
Φ	non-dimensional frequency of pressure oscillations

ϕ	equivalence ratio
χ	non-dimensional parameter $= (P_0/P_3)^{(\gamma-1)/\gamma}$
Ω	engine control volume
Ω_i	chemical reaction rate
ω	frequency of pressure oscillations

Subscripts: general notations (unless specified otherwise in text)

0	freestream
3	stagnant region behind Taylor wave during detonation process
C	acoustic cavity (or plenum)
CJ	Chapman-Jouguet
dt	detonation tube
eq	equilibrium
f	state of detonation products at the end of blowdown process
fr	frozen
i	state of reactants before detonation initiation at the end of filling process
is	isentropic
r	plane upstream of fuel injectors in ramjet
V	valve plane
*	choked flow at throat
^{o}	model value during open part of cycle

Chapter 1

Introduction

1.1 Detonations

A detonation is a supersonic combustion wave which can be described as a shock wave coupled with a reaction zone. The shock wave compresses and heats the gases, which react rapidly after an induction period. The energy released by the chemical reaction triggers a volumetric expansion of the burned gases and drives the shock wave. Self-sustaining detonation waves are characterized by a strong coupling of the shock wave and the reaction zone. First, the hydrodynamic discontinuity model of detonation waves is presented, then the idealized one-dimensional structure of the wave front is considered before the actual multi-dimensional cellular structure of the front and its associated instability are discussed. Finally, the flow field associated with a detonation propagating in a tube is presented.

1.1.1 Chapman-Jouguet theory

The earliest and most elementary theory on detonations is due to Chapman (1899) and Jouguet (1905). The theory assumes that the detonation wave is steady, planar, and one-dimensional, and models it as a hydrodynamic discontinuity, across which energy release occurs. The detonation wave is analyzed using a control volume surrounding the shock wave followed by the reaction zone, as shown in Fig. 1.1.

The mass, momentum, and energy conservation equations are applied to the con-

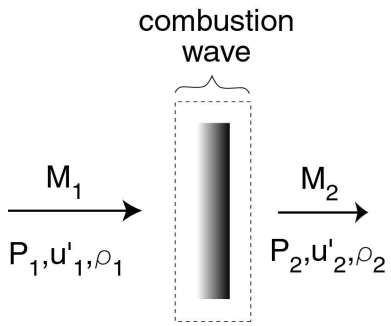

Figure 1.1: Control volume used in the Chapman-Jouguet theory.

trol volume.

$$\rho_1 u_1' = \rho_2 u_2' \tag{1.1}$$

$$P_1 + \rho_1 {u_1'}^2 = P_2 + \rho_2 {u_2'}^2 \tag{1.2}$$

$$h_1 + {u_1'}^2/2 = h_2 + {u_2'}^2/2 \tag{1.3}$$

States 1 and 2 correspond respectively to the reactants upstream of the wave and the products downstream of the wave. From these equations, the Hugoniot relationship can be obtained

$$h_2 - h_1 = \frac{1}{2}(P_2 - P_1)(1/\rho_1 + 1/\rho_2) \; . \tag{1.4}$$

The Hugoniot determines the locus of the possible solutions for state 2 from a given state 1 and a given energy release. In particular, it is instructive to plot the Hugoniot on a pressure-specific volume diagram. Figure 1.2 displays a schematic of the Hugoniot curve with energy release, as well as the shock Hugoniot (no energy release). The Rayleigh line, which relates the initial to the final state, is given by

$$P_2 - P_1 = -(\rho_1 u_1')^2 (1/\rho_2 - 1/\rho_1) \; . \tag{1.5}$$

From this equation, it is obvious that region III of Fig. 1.2 does not represent real solutions and can be eliminated. The solutions located in regions I and II correspond to supersonic waves (detonations), whereas the solutions located in regions IV and V correspond to subsonic waves (deflagrations).

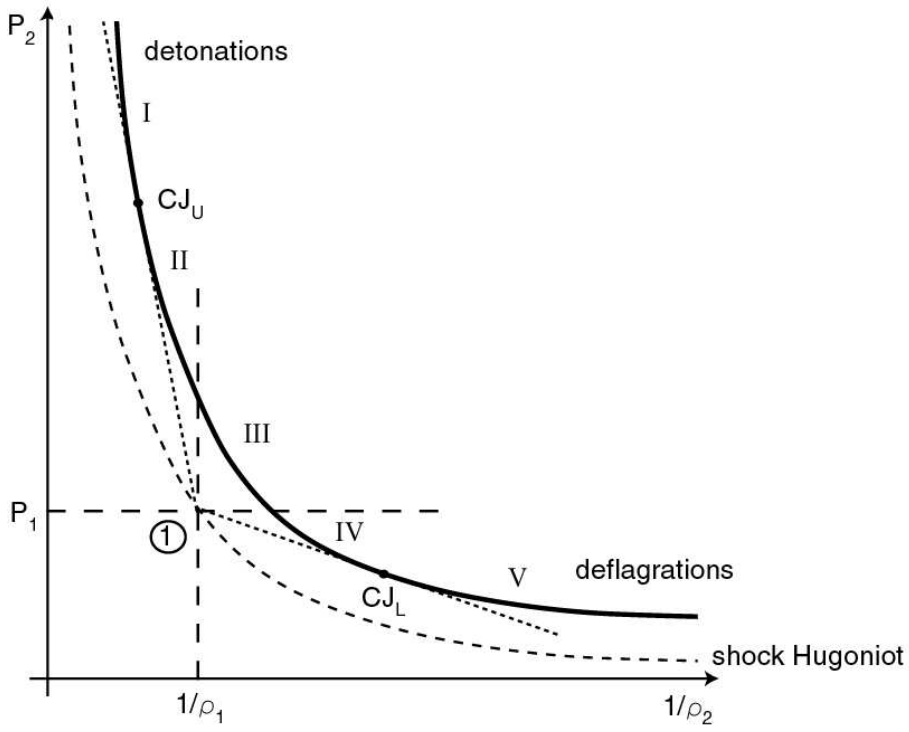

Figure 1.2: Hugoniot curve with energy release and shock Hugoniot.

The solution to Eqs. 1.1–1.3 is uniquely determined only with some additional consideration. For deflagrations, the structure of the combustion wave and turbulent and diffusive transport processes determine the actual propagation speed. For detonations, gas dynamic considerations are apparently sufficient to determine the propagation speed, independent of the actual structure of the wave. These considerations were independently made by Jouguet (1905) and Chapman (1899), who proposed that detonations travel at one particular velocity, which is the minimum velocity for all the solutions on the detonation branch. Chapman (1899) postulated that at the solution point, the Hugoniot and the Rayleigh line were tangent. He also established that these curves were tangent to the isentrope. From these considerations, it is possible to show that the flow behind the wave is sonic relative to the wave, i.e., $M_2 = 1$. The point where the Hugoniot, Rayleigh line, and isentrope are all tangent is called the Chapman-Jouguet (CJ) point. There exist two CJ points on the Hugoniot, the upper CJ point ($\mathrm{CJ_U}$) and the lower CJ point ($\mathrm{CJ_L}$), located respectively on the detonation and deflagration branches of the Hugoniot. These points divide the Hugoniot

into four regions (region III has already been eliminated for real solutions). Region IV corresponds to weak deflagrations (subsonic flow to subsonic) and encompasses the laminar flame solutions. Region V corresponds to strong deflagrations (subsonic flow to supersonic). However, in a constant-area duct, it is not possible to have heat addition and to proceed past the sonic condition (Anderson, 1990, pp. 77–85). Thus, region V is not a physically possible region of steady solutions and is ruled out. Region I corresponds to strong detonations (supersonic flow to subsonic) but these are observed only in the transient state or if there is an "effective" piston created by the flow following the wave. They are unstable because rarefaction waves propagating behind the detonation wave (expansion waves following detonations are due, for example, to friction, heat loss, turbulence...) will catch up with the detonation front and move the solution point towards CJ_U. Finally, region II, which corresponds to weak detonations (supersonic flow to supersonic), can be ruled out except in extraordinary situations by considering the reaction zone structure.

The physically acceptable solutions for steady waves are on branches I and IV only (Courant and Friedrichs, 1967, Chap. III.E). Region III is impossible due to the conservation laws. Regions II and V appear to be exotic possibilities ("eigenvalue" solutions) that occur only in exceptional situations with very special restrictions on the reaction mechanism, rates, and thermochemistry. For subsonic waves (region IV), there is no unique solution from a gas dynamic view point and other processes, such as turbulence and molecular diffusion, have to be considered. For supersonic waves (region I), there is one special solution, CJ_U, that is singled out from a thermodynamic point of view. It is also possible to have steady overdriven detonation waves (with a velocity higher than U_{CJ}) if there is some type of piston following the wave.

1.1.1.1 Properties of the upper CJ point

The parameters at the CJ point can be determined by equilibrium computations based on realistic thermochemistry and a mixture of the relevant gas species in reactants and products using an equilibrium code such as STANJAN (Reynolds, 1986). The main result of the CJ theory is the calculation of the velocity of the propagating detonation

wave U_{CJ}. Experimentally measured detonation velocities are typically found to be within 2% of the calculated CJ velocity (Lewis and von Elbe, 1961, pp. 524–528), as long as the characteristic dimension of the facility is large compared to the length scale of the cellular instability of the mixture. Table 1.1 lists the CJ velocity and pressure for a range of mixtures.

Mixture	$U_{CJ}(m/s)$	P_{CJ} (bar)
$2H_2+O_2$	2840.4	18.72
$2H_2+O_2+3.76N_2$	1970.7	15.51
$C_2H_4+3O_2$	2375.8	33.27
$C_2H_4+3O_2+11.28N_2$	1824.6	18.25
$C_3H_8+5O_2$	2359.6	36.04
$C_3H_8+5O_2+18.8N_2$	1800.6	18.15
$JP10+14O_2$	2293.6	38.89
$JP10+14O_2+52.64N_2$	1783.5	18.4

Table 1.1: CJ detonation velocity and pressure for a range of mixtures at 1 bar and 300 K initial conditions.

The CJ points have another interesting property related to entropy. The rate of change of entropy along the Hugoniot is given by

$$T_2\left[\frac{ds_2}{d(1/\rho_2)}\right]_H = \frac{1}{2}\left(\frac{1}{\rho_1}-\frac{1}{\rho_2}\right)\left(-\frac{P_1-P_2}{1/\rho_1-1/\rho_2}+\left[\frac{dP_2}{d(1/\rho_2)}\right]_H\right) , \qquad (1.6)$$

where H is used to emphasize differentiation along the Hugoniot curve (Courant and Friedrichs, 1967, p. 213). At the CJ point, the Hugoniot, Rayleigh line, and isentrope are all tangent, and, therefore, $ds_2/d(1/\rho_2)$=0. Hence, the CJ points correspond to extrema of the entropy along the Hugoniot. Differentiating the previous equation at the CJ points, one obtains

$$\left[\frac{d^2s_2}{d(1/\rho_2)^2}\right]_H = \frac{1/\rho_1-1/\rho_2}{2T_2}\left[\frac{d^2P_2}{d(1/\rho_2)^2}\right]_H . \qquad (1.7)$$

Because the Hugoniot is convex everywhere, i.e., $[d^2P_2/d(1/\rho_2)^2]_H > 0$, $[d^2s_2/d(1/\rho_2)^2]_H > 0$ at the upper CJ point and the entropy goes through a minimum (Courant and Friedrichs, 1967, pp. 212–214). Similarly, the lower CJ point corresponds to maximum entropy. Hence, the upper CJ point is the point of minimum entropy for the

combustion products along the Hugoniot.

1.1.1.2 Detonation in a perfect gas

For a CJ detonation in a perfect gas, analytic solutions for the CJ_{U} point may be obtained assuming different values of the specific heat ratio and the perfect gas constant in the reactants and products. The heat of combustion q_c is introduced by writing $h_1 = h_1^0 + C_p T_1$ and $h_2 = h_2^0 + C_p T_2$, with $q_c = h_1^0 - h_2^0$. Using the CJ condition ($M_2 = 1$) in the conservation equations (Eqs. 1.1–1.3), the so-called two-γ model (Thompson, 1988, pp. 353–354) can be derived

$$M_{CJ} = \sqrt{\mathcal{H} + \frac{(\gamma_1 + \gamma_2)(\gamma_2 - 1)}{2\gamma_1(\gamma_1 - 1)}} + \sqrt{\mathcal{H} + \frac{(\gamma_2 - \gamma_1)(\gamma_2 + 1)}{2\gamma_1(\gamma_1 - 1)}}\,, \tag{1.8}$$

where the non-dimensional heat of combustion $\mathcal{H}$ is given by

$$\mathcal{H} = \frac{(\gamma_2 - 1)(\gamma_2 + 1) q_c}{2\gamma_1 R_1 T_1}\,. \tag{1.9}$$

The other CJ properties can be found by substitution into the conservation equations.

$$U_{CJ} = M_{CJ} c_1 \tag{1.10}$$

$$\frac{P_2}{P_1} = \frac{\gamma_1 M_{CJ}^2 + 1}{\gamma_2 + 1} \tag{1.11}$$

$$\frac{\rho_2}{\rho_1} = \frac{\gamma_1(\gamma_2 + 1) M_{CJ}^2}{\gamma_2(\gamma_1 M_{CJ}^2 + 1)} \tag{1.12}$$

$$\frac{T_2}{T_1} = \frac{R_1}{R_2}\frac{P_2}{P_1}\frac{\rho_1}{\rho_2} \tag{1.13}$$

$$u_2 = U_{CJ}\left(1 - \frac{\rho_1}{\rho_2}\right) \tag{1.14}$$

If we further simplify the model and use only a single value of the specific heat ratio and the perfect gas constant common to reactants and products, we derive the equations for the one-γ model (Fickett and Davis, 2001, pp. 52–53)

$$M_{CJ} = \sqrt{\mathcal{H} + 1} + \sqrt{\mathcal{H}}\,, \tag{1.15}$$

where

$$\mathcal{H} = \frac{(\gamma^2 - 1)q_c}{2\gamma R T_1} \,. \tag{1.16}$$

The CJ properties are then given by

$$\frac{P_2}{P_1} = \frac{\gamma M_{CJ}^2 + 1}{\gamma + 1} \,, \tag{1.17}$$

$$\frac{\rho_2}{\rho_1} = \frac{(\gamma + 1)M_{CJ}^2}{1 + \gamma M_{CJ}^2} \,, \tag{1.18}$$

$$\frac{T_2}{T_1} = \frac{(1 + \gamma M_{CJ}^2)^2}{(\gamma + 1)^2 M_{CJ}^2} \,. \tag{1.19}$$

A further approximation is to assume that the detonation Mach number is much larger than unity, which corresponds to the "strong detonation" approximate solution (Fickett and Davis, 2001, p. 54). It is then found that, within this approximation, the detonation propagation velocity is proportional to the square root of the energy release, the CJ pressure scales with the product of the initial mixture density and the energy release, and the CJ temperature is directly proportional to the energy release.

$$U_{CJ} \approx \sqrt{2(\gamma_2^2 - 1)q_c} \tag{1.20}$$

$$\rho_2 \approx \frac{\gamma_2 + 1}{\gamma_2}\rho_1 \tag{1.21}$$

$$P_2 \approx \frac{1}{\gamma_2 + 1}\rho_1 U_{CJ}^2 \approx 2(\gamma_2 - 1)\rho_1 q_c \tag{1.22}$$

$$T_2 \approx \frac{2\gamma_2(\gamma_2 - 1)}{\gamma_2 + 1}\frac{q_c}{R} \tag{1.23}$$

$$u_2 \approx \frac{U_{CJ}}{\gamma_2 + 1} \tag{1.24}$$

1.1.2 ZND model

Zel'dovich (1940a), von Neumann (1942), and Döring (1943) independently arrived at a theory for the structure of the detonation wave. The ZND theory models the detonation wave as a strong shock wave coupled with a reaction zone. The planar shock wave brings the gas to the post-shock, or von Neumann, state. Chemical reactions are initiated at the von Neumann state. The region just after the shock, the induction

zone, is characterized by the generation of radicals in chain-branching reactions and is usually thermally neutral. After the induction period, the temperature rises due to the energy release caused by the reaction, while the pressure and density decrease due to the expansion of the hot products. This expansion maintains the strength of the leading shock front. The reaction zone, which encompasses the induction and energy release zones, terminates at the Chapman-Jouguet plane, where chemical equilibrium is reached and the flow velocity is sonic relative to the shock wave.

The ZND model assumes that the flow is one-dimensional, and models the shock wave as a discontinuity, neglecting transport effects. The model includes chemical kinetics with a finite reaction rate. Detailed chemical mechanisms or simplified mechanisms such as one-step irreversible reactions can be used. The reactive Euler equations are solved in the shock wave frame to calculate the thermodynamic properties and chemical species concentrations through the reaction zone.

$$\frac{D\rho}{Dt} = -\rho\frac{du}{dx} \tag{1.25}$$

$$\frac{Du}{Dt} = -\frac{1}{\rho}\frac{dP}{dx} \tag{1.26}$$

$$\frac{D(h+u^2/2)}{Dt} = \frac{1}{\rho}\frac{\partial P}{\partial t} \tag{1.27}$$

$$\frac{DY_i}{Dt} = \Omega_i \qquad i = 1...N \tag{1.28}$$

Looking for a steady solution to these equations corresponding to the steady shock-reaction zone configuration, we may rewrite the Euler equations in the wave reference frame as

$$u'\frac{d\rho}{dx} = -\frac{\rho\dot{\sigma}}{1-M^2}\ , \tag{1.29}$$

$$u'\frac{dw}{dx} = \frac{u'\dot{\sigma}}{1-M^2}\ , \tag{1.30}$$

$$u'\frac{dP}{dx} = -\frac{\rho u'^2\dot{\sigma}}{1-M^2}\ , \tag{1.31}$$

$$u'\frac{dY_i}{dx} = \Omega_i \qquad i = 1...N\ , \tag{1.32}$$

where $u' = U_S - u$ and the thermicity is defined (Fickett and Davis, 2001, p. 77) as

$$\dot{\sigma} = \sum_i^N \frac{\Omega_i}{\rho c^2} \left(\frac{\partial P}{\partial Y_i} \right)_{\rho, c, Y_{k \neq i}} . \tag{1.33}$$

To avoid a singularity in the solution, the thermicity must vanish as the flow Mach number $M = u'/c_{fr}$, where c_{fr} is the frozen speed of sound, approaches one. Hence, for a wave traveling at the CJ velocity, the equilibrium state is reached at the sonic plane.

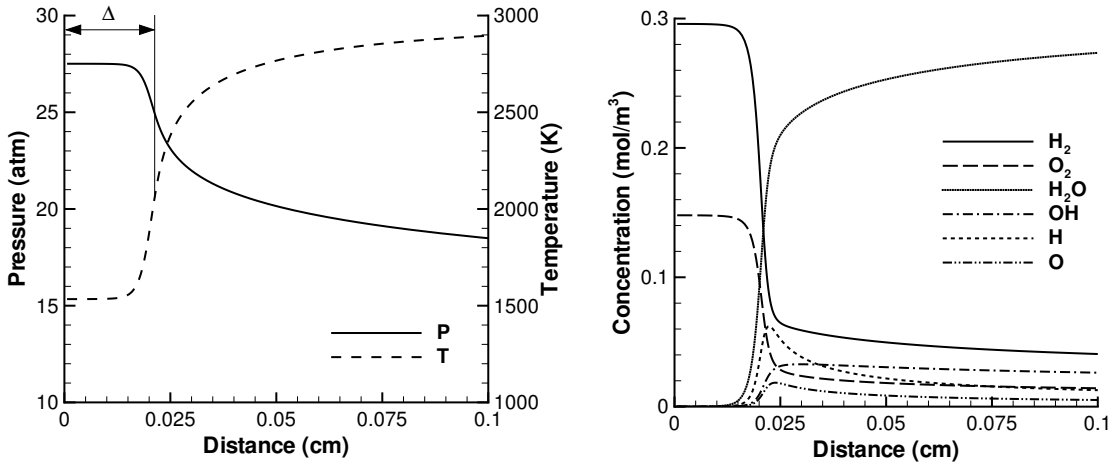

Figure 1.3: ZND profile for a detonation in a stoichiometric hydrogen-air mixture at 1 atm and 300 K initial conditions. The detailed mechanism of Konnov (1998) is used. The leading shock front is located at $x = 0$. Left: pressure and temperature profiles. Right: species concentration profiles.

The thermodynamic properties and the species concentrations behind the shock front can be calculated using a numerical solution of the ZND model (Shepherd, 1986). This solution requires a validated detailed chemical kinetics mechanism and is based on the CHEMKIN II package (Kee et al., 1989). An example case is shown in Fig. 1.3 for a stoichiometric hydrogen-air mixture using the detailed mechanism of Konnov (1998). The induction zone starts at the post-shock state and ends with a sharp increase in radical concentration and temperature, corresponding to the beginning of the energy release zone. The energy release zone is characterized by a strong radical concentration, which decays as the major products are formed. The pressure,

temperature, and species concentrations asymptote to their equilibrium values at the end of the energy release zone. The induction zone length Δ is usually defined as the distance from the leading shock front to the point of maximum heat release (thermicity). It depends on the mixture composition, initial conditions, chemical kinetic rate, and is a strong function of the post-shock temperature. The induction zone length is a length scale that can be used to characterize the thickness of the detonation front.

1.1.3 Cellular structure of the detonation front

The tight coupling between the leading shock front and the reaction zone in detonation waves results in an intrinsic unstable dynamic behavior. Small variations in the leading shock strength result in large variations in reaction rates in the flow behind the shock since typical reaction rates are extremely sensitive to the post-shock temperature. The changes in reaction rates in turn affect the leading shock strength since the flow through the reaction zone is subsonic. This feedback mechanism is responsible for the nonlinear instability of the detonation wave front. All experimentally observed detonation waves display this unstable behavior (Fickett and Davis, 2001, Chap. 7). The consequence of this instability is that the detonation front is not one-dimensional such as idealized in the ZND model (Fig. 1.3), but is actually three-dimensional and characterized by an oscillatory motion.

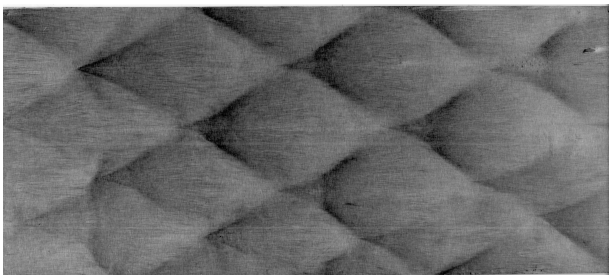

Figure 1.4: Pattern left on a sooted foil by a detonation propagating in $2H_2$-O_2-17Ar at 20 kPa and 295 K initial conditions (from Austin, 2003).

The detonation front instability is characterized by the production of transverse waves, which propagate in directions normal to the leading shock front (Fickett and

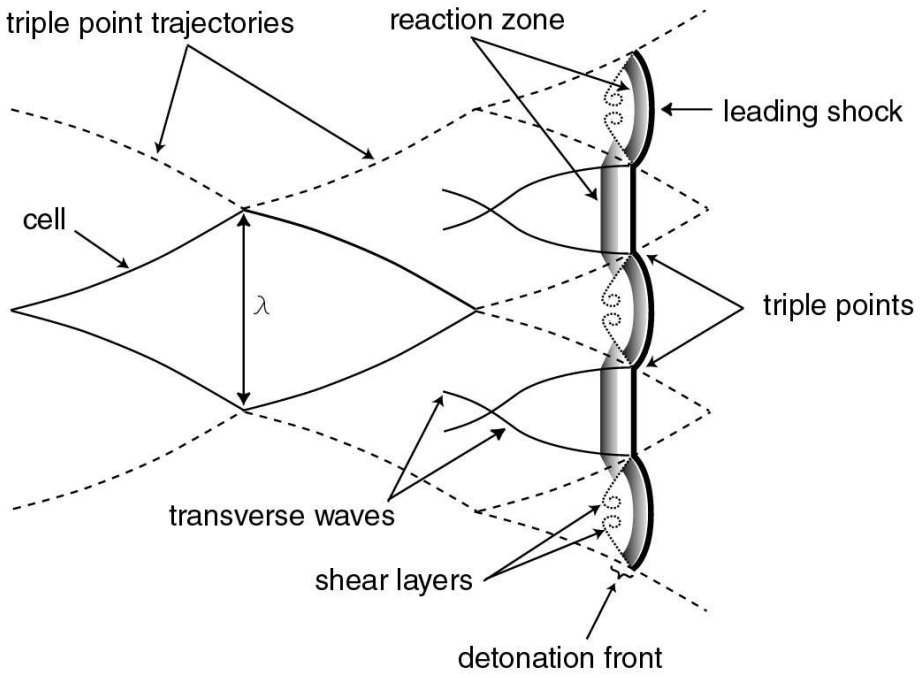

Figure 1.5: Cellular structure of the detonation front. The triple point tracks form a cellular pattern, defining the cell width λ.

Davis, 2001, Chap. 7). The periodic collision of these transverse waves generates regions of high pressure and temperature, which accelerate the local lead shock relative to the weaker neighboring parts of the front. After the transverse wave collision, the lead shock decays until the next collision occurs. This mechanism explains the oscillatory motion of the detonation front. The triple points at the junction of the transverse waves and the leading shock front propagate along the shock front as the detonation moves forward. The cellular pattern observed on sooted foils after a detonation has propagated over them (Fig. 1.4) is a record of the trajectories of the triple points (Urtiew and Oppenheim, 1966). The width of the cells λ observed on the sooted foils is a measure of the transverse wave spacing and is a characteristic length scale of the mixture. Figure 1.5 is a schematic of the cellular structure in two dimensions. The portions of the leading shock front at the beginning of the cell are stronger than those at the end of the cell due to the recent transverse wave collision. The reaction zone is, therefore, shorter because the chemical processes are faster due to the higher temperature behind the shock. This idealized cellular structure is ex-

perimentally observed in detonations in regular mixtures in a narrow channel facility (Austin, 2003), as shown in Fig. 1.6.

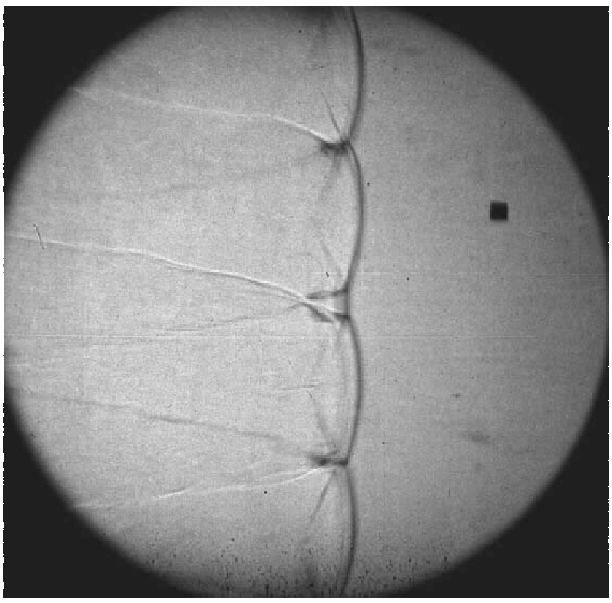

Figure 1.6: Shadowgraph of detonation front in $2H_2$-O_2-12Ar mixture at 20 kPa initial mixture and 295 K initial temperature (from Austin, 2003).

The cell width λ is representative of the sensitivity of the mixture to detonation. Mixtures with small cell widths are more sensitive to detonation than mixtures with larger cell widths. Some efforts (Gavrikov et al., 2000) have focused on trying to predict the cell width, but there is still no appropriate theory for cell width prediction. It has been suggested that the cell width is proportional to the other detonation characteristic length scale, the induction zone length Δ (Shchelkin and Troshin, 1965, Westbrook and Urtiew, 1982), with a constant of proportionality $\mathcal{A}$: $\lambda = \mathcal{A}\Delta$. However, Shepherd (1986) showed that the constant $\mathcal{A}$ varies strongly with equivalence ratio, between 10 and 50 for common fuel-air mixtures at stoichiometric conditions, and between 2 and 100 for off-stoichiometric mixtures. The cell width λ has been proposed to be the most fundamental parameter characterizing the dynamic properties of detonations (Lee, 1984). For fixed mixture composition and initial conditions, the critical values of the relevant physical parameters that determine detonation failure or propagation are called the dynamic parameters of detonations (Lee, 1984). They include the critical tube diameter for diffraction of a detonation from a tube into an

unconfined space, the minimum energy for direct initiation of detonation, and the minimum tube diameter for stable detonation propagation in a tube. The critical conditions can be estimated by empirical correlations based on the cell width (Lee, 1984).

1.1.4 Flow field behind a detonation wave in a tube

A detonation wave propagating from the closed end of a tube is followed by an expansion wave in order to satisfy the boundary conditions at the closed end of the tube. This self-similar expansion wave, called the Taylor wave, brings the flow to rest and decreases the pressure at the closed end of the tube (Zel'dovich, 1940a, Taylor, 1950). The Taylor wave is followed by a stagnant region extending from its rear to the closed end of the tube. Figure 1.7 is a space-time diagram of the flow behind the detonation wave and shows the different regions mentioned.

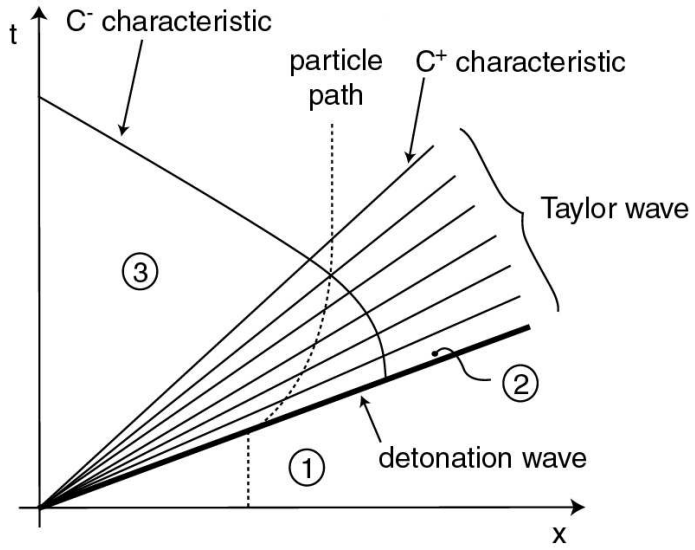

Figure 1.7: Space-time diagram of the flow field behind a propagating detonation wave in a closed tube. State 1 is the initial reactant state, state 2 is the CJ state, while state 3 is the state of the products behind the Taylor wave.

The properties within the Taylor wave can be determined by assuming a similarity solution for the flow and using the method of characteristics (Zel'dovich, 1940a, Taylor, 1950). Modeling the detonation wave as a discontinuity, we consider the network

of characteristics within the Taylor wave. There are two sets of characteristics, C^+ and C^-, defined by

$$C^+ \qquad \frac{dx}{dt} = u + c \,, \tag{1.34}$$

$$C^- \qquad \frac{dx}{dt} = u - c \,. \tag{1.35}$$

The most general characteristic equations for one-dimensional, constant-area, inviscid and unreactive flow with no body forces are (Thompson, 1988, pp. 375–377)

$$dP + \rho c du = 0 \qquad \text{on} \quad C^+ \,, \tag{1.36}$$

$$dP - \rho c du = 0 \qquad \text{on} \quad C^- \,. \tag{1.37}$$

Integrating these equations defines the Riemann invariants

$$J^{\pm} = u \pm \int_{P_0}^{P} \frac{dP}{\rho c} = 0 \qquad \text{on} \quad C^{\pm} \,, \tag{1.38}$$

where P_0 corresponds to a reference state of zero flow velocity. This is the most general form of the Riemann invariant. In our case, the Riemann invariant J^- is conserved along a C^- characteristic going through the Taylor wave.

$$J^- = u - \int_{P_0}^{P} \frac{dP}{\rho c} = u - \int_{\rho_0}^{\rho} c \frac{d\rho}{\rho} \tag{1.39}$$

For a real dissociating gas, it is valid for either frozen or equilibrium flow, but not for finite rate kinetics. Equation 1.39 is often simplified for the perfect gas case assuming a constant polytropic exponent γ through the Taylor wave.

$$J^- = u - \frac{2c}{\gamma - 1} = u_2 - \frac{2c_2}{\gamma - 1} = -\frac{2c_3}{\gamma - 1} \tag{1.40}$$

The speed of sound in state 3 can be calculated from the previous equation as

$$c_3 = c_2 - \frac{\gamma - 1}{2} u_2 = \frac{\gamma + 1}{2} c_2 - \frac{\gamma - 1}{2} U_{CJ} \,. \tag{1.41}$$

Inside the Taylor wave, the C^+ characteristics are straight lines with a slope given by $x/t = u + c$, for $c_3 \leq x/t \leq U_{CJ}$. Using the Riemann invariant J^- to relate u and c to the flow parameters in state 3, the flow properties in the Taylor wave can be derived. The speed of sound is

$$\frac{c}{c_3} = \frac{2}{\gamma+1} + \frac{\gamma-1}{\gamma+1}\frac{x}{c_3 t} = 1 - \left(\frac{\gamma-1}{\gamma+1}\right)\left[1 - \frac{x}{c_3 t}\right] \ . \tag{1.42}$$

Equation 1.42 is valid in the expansion wave, for $c_3 t \leq x \leq U_{CJ} t$. The pressure in the Taylor wave can be computed using the isentropic flow relations

$$P = P_3 \left(1 - \left(\frac{\gamma-1}{\gamma+1}\right)\left[1 - \frac{x}{c_3 t}\right]\right)^{\frac{2\gamma}{\gamma-1}} \ , \tag{1.43}$$

where the pressure P_3 behind the Taylor wave is given by $P_3 = P_2(c_3/c_2)^{\frac{2\gamma}{\gamma-1}}$. The region following the Taylor wave is a uniform region of stagnant flow. Figure 1.8 shows the profile of the flow behind the detonation wave. The Taylor wave extends from $x = c_3 t$ to $x = U_{CJ} t$, which means that its end is always located at a fractional distance of c_3/U_{CJ} behind the detonation front. This quantity can be expressed from the detonation jump conditions and the Riemann invariant relationship.

$$\frac{c_3}{U_{CJ}} = \frac{\gamma+1}{\gamma}\frac{\rho_1}{\rho_2} - \frac{\gamma-1}{2} \tag{1.44}$$

In the limit of large CJ Mach numbers, the density ratio $\rho_1/\rho_2 \to \gamma/(\gamma+1)$ and the ratio $c_3/U_{CJ} \to 1/2$. The stagnant region extends half of the distance travelled by the detonation from the closed end of the tube. Experience with computations using realistic values of the flow properties indicates that this is a fairly reliable rule of thumb for fuel-oxygen-nitrogen mixtures.

1.2 Steady-flow air-breathing propulsion

Air-breathing propulsion systems are based on the jet propulsion principle: they develop thrust by imparting momentum to the fluid passing through them. These

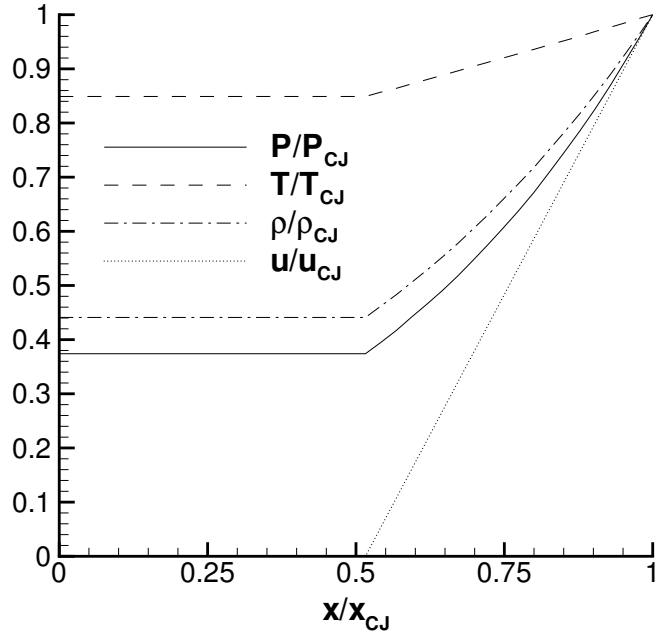

Figure 1.8: Profile of pressure, temperature, density, and flow velocity behind an ideal detonation wave modeled using the one-γ model. $\gamma = 1.2$, $q/RT_1 = 40$.

propulsion systems are steady-flow devices and include propellers, which are more efficient at low flight speeds, and turbojet, turbofan, and ramjet engines, which have a higher performance at high subsonic or supersonic flight speeds. Since we are interested in high-speed propulsion applications, we do not consider propellers, but focus on engines such as the turbojet and ramjet that are based on the Brayton cycle. The Brayton cycle involves deceleration and compression of the inlet air, fuel addition, combustion, and expansion and acceleration of the combustion products to generate thrust. The combustion taking place in these engines consists of low-speed (subsonic) deflagration. This section describes the framework in which the laws of thermodynamics and mechanics can be applied to determine the performance as a function of principal design parameters.

1.2.1 Thrust and efficiencies

The general equations for thrust and efficiency of air-breathing jet engines are derived from the mass, momentum, and energy conservation equations without consideration of the internal mechanisms of the engines. The thrust is usually calculated by considering a control volume completely surrounding the engine, extending far upstream and on the sides, and including the exit plane of the engine, as shown in Fig. 1.9. The engine considered is assumed to have a single exhaust stream. The following analysis is described in detail in Hill and Peterson (1992, pp. 147–149) but is shown here because of its relevance to the thrust calculation for unsteady-flow devices discussed later.

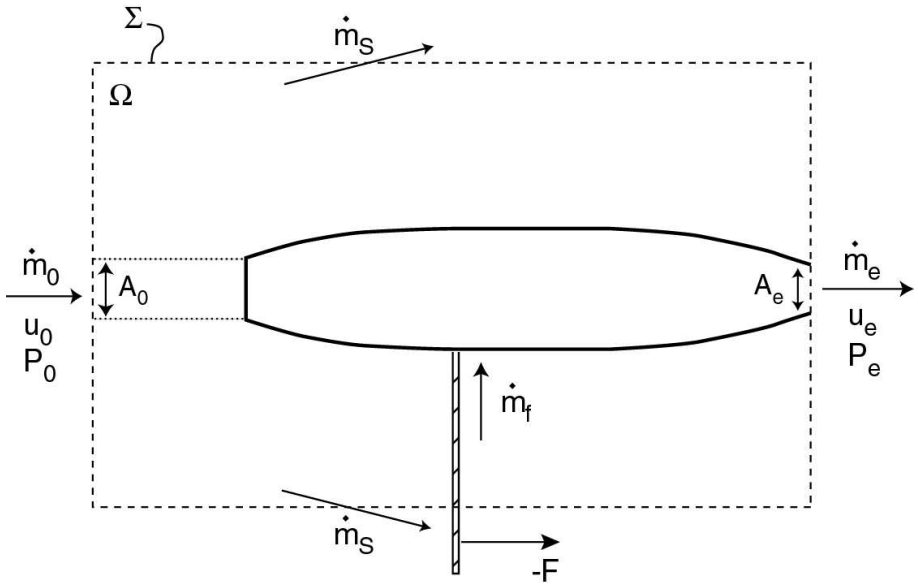

Figure 1.9: Control volume Ω used for the calculation of thrust produced by a general steady-flow propulsion system.

The steady-flow mass equation for the control volume Ω is

$$\int_{\Sigma} \rho(\mathbf{u} \cdot \mathbf{n}) dS = 0 \,, \tag{1.45}$$

which results in $\dot{m}_s = \dot{m}_f + (\rho_0 u_0 - \rho_e u_e) A_e$. The mass flow rate through the side surfaces $\dot{m}_s$ is calculated by considering the additional mass balance through the

engine: $\dot{m}_e = \dot{m}_0 + \dot{m}_f$. Combining the two, we get the following expression for $\dot{m}_s$

$$\dot{m}_s = \rho_0 u_0 (A_e - A_0) \ . \tag{1.46}$$

The steady-flow momentum equation is applied to the control volume Ω

$$\int_\Sigma \rho \mathbf{u} (\mathbf{u} \cdot \mathbf{n}) dS = \Sigma \mathbf{F} \ . \tag{1.47}$$

The forces on the system consist of the pressure forces and the reaction to the thrust. Assuming idealized external flow, the pressure and velocity are assumed constant over the entire control surface, except over the exhaust area of the engine. If the sides of the control volume are sufficiently distant from the engine, the flow crosses the sides with an essentially undisturbed velocity component in the x-direction, and the corresponding momentum term in Eq. 1.47 is $\dot{m}_s u_0$. Rewriting Eq. 1.47 using the result of Eq. 1.46, the momentum equation becomes

$$\begin{aligned} F &= \dot{m}_e u_e - \dot{m}_0 u_0 + (P_e - P_0) A_e \\ &= \dot{m}_0 [(1+f) u_e - u_0] + (P_e - P_0) A_e \ . \end{aligned} \tag{1.48}$$

The steady-flow energy conservation equation for the control volume Ω can be written

$$\int_\Sigma \rho (e + u^2/2)(\mathbf{u} \cdot \mathbf{n}) dS = -\int_\Sigma P (\mathbf{u} \cdot \mathbf{n}) dS + \int_\Omega q dV \tag{1.49}$$

in the absence of body forces. The evaluation of each term on the sides of the control volume eventually leads to

$$\dot{m}_e (h + u^2/2)_e = \dot{m}_0 (h + u^2/2)_0 + \dot{m}_f h_{tf} \ . \tag{1.50}$$

Lean combustion is characteristic of air-breathing propulsion systems, and only a portion of the incoming air mass flow rate reacts with the fuel. Thus, the exit plane

flow consists of a mixture of air and combustion products. We write

$$\dot{m}_e = \phi\dot{m}_0(1+f_{st}) + (1-\phi)\dot{m}_0 \ , \tag{1.51}$$

where f_{st} is the fuel-air mass ratio at stoichiometric conditions and $\phi = f/f_{st} < 1$ is the equivalence ratio. The first term on the right-hand side of Eq. 1.51 represents the mass flow rate of the combustion products and the second term represents the mass flow rate of the unburned air at the exit plane. Similarly, the total enthalpy term is the sum of the contributions of the combustion products and the unburned air.

$$\dot{m}_e h_{te} = \phi\dot{m}_0(1+f_{st})h_{tpr} + (1-\phi)\dot{m}_0 h_{tair} \tag{1.52}$$

Expressing the enthalpy as the sum of the enthalpy of formation at a reference temperature T_{ref} and the sensible enthalpy assuming constant specific heats, the energy equation, Eq. 1.50, can be expressed as

$$\begin{aligned}\phi\dot{m}_0(1+f_{st})\left[\Delta_f h^0_{pr} + C^{pr}_p(T_e - T_{ref})\right] + (1-\phi)\dot{m}_0\left[\Delta_f h^0_{air} + C^{air}_p(T_e - T_{ref})\right] + \dot{m}_e u_e^2/2 = \\ \dot{m}_0\left[\Delta_f h^0_{air} + C^{air}_p(T_0 - T_{ref}) + u_0^2/2\right] + \dot{m}_f\left[(\Delta_f h^0_f + C^f_p(T_f - T_{ref}) + u_f^2/2)\right] \ .\end{aligned} \tag{1.53}$$

The heat of combustion per unit mass of fuel q_f is defined for stoichiometric combustion of fuel and air:

$$q_f = \Delta_f h^0_f + \frac{1}{f_{st}}\Delta_f h^0_{air} - \frac{1+f_{st}}{f_{st}}\Delta_f h^0_{pr} \ , \tag{1.54}$$

which is related to the heat of combustion per unit mass of mixture by $q_c = f_{st}q_f/(1+f_{st})$. Rewriting Eq. 1.53 in terms of the heat of combustion and the total temperature,

$$\dot{m}_e\overline{C_p}(T_{te} - T_{ref}) = \dot{m}_0 C^{air}_p(T_{t0} - T_{ref}) + \dot{m}_f\left[(C^f_p(T_f - T_{ref}) + u_f^2/2)\right] + \dot{m}_f q_f \ , \tag{1.55}$$

where $\overline{C_p}$ is the average specific heat capacity in the exhaust flow

$$\overline{C_p} = \frac{\phi \dot{m}_0 (1 + f_{st}) C_p^{pr} + (1 - \phi) \dot{m}_0 C_p^{air}}{\dot{m}_e} \ , \tag{1.56}$$

and the stagnation temperature at the exit plane is defined with respect to $\overline{C_p}$. Equation 1.55 is usually simplified by neglecting the contribution of the fuel sensible enthalpy and velocity terms compared to the heat of combustion per unit mass of fuel. We also assume equal specific heats for the inlet air and the combustion products. Using the mass balance through the engine, Eq. 1.55 becomes

$$(1 + f) C_p T_{te} = C_p T_{t0} + f q_f \ . \tag{1.57}$$

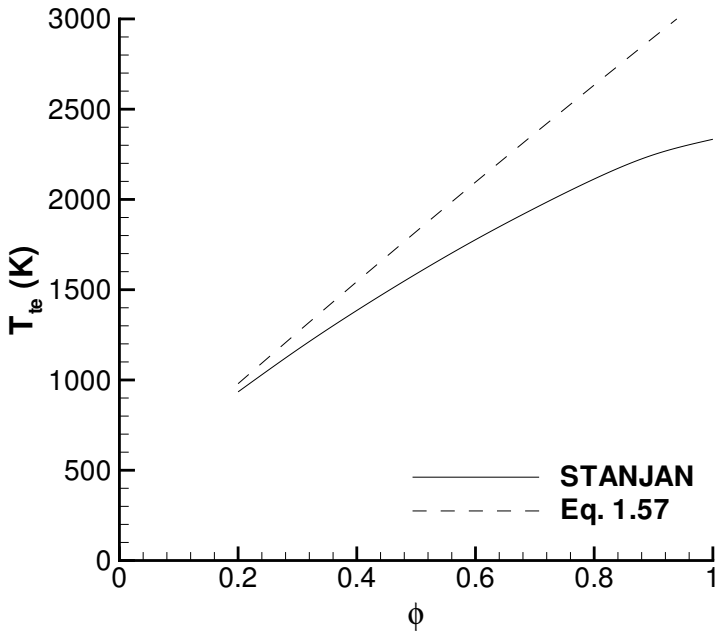

Figure 1.10: Total temperature at the exit plane of a constant-pressure combustor as a function of equivalence ratio for propane-air mixtures. Initial stagnation conditions at the combustor inlet are 400 K and 2 bar.

The result of Eq. 1.57 assumes that the combustion products consist of the major products of the fuel-air chemical reaction. This assumption is acceptable for very lean mixtures. However, as the equivalence ratio increases, the increasing degree

of dissociation in the combustion products caused by the higher combustion temperature decreases the effective energy released into the flow. This is illustrated in Fig. 1.10 where the total temperature at the exit plane of a constant-pressure combustor is plotted as a function of the equivalence ratio. Equilibrium calculations using realistic thermochemistry with STANJAN (Reynolds, 1986) are compared with the simple model of Eq. 1.57. Although both computations agree at very low values of the equivalence ratio, the simple model predicts much larger values for the exit plane total temperature than the equilibrium computations as the equivalence ratio approaches one. Although the agreement could be somewhat improved by computing different values of the heat capacity for combustion products and incoming air, the large discrepancies caused by dissociation effects near stoichiometric point out the limitations of this simple model.

It is useful to define several efficiencies in describing the performance of jet engines. The thermal efficiency η_{th} is defined as the ratio of the rate of addition of kinetic energy to the propellant to the total energy consumption rate

$$\eta_{th} = \frac{u_e^2/2 - u_0^2/2}{f q_f} \ . \tag{1.58}$$

The propulsive efficiency η_p is the ratio of the thrust power to the rate of production of propellant kinetic energy

$$\eta_p = \frac{F u_0}{\dot{m}_0 [u_e^2/2 - u_0^2/2]} \ . \tag{1.59}$$

For air-breathing engines, $f \ll 1$ (usually less than 5% for lean hydrocarbon-air combustion). For a pressure-matched exit nozzle ($P_e = P_0$), the propulsive efficiency may be approximated by

$$\eta_p \approx \frac{2u_0/u_e}{1 + u_0/u_e} \ . \tag{1.60}$$

Finally, the overall efficiency η_0 is the ratio of the thrust power to the rate of energy consumption

$$\eta_0 = \eta_{th}\eta_p = \frac{F u_0}{\dot{m}_f q_f} \ . \tag{1.61}$$

1.2.2 Ramjet

The ramjet is the simplest of all air-breathing jet engines. A standard ramjet consists of an inlet diffuser through which the air flow is decelerated to a low subsonic Mach number and mixed with the fuel, a combustor where the mixture is burned, and an exit nozzle through which the hot products are expelled due to the pressure rise in the diffuser (Hill and Peterson, 1992, Chap. 5.3). A schematic of a ramjet is shown in Fig. 1.11, including the corresponding variations of pressure and temperature throughout the engine. A typical fluid element undergoes a compression through the inlet between stations 0 and 4, then a heat addition process in the combustor (station 4 to 5) before undergoing an expansion through the nozzle (station 5 to 9). Ramjets can operate at subsonic flight conditions, but the increasing pressure rise accompanying higher flight speeds makes them more suitable for supersonic flight.

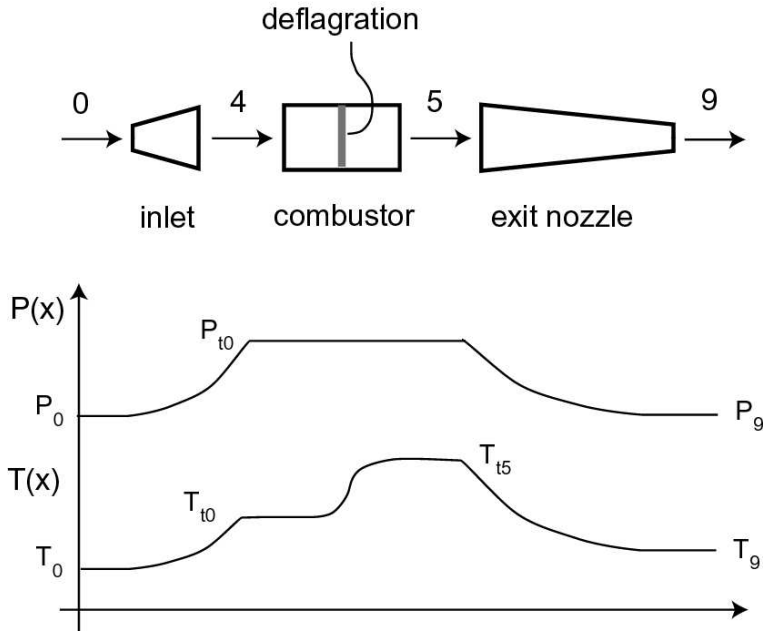

Figure 1.11: Schematic representation of a ramjet. The pressure and temperature profiles through the engine are shown.

The performance of the ideal ramjet can be calculated based on flow path analysis (Hill and Peterson, 1992, Oates, 1984). The simplest performance model of an ideal ramjet is derived assuming that the compression and expansion processes are isentropic and that the combustion process takes place at constant pressure and very

low Mach number. These assumptions are, of course, not realistic due to the presence of irreversible processes such as inlet shocks, mixing, wall friction, and heat transfer. In the ideal ramjet model, we consider steady, inviscid, and adiabatic flow of an ideal gas. Products and reactants are assumed to have the same heat capacity and specific heat ratio. Dissociation of the combustion products is not taken into account. The performance characteristics of an ideal ramjet are usually derived assuming a maximum temperature T_{max} at the combustor outlet due to material limitations (Hill and Peterson, 1992, Chap. 5.3). This maximum temperature implies a limitation on the total temperature at the combustor outlet T_{t5} since it is the temperature of a stationary material element in the flow. The performance of an air-breathing propulsion system is usually expressed in terms of specific thrust, specific impulse, overall efficiency, and thrust-specific fuel consumption. It can be shown that the maximum thrust is generated when the nozzle is pressure-matched, i.e., $P_9 = P_0$ (Hill and Peterson, 1992). For a ramjet with a pressure-matched exit nozzle, the thrust equation, Eq. 1.48, becomes

$$F = \dot{m}_0[(1+f)u_9 - u_0] \; . \tag{1.62}$$

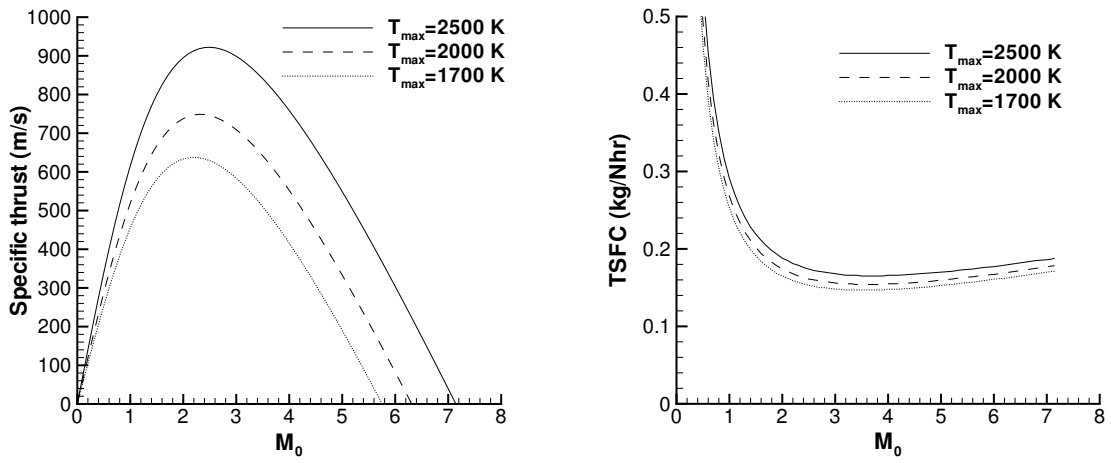

Figure 1.12: Specific thrust (left) and thrust-specific fuel consumption (right) of the ideal ramjet for various values of T_{max}. $q_f = 45$ MJ/kg, $T_0 = 223$ K.

The fuel-air mass ratio f is dictated by the maximum temperature condition and the energy balance for the combustion process (Eq. 1.57), assuming the heat capacity

is constant and equal to a common value for reactants and products

$$C_p T_{t4} + f q_f = (1+f) C_p T_{t5} \; . \tag{1.63}$$

In practice, $f \ll 1$ (usually less than 5% for hydrocarbon fuels) and the fuel mass addition will be neglected. Hence, $F \approx \dot{m}(u_9 - u_0)$. Assuming the nozzle isentropically expands the combustion products to the ambient pressure, the performance parameters of interest (Hill and Peterson, 1992) are the specific thrust

$$\frac{F}{\dot{m}_0} = M_0 c_0 \left[\sqrt{\frac{T_{max}}{T_0}} \left(1 + \frac{\gamma - 1}{2} M_0^2 \right)^{-1/2} - 1 \right] \; , \tag{1.64}$$

the fuel-based specific impulse

$$I_{SPF} = \frac{F}{\dot{m}_f g} \; , \tag{1.65}$$

and the thrust-specific fuel consumption

$$TSFC = \frac{\dot{m}_f}{F} = \frac{f}{F/\dot{m}} \; . \tag{1.66}$$

The specific thrust and thrust-specific fuel consumption of the ideal ramjet are plotted in Fig. 1.12 as a function of the flight Mach number for a heat of combustion representative of hydrocarbon fuels. The decrease in specific thrust at high flight Mach numbers is due to the limitation of the combustor outlet temperature. Lower maximum temperatures decrease the specific thrust because less fuel can be added and the combustion has to occur at a leaner composition. The thrust-specific fuel consumption decreases from high values at subsonic flight Mach numbers and remains finite as the specific thrust approaches zero due to the maximum temperature condition. The ideal ramjet model is a useful tool to draw an upper bound on the possible performance of real ramjets, since all the processes are assumed to be ideal. In practice, stagnation pressure losses due to shock systems in the inlet, mixing, wall friction and heat transfer will generate performance losses compared to the ideal case.

Methodologies have been developed to take into account the non-ideal behavior of the various engine components (Hill and Peterson, 1992, Oates, 1984).

1.2.3 Turbojet

Because the compression in the ramjet engine is uniquely due to the ram effect, the ramjet cannot develop takeoff thrust. In fact, ramjets do not perform well unless the flight speed is considerably above the speed of sound. One way to overcome this disadvantage is to install a mechanical compressor upstream of the combustion chamber so that even at zero speed, air can be drawn into the engine to produce thrust. The presence of the compressor requires the presence of a turbine driven by the hot gas expanding from the combustion chamber into the nozzle in order to supply the power needed by the compressor. Thus, a turbojet engine includes a compressor, which is used to add work to the flow, and a turbine, which powers the compressor, as seen in Fig. 1.13.

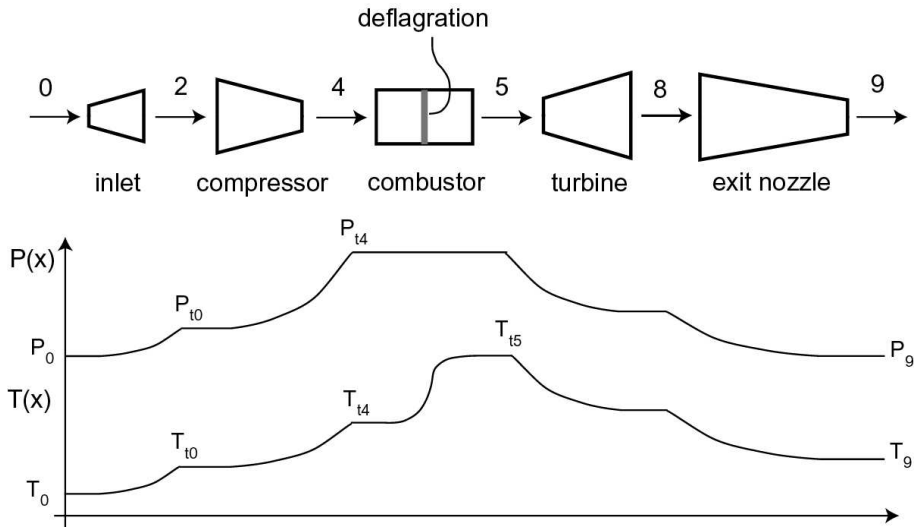

Figure 1.13: Schematic of a turbojet engine, including the variation of pressure and temperature across the engine.

The turbine blades are subjected to high temperatures, and a limitation is usually placed on the temperature at the combustor outlet due to material considerations. The ideal turbojet can be analyzed in the same fashion as the ramjet, assuming that

all processes except combustion are isentropic (Hill and Peterson, 1992, Chap. 5.4). We use the same assumptions as those used in the ideal ramjet model. The flow undergoes an isentropic compression through the inlet: $P_{t2} = P_{t0}$ and $T_{t2} = T_{t0}$. The compressor is characterized by a compression ratio π_c, which is usually specified. Assuming the compression is isentropic, $P_{t4} = \pi_c P_{t2}$ and $T_{t4} = \pi_c^{(\gamma-1)/\gamma} T_{t2}$. The combustion occurs at constant pressure. The flow then goes through the turbine, which must supply the power required to drive the compressor. For steady adiabatic flow in both components, an energy balance can be written between the compressor and the turbine

$$(1+f)\dot{m}_0(h_{t8} - h_{t5}) = \dot{m}_0(h_{t4} - h_{t2}) \; . \tag{1.67}$$

Assuming $f \ll 1$ and that the specific heat capacity of the products is the same as that of the reactants, the equation simplifies to $T_{t8} \approx T_{t5} + T_{t4} - T_{t2}$. After its passage through the turbine, the flow is expanded through an exit nozzle into the atmosphere. For a pressure-matched nozzle, the specific thrust of an ideal turbojet engine is given below and the other relevant performance parameters can be calculated using it.

$$\frac{F}{\dot{m}_0} = c_0 \left[\sqrt{\frac{2}{\gamma - 1} \left[\left(\frac{T_{max}}{T_{t0}} - (\pi_c^{\frac{\gamma-1}{\gamma}} - 1) \right) \left(1 + \frac{\gamma - 1}{2} M_0^2 \right) - \pi_c^{-\frac{\gamma-1}{\gamma}} \frac{T_{max}}{T_{t0}} \right]} - M_0 \right] \tag{1.68}$$

Figure 1.14 shows the variation of the specific thrust of the ideal turbojet with flight Mach number for different compression ratios. The case with $\pi_c = 1$ is the baseline case corresponding to the ramjet. As the compression ratio increases, the specific thrust of the turbojet increases, in particular at subsonic flight speeds. However, the thrust-producing range of the turbojet becomes smaller with increasing π_c due to the maximum temperature limitation. Similarly, for high compression ratio values (above 20), increasing π_c does not benefit the specific thrust because less fuel has to be added in order to satisfy the maximum temperature condition. The compression ratio is usually chosen based on consideration of both specific thrust and thrust specific fuel consumption, and depends strongly on the design point. The influence of irreversible processes through the different components of the engine on the perfor-

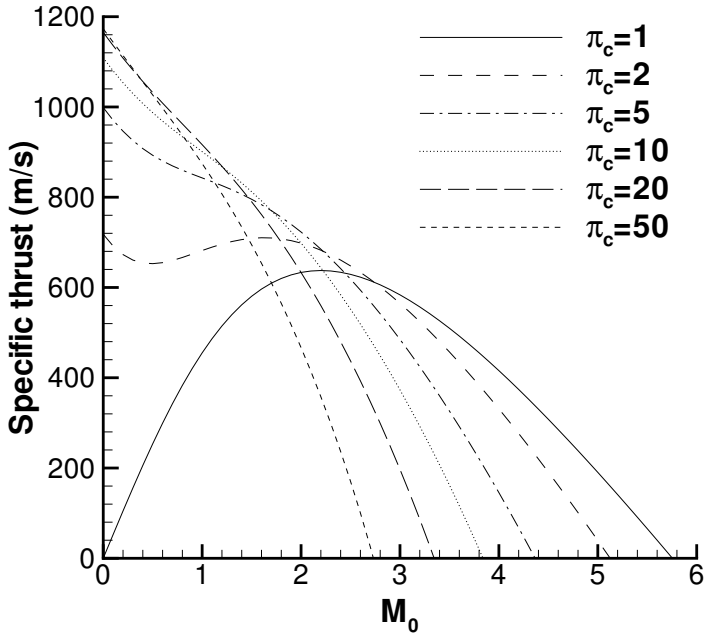

Figure 1.14: Specific thrust of the ideal turbojet as a function of flight Mach number for varying compression ratios. $T_{max} = 1700$ K, $q_f = 45$ MJ/kg, $T_0 = 223$ K.

mance parameters can be estimated, and some of the procedures developed for this purpose are described in Hill and Peterson (1992) and Oates (1984). In particular, turbojet operation at $M_0 \gg 1$ (see Fig. 1.14) is not realistic due to losses in real inlet diffusers.

1.2.4 Thermodynamic cycle analysis

A very useful method to estimate performance for steady-flow propulsion systems is to represent the various processes occurring inside the engine on a thermodynamic state diagram. The results obtained previously, based on flow path analysis for the ideal ramjet and the ideal turbojet, can all be obtained using a thermodynamic approach, which considers the processes from a thermodynamic standpoint, without associating them with the actual flow through the engine. This approach is possible only because of the correspondence (for steady flow) between thermodynamic state points and flow locations within the engine. We start by describing the general cycle analysis for

thermodynamic systems.

1.2.4.1 General cycle analysis

The thermodynamic processes encountered in air-breathing propulsion involve sequential compression, combustion, and expansion. This sequence is turned into a closed cycle through a constant-pressure process during which the fluid exhausted into the atmosphere at the end of the expansion process is converted into the inlet fluid by exchanging heat and work with the surroundings. The thermal efficiency of an arbitrary cycle involving adiabatic combustion can be defined as the ratio of the work done by the system to the heat of combustion of the mixture.

$$\eta_{th} = \frac{w}{q_c} \tag{1.69}$$

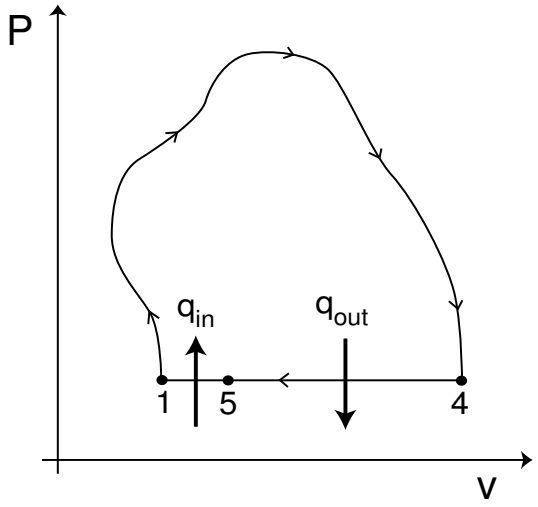

Figure 1.15: Arbitrary thermodynamic cycle ending with constant-pressure process.

The work done and mixture heat of combustion can be clarified by considering a thermodynamic cycle consisting of an arbitrary adiabatic process taking the system from its initial state 1 to state 4, and ending with a constant-pressure process taking the system back to state 1. As shown in Fig. 1.15, there is an intermediate state 5 between 4 and 1. The heat interaction between steps 4 and 5 is required to remove an amount of thermal energy $q_{out} > 0$ from the products of combustion and cool

the flow down from the exhaust temperature to the ambient conditions. Since this process occurs at constant pressure, the heat interaction can be determined from the enthalpy change

$$q_{out} = h_4 - h_5 \ . \tag{1.70}$$

The heat interaction between steps 5 and 1 is required to add an amount of thermal energy $q_{in} > 0$ in order to convert the combustion products back to reactants. This interaction also takes place at constant pressure so that

$$q_{in} = h_1 - h_5 \ . \tag{1.71}$$

Note that this defines the quantity $q_c = q_{in}$ in a fashion consistent with standard thermochemical practice if the ambient conditions correspond to the thermodynamic standard state. Applying the First Law of Thermodynamics around the cycle, the work done by the system can be computed as

$$w = q_{in} - q_{out} = h_1 - h_4 \ . \tag{1.72}$$

The thermal efficiency can, therefore, be written as

$$\eta_{th} = \frac{h_1 - h_4}{h_1 - h_5} = \frac{h_1 - h_4}{q_c} \ , \tag{1.73}$$

which agrees with the definition given in Eq. 1.69 in terms of the mixture heat of combustion.

For an ideal (reversible) process, the heat removed during the constant-pressure process 4–5 can be expressed as

$$q_{out} = \int_{s_5}^{s_4} T ds \tag{1.74}$$

and the thermal efficiency is

$$\eta_{th} = 1 - \frac{\int_{s_5}^{s_4} T ds}{q_c} \ . \tag{1.75}$$

For a given initial state 1 and a given mixture, state 5 is fixed and the value of the entropy is determined by the heat of combustion and the product and reactant composition. Thus, the heat removed q_{out} increases and the thermal efficiency decreases with increasing values of s_4. In general, the thermal efficiency is maximized when the entropy rise during process 1–4 is minimized.

This general result can be computed explicitly if we consider a perfect gas and take $s_5 = s_1$, which is approximately satisfied for real mixtures and exactly so for the equivalent heat addition model. This model considers the case of the perfect gas $P = \rho RT$ and models the combustion process as the addition of an amount of heat equal to the heat of combustion of the mixture. We assume equal specific heat capacities for reactants and products

$$C_p = \frac{\gamma}{\gamma - 1} R \tag{1.76}$$

and the enthalpy in the reactants and products can be expressed as

$$h_1 = C_p T_1 \qquad h_2 = C_p T_2 - q_c \; . \tag{1.77}$$

In the simple heat addition model, the heat rejected during the final constant-pressure portion of the cycle is a function of the temperature at states 1 and 4

$$q_{out} = C_p (T_4 - T_1) \; . \tag{1.78}$$

The thermal efficiency is written as

$$\eta_{th} = 1 - \frac{C_p (T_4 - T_1)}{q_c} \; . \tag{1.79}$$

The integral of Eq. 1.74 can also be calculated explicitly as a function of the entropy rise between states 1 and 4, and the thermal efficiency becomes

$$\eta_{th} = 1 - \frac{C_p T_1}{q_c} \left[\exp\left(\frac{s_4 - s_1}{C_p} \right) - 1 \right] \; . \tag{1.80}$$

The overall entropy rise is the sum of the entropy rise generated by combustion and

of the entropy increments generated by irreversible processes such as shocks, friction, heat transfer, Rayleigh losses (combustion or equivalent heat addition at finite Mach number), or fuel-air mixing (Foa, 1960). The entropy increment associated with the combustion process is often the largest of all increments in the cycle. Because of the dependence of the thermal efficiency on the total entropy rise, the selection of the combustion mode is critical to engine performance.

1.2.4.2 Cycle analysis for propulsion systems

For steady-flow engines, the cycle analysis based on a closed system (fixed mass of material) is completely equivalent to the flow path analysis based on an open system, as long as the mass and momentum contributions of the fuel are negligible and the exhaust flow is fully expanded at the exit plane (Foa, 1960, Chap. 13). Within these assumptions, we can make a correspondence between states in the cyclic process of Fig. 1.15 and an open thermodynamic cycle. If the states in the open and closed cycles are equivalent, then the thermal efficiencies are the same for the two processes. The equivalence is based on the control volume analysis of the energy balance in an open system whose inlet plane is at state 1 and exit plane is at state 4.

$$h_1 + u_1^2/2 = h_4 + u_4^2/2 \tag{1.81}$$

Using the cycle thermal efficiency as defined in Eq. 1.69, we find that

$$\eta_{th} = \frac{u_4^2 - u_1^2}{2q_c} \ . \tag{1.82}$$

Based on this equivalence, the thrust of a steady pressure-matched propulsion system can be directly calculated from the thermal efficiency (Foa, 1960, Chap. 13).

$$F = \dot{m}_1 \left(u_4 - u_1\right) = \dot{m}_1 \left(\sqrt{u_1^2 + 2\eta_{th} q_c} - u_1\right) \tag{1.83}$$

In air-breathing propulsion system analysis, the heat of combustion per unit mass of the mixture is often replaced in terms of the heat of combustion per unit mass of fuel

and the fuel-air ratio: $q_c = fq_f/(1+f)$.

Equations 1.80 and 1.83 allow to calculate the thermal efficiency of the propulsive flow through computation of the entropy increments associated with all the processes to which the flow is subjected through the cycle. The overall entropy increment is the sum of the increments associated with each process. The thermal efficiency decreases with increasing entropy rise.

Flow path analysis shows that stagnation pressure losses through the engine are detrimental to the thermal efficiency and the performance. Stagnation pressure losses are generated by entropy increments and can be related to them the following way. Consider a steady process bringing the flow from a state a to a state b. Using isentropic processes to connect those states to their respective stagnation states, the entropy rise can be expressed as a function of the stagnation properties.

$$\frac{\Delta s}{R} = \frac{\gamma}{\gamma - 1} \ln\left(\frac{T_{tb}}{T_{ta}}\right) - \ln\left(\frac{P_{tb}}{P_{ta}}\right) \tag{1.84}$$

The largest entropy rise is usually associated with the combustion process. For adiabatic processes ($T_{tb} = T_{ta}$), the stagnation pressure ratio can be related to the entropy increment Δs

$$\frac{P_{tb}}{P_{ta}} = \exp\left(-\frac{\Delta s}{R}\right) . \tag{1.85}$$

The propulsive performance calculation of Eq. 1.83 using the entropy increments through the cycle has been called the "entropy method" by Foa (1960, p. 282). It does not require any consideration of the flow path since the effects of the cycle processes are all accounted for in the cycle calculation of the thermal efficiency. Foa (1959, p. 382) proposes a method to extend the entropy method to conditions when the exit plane flow is not fully expanded by correcting the exit velocity for fully expanded flow. For low pressure ratios between the exit plane and the freestream, the correction factor is found to be very close to 1 and Foa (1959) concludes that the exhaust may be treated in good approximation as completely expanded. Foa (1951, 1959, 1960) describes how to calculate the entropy increments associated with the compression, expansion, and combustion processes, as well as those induced by pressure exchange

and mixing.

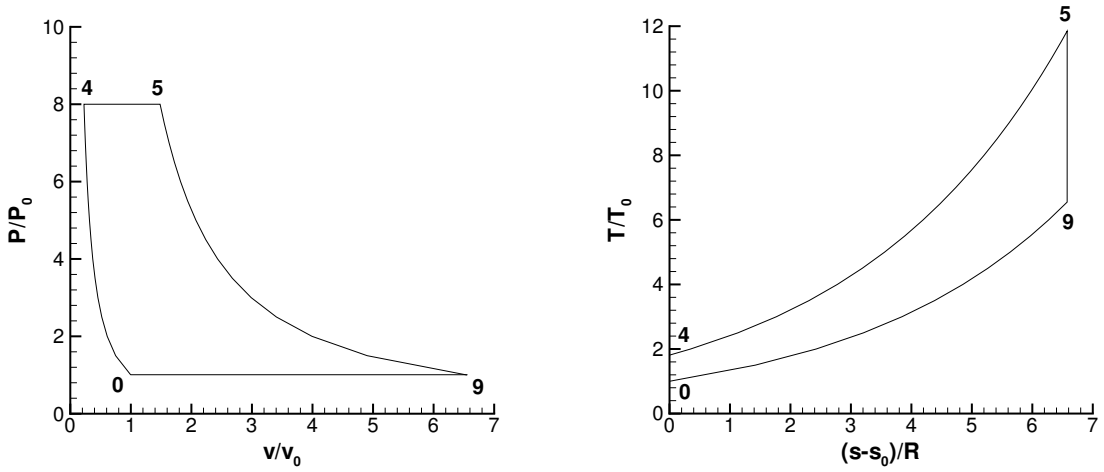

Figure 1.16: Brayton cycle plotted in the pressure-specific volume plane (left) and the temperature-entropy plane (right). $q_f = 45$ MJ/kg, $f = 0.05$, $\gamma = 1.4$, $T_0 = 223$ K, $P_4/P_0 = 8$.

Both the ramjet and turbojet engines operate following the same thermodynamic cycle, called the Brayton cycle. The Brayton cycle consists of the following processes: isentropic compression from state 0 to state 4, constant-pressure combustion from state 4 to state 5, isentropic expansion from state 5 to state 9, and constant-pressure heat removal from state 9 to state 0. The ideal Brayton cycle is plotted in the pressure-specific volume plane and the temperature-entropy plane in Fig. 1.16. The thermal efficiency of the Brayton cycle is obtained from Eq. 1.79

$$\eta_{th} = 1 - \frac{C_p T_0}{f q_f}\left(\frac{T_9}{T_0} - 1\right) . \tag{1.86}$$

The temperature ratio can be calculated using the isentropic flow relationships and the assumption of constant-pressure combustion ($P_4 = P_5$).

$$\begin{aligned} \frac{T_9}{T_0} &= \frac{T_9}{T_5}\cdot\frac{T_5}{T_4}\cdot\frac{T_4}{T_0} \\ &= \left(\frac{P_0}{P_5}\right)^{\frac{\gamma-1}{\gamma}}\left(1 + \frac{f q_f}{C_p T_4}\right)\left(\frac{P_4}{P_0}\right)^{\frac{\gamma-1}{\gamma}} \\ &= 1 + \frac{f q_f}{C_p T_4} \end{aligned} \tag{1.87}$$

We obtain the classical expression for the thermal efficiency of the Brayton cycle (Oates, 1984, pp. 123–124)

$$\eta_{th} = 1 - \frac{T_0}{T_4} \; . \tag{1.88}$$

The performance parameters presented in Sections 1.2.2 and 1.2.3 can be derived from Eq. 1.88 using the entropy method, as long as conditions 1. and 2. are satisfied. The efficiency of the Brayton cycle increases with increasing static temperature at the beginning of the combustion process. According to Foa (1960, pp. 283–287), this result can be generalized to a variety of combustion modes.

1.3 Unsteady-flow air-breathing propulsion

An entirely different class of air-breathing engines is based on the unsteady generation of jets from a combustion chamber. The concept of intermittent combustion jet engines was actually the precursor of steady-flow concepts that led to the development of the gas turbine (Foa, 1959, Chap. 14). Unsteady-flow propulsion concepts present advantages related to the unsteady nature of the flow, such as inertia effects for scavenging of the combustion chamber and pressure exchange for precompression of the reactants. However, some of the characteristic features of unsteady flows have not yet been fully understood and exploited, in spite of significant efforts in the 1950s on pulsejet engines and, more recently, on pulse detonation engines. Due to the complexity of the unsteady flow in these engines, there are no unsteady-flow analogs to the ideal ramjet or turbojet models. We present a flow path analysis for unsteady air-breathing engines before considering to what extent thermodynamic cycle analysis can be applied to unsteady propulsion[1]. Then, we review some of the literature on the two principal types of unsteady air-breathing engines studied, the pulsejet and the pulse detonation engine.

[1] The analysis of Sections 1.3.1 and 1.3.2 is based on work presented in Wintenberger et al. (2004).

1.3.1 Flow path analysis

We consider a general unsteady propulsion system during steady flight with a steady inflow and an unsteady outflow. The unsteadiness is assumed to be confined to the interior of the engine and downstream of the exit plane. The assumption of steady inflow is more realistic in terms of the conventional steady inlets under consideration for pulse detonation engine applications (Mullagiri et al., 2003, Nori et al., 2003). We perform a control volume analysis for the control volume of Fig. 1.9 completely surrounding the engine. However, in the unsteady case, the properties at the exit plane of the engine are time-dependent. We consider the unsteady equations for mass, momentum, and energy conservation (Hill and Peterson, 1992).

$$\frac{d}{dt}\int_{\Omega}\rho dV + \int_{\Sigma}\rho(\mathbf{u}\cdot\mathbf{n})dS = 0 \tag{1.89}$$

$$\frac{d}{dt}\int_{\Omega}\rho\mathbf{u}dV + \int_{\Sigma}\rho\mathbf{u}(\mathbf{u}\cdot\mathbf{n})dS = \Sigma\mathbf{F} \tag{1.90}$$

$$\frac{d}{dt}\int_{\Omega}\rho(e+u^2/2)dV + \int_{\Sigma}\rho(e+u^2/2)(\mathbf{u}\cdot\mathbf{n})dS = -\int_{\Sigma}P(\mathbf{u}\cdot\mathbf{n})dS \tag{1.91}$$

The first term in each equation represents the contribution due to storage in the control volume. Assuming that the engine operates in a cyclic mode, there can be no storage during steady flight and the time derivatives of volume integrals vanish when integrated over a cycle. We average those equations over a cycle, assuming that the unsteadiness is limited to the exhaust flow and does not affect the assumption of ideal external flow around the engine. The mass equation, Eq. 1.89, yields a result identical to the steady case (Eq. 1.46), using the mass balance in the engine $\overline{\dot{m}_e(t)} = \dot{m}_0 + \overline{\dot{m}_f(t)}$, where $\overline{()}$ represents temporal averaging over a cycle. Based on this result, the average mass and energy equations can be expressed as

$$\overline{F} = \frac{1}{\tau}\int_0^{\tau}F(t)dt = \overline{\dot{m}_e(t)u_e(t)} - \dot{m}_0u_0 + A_e\left(\overline{P_e(t)} - P_0\right)\ , \tag{1.92}$$

$$\overline{\dot{m}_e(t)h_{te}(t)} = \dot{m}_0h_{t0} + \overline{\dot{m}_f(t)}\cdot q_f\ . \tag{1.93}$$

These equations clearly show that the standard results for steady flow (Eqs. 1.48 and 1.57) do not apply in the unsteady case and that the thrust depends on the details of the time dependence of the pressure, velocity, and mass flow rate at the engine exit. For subsonic flow, the problem is even more involved because the unsteadiness can potentially extend to the inlet flow, rendering the analysis more complicated. Even if the exit is pressure-matched on average ($\overline{P_e} = P_0$), this does not mean that the thrust is optimized or uniquely determined by the time-averaged exit plane properties. Hence, for a general unsteady propulsion system, it is necessary to carry out the integration of the exit plane properties to calculate the thrust.

1.3.2 Thermodynamic cycle analysis

A key issue that must be dealt with in any unsteady propulsion system analysis is the role of unsteady flow in the conversion of thermal energy into impulse. In the case of steady flow, it is sufficient to consider the total enthalpy $h + u^2/2$, and the usual idealized isentropic compressions and expansions accomplish the conversion between thermal and kinetic energy. This is the standard approach used in flow path analysis of air-breathing systems such as turbines, ramjets, and scramjets (Section 1.2.4). For these conventional steady-flow propulsion systems, the energy conservation and known entropy changes uniquely determine the exit velocity, and it is possible to focus on a thermodynamic interpretation based solely on thermodynamic variables (the entropy method).

However, in the case of unsteady flow, the conversion of thermal energy into impulse is not uniquely determined by the thermodynamic state changes. This means that energy balance statements for the total energy $e + u^2/2$ must be considered and that the unsteady conversion of thermal energy into kinetic energy, including wave propagation processes, has to be computed for idealized representations of the processes in the engine. This has been recognized by Foa (1960, Chap. 15), who explicitly computes the wave processes using the method of characteristics to analyze a valved pulsejet. In the case of internal combustion engines, the Otto and Diesel

cycles are indeed analyzed with a state approach using only thermodynamic variables, most commonly (P,v) or (T,s). In those examples, the energy balance statement is simplified by neglecting the kinetic energy of the gas. For an arbitrary unsteady-flow air-breathing propulsion system, there is no way to uniquely and rigorously use a given sequence of thermodynamic states to define the conversion of thermal energy to velocity - a conversion that is required in order to compute the momentum balance and net force on the engine.

It is possible to extend the entropy method to estimate the performance of a limited range of unsteady propulsion systems. The entropy method, described in Section 1.2.4, assumes that the mass and momentum contributions of the fuel input are negligible ($f \ll 1$) and that the exit velocity is pressure-matched ($P_e = P_0$). Recognizing that it is difficult to maintain complete flow expansion in an unsteady exhaust flow, we adopt the method of Foa (1959, p. 382) to account for conditions when the flow is not fully expanded, by multiplying the exit velocity for fully-expanded flow by a correction factor, which can be estimated assuming quasi-steady flow. Thus, the results for under-expanded flow at the exit plane can be deduced from the results for fully-expanded flow, and we now assume that $\overline{P_e} = P_0$.

The entropy method is based upon the steady-flow energy equation (Eq. 1.57). In general, the cycle average of the unsteady energy equation, Eq. 1.93, is not equivalent to the classical steady-flow result. For example, in unsteady inviscid flow, the rate of change of the stagnation enthalpy is actually related instantaneously to the local rate of pressure change

$$\frac{Dh_t}{Dt} = \frac{1}{\rho}\frac{\partial P}{\partial t} \ . \tag{1.94}$$

This can result in unsteady exit velocities that are significantly different than in the steady case. In order to illustrate this point, the pressure-velocity diagram of Fig. 1.17 shows the different exit velocities that can be reached from the same initial state (labeled 5) through a steady and an unsteady expansion. In steady flow, the exit velocity is calculated using the conservation of stagnation enthalpy through the

expansion process.

$$\frac{u_e}{c_5} = \sqrt{\frac{2}{\gamma - 1}\left[1 - \left(\frac{P_e}{P_5}\right)^{\frac{\gamma}{\gamma-1}}\right]} \tag{1.95}$$

For unsteady flow, the instantaneous exit velocity is calculated by using the Riemann invariant along a C^+ characteristic going across the left-facing expansion wave.

$$\frac{u_e}{c_5} = \frac{2}{\gamma - 1}\left[1 - \left(\frac{P_e}{P_5}\right)^{\frac{\gamma-1}{2\gamma}}\right] \tag{1.96}$$

At the same pressure ratio, values both lower and higher than the steady state values can be obtained through an unsteady expansion, depending on the pressure ratio. In reality, the exit velocity does not take a single value during an unsteady process and the value shown here is only representative of the beginning of the process. However, this comparison shows that the value of the velocity at the exit plane is not uniquely determined by thermodynamics alone and also that this value does not uniquely determine the specific impulse.

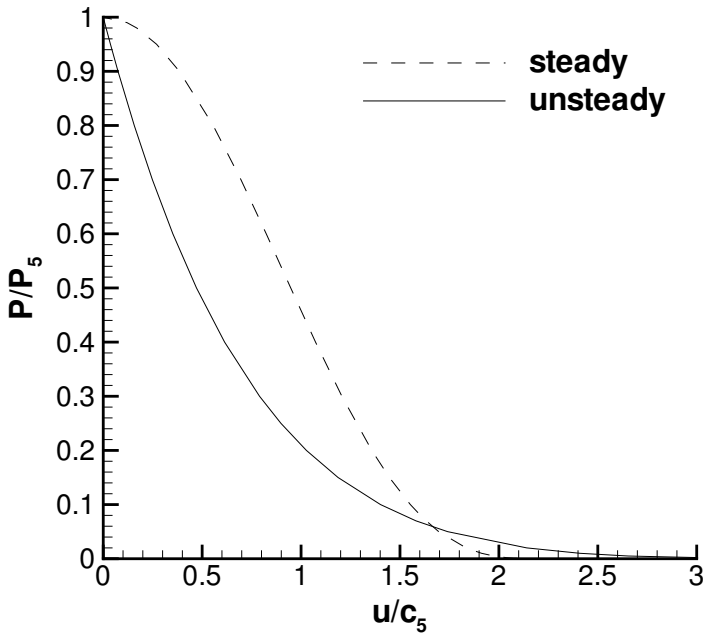

Figure 1.17: Steady- and unsteady-flow expansion from the same initial state. $\gamma = 1.4$.

Hence, it is unclear whether the entropy method can be extended to an arbitrary unsteady flow. Foa (1951, 1959, 1960) suggested an extension to the entropy method for unsteady flows by redefining the average of the exit plane properties as

$$\langle X_e \rangle = \frac{1}{\tau \overline{\dot{m}_e}} \int_0^\tau \dot{m}_e(t) X_e(t) dt \ . \tag{1.97}$$

Using this averaging method and assuming the conditions for use of the entropy method are satisfied (i.e., $f \ll 1$ and $\overline{P_e} = P_0$), Eqs. 1.92 and 1.93 can be rewritten the following way

$$\overline{F} = \dot{m}_0(\langle u_e \rangle - u_0) \ , \tag{1.98}$$

$$\langle h_{te} \rangle = h_{t0} + f q_f \ , \tag{1.99}$$

defining f as $f = \overline{\dot{m}_f}/\dot{m}_0$. These equations are analogous to the steady-flow equations used in the entropy method. This means that the thermal efficiency can be defined for unsteady flows as well

$$\eta_{th} = \frac{\langle u_e^2 \rangle - u_o^2}{2 f q_f} \tag{1.100}$$

and using the energy conservation equation (Eq. 1.99), this is equivalent to

$$\eta_{th} = 1 - \frac{\langle h_e \rangle - h_0}{f q_f} \ . \tag{1.101}$$

This is the desired extension to the steady-flow result of the entropy method. In order to calculate performance from Eqs. 1.100 and 1.101, the averages $\langle u_e \rangle$ and $\langle u_e^2 \rangle$ have to be calculated. The key point of difference with the conventional steady-flow analysis is that, in general, $\langle u_e \rangle^2 \neq \langle u_e^2 \rangle$. Foa (1960, p. 281) suggests that the differences be taken into account by defining an efficiency of non-uniformity

$$\eta_\nu = \frac{\langle u_e \rangle^2}{\langle u_e^2 \rangle} \ . \tag{1.102}$$

By definition, the efficiency of non-uniformity is less than one and equals one only

when the exhaust flow is steady or a square wave function of time, corresponding to an intermittent constant-exit velocity discharge of the gas. The entropy method is then generalized to unsteady flows (Foa, 1951)

$$\overline{F} = \dot{m}_0 \left(\sqrt{\eta_\nu (2\eta_{th} f q_f + u_o^2)} - u_0 \right) . \tag{1.103}$$

Equation 1.103 shows that fluctuations from the steady exit velocity profile, corresponding to $\eta_\nu \leq 1$, result in performance losses compared to the steady-flow case. The maximum performance is obtained when $\eta_\nu = 1$, i.e., when the exhaust flow is steady or a square wave function of time. This approach assumes that the average exit pressure is equal to the ambient pressure and requires an estimate of the magnitude of η_ν. The verification of this assumption and the calculation of η_ν require detailed experimental measurements, unsteady analytical models, or numerical simulations. In conclusion, the entropy method as described in Section 1.2.4 ($\eta_\nu = 1$) is rigorously applicable only to propulsion systems for which the exhaust flow is either steady or a square wave function of time. The latter option represents an ideal case for unsteady propulsion; however, whether it is representative of the exhaust flow in a practical unsteady engine is unclear.

The various efficiencies associated with the flow through an unsteady air-breathing propulsion system have to be defined more generally (Foa, 1960, Chap. 13) than for steady-flow propulsion systems (Eqs. 1.58, 1.59, 1.61). The overall efficiency is defined as the ratio between the propulsive power and the energy input

$$\eta_0 = \frac{F u_0}{\overline{\dot{m}_f} q_f} = \frac{u_0 (\langle u_e \rangle - u_0)}{f q_f} . \tag{1.104}$$

The propulsive efficiency is defined as the ratio between the propulsive power and the mechanical energy output from the transformations in the propulsive flow, which is the sum of the propulsive work and the kinetic energy of the exhaust

$$\eta_p = \frac{F u_0}{F u_0 + \frac{1}{2} \dot{m}_e \langle (u_e - u_0)^2 \rangle} , \tag{1.105}$$

which, for fully expanded flow ($\overline{P_e} = P_0$) and with $f \ll 1$, becomes

$$\eta_p = \frac{2(\langle u_e \rangle - u_0)u_0}{\langle u_e^2 \rangle - u_0^2} \,. \tag{1.106}$$

The type of exit velocity profile most favorable from the standpoint of propulsive efficiency, for given flight conditions and thermal efficiency, corresponds to maximum $\langle u_e \rangle$, with $\langle u_e^2 \rangle$ held constant. Foa (1951) shows that this condition is reached for $\eta_\nu = 1$, i.e., for steady or square wave-type exit velocity profiles. Hence, propulsive flows characterized by $\eta_\nu = 1$ have a maximized propulsive efficiency.

1.3.3 Selection of the combustion mode

We consider a general unsteady propulsion system which satifies the conditions of application of the entropy method. Since the entropy increment associated with combustion is the largest component of the total entropy rise that determines the thermal efficiency, it is critical to select the combustion mode minimizing the entropy increment for the application considered.

The type of constraints on the propulsion system strongly influences the optimal combustion mode. In particular, whether the initial temperature before combustion, T_i, is prescribed or a maximum temperature, T_{max}, is fixed at the combustor outlet (usually for material considerations) modifies the trends observed. Foa (1951) showed that the optimal combustion mode for the ramjet, where T_{max} is usually prescribed, is constant-pressure combustion. However, in the case of pulsejets where the initial temperature before combustion, T_i, is prescribed, the optimal combustion mode is found to be constant-volume combustion at low flight Mach numbers (Foa, 1951). The use of unsteady combustion modes offers the possibility of avoiding continuous exposure of the materials to the peak combustion temperatures. Therefore, the maximum allowable temperature of the burned gases is often considerably higher with unsteady than with steady combustion modes, which may result in a lower entropy rise and higher performance. These considerations led Foa (1960, pp. 345–346) to conclude that the most efficient jet engine is characterized by a steady inflow, an

unsteady combustion mode, and a steady or square wave-type exhaust flow.

Detonation appears as a particularly attractive combustion mode due to the fact that the Chapman-Jouguet detonation corresponds to the end state of minimum entropy on the Hugoniot curve. However, end states on the Hugoniot curve correspond to processes starting from the same initial state. In unsteady flows, a variety of combustion processes can be started from a given initial state, whereas in steady-flow engines, the processes are constrained because the reaction front has to be stationary. This constraint requires a much higher stagnation temperature upstream of the combustion chamber, as shown in Section 3.2.1. At given flight conditions and in the absence of precompression, the static temperature upstream of the combustion chamber will be lower for detonations than for deflagrations due to the high flow velocity required to stabilize the detonation wave in the combustor. When considering this fact, Foa (1960, pp. 285–286) concludes that detonation produces, in steady-flow engines, a higher entropy rise than deflagration. Based on this argument, Foa (1960) suggests that detonations offer better promise as an unsteady than as a steady combustion mode. This point will be discussed in more detail in Section 2.1.

1.3.4 Pulsejet

The pulsejet is a compressorless, unsteady-flow jet engine without wave precompression of the combustible charge. A pulsejet is mechanically very simple and consists of a short inlet diffuser leading to a set of flow check valves, followed by a combustion chamber and a shaped tube, as shown in Fig. 1.18. A fuel injection system is located downstream of the valves. The air flowing into the engine through the valves is mixed with a fuel spray, and the mixture is ignited. As a result of the pressure rise generated by the explosion, the inlet flow check valves close and the exhaust gases expand outside through the exhaust tube. The exhaust of the burned gases generates expansion waves that reduce the pressure behind the check valves until they open again and a fresh charge of air enters. The cycle is then repeated. A spark is required only to start because after the first cycle, the hot gases from the previous cycle ignite

the fresh combustible charge. The most common version of the pulsejet is the valved pulsejet; however, there exist valveless pulsejets, which rely on wave processes in an adequately designed inlet to achieve the same function as intake valves in the valved pulsejet.

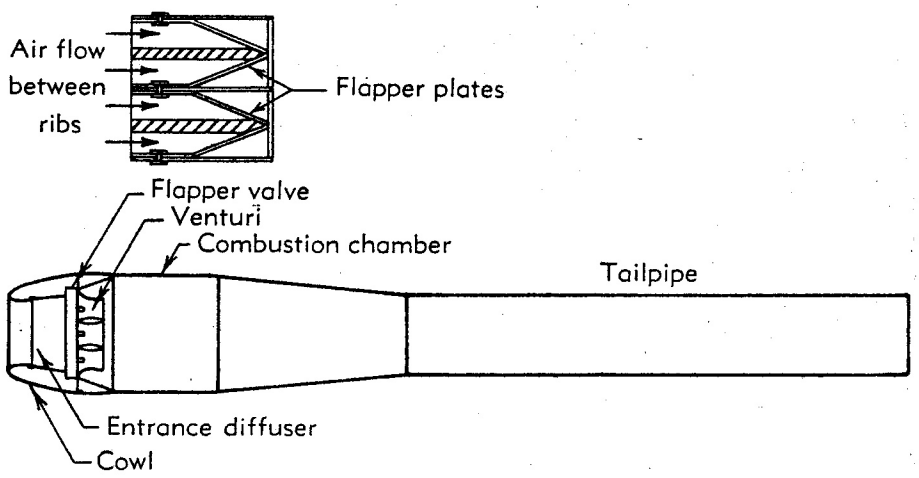

Figure 1.18: Schematic of a valved pulsejet (from Foa, 1959).

The pulsejet was invented at the beginning of the twentieth century and the concept was actually a precursor to the steady-flow concept now used in conventional gas turbine engines (Foa, 1959). A review of the early developments of the pulsejet is given by Edelman (1947). The use of unsteady combustion modes was thought promising, with the ultimate goal of achieving constant-volume combustion (Eidelman et al., 1991). Significant efforts were focused on the pulsejet in the late 1940s and 1950s. Some of the reviews on pulse detonation engines include extensive references to this work (Eidelman et al., 1991, Bussing and Pappas, 1996, Lynch and Edelman, 1996). Foa (1959, 1960) also gives an extensive review of the development of the pulsejet.

The first extensive analysis of pulsejet operation was conducted by Schultz-Grunow (1947), using the method of characteristics. The results helped explain some experimental observations and the effect of design parameters on performance. Zipkin and Lewis (1948) carried out analytical and experimental investigations of an explosion-cycle combustion chamber. Explosion pressure ratios from 1.7 to 5 were obtained in

a combustion chamber with a timed inlet valve and various fixed-area exhaust nozzles. The effects of explosion pressure ratio and combustion time on cycle frequency, inlet pressure, jet thrust, and thrust specific fuel consumption were investigated. In particular, the calculations showed that a reduction in combustion time would result in strong increases in explosion pressure ratio and thrust. Several experimental efforts later investigated the possibility of a resonant wave engine for subsonic propulsion applications (Logan, 1954, Hertzberg and Russo, 1954). Researchers also quickly realized that engines with multiple combustion chambers had a lower degree of unsteadiness and higher potential performance. A number of studies proposed multiple-chamber concepts (Bollay and Bitondo, 1954, Hertzberg and Russo, 1954, Lawrence and Weatherston, 1954).

One of the main questions in pulsejet performance analysis is: what is the combustion mode? It is obviously a strong function of cycle frequency and valve timing. For example, when the valve opening ratio is increased beyond a certain value, the amplitude of the flow pulsations decreases and constant-pressure combustion is approached (Schultz-Grunow, 1947, Foa, 1959). Based on several experimental observations, Foa (1959) claims that a polytropic combustion mode, characterized by $P/\rho^n = \text{constant}$, with a polytropic exponent of -1 is representative of the explosion process in pulsejets. A value of $n = -1$ corresponds to explosion ratios around 2.5, which is in good agreement with experimental measurements (Zipkin and Lewis, 1948).

Foa (1951) modeled the performance of the pulsejet based on quasi-steady blowdown of a combustion chamber and shows that the pulsejet has a higher performance than the ramjet not only in the subsonic flight domain but also well into the supersonic domain. Foa (1960, pp. 373–376) introduces the model of the ideal pulsejet, based on the entropy method. This ideal model assumes that the conditions of application of the entropy method are satisfied (Section 1.3.2) and that the flow velocity in the combustion chamber is very low, so that the initial temperature before combustion is equal to the freestream stagnation temperature. Under these conditions and assuming constant specific heats, the thermal efficiency for a polytropic combustion

mode is

$$\eta_{th} = 1 - \frac{C_p T_0}{f q_f} \left[\left(1 + \frac{n-1}{n-\gamma} \frac{f q_f}{C_v T_{t0}} \right)^{\frac{n-\gamma}{\gamma(n-1)}} \exp \frac{\Delta s}{C_p} - 1 \right] , \tag{1.107}$$

where the term $\exp(\Delta s/C_p)$ represents the losses associated with processes other than combustion. Moreover, in the ideal pulsejet model, all flow processes except combustion are assumed to be isentropic (hence, $\Delta s = 0$) and the exhaust velocity is assumed to be a square wave function of time, corresponding to $\eta_\nu = 1$. It is then possible to calculate the thrust from Eqs. 1.107 and 1.103. The specific impulse of the ideal pulsejet is shown in Fig. 1.19 as a function of flight Mach number for a polytropic exponent $n = -1$ (Foa, 1959, 1960). The ideal ramjet case ($n = 0$) is given for comparison. The ideal pulsejet is seen to present a significant performance advantage over the ramjet, at least at low flight Mach numbers.

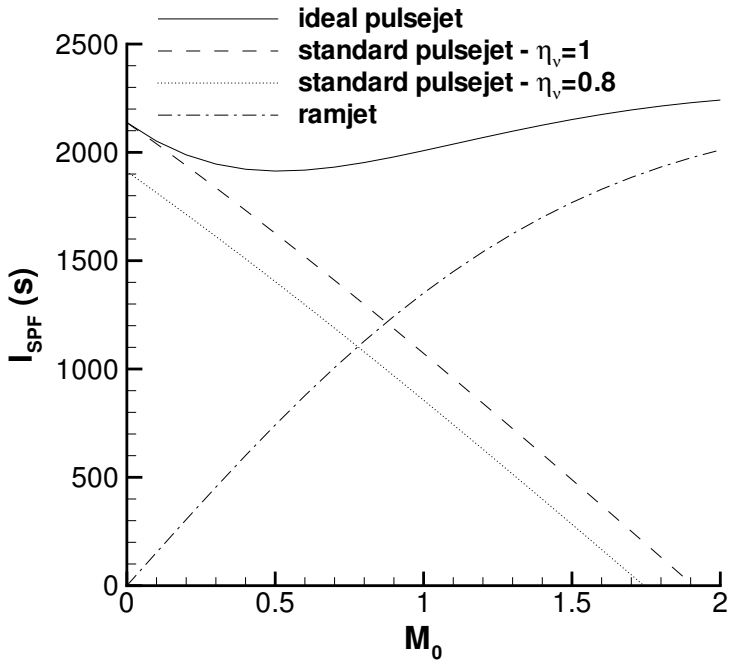

Figure 1.19: Specific impulse of ideal and standard pulsejet without backflow, calculated using the entropy method (Foa (1959, 1960)). $\gamma = 1.4$, $q_f = 45$ MJ/kg, $f = 0.035$, $T_0 = 278$ K, $n = -1$.

The actual performance of the pulsejet is quite different from the ideal case of Fig. 1.19. The main difference is attributed to its inability to sustain ram pressure

(Foa, 1960, pp. 373–376) in the combustion chamber during the charging phase of the cycle. The pressure in the combustion chamber depends strongly on the exit boundary conditions and is very close to the freestream static pressure. Foa (1959, 1960) accounts for the entropy increment associated with the stagnation pressure loss by defining the standard pulsejet, for which combustion occurs at the freestream static pressure and $\Delta s/C_p = \ln(T_{t0}/T_0)$. Specific impulse predictions for the standard pulsejet are shown in Fig. 1.19 for the ideal square wave case ($\eta_\nu = 1$) and for $\eta_\nu = 0.8$ in order to evaluate the performance loss associated with exit velocity fluctuations. The standard pulsejet specific impulse decreases quasi-linearly with increasing flight Mach number from the ideal pulsejet specific impulse value at $M_0 = 0$ and vanishes below Mach 2.

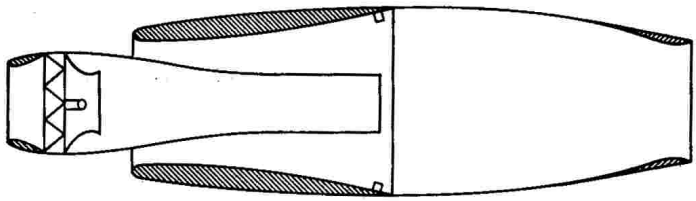

Figure 1.20: Schematic of a ducted pulsejet with tail shrouding.

Thrust augmentation can be achieved for the pulsejet when some of the energy of the combustion products is transferred to secondary air flows (Foa, 1960, Chap. 15c). There are two main ways of thrust augmentation, using backflow and shrouding. Backflow occurs at low speeds and is beneficial because of the energy transfer from the hot combustion products to the cold backflow air (Foa, 1959, 1960). Shrouding can be used to improve pulsejet performance by thrust augmentation and through utilization of ram precompression for full shrouding. The ducted pulsejet has a higher performance due to energy transfer of the primary pulsejet flow to the secondary flow through pressure exchange and mixing. This type of thrust augmentation is more efficient for unsteady than for steady flows. Significant thrust augmentation ratios (higher than 1.5) can be obtained for the ducted pulsejet (Rudinger, 1951, Lockwood, 1954, Foa, 1960). The performance of the ducted pulsejet was investigated by

Lawrence and Weatherston (1954) and Lockwood (1954). Lawrence and Weatherston (1954) predicted that a ducted multiple-tube pulsejet has a superior performance than the ramjet or the turbojet with afterburner at all supersonic speeds. They also investigated the potential use of the pulsejet as the combustion chamber in a turbojet. Lockwood (1954) studied the ducted pulsejet at high subsonic flight Mach numbers (around 0.9) and altitudes of 30,000 to 40,000 ft. His most optimistic predictions showed that the performance of the ducted pulsejet is comparable to that of the turbojet.

1.3.5 Pulse detonation engine

A pulse detonation engine is an intermittent propulsion system that uses the repetitive generation of detonations to produce thrust. In a sense, it is a pulsejet with a particular type of combustion (detonation). A pulse detonation engine (PDE) typically consists of an inlet, a valve or series of valves, a fuel injection system, one or multiple detonation tubes, and an exit nozzle. The basic PDE cycle consists of the following steps, described in Fig. 1.21:

a) A detonation is initiated in a detonation tube filled with reactants.

b) The detonation propagates through the detonation tube and exits at the open end.

c) The combustion products exhaust through a blowdown process.

d) At the end of the exhaust process, the tube contains expanded combustion products.

e) The valve opens and reactants flow into the tube, pushing the combustion products out of the tube.

f) When the tube is filled with reactants, the valve closes and the cycle repeats.

Detonation is an attractive combustion mode for propulsion applications because of the fast heat release rate and high peak pressures generated. The rapidity of

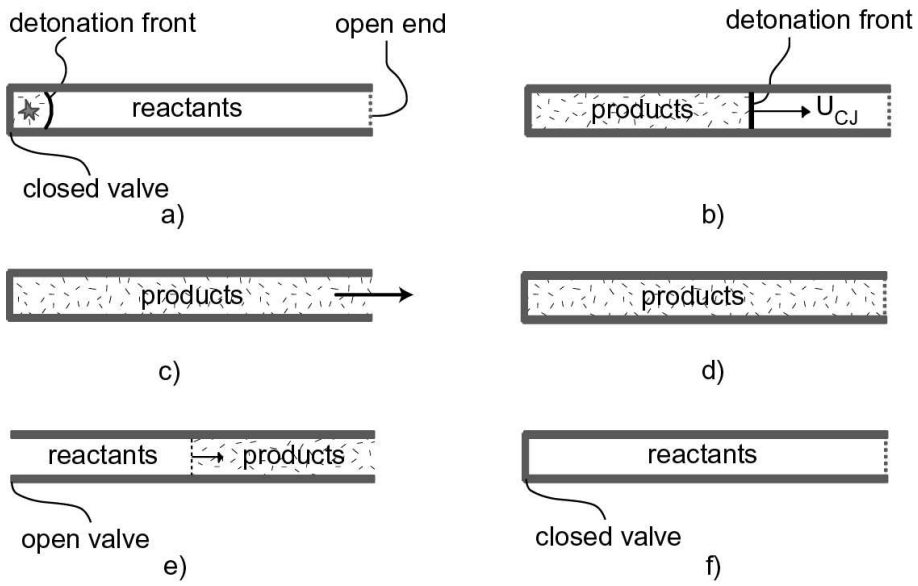

Figure 1.21: Pulse detonation engine cycle.

the process makes it thermodynamically closer to a constant-volume process than a constant-pressure combustion process typical of conventional steady-flow propulsion systems (Eidelman et al., 1991, Bussing and Pappas, 1996, Kailasanath, 2000). Based on thermodynamic cycle analysis, constant-volume combustion cycles yield a higher thermal efficiency than the constant-pressure combustion cycle (Section 2.4.1). This can translate into potential performance advantages for unsteady propulsion systems using constant-volume combustion over typical steady propulsion systems based on constant-pressure combustion, provided that the entropy method can be applied and the exit velocity is a square wave function of time. Another advantage, pointed out by Lynch and Edelman (1996), is that the operating frequency of a PDE is not determined by the acoustics of the system as is typically the case in pulsejets, but can be directly controlled. This also means that propulsion systems based on pulsed detonations can be scaled, and their operating parameters can be modified for different types of applications.

The first reported work on intermittent detonation engines is attributed to Hoffmann (1940), who operated with acetylene- and benzine-oxygen mixtures. Nicholls et al. (1958) performed single-cycle and multi-cycle thrust measurements of a det-

onation tube operating with hydrogen-oxygen, hydrogen-air, acetylene-oxygen, or acetylene-air. They obtained fuel specific impulses as high as 2100 s and maximum operating frequencies of 35 Hz and concluded that the concept held promise. It is interesting to note that Nicholls et al. (1958) proposed the concept of a PDE with multiple detonation tubes connected to a common air inlet using a rotary valve, which is currently under development (Bussing, 1995). Krzycki (1962) performed an experimental investigation of intermittent detonation engines with frequencies up to 60 Hz, using a setup similar to that of Nicholls et al. (1958). Due to low spark energy at high frequencies, a substantial part of the experiments involved deflagrations rather than detonations, leading Krzycki (1962) to conclude that thrust was possible from such a device but practical applications did not appear promising. At this point, all experimental work related to the PDE concept stopped. Indirectly related work was performed at the Jet Propulsion Laboratory by Back et al. (1983), who studied the feasibility of a rocket thruster powered by intermittent detonations of solid explosive for dense or high-pressure atmosphere applications. Work on PDEs started again in the late 1980s and early 1990s, involving substantial experimental (Helman et al., 1986), numerical (Eidelman et al., 1991, Lynch and Edelman, 1996, Cambier and Tegner, 1998), and modeling (Bratkovich and Bussing, 1995) efforts. Most of the recent work on PDEs has been reviewed by Eidelman et al. (1991), Bussing and Pappas (1996), Lynch and Edelman (1996), Kailasanath (2000), and Kailasanath (2002).

A wide number of applications have been proposed for PDEs, perhaps due to the uncertainty in PDE performance estimates and the remaining difficulties of obtaining reliable operation with practical fuels (Kailasanath, 2002). Applications in air-breathing configurations include supersonic vehicles, miniature cruise missiles, afterburners, low cost UAV and UCAV applications, and SSTO launchers (Kailasanath, 2002). Rocket engine applications have also been considered (Bratkovich et al., 1997, Coy, 2003). The rocket mode of operation is similar to the air-breathing mode except that the oxidizer is also injected into the system periodically. Other applications involving combined cycle modes, such as hybrid PDE-piston or detonation wave rotor engine configurations, have been reviewed by Dean (2003).

There are a number of key issues in PDE design, which have been highlighted by Bussing and Pappas (1996) and, more recently, by Kailasanath (2002). For air-breathing configurations, inlets are a critical component of the engine. They have to undergo significant pressure fluctuations during multi-cycle operation (Mullagiri et al., 2003). Unsteady valveless (Brophy et al., 2003) and valved (Bussing, 1995) inlet designs exist. In parallel, some researchers are now focusing on using conventional steady inlets in PDE configurations (Mullagiri et al., 2003, Nori et al., 2003). The injection system has to be able to rapidly and reliably inject and mix fuel and oxidizer. Many practical applications require the use of liquid fuels. The issue of atomization and uniformity of the fuel-oxidizer distribution under pulsed conditions is discussed by Lasheras et al. (2001). Detonation initiation is critical due to the requirement to repeatedly initiate practical but insensitive mixtures of liquid jet fuel and air (in air-breathing applications) using a weak ignition source. Direct detonation initiation in typical mixtures of jet fuel and air requires an impractical amount of energy, and indirect initiation methods are necessary. One of these methods is deflagration to detonation transition (DDT), which satisfies the requirements mentioned above, but typically results in long detonation formation distances (Shepherd and Lee, 1992). Other approaches include the use of a sensitized predetonator (Brophy et al., 2002, Saretto et al., 2003) or shock focusing through the generation of a toroidal imploding detonation wave (Jackson and Shepherd, 2002).

Another key issue in PDE design, which is explored in the current work, is that of performance. Because of the intrinsically unsteady nature of the flow field associated with the detonation process, it is difficult to evaluate the performance of PDEs, and performance bounds have been elusive. Researchers started by focusing on the simplest PDE configuration consisting of a straight tube closed at one end and open at the other end. The results of several studies, including the one presented in Chapter 4, now seem to agree on the impulse generated by a straight detonation tube (Kailasanath, 2002, Dean, 2003). In order to optimize the thrust, an exit nozzle is desirable whose role is to efficiently convert thermal energy into kinetic energy. However, due to the unsteady nature of the flow field in the detonation tube, it is still

unclear what the optimal configurations are (Kailasanath, 2001). Substantial specific impulse increases have been observed with the addition of a simple straight extension filled with air in single-cycle (Cooper and Shepherd, 2002, Falempin et al., 2001) and multi-cycle (Schauer et al., 2001) static experiments. This effect has been shown to be a purely unsteady gasdynamic effect (Li and Kailasanath, 2001). Recent work by Morris (2003) indicates that, as in steady-flow nozzles, these optimal configurations are a function of the pressure ratio. These results and the unsteady-flow effects mentioned previously highlight the complexity of predicting the effects of nozzles on performance. Another approach to enhancing performance, similar to what was used for pulsejets, is the addition of ejectors and is currently under investigation (Rasheed et al., 2003). Because of the uncertainties about the influence of exit nozzles and the complexity of the unsteady reactive flow field with moving body parts in PDEs, very few efforts have attempted to develop a system level model of air-breathing PDE operation (Wu et al., 2003). Although several researchers (Kentfield, 2002, Heiser and Pratt, 2002, Dyer and Kaemming, 2002) have developed thermodynamic cycle models for PDEs, there is currently no widely accepted model for performance prediction based on thermodynamic cycle analysis (Dean, 2003). Consequently, there is still much uncertainty about system level performance estimates (Kailasanath, 2002).

1.4 Thesis outline

This thesis investigates the applications of detonations to air-breathing propulsion. Chapter 1 presents an introduction to detonations and air-breathing propulsion and reviews the fundamentals of these fields. Chapter 2 analyzes, from a thermodynamic point of view, the potential of detonations for developing useful work and infers conclusions upon steady and unsteady detonation-based propulsion systems. The subsequent chapters are focused on specific engine concepts that utilize detonations in a steady (Chapter 3) and an unsteady mode (Chapters 4 and 5). Chapter 3 presents a flow path analysis of steady detonation engines. The performance of these engines is computed as a function of flight conditions and compared with conventional

propulsion systems. The limitations associated with the use of steady detonations in a combustor are presented and their influence on performance is discussed. Chapters 4 and 5 focus on pulse detonation engines. The unsteady generation of thrust in a PDE is first analyzed and modeled in its simplest configuration consisting of a straight detonation tube in Chapter 4. Chapter 5 builds on the results of Chapter 4 to predict the performance of an air-breathing PDE based on gas dynamics and control volume analysis. The performance of a supersonic single-tube PDE with no exit nozzle is calculated for various flight conditions and compared with that of the ramjet.

Chapter 2

Thermodynamic Analysis of Combustion Processes for Propulsion Systems

A key issue in conceptual design and analysis of proposed propulsion systems is the role of the combustion mode in determining the overall efficiency of the system. In particular, what mode of combustion should be used to extract the maximum amount of work from a given combustible mixture? This issue is addressed by thermodynamic considerations for ideal thermal cycles that simulate common combustion modes such as constant-pressure (Brayton cycle) or constant-volume combustion (Humphrey cycle). Our goal is to understand, based on thermodynamics, the merits of detonative combustion relative to deflagrative combustion characteristic of conventional ramjet and turbojet engines. After reviewing detonation thermodynamics, we analyze the merits of detonations for steady-flow systems and highlight the importance of the irreversible portion of the entropy rise in steady-flow analysis. This leads us to consider the situation for unsteady, i.e., intermittent or pulsed, combustion systems which use various modes of operation. For unsteady detonation waves, we consider a notional cyclic process for a closed system (the Fickett-Jacobs cycle) in order to circumvent the difficulties associated with analyzing a system with time-dependent and spatially inhomogeneous states. We compute a thermal efficiency for detonations based on the ideal mechanical work produced by the cycle and compare it with the Brayton and

This chapter is based on work presented in Wintenberger and Shepherd (2004).

Humphrey cycles. The similar thermal efficiency values obtained for constant-volume combustion and detonation motivate further comparison of these two combustion modes. Finally, a gas-dynamics based model using constant-volume combustion is developed to predict the performance of unsteady propulsion systems.

2.1 Entropy variation along the Hugoniot

The different combustion modes that can be obtained in steady flow are usually analyzed using a control volume surrounding the combustion wave, such as that of Fig. 1.1. The mass, momentum, and energy conservation equations are applied for steady, constant-area, and inviscid flow (Eqs. 1.1–1.3). Solving these equations yields the Hugoniot curve (Fig. 2.1), which is the locus of all possible solutions for state 2 from a given state 1 and a given energy release q_c. In Section 1.1.1, we showed that the entropy rise during combustion was minimum at the CJ detonation point, based on the curvature of the Hugoniot. We now illustrate this point for the perfect gas and discuss its relevance to thermodynamic cycle analysis.

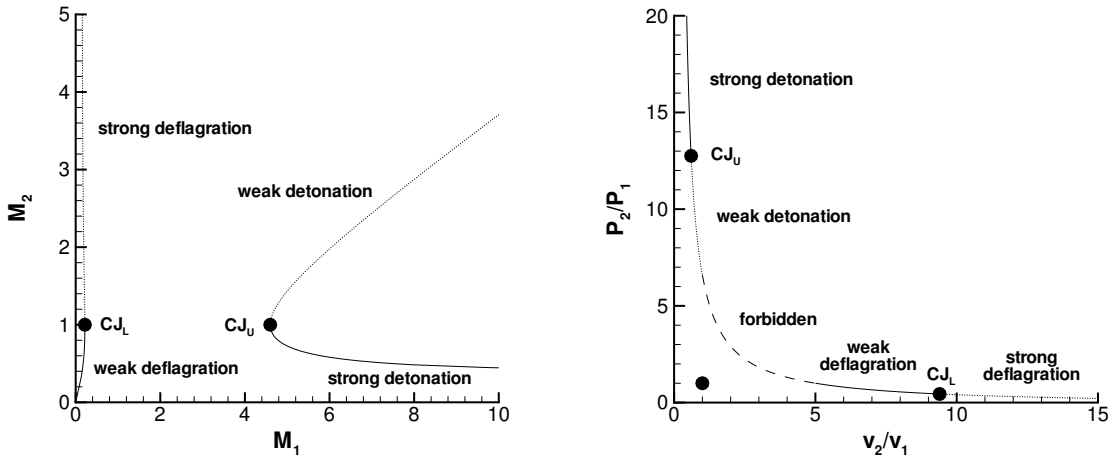

Figure 2.1: Solutions of the conservation equations for the Hugoniot for M_2 as a function of M_1 (left) and Hugoniot curve in the pressure-specific volume plane (right) for a perfect gas with $\gamma = 1.4$ and $q_c/C_pT_1 = 4$.

The set of Eqs. 1.1–1.3 can be rewritten for a perfect gas as a function of the Mach

numbers upstream and downstream of the wave.

$$\frac{\rho_2}{\rho_1} = \frac{M_1^2(1+\gamma M_2^2)}{M_2^2(1+\gamma M_1^2)} \tag{2.1}$$

$$\frac{P_2}{P_1} = \frac{1+\gamma M_1^2}{1+\gamma M_2^2} \tag{2.2}$$

$$\frac{q_c}{C_p T_1} + 1 + \frac{\gamma-1}{2}M_1^2 = \frac{M_2^2(1+\gamma M_1^2)^2}{M_1^2(1+\gamma M_2^2)^2}\left(1+\frac{\gamma-1}{2}M_2^2\right) \tag{2.3}$$

This set of equations can be solved analytically for a given q and initial state. The Mach number downstream of the wave M_2 is plotted as a function of the Mach number upstream of the wave M_1 in Fig. 2.1, along with the Hugoniot curve in the pressure-specific volume plane. The lower CJ point yields the highest deflagration Mach number, while the upper CJ point corresponds to the lowest detonation Mach number.

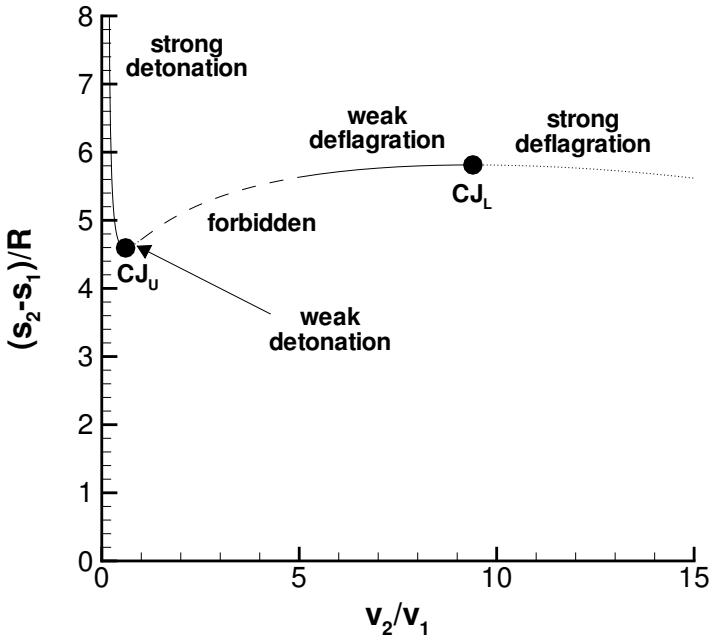

Figure 2.2: Variation of the total entropy rise along the Hugoniot. $\gamma = 1.4$, $q_c/C_pT_1 = 4$.

The entropy rise associated with the combustion process can be computed from

Eqs. 2.1 and 2.2.

$$\frac{s_2 - s_1}{R} = \frac{\gamma}{\gamma - 1} \ln\left(\frac{T_2}{T_1}\right) - \ln\left(\frac{P_2}{P_1}\right) \tag{2.4}$$

The entropy rise is plotted in Fig. 2.2 as a function of the specific volume. The different solution regions are shown and the entropy rise is minimum at the CJ detonation point and maximum at the CJ deflagration point. Thus, from Eq. 1.80, it appears as if a cycle using detonative combustion will yield the highest thermal efficiency since it has the lowest entropy rise.

2.2 The role of irreversibility in steady-flow propulsion

The fact that the entropy rise is minimum at the CJ detonation point, in conjunction with the result of Eq. 1.75, has motivated several efforts to explore detonation applications to steady-flow propulsion (Dunlap et al., 1958, Sargent and Gross, 1960, Wintenberger and Shepherd, 2003b). However, in spite of the apparent lower entropy rise generated by detonations as compared with deflagrations, these studies concluded that the performance of steady detonation-based engines is systematically and substantially lower than that of the ramjet (Section 3.3.2).

The explanation of this apparent contradiction lies in considering the role of entropy generation and irreversible processes in the combustor. It is a general conclusion of thermodynamics and can be explicitly shown using availability arguments (Clarke and Horlock, 1975) that the work obtained is maximized when the irreversibility is minimized. When portions of the propulsion system involve losses and irreversible generation of entropy, the efficiency is reduced and the reduction in performance (specific thrust) can be directly related to the irreversible entropy increase (Riggins et al., 1997).

The entropy rise occurring during premixed combustion in a flowing gas has a minimum component due to the energy release and the chemical reactions, and an additional, irreversible, component due to the finite velocity and, in the case of a

detonation, the leading shock wave.

$$s_2 - s_1 = \Delta s_{min} + \Delta s_{irr} \tag{2.5}$$

For a combustion wave such as Fig. 1.1, we propose that the minimum entropy rise (for a *fixed* upstream state and velocity) can be computed by considering the ideal stagnation or total state.[1] The total properties at a point in the flow are defined as the values obtained by isentropically bringing the flow to rest. For example, the total enthalpy is

$$h_t = h + \frac{u^2}{2} \tag{2.6}$$

and the total pressure and temperature are defined by

$$h(P_t, s) = h_t \qquad h(T_t, s) = h_t \ , \tag{2.7}$$

where by definition $s_t = s$. The process of computing the stagnation state is illustrated graphically in the (h,s) or Mollier diagram of Fig. 2.3. At fixed total enthalpy, the total pressure decreases with increasing entropy

$$dP_t = -\rho_t T_t ds \tag{2.8}$$

so that the minimum entropy rise is associated with the highest total pressure, which is the upstream value P_{t1}. This is illustrated graphically in Fig. 2.3, showing the additional entropy increment Δs_{irr} associated with a total pressure decrement $P_{t1} - P_{t2}$.

For a given stagnation state, the minimum entropy rise can be determined for gas mixtures with realistic thermochemistry by considering an ideal constant-pressure (zero velocity) combustion process. The first step is to determine the total tempera-

[1] This conjecture is easy to demonstrate for a perfect gas with an effective heat addition model of combustion; for example, see Oates (1984, p. 44). We also demonstrate the correctness of this idea explicitly in subsequent computations for the one-γ detonation model and numerical solutions with realistic thermochemistry.

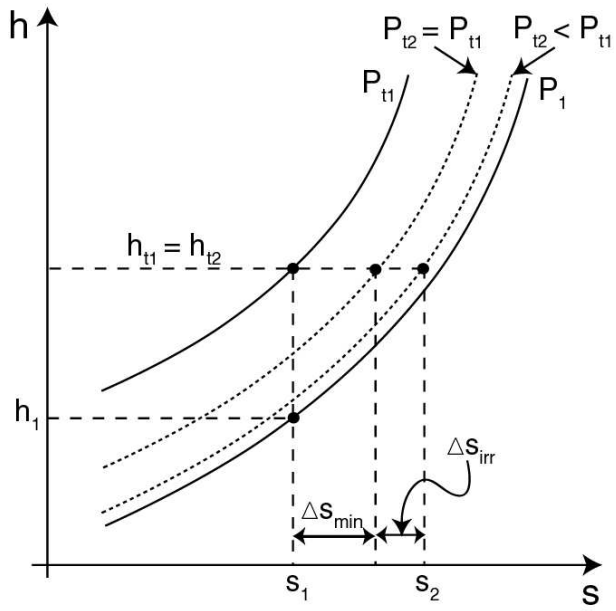

Figure 2.3: Mollier diagram used to calculate minimum entropy component. Solid lines are isobars for reactants and dotted lines are isobars for products.

ture in the products from the energy balance equation

$$h_2(T_{t2}) = h_1(T_{t1}) \ , \tag{2.9}$$

where the species in state 2 are determined by carrying out a chemical equilibrium computation. The second step is to determine the entropy rise across the combustion wave by using the stagnation pressures, temperatures, and compositions to evaluate the entropy for reactants and products

$$\Delta s_{min} = s_2(T_{t2}, P_{t1}) - s_1(T_{t1}, P_{t1}) \ . \tag{2.10}$$

The total entropy jump across the wave is

$$s_2 - s_1 = s_2(T_2, P_2) - s_1(T_1, P_1) \ , \tag{2.11}$$

where state 2 in the products is determined by solving the jump conditions. The irreversible component can then be computed by using Eq. 2.5.

For a perfect gas model, the entropy change can be explicitly computed as

$$s_2 - s_1 = C_p \ln\left(\frac{T_{t2}}{T_{t1}}\right) - R \ln\left(\frac{P_{t2}}{P_{t1}}\right) \ . \tag{2.12}$$

From Eq. 2.10, the minimum entropy rise is

$$\Delta s_{min} = C_p \ln\left(\frac{T_{t2}}{T_{t1}}\right) \tag{2.13}$$

and the irreversible component is

$$\Delta s_{irr} = -R \ln\left(\frac{P_{t2}}{P_{t1}}\right) \ . \tag{2.14}$$

The minimum component can be identified as the amount of entropy increase that would occur with an equivalent *reversible* addition of heat

$$ds = \frac{dq}{T} \tag{2.15}$$

at constant pressure, for which

$$dq = dh = C_p dT \ . \tag{2.16}$$

Substituting and integrating from stagnation state 1 to 2, we find that

$$\Delta s_{rev} = C_p \ln\left(\frac{T_{t2}}{T_{t1}}\right) \ , \tag{2.17}$$

which is identical to the expression for the minimum entropy rise found from evaluating the entropy change using the prescription given above. In what follows, we will also refer to the minimum entropy rise as the *reversible* entropy rise. Using these definitions, we show in Fig. 2.4 the partition of the entropy into these two portions for the one-γ model of detonation considered earlier.

Although the total entropy rise is lower for the detonation branch than the deflagration branch, a much larger portion (greater than 50%) of the entropy rise is

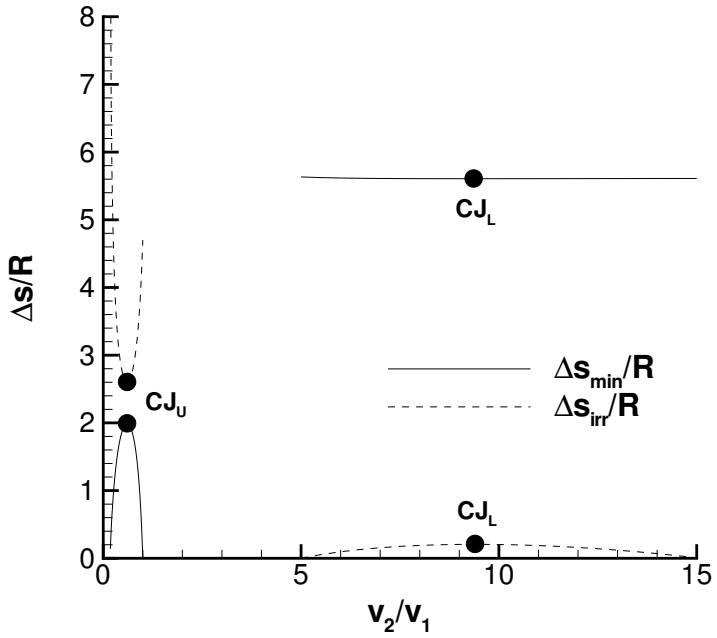

Figure 2.4: Reversible and irreversible components of the entropy rise along the Hugoniot, $\gamma = 1.4$, $q_c/C_pT_1 = 4$.

irreversible for detonations than for deflagrations (less than 5%). Separate computations show that the majority of the irreversible portion of the entropy rise for detonations is due to the entropy jump across the shock front, which can be obtained directly from the total pressure decrease across the shock wave and Eq. 2.12. This loss in total pressure is orders of magnitude larger for detonation than for deflagration solutions and is shown in Section 3.3.2 to be responsible for the lower performance of detonation-based engines relative to the ramjet. Hence, the paradox mentioned earlier can be resolved by considering not just the total entropy rise, but by determining what part of this is irreversible. An alternative way to look at this issue is given in the next section, where we reformulate the jump conditions so that the role of irreversible entropy rise in the calculation of the thermal efficiency can be demonstrated explicitly.

2.2.1 Irreversible entropy rise and thermal efficiency

The role of the irreversible part of the entropy rise can be explored further by considering Eq. 1.75. In order to compare objectively different combustion modes, the engine has to be studied in a given flight situation for a fixed amount of energy release during the combustion, as shown in Fig. 2.5. Our conceptual engine consists of an inlet, a combustion chamber with a steady combustion wave, and a nozzle. Note that the conditions for combustion wave stabilization are not considered here, but are explored in detail for detonation waves in Section 3.2.

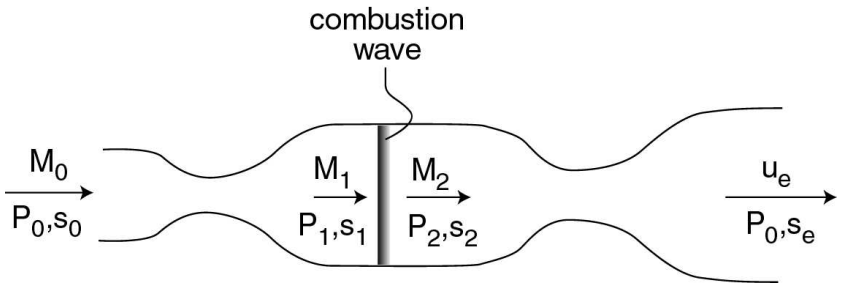

Figure 2.5: Ideal steady engine in flight showing the location of the combustion wave.

The entropy rise between the inlet and exit planes is the sum of the entropy rise through the combustion and the irreversible entropy increments through the inlet and nozzle. Grouping together the irreversible entropy increments through the inlet, the combustion chamber, and the nozzle,

$$s_e - s_0 = \Delta s_{min} + \Delta s_{irr} \ . \tag{2.18}$$

The minimum part of the entropy rise during combustion is constant for a fixed energy release and a fixed stagnation state upstream of the wave. From the general principles of thermodynamics and consistent with Eq. 1.75, the highest efficiency is obtained with the minimum irreversibility for a given chemical energy release q_c.

This general statement can be shown explicitly for the case of the perfect gas. The minimum component of the entropy rise for the one-γ model is

$$\Delta s_{min} = C_p \ln\left(1 + \frac{q_c}{C_p T_{t1}}\right) \ . \tag{2.19}$$

Substituting Eq. 2.18 into Eq. 1.80, and using the result of Eq. 2.19, the thermal efficiency can be expressed as a function of the irreversible entropy rise

$$\eta_{th} = 1 - \frac{C_p T_0}{q_c}\left[\left(1 + \frac{q_c}{C_p T_{t1}}\right)\exp\left(\frac{\Delta s_{irr}}{C_p}\right) - 1\right] . \tag{2.20}$$

From Eq. 2.20, the highest efficiency is obtained for $\Delta s_{irr} = 0$

$$\eta_{th} < \eta_{th}(\Delta s_{irr} = 0) = 1 - \frac{T_0}{T_{t1}} , \tag{2.21}$$

which is the classical expression for the ideal Brayton cycle.

Consider an idealized version of our conceptual engine, for which the thermal efficiency is determined only by the irreversible entropy rise during combustion. In order to compare different combustion modes, we need to calculate the irreversible entropy rise for all the possible solutions to Eqs. 1.1–1.3. However, the result of Fig. 2.2 does not apply directly because the velocity of the initial state and, consequently, the total enthalpy are not constant for the conventional Hugoniot analysis. Instead, it is necessary to compute another solution curve corresponding to a fixed freestream stagnation state, which we will refer to as the stagnation Hugoniot.

2.2.2 The stagnation Hugoniot

The stagnation Hugoniot is the locus of the solutions to the conservation equations (Eqs. 1.1-1.3) for a given stagnation state upstream of the combustion wave. The initial temperature and pressure upstream of the wave vary with the Mach number M_1. We compute explicitly the stagnation Hugoniot for a perfect gas, based on Eqs. 2.1–2.3. Equation 2.3 has to be rewritten as a function of the parameter $q_c/C_p T_{t1}$, which has a fixed value for a given freestream condition.

$$1 + \frac{q_c}{C_p T_{t1}} = \frac{M_2^2(1+\gamma M_1^2)^2(1+\frac{\gamma-1}{2}M_2^2)}{M_1^2(1+\gamma M_2^2)^2(1+\frac{\gamma-1}{2}M_1^2)} \tag{2.22}$$

This equation can be solved analytically, and the solution for M_2 as a function of M_1 is plotted in Fig. 2.6. The solution curves are very similar to those of Fig. 2.1, with the CJ points yielding the maximum deflagration and minimum detonation Mach numbers. There is, however, a difference for the weak detonation branch. As $M_1 \to \infty$, M_2 asymptotes to a constant value instead of becoming infinite as for the Hugoniot.

$$M_2 \to \sqrt{\frac{1-(\gamma-1)\frac{q_c}{C_pT_{t1}}+\sqrt{1-(\gamma^2-1)\frac{q_c}{C_pT_{t1}}}}{\gamma(\gamma-1)\frac{q_c}{C_pT_{t1}}}} \tag{2.23}$$

This is due to the fact that the stagnation conditions at state 2 are fixed by the stagnation conditions at state 1 and the heat release. Detonation solutions are found to be possible only for

$$\frac{q_c}{C_pT_{t1}} < \frac{1}{\gamma^2-1}\,. \tag{2.24}$$

This condition is imposed by the requirement that $T_1 > 0$ which is necessary for the limiting value of Eq. 2.23 to be real. For higher values of q_c/C_pT_{t1}, the total enthalpy is not high enough to enable a steady detonation in the combustor for the given value of the heat release, and no steady solutions exist (Section 3.2).

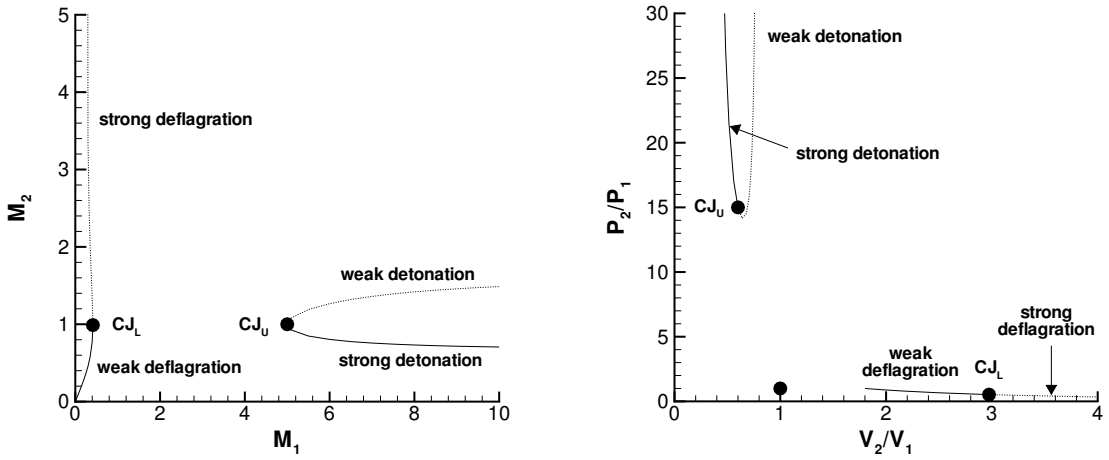

Figure 2.6: Solutions of the conservation equations for the stagnation Hugoniot for M_2 as a function of M_1 (left) and stagnation Hugoniot curve in the pressure-specific volume plane (right) for a perfect gas with $\gamma = 1.4$ and $q_c/C_pT_1 = 0.8$.

For the conventional Hugoniot, Fig. 2.1, the entropy, pressure, and temperature at

state 2 are finite for a constant-volume ($v_2 = v_1$) explosion process even though, in this limit, $M_1 \to \infty$. However, in the stagnation Hugoniot representation, the pressure ratio along the weak detonation branch becomes infinite as this limit is approached. As $M_1 \to \infty$, the static pressure at state 1 decreases towards zero because the total pressure is fixed, but the static pressure at state 2 remains finite due to the finite value of M_2. This explains the unusual shape of the stagnation Hugoniot, which is plotted in the pressure-specific volume plane for $\gamma = 1.4$ and $q_c/C_pT_{t1} = 0.8$ in Fig. 2.6. Just as for the conventional Hugoniot, there is no solution in the positive quadrant of the pressure-specific volume plane for Rayleigh processes (Eq. 1.5). However, unlike the conventional Hugoniot, the stagnation Hugoniot curve is not continuous across this forbidden region. This means that the detonation and deflagration branches are disjoint.

The total entropy rise along the stagnation Hugoniot is shown in Fig. 2.7 as a function of the specific volume ratio. For a fixed heat release and initial stagnation state, the minimum entropy rise is constant (Eq. 2.19). As in the conventional Hugoniot, the CJ points correspond to extrema of the entropy. However, they are only local extrema because of the discontinuity of the solution curve in the pressure-specific volume plane. The CJ detonation point corresponds to a minimum in entropy along the detonation branch, while the CJ deflagration point corresponds to a maximum in entropy along the deflagration branch. However, the entropy rise associated with the CJ detonation point is much larger than that associated with the CJ deflagration point for all possible values of q_c/C_pT_{t1}. In general, the irreversible entropy rise associated with any physical solution on the deflagration branch is much lower than that for any detonation solution. Of all physically possible steady combustion modes, constant-pressure (CP) combustion at zero Mach number is the process with the smallest entropy rise for a fixed stagnation condition.

We now use the result of Eq. 2.21 to compare the thermal efficiency of ideal steady propulsion systems as a function of the combustion mode selected. Losses associated with shock waves, friction, mixing, or heat transfer are neglected, and the compression and expansion processes are assumed to be isentropic. The thermal efficiency for

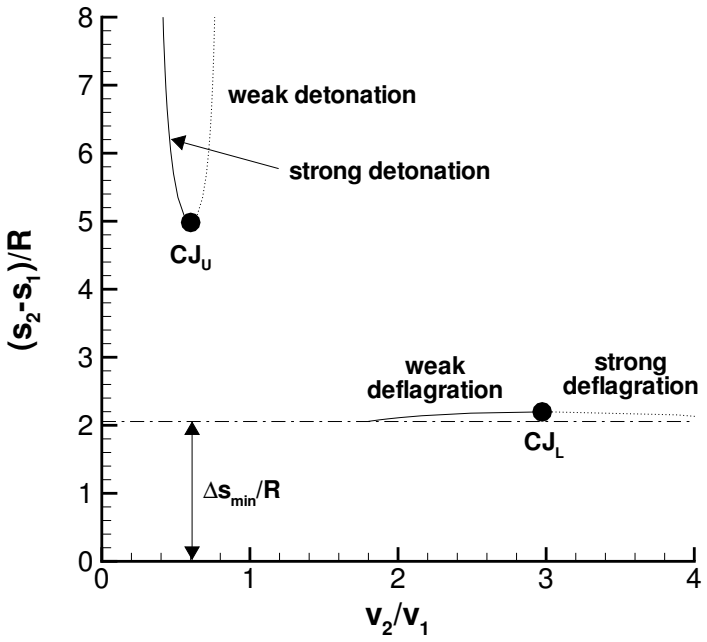

Figure 2.7: Total entropy rise along the stagnation Hugoniot. The minimum component of the entropy rise is fixed along the stagnation Hugoniot and is shown as the straight line. The total entropy variation is due to the irreversible component only. $\gamma = 1.4$, $q_c/C_pT_{t1} = 0.8$.

an ideal steady propulsion system flying at a Mach number of 5 is plotted in Fig. 2.8. The irreversible entropy rise in detonations strongly penalizes the efficiency of steady detonation-based engines compared to the conventional ideal ramjet. The values for the thermal efficiency at the upper CJ point obtained based on the stagnation Hugoniot are identical to those predicted by flow path analysis for ideal detonation ramjets (Section 3.3.2). Thus, this approach reconciles flow path analysis and thermodynamic cycle analysis for detonation ramjets. The values of the thermal efficiency of Fig. 2.8 are not representative of practical propulsion systems at a flight Mach number $M_0 = 5$ because the total temperature at the combustor outlet is too high to be sustained by the chamber walls. More realistic studies limit the total temperature at the combustor outlet based on material considerations, which decreases substantially the thermal efficiency. The analysis of steady detonation-based ramjets also has to take into account effects such as condensation or auto-ignition of the fuel-air mixture

and limitations associated with fuel sensitivity to detonation (Section 3.3.2). The net effect is that propulsion systems based on *steady* detonation waves have a very small thrust-producing range and the maximum performance is always substantially lower than conventional turbojets or ramjets (Section 3.3.2).

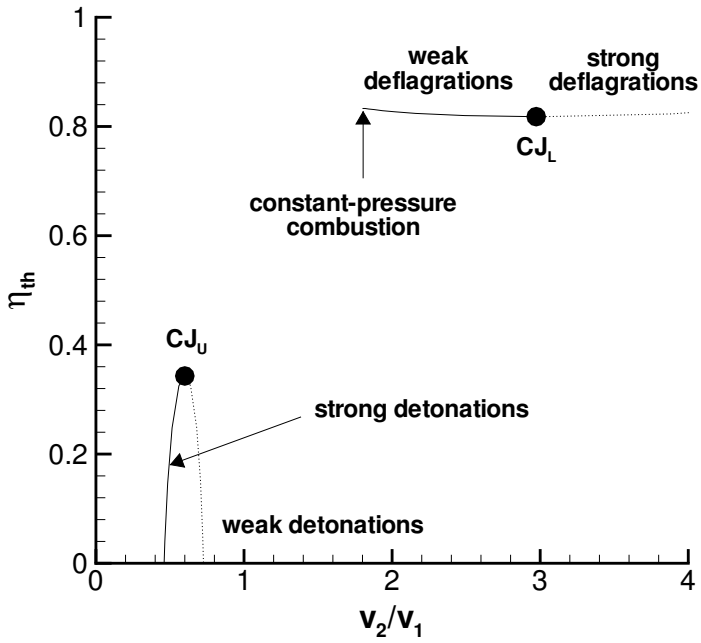

Figure 2.8: Thermal efficiency of an ideal engine flying at $M_0 = 5$ as a function of the combustion mode selected, $\gamma = 1.4$, $q_c/C_pT_{t1} = 0.8$.

For our ideal propulsion system, the constant-pressure (CP) combustion process yields the highest thermal efficiency of all physical solutions to the conservation equations. Foa (1951) concluded that CP combustion was always the optimum solution for steady flow using an argument based on a polytropic approximation of the combustion mode for the perfect gas. We have now extended his result to all physically possible steady combustion modes for the perfect gas. However, in order to compare practical propulsion systems based on different combustion modes, one also has to compute the irreversible entropy rise through the other components of the engine. The entropy rise associated with irreversible processes such as shocks, friction, mixing, or heat transfer may become significant (Riggins et al., 1997) and dominate the results, particularly at high supersonic flight Mach numbers.

2.3 Detonation applications in unsteady flow: the Fickett-Jacobs cycle

The entropy minimum corresponding to CJ detonations and its implications on the thermal efficiency have also motivated significant efforts to apply unsteady detonations to propulsion, in particular through the research on pulse detonation engines (Kailasanath, 2000). Unsteady detonations can be analyzed on a thermodynamic basis by considering a closed system. The Fickett-Jacobs (FJ) cycle is a conceptual thermodynamic cycle that can be used to compute an upper bound to the amount of mechanical work that can be obtained from detonating a given mass of explosive. The advantage of the FJ cycle is that it provides a simple conceptual framework for handling detonations in a purely thermodynamic fashion, avoiding the complexity of unsteady gas dynamics (Wu et al., 2003, Wintenberger and Shepherd, 2003a) of realistic pulse detonation or pulsejet engines.

2.3.1 Basic FJ cycle

The FJ cycle for detonations is described in Fickett and Davis (2001, pp. 35–38) and is an elaboration of the original ideas of Jacobs (1956). The notion of applying thermodynamic cycles to detonation was independently considered by Zel'dovich (1940b) 15 years before Jacobs, but Zel'dovich's ideas were not known[2] to Jacobs or Fickett and, until recently, there was no appreciation in the West of this work by Zel'dovich.

The idea of the FJ cycle is similar to standard thermodynamic cycles such as the Otto and Brayton cycles that are the basis for computing the ideal performance of internal combustion and gas turbine engines. The basis of the cycle is the piston-cylinder arrangement (Fig. 2.9) of elementary thermodynamics. The reactants and explosion products are at all times contained within the cylinder and pistons so that we are always considering a fixed mass. The explosive, pistons, and cylinder will be considered as a closed thermodynamic system. All confining materials are assumed

[2]Personal communication from W. C. Davis, April 2003

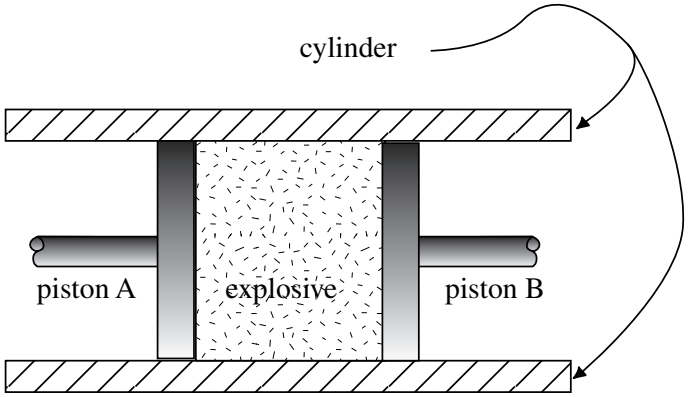

Figure 2.9: Piston cylinder arrangement used to implement Fickett-Jacobs cycle.

to be rigid, massless, and do not conduct heat. The pistons can be independently moved and there is a work interaction W (> 0 for work done by the system) with the surroundings that results from these motions. In order to have a complete cycle, there will be a heat interaction Q (> 0 for heat transferred into the system) between the system and the surroundings. The piston-cylinder arrangement initially contains reactants at pressure P_1 and temperature T_1.

The steps in the cycle are shown in Fig. 2.10. The cycle starts with the system at state 1 and the application of external work to move the piston on the left at velocity u_p. It instantaneously initiates a detonation front at the piston surface (step a). The detonation propagates to the right with a velocity U_{CJ} consistent with u_p. The detonation products following the wave are in a uniform state. When the detonation reaches the right piston, it instantaneously accelerates to velocity u_p, and the entire piston-cylinder arrangement moves at constant velocity u_p (step b). The system is then at state 2. The energy of this mechanical motion is converted to external work (step c) by bringing the detonation products to rest at state 3. Then the products are adiabatically expanded to the initial pressure (step d) to reach state 4. Heat is extracted by cooling the products at constant pressure (step e) to the initial temperature (state 5). Finally, the cycle is completed by converting products to reactants at constant temperature and pressure (step f) and the system reaches state 1.

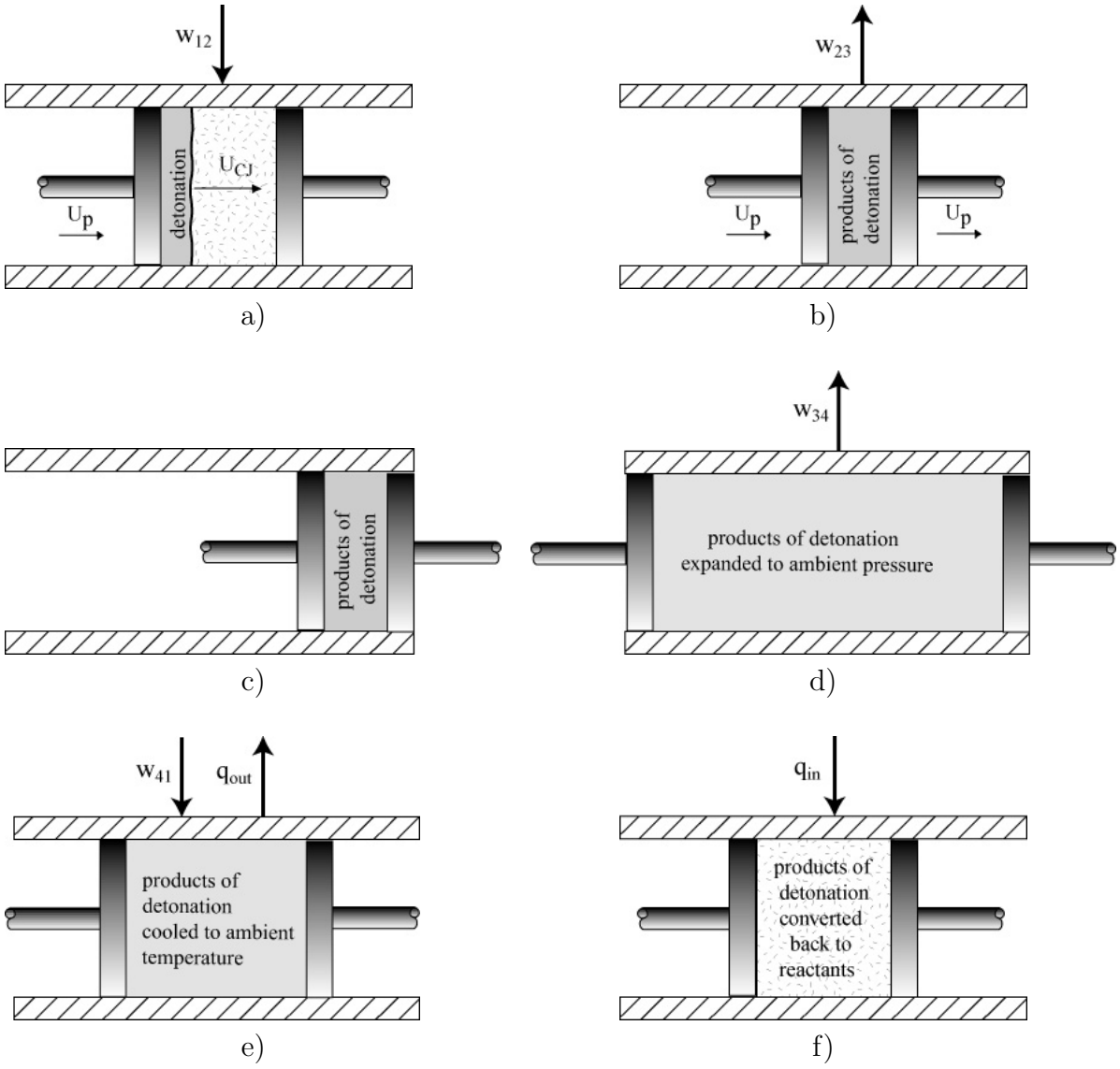

Figure 2.10: Physical steps that make up the Fickett-Jacobs cycle. a) Detonation moving to right with simultaneous application of external work to move piston on left at velocity u_p. b) Instantaneous acceleration of piston on right when detonation has consumed all the material. c) Conversion of mechanical motion to external work to bring detonation products to rest. d) Expansion of products back to atmospheric pressure. e) Extraction of energy as heat at constant pressure to return detonation products to initial temperature. f) Conversion of products to reactants at constant temperature and pressure. The flows of work and heat corresponding to the various steps are shown.

Based on this sequence of steps, it is possible to calculate the work done by the system. During the detonation part of the cycle (step a), from state 1 to 2, the work

received by the system is $W_{12} = -P_2 u_p (t_2 - t_1) A$, since the piston exerts a force P_2 while moving at velocity u_p for a time $t_2 - t_1 = L/U_{CJ}$ required by the wave to propagate across the explosive. Using the fact that $\rho_1 L A$ is the mass $\mathcal{M}$ of the explosive, the work received by the system per unit mass of explosive is

$$w_{12} = -\frac{P_2 u_p}{\rho_1 U_{CJ}} \, . \tag{2.25}$$

The work done by the system when extracting the energy of the mechanical motion (state 2 to 3) is equal to the kinetic energy of the system. Hence, the work per unit mass of explosive is

$$w_{23} = \frac{u_p^2}{2} \, . \tag{2.26}$$

The work per unit mass of explosive obtained during the isentropic expansion of the detonation products to initial pressure (state 3 to 4) is

$$w_{34} = \int_3^4 P dv \, . \tag{2.27}$$

The last steps from state 4 to state 1 involve the exchange of heat and mechanical work used to keep the system at constant pressure. The work per unit mass is

$$w_{41} = P_1 (v_1 - v_4) \, . \tag{2.28}$$

The net work done by the system is equal to or less than the net work of the cycle $w_{net} = w_{12} + w_{23} + w_{34} + w_{41}$. Hence, w_{net} represents the maximum amount of work that can be obtained from a detonation. The FJ cycle can be represented in a pressure-specific volume diagram (Fig. 2.11) and w_{net} geometrically represents the area contained within the triangle formed by the state points. Fickett and Davis (2001, pp. 35–38) do not account for the work interaction during the process 4–1 in their definition of the net work. They do not consider steps e) and f) to be physical since the detonation products just mix with the surroundings, and they consider the work generated between states 4 and 1 to be "lost" work. However, these interactions

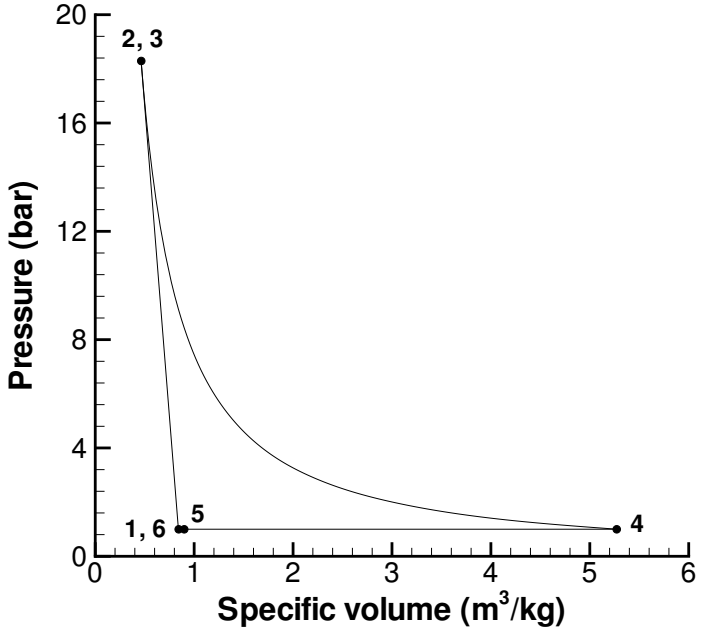

Figure 2.11: Pressure-specific volume diagram showing the sequence of states and connecting paths that make up the FJ cycle for a stoichiometric propane-air mixture at 300 K and 1 bar initial conditions.

have to be included for consistency with the First Law of Thermodynamics[3]. In high-explosive applications, $P_1 \ll P_2$ and the additional work term corresponding to w_{41} may be small compared to the other work terms.

For all steps in the cycle, the First Law of Thermodynamics applies. Using the sign convention defined previously,

$$\Delta E = Q - W \ , \tag{2.29}$$

where E is the total energy in the system, composed of the internal and kinetic energies. The only heat exchange between the system and the surroundings occurs between steps 4 and 1. Hence, the work done by the system per unit mass of explosive can be calculated for each process as a function of the total energy per unit mass and

[3]Our first effort (Cooper and Shepherd, 2002) to apply the FJ cycle to modeling impulse from detonation tubes used Fickett and Davis' interpretation of the available work rather than the approach taken here. As a consequence, the numerical values of the efficiencies given in Cooper and Shepherd (2002) are different than given here.

$w_{14} = e_1 - e_4$. Using Eq. 2.28, the net work done by the system over the FJ cycle is

$$w_{net} = e_1 - e_4 + P_1(v_1 - v_4) = h_1 - h_4 \; . \tag{2.30}$$

This result is consistent with Eq. 1.72 resulting from the general thermodynamic cycle analysis for closed systems undergoing a cycle starting with an arbitrary process between states 1 and 4 and ending with a constant pressure process between states 4 and 1. This consistency is achieved only if w_{41} is included in the computation. It shows that the FJ cycle is a consistent conceptual framework to calculate the amount of work available from a detonation. Since all processes other than the detonation are ideal, the work computed is an upper bound to what can be obtained by any cyclic process using a propagating detonation for the combustion step.

It can be verified using the detonation jump conditions that this result can also be obtained by computing the amount of work done during each individual process. Although it is straightforward from the First Law of Thermodynamics and Eq. 2.27 that $w_{34} = e_3 - e_4$, it is not obvious that $w_{13} = w_{12} + w_{23} = e_1 - e_3$. We write the detonation wave jump conditions in terms of the velocities in a fixed reference frame.

$$\rho_2(U_{CJ} - u_p) = \rho_1 U_{CJ} \tag{2.31}$$

$$P_2 = P_1 + \rho_1 U_{CJ} u_p \tag{2.32}$$

$$h_2 = h_1 - u_p^2/2 + U_{CJ} u_p \tag{2.33}$$

The work per unit mass generated between states 1 and 3, which correspond respectively to reactants and detonation products at rest, can be calculated using the results of Eqs. 2.31–2.33. Note that the thermodynamic properties of states 2 and 3 are identical, but the system at state 3 is at rest whereas it is moving at velocity u_p at state 2. From Eqs. 2.25 and 2.26,

$$\begin{aligned} w_{12} + w_{23} &= u_p^2/2 - \frac{P_2 u_p}{\rho_1 U_{CJ}} \\ &= h_1 - h_2 + U_{CJ} u_p - \frac{P_2 u_p}{\rho_1 U_{CJ}} \; . \end{aligned} \tag{2.34}$$

The third term on the right-hand side of the previous equation can be expressed using Eq. 2.32, and Eq. 2.34 becomes

$$w_{12} + w_{23} = h_1 - h_2 + \frac{P_2}{\rho_1}\left(1 - \frac{u_p}{U_{CJ}}\right) - \frac{P_1}{\rho_1} \ . \tag{2.35}$$

Using the result of Eq. 2.31, and after some algebra, this equation yields

$$w_{12} + w_{23} = e_1 - e_3 \ , \tag{2.36}$$

where $e = h - P/\rho$ is the specific internal energy per unit mass of the mixture. Combining this with the previous results, we have

$$w_{net} = w_{12} + w_{23} + w_{34} + w_{41} = h_1 - h_4 \tag{2.37}$$

in agreement with Eq. 2.30. Thus, we have verified that our two treatments give identical results. This gives us additional confidence that the FJ physical model of the detonation cycle is correct since the detailed energy balance agrees with the simpler thermodynamic system approach.

2.3.2 Thermal efficiency

The FJ cycle is also used to define a thermal efficiency for the conversion of chemical energy into mechanical work. The thermal efficiency is defined as

$$\eta_{FJ} = \frac{w_{net}}{q_c} = \frac{h_1 - h_4}{q_c} \ . \tag{2.38}$$

For mixtures with a higher enthalpy at the end of the expansion process (state 4), a higher portion of the useful work is lost through heat transfer during the constant pressure processes between states 4 and 5.

We first investigate the values of the thermal efficiency for a perfect gas model. The detonation process is represented using the one-γ model of detonation (Eqs. 1.15–1.19) for values of γ representative of products from hydrocarbon fuel detonations with

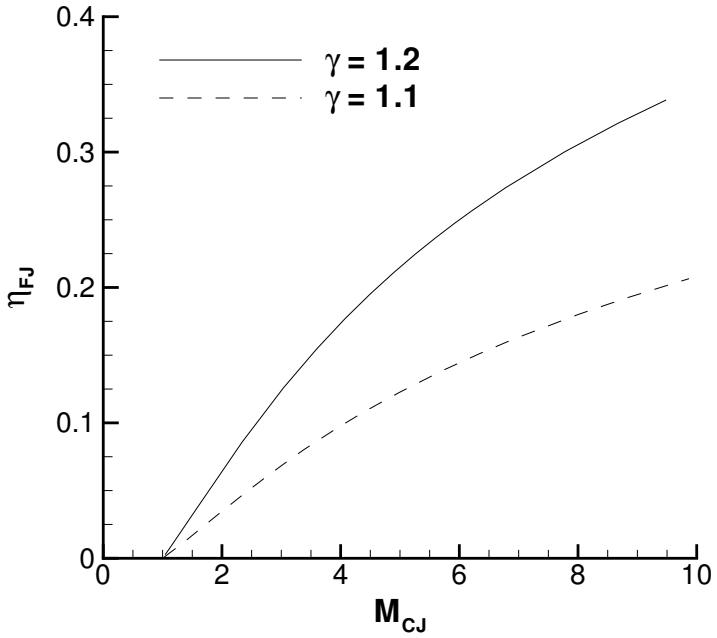

Figure 2.12: FJ cycle thermal efficiency as a function of CJ Mach number for the one-γ model of detonation for two values of γ representative of fuel-oxygen ($\gamma = 1.1$) and fuel-air ($\gamma = 1.2$) detonations.

oxygen and air. The thermal efficiency for the FJ cycle is calculated for a perfect gas as

$$\eta_{FJ} = 1 - \frac{C_p T_1}{q_c} \left[\frac{1}{M_{CJ}^2} \left(\frac{1 + \gamma M_{CJ}^2}{1 + \gamma} \right)^{\frac{\gamma+1}{\gamma}} - 1 \right] . \tag{2.39}$$

The FJ cycle thermal efficiency is represented in Fig. 2.12 as a function of the CJ Mach number for two values of γ representative of fuel-oxygen and fuel-air detonations. The thermal efficiency increases with increasing CJ Mach number, which is itself an increasing function of the heat of combustion q_c (Eq. 1.15). As q_c increases, a lower fraction of the heat released in the detonation process is rejected during the final constant pressure process. In the limit of large M_{CJ}, the thermal efficiency approaches 1 with $1 - \eta_{FJ} \propto (1/M_{CJ}^2)^{1-1/\gamma}$. Looking at the detonation as a ZND process (Section 1.1.2), this result may be interpreted as follows: a higher heat of combustion results in a higher precompression of the reactants through the shock wave before combustion and yields a higher thermal efficiency.

Figure 2.12 also shows that the variation of the thermal efficiency depends strongly on the value chosen for γ. At constant CJ Mach number, a lower value of γ in the detonation products yields a lower efficiency. The parameter $\gamma - 1$ controls the slope of the isentrope 3–4 in the pressure-temperature plane. Lower values of γ generate lower temperature variations for a fixed pressure ratio P_4/P_3. This means that the temperature at state 4 is higher and the heat rejected during process 4–5 is larger, decreasing the thermal efficiency. In order to gain some deeper insight into the influence of γ on the thermal efficiency, we used the two-γ model of detonations (Eqs. 1.8–1.14), which allows for property variations across the detonation wave front, to calculate the thermal efficiency.

$$\eta_{FJ} = 1 - \frac{C_{p2}T_1}{q_c}\left[\frac{\gamma_2}{\gamma_1 M_{CJ}^2}\left(\frac{1+\gamma_1 M_{CJ}^2}{1+\gamma_2}\right)^{\frac{\gamma_2+1}{\gamma_2}} - 1\right] \tag{2.40}$$

The thermal efficiency for the two-γ model of detonations is represented in Fig. 2.13 as a function of the CJ Mach number for different values of γ_2. The thermal efficiency has a very different behavior depending on the value chosen for γ_2. For $\gamma_1 = \gamma_2$, it reproduces the results of the one-γ model with η_{FJ} increasing with M_{CJ}. However, for $\gamma_2 < \gamma_1$, it has a minimum, which depends on the value of γ_2. For high enough M_{CJ}, the thermal efficiency increases with increasing M_{CJ} and tends to 1 for large values of the Mach number. The parameter $\gamma_2 - 1$ determines the slope of the isentrope 3–4 along which the expansion process takes place, and therefore has a strong influence on the magnitude of the heat rejected and the thermal efficiency. However, typical fuel-air mixtures, for which $\gamma_2 \approx 1.2$ and $M_{CJ} > 4$, and typical fuel-oxygen mixtures, for which $\gamma_2 \approx 1.1$ and $M_{CJ} > 5$, are located on the part of the curves in Fig. 2.13 where the thermal efficiency is an increasing function of M_{CJ}. This general behavior exhibited by the thermal efficiency will help us explain some of the trends observed in real gases.

The most realistic approach to accounting for property variations is to use fits or tabulated thermochemical properties as a function of temperature for each species and the ideal gas model to find mixture properties. In keeping with the spirit of

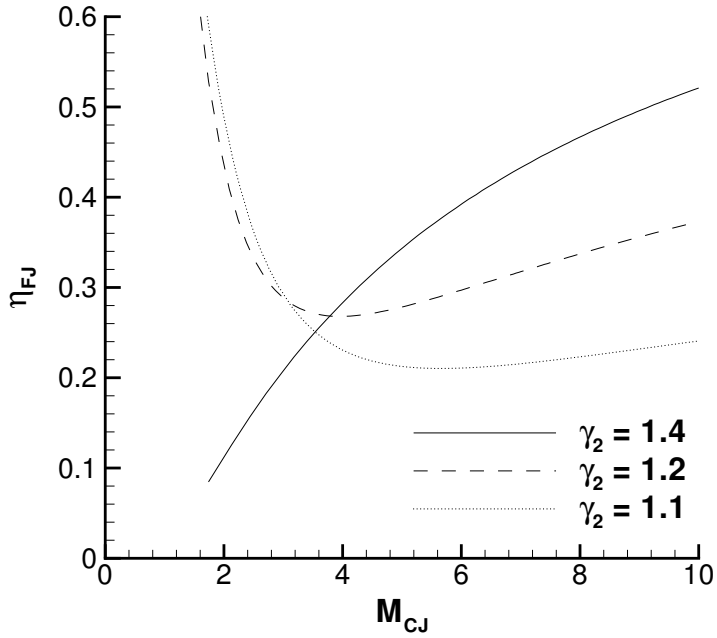

Figure 2.13: FJ cycle thermal efficiency as a function of CJ Mach number for the two-γ model of detonation with $\gamma_1 = 1.4$.

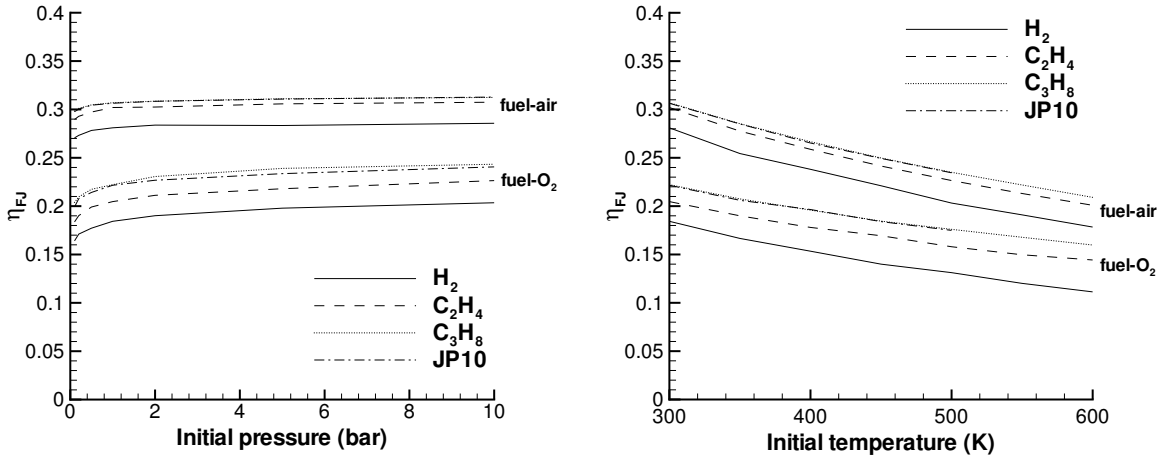

Figure 2.14: FJ cycle thermal efficiency for stoichiometric hydrogen, ethylene, propane, and JP10 mixtures with oxygen and air as a function of initial pressure at 300 K (left) and initial temperature at 1 bar (right).

cycle analysis, all chemical states involving combustion products are assumed to be in equilibrium. The FJ cycle thermal efficiency was calculated using realistic thermochemistry for hydrogen, ethylene, propane, and JP10 fuels with oxygen and air. The

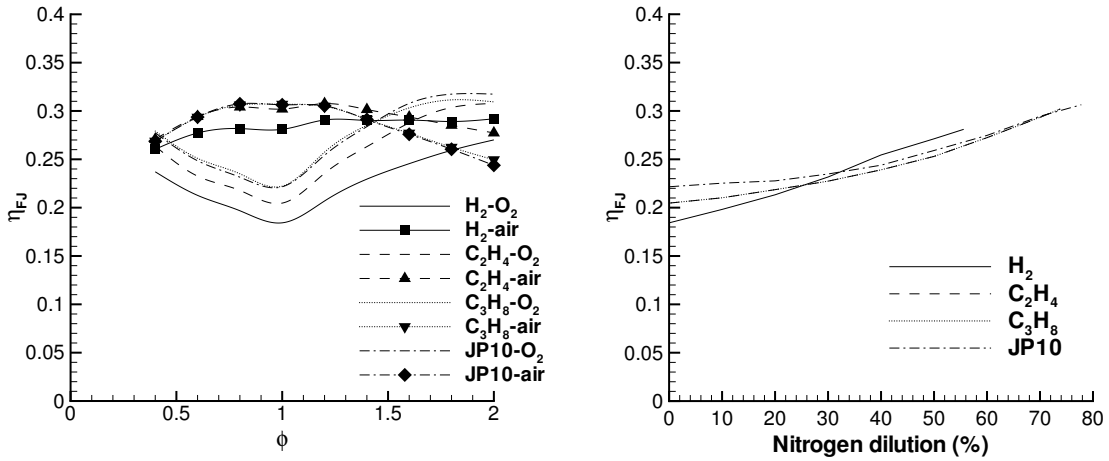

Figure 2.15: Left: FJ cycle thermal efficiency as a function of equivalence ratio at 300 K and 1 bar initial conditions for hydrogen, ethylene, propane and JP10. Right: FJ cycle thermal efficiency as a function of nitrogen dilution for stoichiometric fuel-oxygen mixtures at 300 K and 1 bar initial conditions for hydrogen, ethylene, propane and JP10.

equilibrium computations were carried out using STANJAN (Reynolds, 1986). The thermal efficiency was determined using Eq. 2.38. The results are significantly influenced by the variation of the specific heat capacity with temperature in the detonation products and the dissociation and recombination processes.

The thermal efficiency is shown in Fig. 2.14 as a function of initial pressure. The thermal efficiency decreases with decreasing initial pressure due to the increasing importance of dissociation at low pressures. Dissociation is an endothermic process and reduces the effective energy release through the detonation, and the maximum amount of work that can be obtained from the FJ cycle. Exothermic recombination reactions are promoted with increasing initial pressure and the amount of work generated during the FJ cycle increases. At high initial pressures, the major products dominate and the CJ detonation properties tend to constant values. Thus, the amount of work generated by the detonation and the thermal efficiency asymptote to constant values. Figure 2.14 shows that η_{FJ} decreases with increasing initial temperature. Because the thermal efficiency is an increasing function of the CJ Mach number (Fig. 2.12), the decrease in initial mixture density and M_{CJ} caused by the increasing

initial temperature (Eq. 1.15) is responsible for the decreasing thermal efficiency.

The influence of equivalence ratio on the FJ cycle thermal efficiency is shown in Fig. 2.15. The trends for fuel-oxygen and fuel-air mixtures are very different. The thermal efficiency for fuel-air mixtures is maximum at stoichiometry, whereas it is minimum for fuel-oxygen mixtures. This behavior illustrates clearly the strong influence of dissociation processes on the thermal efficiency. Fuel-air mixtures generate much lower CJ temperatures than fuel-oxygen mixtures. The effect of dissociation in fuel-air mixtures is weak because a significant part of the energy release is used to heat up the inert gas (nitrogen) and the temperatures are lower than in the fuel-oxygen case. Because of the weak degree of dissociation, these mixtures tend to follow the same trends as the perfect gas and yield a maximum efficiency when the energy release is maximized near stoichiometry. Lean mixtures have very little dissociation and the CJ Mach number increases with the equivalence ratio from 4 to 5 or 6 at stoichiometry. Thus, the thermal efficiency increases with increasing equivalence ratio for $\phi < 1$. Rich mixtures ($\phi > 1$) have significant amounts of carbon monoxide and hydrogen due to the oxygen deficit and the dissociation of carbon dioxide and water, reducing the effective energy available for work and the thermal efficiency.

On the other hand, fuel-oxygen mixtures are characterized by high CJ temperatures, in particular near $\phi = 1$. Endothermic dissociation reactions reduce the effective energy release during the detonation process. During the subsequent expansion process 3–4, the radicals created by the dissociation reactions start recombining. However, the temperature in the detonation products of fuel-oxygen mixtures remains high during this process and only partial recombination occurs. The products at state 4 are still in a partially dissociated state and a significant part of the energy released by the detonation is not available for work. This extra energy is released during the constant pressure process 4–5 under the form of heat and reduces the net work. The influence of this phenomenon increases with increasing CJ temperature, which explains why fuel-oxygen mixtures have a lower efficiency near stoichiometry.

In order to illustrate this point, we compare the mixture composition of stoichiometric propane-air and propane-oxygen mixtures at state 4 (initial conditions 300 K

and 1 bar). The propane-air mixture has a temperature of 1798 K and the major products CO_2 and H_2O dominate. All other species have mole fractions on the order of 10^{-3} and lower. On the other hand, the propane-oxygen mixture has a temperature of 2901 K and has a much higher degree of dissociation. The major species include CO_2 (with a mole fraction of 20%), H_2O (39.5%), but also CO (16%), O_2 (8%), H_2 (4.5%), and radicals such as OH (7%), H (2.5%), and O (2%). The presence of these radicals indicates that the major combustion products have dissociated. A significant part of the energy released by the detonation has been absorbed by the endothermic dissociation reactions and is therefore unavailable for work.

The influence of nitrogen dilution is also investigated in Fig. 2.15. The thermal efficiency is plotted as a function of nitrogen dilution for stoichiometric mixtures varying from fuel-oxygen to fuel-air. It increases with increasing nitrogen dilution and is maximum for fuel-air mixtures. This behavior is explained mainly by the influence of dissociation phenomena. The reduction in mixture specific heat capacity with increasing nitrogen dilution also contributes to this behavior.

Although fuel-oxygen mixtures have a higher heat of combustion than fuel-air mixtures, Fig. 2.15 shows that fuel-air mixtures have a higher thermal efficiency, in particular near stoichiometry. This is attributed mainly to dissociation phenomena, but also to the higher value of the effective ratio of specific heats γ in the detonation products of fuel-air mixtures, which results in a higher thermal efficiency (Fig. 2.12). In general, $1.13 < \gamma_2 < 1.2$ for fuel-oxygen mixtures when varying the equivalence ratio, whereas $1.16 < \gamma < 1.3$ for fuel-air mixtures. The parameter $\gamma - 1$ controls the slope of the isentrope in the pressure-temperature plane. This difference is caused by the influence of recombination reactions in the detonation products. These exothermic reactions are favored in the hot products of fuel-oxygen mixtures, and keep the temperature from dropping as fast as in the colder products of fuel-air mixtures. Note that, although stoichiometric fuel-oxygen mixtures have a lower thermal efficiency than fuel-air mixtures, they generate 2 to 4 times as much work as fuel-air mixtures because of their larger heat of combustion.

In general, hydrogen yields the lowest efficiency. Combustion of hydrogen with

oxygen produces a mole decrement, which generates a much lower CJ pressure compared to hydrocarbon fuel detonations. Because entropy increases with decreasing pressure, a lower pressure translates into a higher entropy rise and a lower thermal efficiency compared with hydrocarbon fuel detonations. In terms of work done, the work generated during the expansion process w_{34} is much lower for hydrogen detonations because of their lower CJ pressure, which reduces the thermal efficiency. Hydrocarbon fuels have a higher thermal efficiency, with propane and JP10 yielding the highest efficiency. These two fuels have the highest molecular weight of all, which translates into a higher initial density, CJ pressure, and propensity to generate work during the expansion process. The values obtained for the FJ cycle efficiency are quite low, generally between 0.2 and 0.3 for the range of mixtures investigated. The typical way to increase low thermal efficiencies is to precompress the reactants before combustion. The FJ cycle with precompression is investigated next.

2.3.3 FJ cycle with precompression

The role of precompression is to reduce the entropy rise through the combustion process by increasing the initial temperature before combustion (Foa, 1960). Since entropy increments are detrimental to the thermal efficiency, the most ideal way to increase the fluid temperature is isentropic compression.

The FJ cycle with precompression is based on the steps described in Fig. 2.10, but it includes an additional process. Before the piston starts moving and initiates the detonation, the reactants are isentropically compressed with the piston to a state 1'. The subsequent sequence of steps is identical to the basic FJ cycle case. The FJ cycle with precompression is represented in Fig. 2.16 in the pressure-specific volume plane for a propane-air mixture with a precompression ratio of 5. The precompression ratio is defined as $\pi_c = P_{1'}/P_1$.

During the initial compression of the reactants from state 1 to state 1', the work per unit mass is

$$w_{11'} = -\int_1^{1'} P dv \ . \tag{2.41}$$

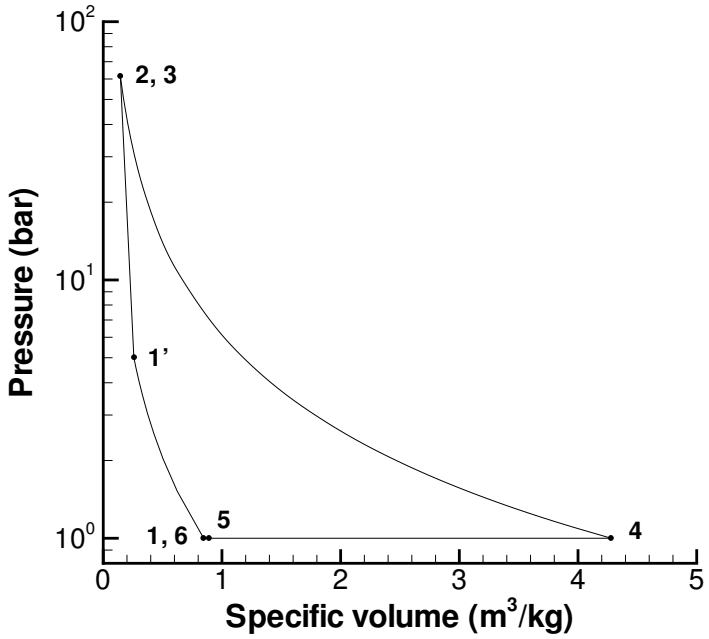

Figure 2.16: Pressure-specific volume diagram showing the sequence of states and connecting paths that make up the FJ cycle with precompression ($\pi_c = 5$) for a stoichiometric propane-air mixture at 300 K and 1 bar initial conditions.

The net work done by the system is then $w_{net} = w_{11'} + w_{1'2} + w_{23} + w_{34} + w_{41}$. Expressions for the terms in the previous equation are given respectively by Eqs. 2.41, 2.25, 2.26, 2.27, and 2.28. Applying the First Law of Thermodynamics, the result obtained for the net work $w_{net} = h_1 - h_4$ is identical to that of Eq. 2.30.

The influence of the compression ratio on the thermal efficiency is investigated first for a perfect gas. The expression for η_{FJ} using the one-γ detonation model is identical to the result of Eq. 2.39 for the basic FJ cycle. However, in the case of the cycle with precompression, the CJ Mach number varies because of the change in initial temperature before detonation initiation. The thermal efficiency is plotted in Fig. 2.17 as a function of π_c for different values of the non-dimensional energy release. The FJ cycle thermal efficiency increases with increasing compression ratio. This increase can be explained by considering the temperature-entropy diagram of Fig. 2.17. The heat rejected during the constant-pressure portion of the cycle 4–5 is the area under the temperature-entropy curve between states 4 and 5 (Eq. 1.74). For

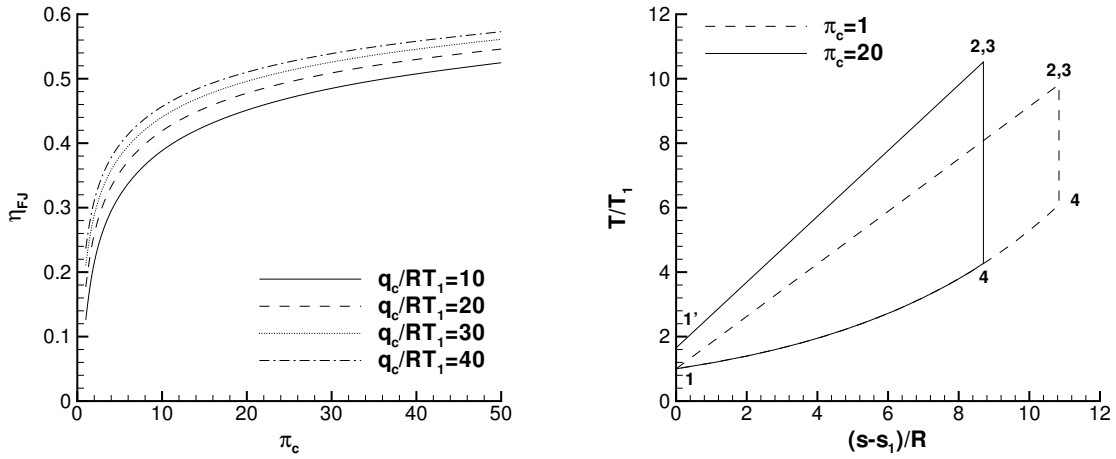

Figure 2.17: Left: FJ cycle thermal efficiency as a function of the compression ratio π_c for the one-γ model of detonation using different values of the non-dimensional heat release. Right: temperature-entropy diagram for FJ cycle without and with precompression ($\pi_c = 20$) using the one-γ model of detonation. $q_c/RT_1 = 40$, $\gamma = 1.2$.

a given state 1 and q_{in}, the thermal efficiency is maximized when q_{out} is minimized, which occurs when $s_4 = s_2$ is minimized. Because the total entropy rise decreases with increasing combustion pressure, the cycle thermal efficiency increases with increasing compression ratio. In terms of net work, precompressing the reactants increases the work done during the expansion process (state 3 to 4). The expansion of the hot gases generates more work than is absorbed by the cold gases during the precompression stage, so that precompression increases the thermal efficiency. This idea applies equally well to other types of thermodynamic cycles such as the Brayton or the Otto cycles.

The result of Eq. 2.39, which also applies to the FJ cycle with precompression, is identical to the result obtained by Heiser and Pratt (2002) in their thermodynamic cycle analysis of pulse detonation engines. They calculated the entropy increments associated with each process in the detonation cycle and formally obtained the same result. However, the numerical values shown in Fig. 2.17 are lower than those given in Heiser and Pratt (2002) due to the difference in the value of the specific heat ratio used. They used a value of $\gamma = 1.4$ corresponding to the reactants, whereas we use values of γ equal to 1.1 or 1.2 since these are more representative of the detonation

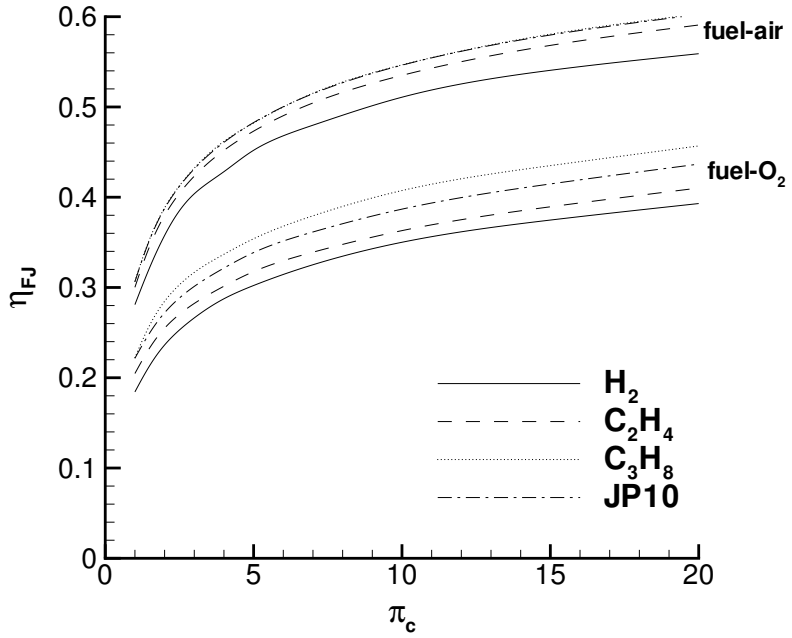

Figure 2.18: FJ cycle thermal efficiency as a function of the compression ratio π_c for hydrogen, ethylene, propane, and JP10 with oxygen and air at initial conditions of 1 bar and 300 K.

products. As illustrated in Fig. 2.12, the value chosen for the specific heat ratio has a strong influence on the results obtained for the thermal efficiency in the one-γ model. A more realistic cycle analysis for a perfect gas involves using the two-γ model of detonations (Fig. 2.13). This approach was applied by Wu et al. (2003), who extended the analysis of Heiser and Pratt (2002) to the two-γ model of detonations.

In reality, one- or two-γ models of these cycles cannot correctly capture all the features of dissociation-recombination equilibria and temperature-dependent properties. It is necessary to carry out numerical simulations with a realistic set of product species and properties. Equilibrium computations using realistic thermochemistry were carried out using STANJAN (Reynolds, 1986) for hydrogen, ethylene, propane, and JP10. The thermal efficiency is given in Fig. 2.18 as a function of the compression ratio. Its behavior is similar to the perfect gas case. The influence of dissociation reactions is reduced with increasing compression ratio, but dissociated species are still present for fuel-oxygen mixtures, even for high values of π_c. The mixture composi-

tion for the stoichiometric propane-oxygen mixture considered in Section 2.3.2 with a precompression factor of 10 includes CO_2 (with a mole fraction of 28%), H_2O (46%), CO (11%), O_2 (6%), H_2 (2.9%), and radicals OH (4%), H (0.9%), and O (0.9%). This partially dissociated state explains why the efficiency of fuel-oxygen mixtures remains much lower compared to fuel-air mixtures.

2.4 Detonation and constant-volume combustion

Constant-volume (CV) combustion has been used as a convenient surrogate for detonation for the purposes of estimating the thermal efficiency (Eidelman et al., 1991, Bussing and Pappas, 1996, Kentfield, 2002). One viewpoint is that CV combustion is an instantaneous transformation of reactants into products. Another view is that CV combustion is the limit of a combustion wave process as the wave speed approaches infinity.

2.4.1 Comparison of FJ cycle with Brayton and Humphrey cycles

Constant-pressure combustion is representative of the process undergone by a fluid particle in an ideal ramjet or turbojet engine (Oates, 1984). The ideal Brayton cycle consists of the following processes: isentropic compression, CP combustion, isentropic expansion to initial pressure, and heat exchange and conversion of products to reactants at constant pressure. For the perfect gas, the thermal efficiency of the Brayton cycle depends only on the static temperature ratio across the compression process (Oates, 1984).

$$\eta_{th} = 1 - \frac{T_1}{T_{1'}} = 1 - \pi_c^{-\frac{\gamma-1}{\gamma}} \tag{2.42}$$

The Humphrey cycle is similar to the Brayton cycle, except that the combustion occurs at constant volume instead of constant pressure. Unlike the Brayton cycle and like the FJ cycle, the efficiency of the Humphrey cycle also depends on the non-

dimensional heat release q_c/CpT_1 and the specific heat ratio γ.

$$\eta_{th} = 1 - \frac{C_p T_1}{q_c}\left[\left(1 + \gamma \frac{q_c}{C_p T_1} \pi_c^{-\frac{\gamma-1}{\gamma}}\right)^{1/\gamma} - 1\right] \tag{2.43}$$

For fixed energy release and compression ratio, the thermal efficiency of the Humphrey cycle is higher than that of the Brayton cycle, which can be related to the lower entropy rise generated by CV combustion compared with CP combustion (Fig. 2.2).

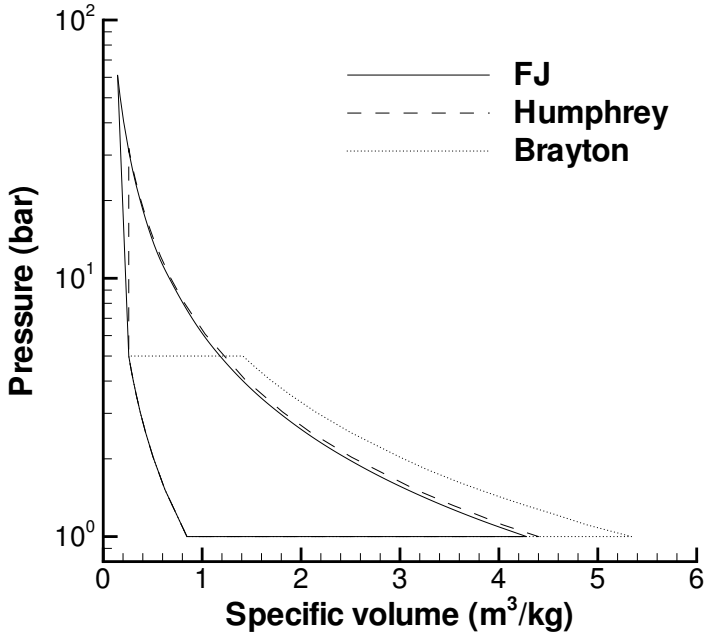

Figure 2.19: Pressure-specific volume diagram comparing the FJ, Humphrey, and Brayton cycles with precompression ($\pi_c = 5$) for a stoichiometric propane-air mixture at 300 K and 1 bar initial conditions.

Equilibrium computations were carried out using STANJAN (Reynolds, 1986) to compute the thermal efficiency of the FJ, Humphrey, and Brayton cycles for a stoichiometric propane-air mixture at 300 K and 1 bar initial conditions. The amount of precompression was varied. In comparing different combustion modes, the question of which of the various pressures produced during the combustion event should be considered (Talley and Coy, 2002). Two possibilities are explored here. The first possibility consists of comparing the cycles based on the same pressure before combus-

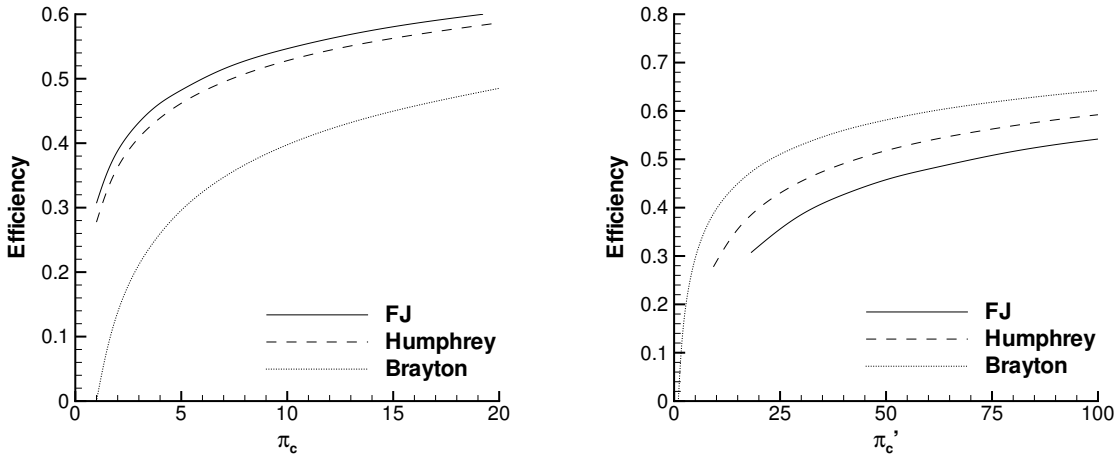

Figure 2.20: Thermal efficiency as a function of compression ratio (left) and combustion pressure ratio (right) for FJ, Humphrey and Brayton cycles for a stoichiometric propane-air mixture at 300 K and 1 bar initial conditions.

tion, which corresponds to propulsion systems having equivalent feed systems. The second possibility is based on the peak combustion pressure, which corresponds to propulsion systems designed to operate at the same level of chamber material stresses.

The cycle efficiencies are shown in Fig. 2.20 as a function of the compression ratio and the combustion pressure ratio. The combustion pressure ratio π_c' is defined as the ratio of post-combustion pressure to initial cycle pressure. Detonation generates the lowest entropy rise, closely followed by CV combustion and finally CP combustion (Fig. 2.2). Thus, for a given compression ratio, the FJ cycle yields the highest thermal efficiency, closely followed by the Humphrey cycle and, finally, the Brayton cycle. This calculation using detailed thermochemistry (Reynolds, 1986) agrees qualitatively with the thermodynamic cycle analysis results of Heiser and Pratt (2002) who used a one-γ model for detonations. The fact that detonation and CV combustion yield very close efficiencies when calculated for the same compression ratio (Fig. 2.20) has motivated some researchers to estimate pulse detonation engine performance by approximating the detonation process with CV combustion (Kentfield, 2002). However, when the thermal efficiency is shown as a function of the combustion pressure ratio (Fig. 2.20), the trend is inverted and the Brayton cycle yields the highest efficiency, followed by

the Humphrey and FJ cycles. The lower efficiency of the FJ cycle can be attributed to the very high peak pressure behind the detonation wave. Although these efficiencies cannot be precisely translated into specific performance parameters, these general results agree with the observations of Talley and Coy (2002) based on specific impulse calculations using a gas dynamic model of CV combustion propulsion. The superiority of the Brayton cycle in the left graph of Fig. 2.20 will be reduced if the Humphrey and FJ cycles are operated at a higher combustion peak pressure or temperature.

The comparison of the thermal efficiencies in Fig. 2.20 shows that unsteady detonations have the potential to generate more mechanical work than CP or CV combustion and, thus, appear to be more efficient combustion process. This result can be directly related to the lower entropy rise associated with detonations and is discussed further in the next section. However, as we have already seen for the case of steady detonation, some care is needed in interpreting thermodynamic results in terms of propulsion system performance. We cannot use these efficiencies directly since performance estimates based on Eq. 1.83 are applicable only to steady propulsion systems. In particular, the initial state (before the detonation wave) and the conversion of thermal energy to impulse in unsteady systems requires detailed consideration of the gas dynamic processes (Wintenberger and Shepherd, 2003a) within the engine.

2.4.2 Entropy generated by a detonation

The results of Fig. 2.20 for a fixed compression ratio are the direct consequence of entropy production during the combustion (see Eq. 1.75), since all the other processes in the cycle are assumed to be isentropic. The lower entropy rise generated by detonations for a given initial state (Section 1.1.1), followed by CV and CP combustion, is responsible for the higher efficiency generated by the FJ cycle (see Section 2.1).

The entropy increases during a combustion process primarily because of the chemical energy release and secondarily because of the change in mixture composition. The

entropy of an ideal gas mixture containing j species can be expressed as

$$s = \sum_{i=1}^{j} N_i \overline{s}_i(T, P_i) \ , \tag{2.44}$$

where $\overline{s}_i(T, P_i)$ is the partial molar entropy evaluated at the mixture temperature T and the partial pressure P_i. The specific entropy of species i can be written as a function of the standard entropy, the pressure (in atmospheres), and the molar fraction of species i

$$\overline{s}_i(T, P_i) = \overline{s}_i^0(T) - \mathcal{R} \ln\left(\frac{N_i}{N}\right) - \mathcal{R} \ln(P) \ . \tag{2.45}$$

The standard entropy $\overline{s}_i^0(T)$ depends only on temperature and is, by definition, zero at the state where the temperature is 0 K and the pressure is 1 atmosphere.

$$\overline{s}_i^0(T) = \int_0^T \frac{C_p(T)}{T} dT \tag{2.46}$$

The entropy of the mixture is

$$s = \sum_{i=1}^{j} N_i \overline{s}_i^0(T) - \mathcal{R} \sum_{i=1}^{j} N_i \ln(N_i) + \mathcal{R} \sum_{i=1}^{j} N \ln(N) - \mathcal{R} N \ln(P) \ . \tag{2.47}$$

The entropy increase during combustion is due mainly to the increase in temperature and the contribution of the first term on the right-hand side of Eq. 2.47. The second and third terms, which result from the change in composition, contribute only a small fraction of the total entropy change. In order to illustrate this point, the calculation of Eq. 2.47 was carried out with realistic thermochemistry for a stoichiometric propane-air detonation at 1 atm and 300 K. The combined contribution of the second and third terms was found to account for less than 11% of the total change in entropy per unit mass. The pressure increase through the detonation reduced the total entropy rise by 25%. The main contributions to the total entropy rise were due to the variations in temperature and pressure, and the influence of the change in

chemical composition was found to be smaller.

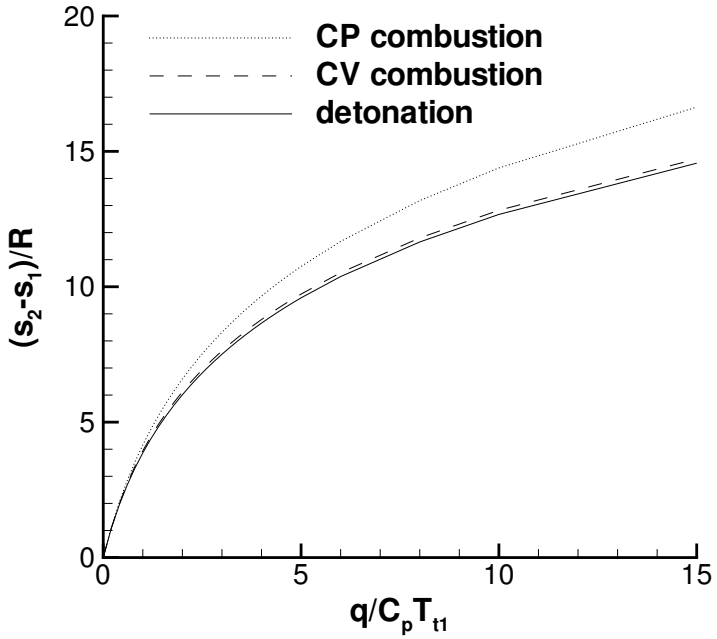

Figure 2.21: Entropy rise generated by CP combustion, CV combustion, and detonation. $\gamma = 1.2$.

This leads us to consider the perfect gas case where we neglect the change in chemical composition. The entropy rise was calculated for a perfect gas as a function of the energy release through combustion based on Eqs. 2.46 and 2.47 assuming a constant specific heat capacity. The entropy rise for CP combustion is given by

$$\frac{s_2 - s_1}{R} = \frac{\gamma}{\gamma - 1} \ln\left(1 + \frac{q_c}{C_p T_{t1}}\right) . \tag{2.48}$$

For CV combustion, the entropy rise can be calculated directly as

$$\frac{s_2 - s_1}{R} = \frac{1}{\gamma - 1} \ln\left(1 + \gamma \frac{q_c}{C_p T_{t1}}\right) . \tag{2.49}$$

The entropy rise for detonation was calculated using the one-γ model for detonation

(Eqs. 1.15–1.19).

$$\frac{s_2 - s_1}{R} = \frac{\gamma}{\gamma - 1} \ln \left[\frac{(1 + \gamma M_{CJ}^2)^2}{(1+\gamma)^2 M_{CJ}^2} \right] - \ln \left(\frac{1 + \gamma M_{CJ}^2}{1 + \gamma} \right) . \tag{2.50}$$

The entropy rise generated by CP combustion is larger than that generated by CV combustion and detonation by up to 14% (compared to detonation) as shown in Fig. 2.21. The entropy rise associated with CV combustion is higher than that associated with detonation by about 2% in the perfect gas case of Fig. 2.21. Equilibrium computations (Reynolds, 1986) for stoichiometric fuel-oxygen and fuel-air mixtures show that for hydrogen, ethylene, propane, and JP10, CV combustion generates an entropy increase up to 2.7% higher than detonation, whereas CP combustion results in an entropy rise up to 24% higher than detonation.

CV combustion represents a limit of combustion phenomena, which is approached for large wave propagation speeds or, in an adiabatic system, at late times when all the wave processes have decayed (Talley and Coy, 2002). In particular, CV combustion is approached following a long time (meaning a large number of wave reflections) after a detonation wave propagates through a closed volume and the resulting fluid motion has been dissipated into thermal energy. In order to illustrate this point, a one-dimensional numerical simulation was carried out with an Euler code under the Amrita software environment (Quirk, 1998). The configuration studied consists of a one-dimensional duct or channel closed at both ends and simulated with reflective boundary conditions. The simulation was started with the detonation wave having propagated to the right end of the duct. The one-γ model for detonation and the Taylor wave solution following the detonation (Eqs. 1.42 and 1.43) were used as an initial condition in the duct. The results of the numerical simulation are presented in Fig. 2.22. The distance-time diagram shows the shock wave reflecting between the ends of the duct. Figure 2.22 shows that the waves decay with time and that the pressure at the left end of the duct asymptotes to the CV pressure. The pressure at the right end of the duct follows a similar behavior. The shock wave reflections generate entropy and the average entropy increases slowly from the CJ value towards

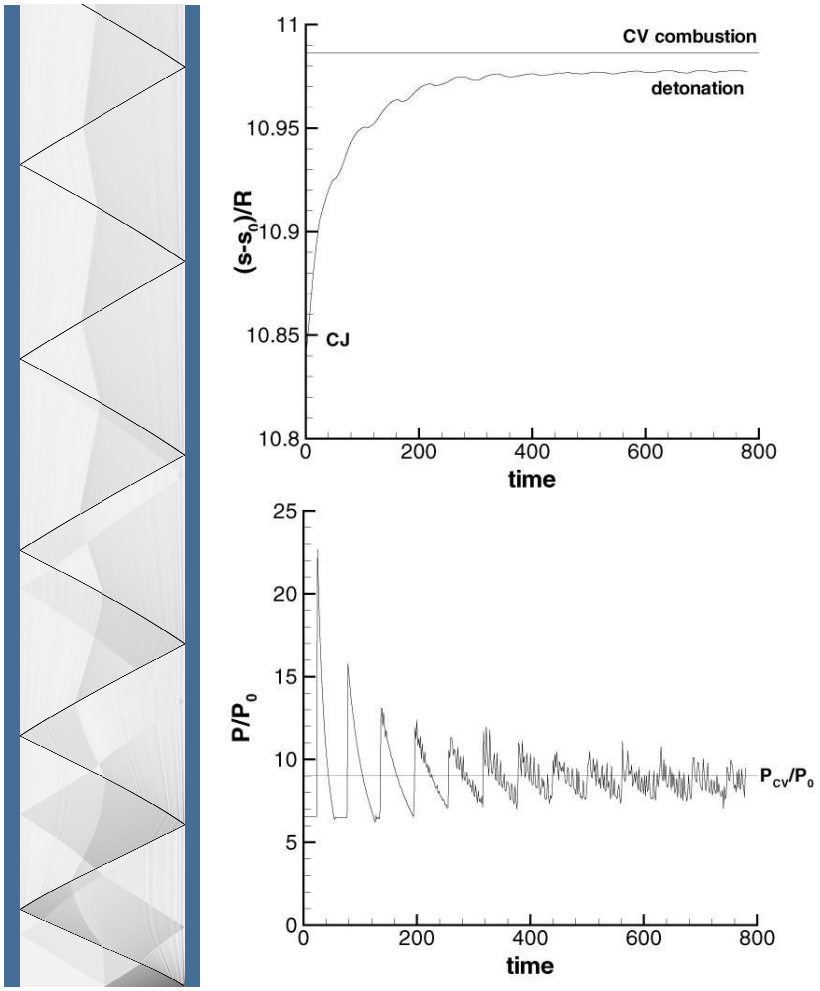

Figure 2.22: Numerical simulation of detonation propagation and reflection in a closed duct. $q/RT_1 = 40$, $\gamma = 1.2$. Left: distance-time diagram (horizontal axis is distance, vertical axis is time). Right: average entropy rise in the duct and pressure at the left end of the duct as a function of time.

the value corresponding to CV combustion. The results obtained from this simulation at late times will not be quantitatively correct since the only dissipative processes in this simulation are purely numerical. Additionally, numerical errors caused by approximating gradients, in particular near the duct ends, accumulate over time and can result in significant errors after a large number of shock reflections. However, the results are in agreement with the exact thermodynamic analysis that the entropy must be less than that obtained from idealized CV combustion of the reactants.

2.4.3 Kinetic energy in detonations

A major difference between detonation waves and idealized CV combustion is that detonations induce a flow behind them, whereas idealized CV combustion represents an instantaneous transformation from reactants to products with no fluid motion. Thus, the question arises as to how much of the energy released by the chemical reactions is converted into thermal energy in a detonation, and how much is converted into kinetic energy. In the case of CV combustion, all of the energy supplied by the chemical reactions is converted into thermal energy. However, due to the substantial flow velocities induced by detonation waves, it is unclear whether the same holds for detonations.

Jacobs (1956) was the first to study this problem when computing the total energy of detonations. He used two approaches to this problem: one by considering a propagating detonation in a closed tube and the following Taylor wave and the second by considering a detonation driven by a moving piston. He found that for typical high explosives (characterized by $\gamma = 3$), the kinetic energy in a detonation wave propagating in a tube accounts for about 10% of the chemical energy released. In gaseous detonations, the effective value of γ is much lower, on the order of 1.1 to 1.2, and we anticipate the results to be quantitatively different.

Following the approach presented by Jacobs (1956), we first consider a one-dimensional propagating gaseous detonation in a closed tube. The Taylor similarity solution applies to the flow following the wave (Fig. 1.8). The total energy in the volume of cross section 1 and length $L(t)$ occupied by the burned products resulting from the detonation of reactants at initial density ρ_0 is

$$E_{total} = \int_0^{L(t)} \rho(x,t) \left[e(x,t) + \frac{u^2(x,t)}{2} \right] dx = \rho_0 q L(t) \; . \tag{2.51}$$

The total energy is the sum of the kinetic and thermal energies defined by

$$E_{kinetic} = \int_0^{L(t)} \rho(x,t)\frac{u^2(x,t)}{2}dx \ , \tag{2.52}$$

$$E_{thermal} = \int_0^{L(t)} \rho(x,t)e(x,t)dx \ . \tag{2.53}$$

The stagnant region following the Taylor wave, which extends about half of the distance from the duct end to the detonation front, does not contribute to the kinetic energy but still contributes to the thermal energy budget. The velocity in the Taylor wave is calculated from Eq. 1.42 using the Riemann invariant. The calculation of the kinetic energy per unit length yields

$$E_{kinetic}/L(t) = \frac{2\gamma}{(\gamma+1)^2}\left(\frac{\gamma-1}{\gamma+1}\right)^{\frac{2}{\gamma-1}}\frac{\rho_3 c_3^3}{U_{CJ}}\int_1^{U_{CJ}/c_3}\left(\xi+\frac{2}{\gamma-1}\right)^{\frac{2}{\gamma-1}}(\xi-1)^2 d\xi \ , \tag{2.54}$$

where $\xi = x/c_3 t$. The integral in Eq. 2.54 is evaluated numerically. The ratio of the kinetic energy to the total energy release was calculated using the one-γ model for detonations. It is found to be quite insensitive to the value of the energy release (it varies from 1.93% to 2.23% when q/RT_1 is increased from 10 to 100 for $\gamma = 1.2$). However, it strongly depends on the value of γ. The variation of the kinetic energy fraction with γ is shown in Fig. 2.23. The kinetic energy fraction increases with increasing γ from zero at $\gamma = 1$ to about 10% at $\gamma = 3$, which is representative of high explosives. The latter value agrees with the results of Jacobs (1956). The interesting point is that for typical gaseous detonations in hydrocarbon-oxygen or -air mixtures, for which γ is on the order of 1.2, the kinetic energy represents only about 2% of the total energy release.

The second approach we follow considers a detonation driven by a piston, such as in Fig. 2.10 a). The piston moves at a velocity u_p and initiates a detonation wave propagating at velocity U_{CJ}. No expansion of the gas occurs behind the detonation because of the work provided by the piston. The energy conservation equation for a

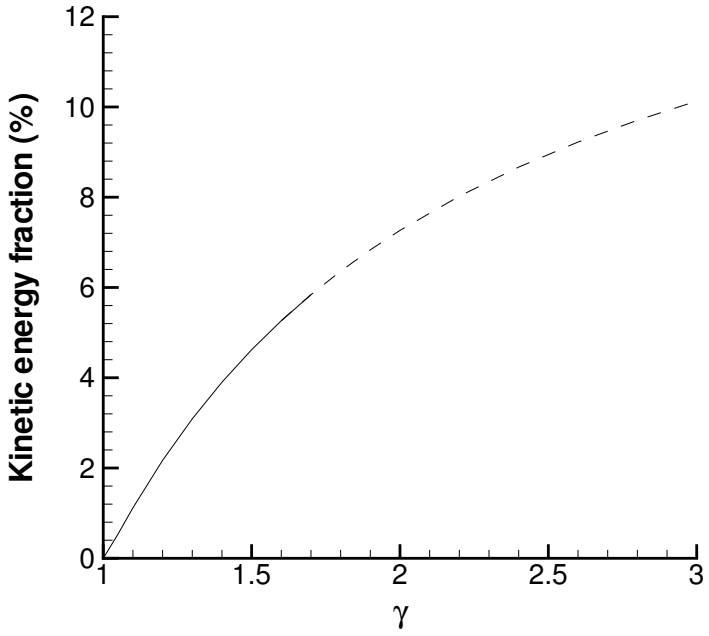

Figure 2.23: Ratio of kinetic energy to total energy release as a function of the adiabatic exponent for a detonation wave propagating in a closed tube. $q_c/RT_1 = 40$. Note that the dashed portion is non-physical for ideal gases but is often used in modeling high explosives.

perfect gas can be written as

$$C_v(T_2 - T_1) + \frac{u_p^2}{2} - P_2(v_1 - v_2) = q_c \; . \tag{2.55}$$

The sum of the thermal and kinetic energies equals the sum of the energy released by the detonation and the work done by the piston. It is instructive to compare the magnitude of the different terms of Eq. 2.55 relative to the heat release. Based on the one-γ model for detonations with $q_c/RT_1 = 40$ and $\gamma = 1.2$, the thermal energy term accounts for +110.4%, the kinetic energy term accounts for +9.1%, while the piston work term represents -19.5%. In the case of a propagating detonation in a closed tube, there are no moving boundaries but the flow plays the role of the piston. Right behind the detonation, Eq. 2.55 applies. Immediately following is the expansion fan

in which the fluid decelerates to rest and

$$\rho \frac{De}{Dt} = -P \frac{Dv}{Dt} \ . \tag{2.56}$$

The internal energy of the fluid particles going through the Taylor wave decreases due to the volume expansion of the fluid. This volume expansion acts as an effective piston and drives the propagating detonation wave.

2.4.4 Performance comparison for a straight detonation tube

The results of the previous sections indicate that detonation and CV combustion are processes with thermodynamic similarities. However, it is still unclear whether these processes result in similar unsteady propulsive performance. This problem is investigated numerically using Amrita (Quirk, 1998) for the simple case of unsteady combustion in a straight tube open to a half space. In the CV combustion case, the initial configuration consisted of the tube entirely filled with combustion products in a uniform state corresponding to CV combustion. The initial configuration for the detonation case consisted of the Taylor wave similarity solution (Zel'dovich, 1940a, Taylor, 1950) assuming the detonation has just reached the open end. The open half space is at temperature T_1 and pressure P_1, while the reactants in the tube prior to combustion are at the same temperature but precompressed with a pressure ratio P_R. For a given energy release q_c/RT_1, the state of the combustion products is computed for CV combustion using the perfect gas relationships (Eq. 2.77) and, for detonation, using the one-γ model of detonation (Section 1.1.1).

The impulse generated by the blowdown process is calculated by integrating the pressure at the closed end of the tube (Section 4.3). Figure 2.24 shows the non-dimensional pressure at the closed end and the integrated impulse. In the case of CV combustion, the pressure at the closed end remains constant while the expansion wave generated at the open end propagates back to the closed end, reflects, and decreases the pressure. In the case of detonation, the pressure remains constant while the detonation propagates to the open end (not simulated but accounted for in Fig. 2.24)

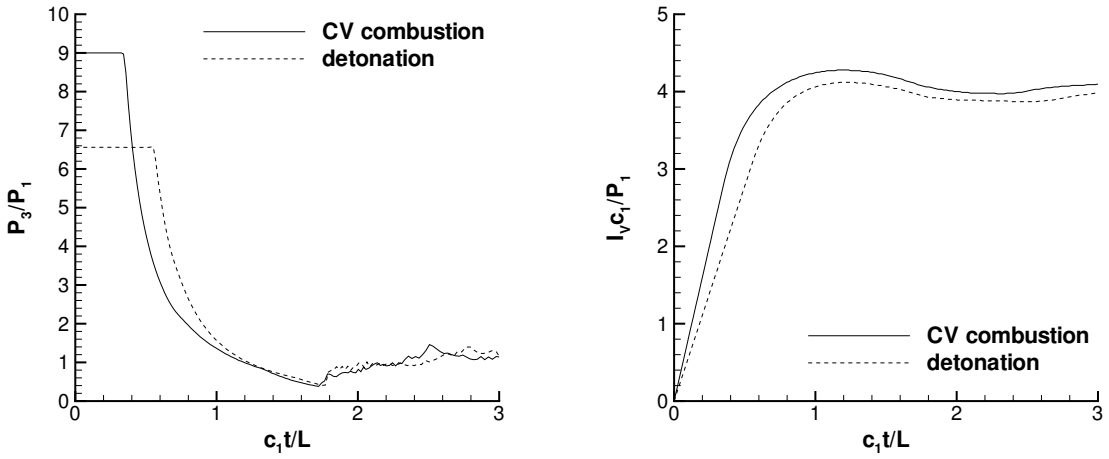

Figure 2.24: Non-dimensionalized pressure at the closed end of the tube and impulse for CV combustion and detonation as a function of time. $q_c/RT_1 = 40$, $P_R = 1$, $\gamma = 1.2$.

and the reflected wave comes back to the closed end. This is followed in both cases by a pressure decrease while the combustion products exhaust from the tube. The flow in the tube becomes overexpanded before reaching mechanical equilibrium. The features of this flow are described in more detail in Section 4.2.4 for the detonation case. The flow overexpansion explains the slight dip in impulse observed in Fig. 2.24 for $c_1 t/L > 2$.

A series of simulations was conducted varying the energy release and the pressure ratio, and the results are presented in Fig. 2.25. The impulse reaches a constant value after a non-dimensional time of about 3 (Fig. 2.25). Thus, all the impulse values presented in Fig. 2.25 were calculated for $c_1 t/L = 3$. In general, CV combustion and detonation generate almost identical impulses at all the conditions tested. The CV combustion impulse is within 4.1% of the detonation impulse when varying the energy release, and within 2.8% when varying the pressure ratio. Although limited to a fixed geometry, these simulations are a good indication that CV combustion and detonation generate very similar propulsive performance. This result can be explained by recognizing that the kinetic energy in the gas behind the detonation is small compared to the thermal energy, as computed in the previous section. The bulk of the impulse is apparently created by the unsteady expansion of the hot products.

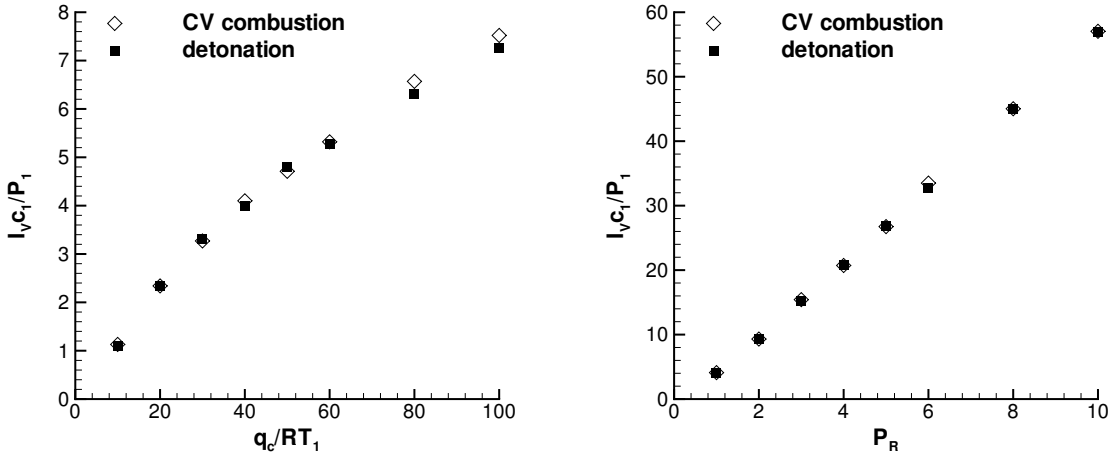

Figure 2.25: Non-dimensionalized impulse for CV combustion and detonation as a function of energy release q_c/RT_1 with $P_R = 1$ (left) and pressure ratio P_R with $q_c/RT_1 = 40$ (right). $\gamma = 1.2$.

Judging from the similarity of the pressure histories at the closed end, the unsteady process is essentially identical for both the CV combustion and detonation processes. Thus, this result suggests that a detonation process can be approximated as infinitely fast for the purposes of propulsion performance computation.

2.5 Blowdown model

Based on the similarities between detonation and constant-volume combustion observed in Section 2.4, a gas dynamics–based model using the CV mode of combustion is useful to consider as a reference case for PDEs. In practice, CV combustion is approached when the blowdown time is much larger than the characteristic wave transit time in the combustion chamber. Our approach is similar to the simple theory for the performance of the aeropulse (or pulsejet) presented in the pioneering book by Tsien (1946). This theory assumes an inlet stagnation pressure ratio of 0.5 and does not model the filling of the combustion chamber, accounting only for the combustion and blowdown events. The results are compared with experimental data for the German V-1 engine (Tsien, 1946). Talley and Coy (2002) followed the same approach to estimate the constant-volume limit of pulsed propulsion, including the chamber filling

process in their analysis. Unlike Talley and Coy (2002) who considered rocket-type engines, we develop our model in the context of air-breathing propulsion systems. We also model the combustion process using realistic thermochemistry for hydrogen and JP10. JP10 is a conventional aviation fuel with a high energy density. It is liquid at ambient conditions, which makes it attractive for volume-limited applications. Unlike other kerosene-based fuels such as JP5, JP8, or Jet A, JP10 is a single-component hydrocarbon (C_10H_{16}), which makes its detonation properties much easier to characterize for PDE applications.

2.5.1 Constant-volume combustion engine

Our ideal constant-volume (CV) combustion engine consists of an inlet and multiple combustion chambers with their own exit nozzle, as shown in Fig. 2.26. The combustion chambers operate out of phase so that the flow upstream decouples from the flow in the chamber and becomes quasi-steady. Two infinitely fast valves are located at the inlet and the outlet of the combustion chambers, and control the introduction of the fuel-air mixture in each combustion chamber and the exhaust of the combustion products. The cycle for a given combustion chamber consists of the following steps, shown in Fig. 2.27. The inlet air is stored within the combustion chamber with the exhaust valve closed. The inlet valve closes while fuel is added, mixing instantaneously with the air. The fuel-air mixture is burned instantaneously at constant volume. Then, the exhaust valve opens and the combustion products exhaust from the combustion chamber, decreasing the chamber pressure. When the chamber pressure equals the initial inlet pressure, the inlet valve opens and the residual combustion products are pushed out of the combustion chamber while the chamber is being filled with inlet air. Such an ideal engine is not practical and we do not attempt to investigate the conditions for cyclic operation. Rather, we are interested in using this conceptual engine to determine bounding estimates for PDE performance.

The cycle consists of two parts, corresponding to CV blowdown during the first part of the cycle and CP blowdown at the end of the cycle when the chamber is being

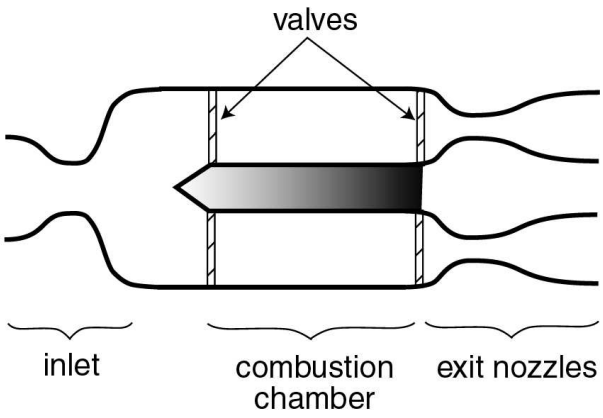

Figure 2.26: Schematic of constant-volume combustion engine.

refilled. The combustion process and the decay of all associated wave processes are instantaneous so that ideal CV combustion is assumed. Heat losses are neglected and the blowdown processes are assumed to be quasi-one-dimensional, quasi-steady, and isentropic. The conditions in the combustion chamber vary with time during the CV blowdown but are assumed to be spatially uniform.

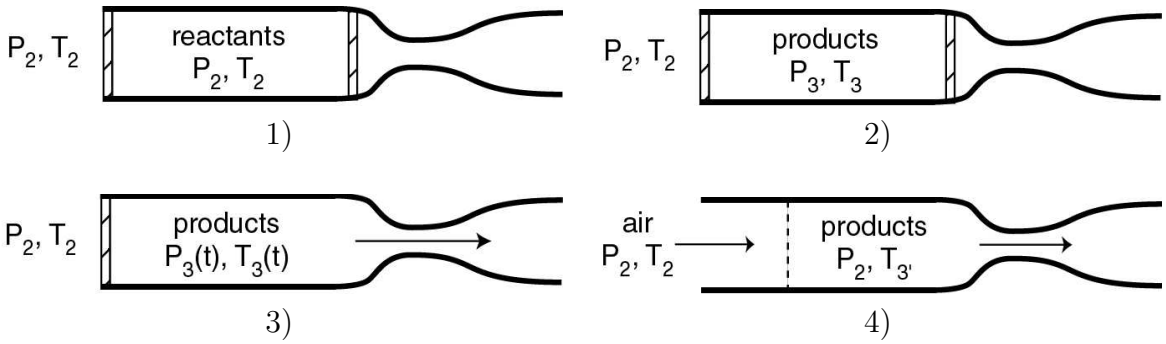

Figure 2.27: CV combustion engine cycle. 1) Combustion chamber contains reactants between closed inlet and outlet valves. 2) Instantaneous CV combustion of reactants. 3) Outlet valve opens and CV blowdown of combustion products begins. 4) When chamber pressure equals inlet pressure, inlet valve opens and air flows in. Residual combustion products are exhausted through CP blowdown. Once the chamber is filled with air, both valves close and fuel is instantaneously injected and mixed with air.

2.5.2 Constant-volume blowdown of a combustion chamber

The impulse generated during the CV blowdown is a function of the conditions inside the combustion chamber. The flow in the chamber can be treated analytically using a control volume approach. We write the mass conservation equation for a control volume surrounding the combustion chamber and the exit nozzle, assuming the flow through the exit nozzle is choked

$$\frac{d\mathcal{M}}{dt} = -\dot{m}^*(t) \ , \tag{2.57}$$

where the mass flow rate at the throat $\dot{m}^*$ is obtained from the stagnation conditions in the chamber.

$$\dot{m}^*(t) = \left(\frac{2}{\gamma+1}\right)^{\frac{\gamma+1}{2(\gamma-1)}} \rho_3(t) c_3(t) A^* \tag{2.58}$$

Writing $\mathcal{M}(t) = \rho_3(t)V$ and using the assumption of isentropic blowdown for a perfect gas, Eq. 2.57 can be rewritten after some algebra as an equation for the speed of sound in the chamber

$$\frac{d(c_3(t)/c_3)}{dt} = -\frac{1}{t_b}(c_3(t)/c_3)^2 \ , \tag{2.59}$$

where t_b is a characteristic timescale of the blowdown process and depends on the initial speed of sound, the ratio of specific heats, and the geometry (throat area and chamber volume).

$$t_b = \frac{2V}{\left(\frac{2}{\gamma+1}\right)^{\frac{\gamma+1}{2(\gamma-1)}} (\gamma-1) A^* c_3} \tag{2.60}$$

t_b is proportional to the transit time of an acoustic wave across a reservoir of volume V and cross-sectional area A^*. Integrating Eq. 2.59, we obtain the following simple expression for the speed of sound in the chamber as a function of time

$$c_3(t) = \frac{c_3}{1 + t/t_b} \ . \tag{2.61}$$

This expression is valid as long as the flow at the throat is choked. The other quantities in the chamber are obtained using the isentropic flow relationships. The CV blowdown

stops when the pressure in the chamber equals the inlet pressure P_2. The flow at the throat is choked during the entire CV blowdown process for

$$\frac{P_2}{P_0} \geq \left(\frac{\gamma+1}{2}\right)^{\frac{\gamma}{\gamma-1}} . \tag{2.62}$$

For an air-breathing engine with no mechanical compression and an ideal inlet, this condition is satisfied only for supersonic flight.

2.5.3 Performance calculation

The thrust of our CV engine is obtained by analyzing a control volume surrounding the entire engine, such as that of Fig. 1.9. We write the cycle-averaged momentum equation (Eq. 1.92). We neglect the interaction between the combustion chamber exhaust flows. Assuming our CV engine contains k identical combustion chambers, the thrust can be expressed as

$$\overline{F} = k\left[\overline{\dot{m}_e(t)u_e(t)} - \dot{m}_{CC}u_0 + A_e(\overline{P_e}(t) - P_0)\right] , \tag{2.63}$$

where the exit quantities are defined for a single nozzle and $\dot{m}_{CC} = \dot{m}_0/k$ is the average mass flow rate through a single combustion chamber. For these idealized conditions, the specific impulse is independent of the number of combustion chambers.

$$I_{SPF} = \frac{\overline{\dot{m}_e(t)u_e(t)} + A_e(\overline{P_e}(t) - P_0)}{\dot{m}_{CC}fg} - \frac{u_0}{fg} \tag{2.64}$$

Fixed expansion ratio exit nozzles can be optimized only for one value of the pressure ratio between the chamber and the atmosphere. However, the chamber pressure is continuously varying during the CV blowdown. Performance losses arise when the flow is not fully expanded to ambient pressure at the nozzle exit. We consider an ideal variable nozzle that expands the flow at its exit plane to ambient pressure at all times of the blowdown processes. This ideal case corresponds to the maximum performance that can be obtained from the blowdown process. Talley and

Coy (2002) compared fixed and variable nozzles for a range of pressure ratios and found that the impulse penalty due to using a fixed expansion ratio nozzle was less than 3% in the cases they considered. Assuming pressure-matched flow at the nozzle exit plane, the expression for the specific impulse is simplified to

$$I_{SPF} = \frac{\overline{\dot{m}_e(t)u_e(t)}}{\dot{m}_{CC}fg} - \frac{u_0}{fg} \ . \tag{2.65}$$

The momentum term at the nozzle exit is the sum of the momentum contributions during the CV blowdown and the CP blowdown portions of the cycle.

$$\overline{\dot{m}_e(t)u_e(t)} = \frac{1}{\tau}\int_0^{\tau} \dot{m}_e(t)u_e(t)dt \tag{2.66}$$

$$= \frac{1}{\tau}\left[\int_0^{t_{CV}} \dot{m}_e(t)u_e(t)dt + \int_{t_{CV}}^{\tau} \dot{m}_e(t)u_e(t)dt\right] \tag{2.67}$$

$$= \frac{1}{\tau}\left[I_{CV} + I_{CP}\right] \tag{2.68}$$

We first analyze the CV blowdown (from time 0 to t_{CV}) using the results of Section 2.5.2. Since we assume that the flow is quasi-steady, we have $\dot{m}_e(t) = \dot{m}^*(t)$, and the velocity at the nozzle exit plane is obtained from the conservation of stagnation enthalpy through the nozzle and the isentropic flow relationships

$$u_e(t) = \sqrt{2C_pT_3\left[\frac{T_3(t)}{T_3} - \left(\frac{P_0}{P_3}\right)^{\frac{\gamma-1}{\gamma}}\right]} \ . \tag{2.69}$$

After some algebra, the impulse generated by the CV blowdown is given by the following integral

$$I_{CV} = \sqrt{\frac{2}{\gamma-1}}\left(\frac{2}{\gamma+1}\right)^{\frac{\gamma+1}{2(\gamma-1)}} A^*\rho_3 c_3^2 \int_0^{t_{CV}} (1+t/t_b)^{-\frac{\gamma+1}{\gamma-1}} \sqrt{(1+t/t_b)^{-2} - \left(\frac{P_0}{P_3}\right)^{\frac{\gamma-1}{\gamma}}}\, dt \ . \tag{2.70}$$

Substituting Eq. 2.60 into Eq. 2.70 and using the change of variables $\xi = 1 + t/t_b$ and

the notation $\chi = (P_0/P_3)^{(\gamma-1)/\gamma}$, the CV blowdown impulse can be expressed as

$$I_{CV} = \left(\frac{2}{\gamma - 1}\right)^{3/2} \rho_3 V c_3 \Gamma_{CV} \ , \tag{2.71}$$

where Γ_{CV} is the non-dimensional integral defined by

$$\Gamma_{CV} = \int_1^{\xi_{CV}} \xi^{-\frac{\gamma+1}{\gamma-1}} \sqrt{\xi^{-2} - \chi} \ d\xi \ . \tag{2.72}$$

Equation 2.72 has to be integrated numerically. The end of the CV blowdown corresponds to the time when the chamber pressure equals the inlet air pressure P_2.

$$\xi_{CV} = \left(\frac{P_3}{P_2}\right)^{\frac{\gamma-1}{2\gamma}} \tag{2.73}$$

The following CP blowdown occurs at constant stagnation conditions as the remaining burned gases are pushed out of the combustion chamber. The exit velocity is, thus, constant and given by

$$u_e = \sqrt{\frac{2c_{3'}^2}{\gamma - 1}\left[1 - \left(\frac{P_0}{P_2}\right)^{\frac{\gamma-1}{\gamma}}\right]} \ , \tag{2.74}$$

where state 3' denotes the state in the products at the end of the CV blowdown. The impulse obtained during the CP blowdown is generated by the complete expulsion of the remaining mass of products $\rho_{3'} V$.

$$I_{CP} = \rho_{3'} c_{3'} V \sqrt{\frac{2}{\gamma - 1}\left[1 - \left(\frac{P_0}{P_2}\right)^{\frac{\gamma-1}{\gamma}}\right]} \tag{2.75}$$

The cycle-averaged mass conservation equation for the combustion chamber yields $\dot{m}_{CC} = \rho_2 V/\tau$ since there is no average mass storage during steady operation. Substituting Eqs. 2.70 and 2.75 in Eq. 2.65 and simplifying, the fuel-based specific impulse

is

$$I_{SPF} = \frac{c_3}{fg}\left[\left(\frac{2}{\gamma-1}\right)^{3/2}\Gamma_{CV} + \left(\frac{P_2}{P_3}\right)^{\frac{\gamma+1}{2\gamma}}\sqrt{\frac{2}{\gamma-1}\left[1-\left(\frac{P_0}{P_2}\right)^{\frac{\gamma-1}{\gamma}}\right]}\right] - \frac{u_0}{fg}\,. \quad (2.76)$$

2.5.4 Hydrogen and JP10 fueled CV engines

The specific impulse of ideal CV engines operating with stoichiometric hydrogen- and JP10-air is shown as a function of the flight Mach number in Fig. 2.28. Equilibrium computations using STANJAN (Reynolds, 1986) were carried out to calculate the CV combustion process and, in particular, the speed of sound c_3 and the pressure P_3. The expansion process was modeled using a constant value of γ obtained from the equilibrium calculations. Calculations showed that this value of γ is around 1.17 for the cases considered and is in good agreement (within 1.1% error) with the effective γ obtained following the isentrope during the expansion process. The specific impulse is shown only for supersonic flight, where the model assumptions are valid.

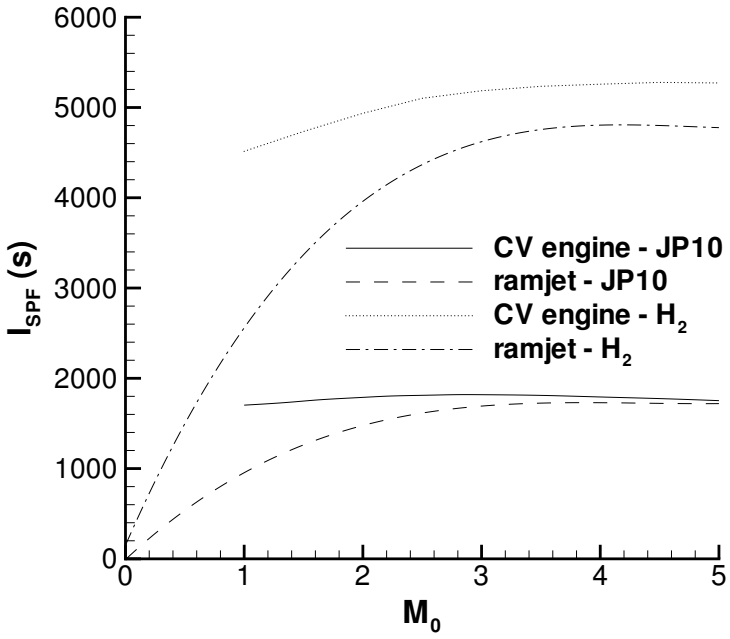

Figure 2.28: Fuel-based specific impulse of stoichiometric hydrogen and JP10 fueled CV engines compared with the ideal ramjet at 10,000 m altitude.

The specific impulse of the ideal CV engines has a weak dependence on the flight Mach number and is around 5000 s for hydrogen and around 1800 s for JP10. It increases slowly with increasing M_0 for hydrogen. Figure 2.28 also displays the specific impulse for the ideal ramjet. The ramjet performance is calculated by following the ideal Brayton cycle. Equilibrium computations are carried out for the combustion and expansion processes, assuming that the flow is in equilibrium at every point in the nozzle. The CV engine specific impulse is significantly higher than that of the ramjet, especially at low flight Mach numbers. The pressure increase associated with CV combustion benefits performance since the combustion products are expanded from a higher stagnation pressure. However, as the flight Mach number increases, the CV engine specific impulse approaches that of the ramjet, which is particularly obvious for JP10. This is attributed to the larger contribution of the CP part of the blowdown process. For CV combustion of a perfect gas, the combustion pressure ratio can be obtained from the energy equation

$$\frac{P_3}{P_2} = \frac{T_3}{T_2} = 1 + \frac{q_c}{C_v T_2} \, . \tag{2.77}$$

It is clear from Eq. 2.77 that the combustion pressure ratio decreases with increasing flight Mach number due to the increased freestream stagnation temperature. This means that the contribution of the CV blowdown decreases compared to that of the CP blowdown, which occurs at P_2. This result is also clear from Eq. 2.76. In the limit of very high flight Mach numbers, it is expected that the CP blowdown will dominate and that the CV blowdown contribution will become negligible. The performance of our CV engine will approach that of a CP combustion engine, which is the ramjet.

These conclusions agree with Talley and Coy (2002), who concluded that a CV engine has a higher specific impulse than a CP device operating at the same fill pressure. Additionally, they observed that the magnitude of the difference between CV and CP devices increased with increasing P_0/P_3. In our case, decreasing the flight Mach number increases P_0/P_3 and corresponds to a larger impulse difference. Finally, Talley and Coy (2002) also concluded that, in the limit of $P_0/P_3 = 0$, the

specific impulse of the CP device can become either slightly higher or slightly lower than the impulse of the CV device, depending on the magnitude of P_3/P_2. The limit $P_0/P_3 = 0$ corresponds, in our case, to very large flight Mach numbers, and the results of Fig. 2.28 agree with these conclusions.

It is also possible to estimate the integral of Eq. 2.72 analytically by approximating the exponent $(\gamma + 1)/(\gamma - 1)$ with an integer n. This approximation yields $\gamma = (m+1)/(m-1)$. A value of $m = 13$ is found to result in $\gamma = 1.1667$, which is within 1.1% of the values of the specific heat ratio obtained from fitting the isentrope with a constant γ for the cases considered ($\gamma - 1$, which controls the gas dynamics, is within 7.5% error). Using the value $m = 13$, Γ_{CV} can be expressed analytically.

$$\Gamma_{CV} = \int_1^{\xi_{CV}} \xi^{-n} \sqrt{\xi^{-2} - \chi}\, d\xi \tag{2.78}$$

$$= \left[\sqrt{1/\xi^2 - \chi} \left(-\frac{1}{13\xi^{12}} + \frac{\chi}{143\xi^{10}} + \frac{10\chi^2}{1287\xi^8} + \frac{80\chi^3}{9009\xi^6} + \frac{32\chi^4}{3003\xi^4} + \frac{128\chi^5}{9009\xi^2} + \frac{256\chi^6}{9009} \right) \right]_1^{\xi_{CV}} \tag{2.79}$$

The values of the specific impulse obtained using this expression are within 0.6% of the values resulting from the numerical integration of Γ_{CV} for the cases considered.

2.6 Conclusions

We have used thermodynamic considerations to investigate the merits of detonative combustion relative to other combustion modes for applications in steady- and unsteady-flow propulsion systems. For steady-flow systems, we have shown that the irreversible component of the entropy rise controls the thermal efficiency. Although detonations generate the minimum amount of total entropy rise along the conventional Hugoniot, they also generate the maximum amount of irreversible entropy rise. For air-breathing propulsion applications, the thermodynamic cycle analysis has to be conducted based on a fixed initial stagnation state, and the conventional Hugoniot analysis does not apply. We analyzed steady combustion waves for a fixed initial stagnation state and derived a new version of the Hugoniot, called the stagnation

Hugoniot. The total entropy rise for the detonation solutions along the stagnation Hugoniot is much higher than the deflagration solutions and, therefore, ideal engines based on steady detonation have much poorer performance than those based on deflagration. These findings reconcile thermodynamic cycle analysis with flow path performance analysis of detonation-based ramjets (Dunlap et al., 1958, Sargent and Gross, 1960, Wintenberger and Shepherd, 2003b). The highest thermal efficiency occurs for the combustion process with the lowest entropy increment, corresponding to the ideal Brayton cycle.

For unsteady-flow systems, we presented a thermostatic approach of a closed system, the Fickett-Jacobs cycle, to compute an upper bound to the amount of mechanical work that can be produced by a cycle using an unsteady detonation process. This cycle is used to calculate a thermal efficiency based on this ideal mechanical work. Values of the thermal efficiency for a variety of mixtures are calculated for the FJ cycle with and without initial precompression. Fuel-air mixtures are found to have a higher thermal efficiency than fuel-oxygen mixtures near stoichiometric due to dissociation phenomena and to the higher value of the effective ratio of specific heats in their detonation products.

Comparison with the Humphrey and Brayton cycles shows that the thermal efficiency of the FJ cycle is only slightly higher than that of the Humphrey cycle, and much higher than that of the Brayton cycle when compared on the basis of pressure at the start of the combustion process. The opposite conclusion is drawn when the comparison is made on the basis of the pressure after the combustion process. Although these efficiencies cannot be precisely translated into propulsive efficiency, these results are useful in comparing unsteady detonation with other combustion modes.

The similar values obtained for the entropy rise and the thermal efficiency of the Humphrey and FJ cycles suggest that CV combustion is a good surrogate for detonation. The kinetic energy in a propagating detonation was shown to represent only a small fraction of the total chemical energy release, which also indicates similarities between CV combustion and detonation. Numerical simulations of unsteady combustion in a straight tube open to a half space showed that these two processes result in

essentially the same propulsive performance. Based on these results, a gas dynamics–based model using CV combustion was developed to calculate the ideal performance of unsteady propulsion systems. This model showed that the ideal CV engine yields a higher specific impulse than the ideal ramjet, in particular, below Mach 3.

Chapter 3

Steady Detonation Engines

3.1 Introduction

The idea of using steady detonation waves for propulsion applications is not new but started in the 1950s when Dunlap et al. (1958) studied the feasibility of a reaction engine employing a continuous detonation process in the combustion chamber. The configuration studied included a converging-diverging nozzle designed to accelerate the flow to a velocity higher than the CJ detonation velocity, a wedge where a normal or oblique detonation could be stabilized, and a diverging nozzle. Their study of a detonation ramjet was carried out without accounting for total pressure losses at supersonic speeds but took into account the supersonic mixing of fuel and air. One important condition in their work was that the static temperature of the unreacted fuel-air mixture be kept below an effective ignition temperature, corresponding to spontaneous ignition of the flowing gas mixture. They also assumed that the detonation waves formed in their engine were intrinsically stable, which may not be the case (Shepherd, 1994). Their results showed that no thrust was produced below a Mach number of 4 for hydrogen-air because the total enthalpy of the incoming flow was too low to stabilize a CJ detonation wave.

Sargent and Gross (1960) carried out a propulsive cycle analysis of a hypersonic detonation wave ramjet. They computed the performance of the normal detonation engine for flight Mach numbers between 2.5 and 10. Their analysis assumes that the

This chapter is based on work presented in Wintenberger and Shepherd (2003b).

flow is slowed down or accelerated to the Chapman-Jouguet conditions just upstream of the detonation. They presented estimates of the air specific impulse, the specific fuel consumption, and the thermal efficiency for a fixed Mach number ahead of the detonation wave varying the flight Mach number, and for a fixed flight Mach number varying the Mach number ahead of the detonation. They concluded that the ramjet always has better performance, although the differences are minor at some flight regimes.

Dabora (1994) presented the results of a comparison of a hypersonic detonation-driven ramjet with a conventional ramjet. The detonation-driven ramjet considered consisted of an inlet, a wedge onto which a normal or oblique detonation wave can be stabilized, and an expanding nozzle. Dabora derived the non-dimensional thrust of this engine assuming the only non-reversible process other than combustion was the expansion in the exit nozzle downstream of the detonation wave. In comparison, all processes were assumed reversible in the ramjet case. His calculations were performed assuming a constant non-dimensional heat release. He showed that no thrust was obtained for the detonation-driven ramjet below a freestream Mach number of 5. The normal wave engine produced thrust only between Mach numbers of 5 and 8.9, whereas the oblique wave engine generated thrust for any Mach number higher than 5. The comparison with the ramjet showed that the performance of both detonation engines was much lower (by at least a factor of 2) than that of the ramjet.

Rubins and Bauer (1994) reviewed some of the early research on stabilized detonation waves and carried out some experiments on stabilized normal and oblique shock-induced combustion. They studied experimentally combustion behind a normal shock generated by oblique shocks induced by wedges. They described the phenomenon observed as shock-induced combustion rather than detonation because the normal shock wave was not directly affected by the combustion. They also investigated the generation of stabilized oblique shock-induced combustion. This type of combustion requires a higher upstream stagnation temperature but creates lower structural constraints than normal shock-induced combustion. They applied these ideas to a hydrogen-fueled high-altitude scramjet concept and proposed a flight en-

velope taking into account the limitations of hydrogen-air combustion kinetics for a two-shock inlet diffuser. They calculated specific impulses based on fuel mass of 1000–1200 s for a hydrogen-air scramjet flying at Mach numbers between 6 and 16.

A substantial amount of work has also focused on oblique detonation waves (Pratt et al., 1991) and oblique detonation wave engines (Cambier et al., 1988, Menees et al., 1992, Ashford and Emmanuel, 1996, Dudebout et al., 1998, Sislian et al., 2001). The oblique detonation wave engine concept was explored for hypersonic applications both numerically and analytically. Oblique detonation waves require hypersonic freestream Mach numbers (typically higher than 8) for stabilization, which places a lower bound on the operating range of an oblique detonation wave engine.

In all of these exploratory studies, no limitation was placed on the combustor outlet temperature, which is definitely an issue for the combustor structure at such high freestream total enthalpies (Hill and Peterson, 1992, Chap. 5). Such limitations create a more realistic upper bound on the performance of any propulsion system, including ramjets.

The idea of using steady detonations as the main combustion mode in an engine has been attractive because of the rapid energy release occurring in detonations. Since detonations are characterized by higher temperatures and pressures than deflagrations, steady detonation engines may offer performance gains over usual air-breathing engines. They also offer other advantages in terms of simplicity (for the detonation ramjet), higher pressure rise in the combustor which facilitates the exhaust of burned gases, and shortened combustion chamber due to a smaller reaction zone. On the other hand, it has also been recognized early (Foa, 1960) that detonations produced, in steady-flow engines, a considerably higher entropy rise than is produced by deflagration, due to the requirement that the reaction front be stationary. Foa (1960) concluded, based on general considerations, that detonations offered better promise for use as a non-steady than as a steady combustion mode.

In this chapter, we study the feasibility of steady propulsion systems using normal detonative combustion. Normal detonation waves require lower freestream Mach numbers than oblique detonation waves for stabilization, and the operating range of a

normal detonation-based propulsion system might be broader than that of an oblique detonation wave engine. However, there are many issues associated with stabilized normal detonation waves. The most obvious one is that the total enthalpy just upstream of the combustor must be high enough so that the flow can be accelerated to the CJ detonation velocity. We first consider these issues and propose some criteria for the generation of stabilized normal detonations. We show that detonation waves can be stabilized only for a limited range of initial conditions. Limitations associated with fuel or oxidizer condensation, mixture pre-ignition, detonation stability, and fuel sensitivity to detonation are presented. Then we apply our solution to an analytical treatment of a detonation ramjet and a detonation turbojet, where detonative combustion replaces the usual deflagrative subsonic combustion. Unlike previous studies, we place a limitation on the maximum temperature in the combustor due to material considerations. Performance figures of merit of steady detonation engines are derived using an ideal model and the results are compared with the analogs that use the standard deflagrative combustion mode.

3.2 Stabilized normal detonations

A propulsive device using a steady detonation wave is constrained by the consideration that the wave be stabilized within the combustor. Propagating detonation waves in hydrocarbon fuel-air mixtures typically move at a Mach number on the order of 5, which requires that the flow Mach number upstream of a combustor with a stabilized, steady detonation be at least this value. Thus, it is clear why experimentally stabilizing a detonation wave may be difficult.

The first reported works on stabilized detonation waves were those of Nicholls et al. (1959), Nicholls and Dabora (1962) and Gross and Chinitz (1960). Nicholls et al. (1959) and Nicholls and Dabora (1962) used heated air going through a highly under-expanded nozzle to generate an accelerating jet. They injected cold hydrogen at the nozzle throat. The jet was characterized by a complex system of waves forming a Mach disk. The conditions behind the Mach disk were such that combustion

occurred. Nicholls proposed some criteria for the establishment of standing detonation waves based on hydrodynamic considerations, the second explosion limit, and ignition delay time considerations. The key result is that the freestream total temperature has to be high enough so that CJ detonations can be established. Gross and Chinitz (1960) studied stabilized detonation waves using a normal shock generated by the intersection of two oblique shocks created by wedges in a Mach reflection configuration. They observed steady detonations behind this shock using hydrogen-air mixtures. They also investigated oblique detonation waves stabilized behind a single wedge. All their experiments were characterized by a hysteresis effect: once the detonation was established, the upstream temperature could be greatly decreased without quenching of the detonation. They considered this hysteresis effect as promising for engine applications operating over a wide range of conditions. It was not observed by Nicholls and Dabora (1962). However, this hysteresis effect was later reported to be due to the use of vitiated air which may have contained residual radicals, inducing combustion at low temperatures (Dabora and Broda, 1993). Although the phenomena obtained in the experiments of Nicholls and Dabora (1962) and Gross and Chinitz (1960) were originally described as standing detonations, the influence of the combustion on the shock wave was very limited and these phenomena are better described as shock-induced combustion (Rubins and Bauer, 1994). Propagating detonations are characterized by a strong coupling between the shock and the reaction zone and by a cellular instability, which we would expect to also observe in the stabilized case as long as the overdrive is sufficiently low. However, neither strong coupling nor transverse instabilities were observed in these experiments.

The primary difficulty in creating standing detonation waves is to obtain a mixture with a total enthalpy that is high enough to stabilize the detonation without igniting the mixture upstream of the shock. For lower total enthalpies, the low post-shock temperature will result in a wider induction zone and a decoupling of the shock and the reaction zone. Shepherd (1994) estimated the necessary total enthalpy by considering the stagnation states upstream of a CJ detonation. A minimum total enthalpy of 2 MJ/kg is required for hydrogen-air mixtures.

3.2.1 Detonation stabilization condition

We propose to study analytically the problem of generating a stabilized normal detonation wave using a flow isentropically expanded from a reservoir at a total temperature T_{t0}. This situation is analog to the experimental setup of Nicholls et al. (1959), except that we assume the expansion takes place entirely through the nozzle, whereas Nicholls et al. expanded the flow through a nozzle and an open jet. A schematic of the problem considered is shown in Fig. 3.1. Air is accelerated to a supersonic velocity from a reservoir of total temperature T_{t0} through a converging-diverging nozzle. Fuel is injected at some location downstream of the nozzle throat. The mixing of fuel and air is not considered in our approach, and we consider that fuel and air mix homogeneously in an instantaneous fashion without total pressure loss. In order to stabilize a normal detonation, the flow has to be accelerated to a velocity greater than or equal to the CJ velocity through the converging-diverging nozzle. For flow velocities higher than U_{CJ}, overdriven detonations are possible but, as discussed later, the requirements for a minimum total pressure loss across the detonation in an engine make them undesirable. Hence, we will consider only Chapman-Jouguet detonation waves.

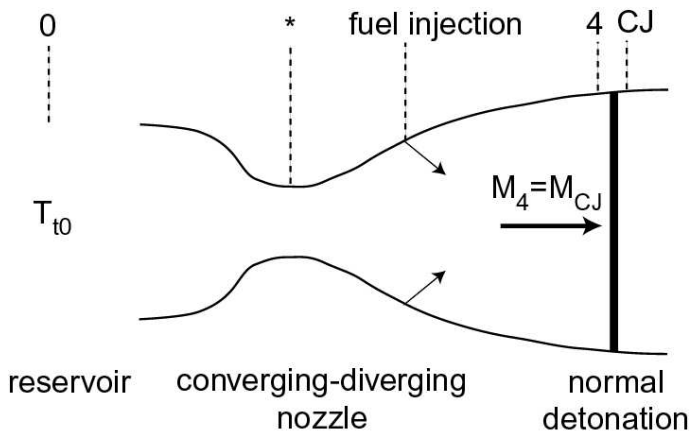

Figure 3.1: Standing detonation generated by the isentropic expansion of an airflow from a reservoir of total temperature T_{t0}, with fuel injection downstream of the nozzle throat.

Assuming steady, adiabatic and inviscid flow of an ideal gas, the detonation sta-

bilization condition can be written as $M_4 = M_{CJ}$, where station 4 corresponds to the location just upstream of the detonation wave. The detonations are modeled as hydrodynamic discontinuities using the one-γ model described in Eqs. 1.15–1.19. This simple model does not include any considerations of the detonation wave structure. The influence of chemical kinetics and the reaction zone structure have to be considered in order to get a more realistic idea of the flow. However, the one-γ model is a useful approximation for studying the thermodynamic aspects of performance. The Mach number M_4 depends on the static temperature T_4 and the total temperature of the flow upstream of the detonation $T_{t4} = T_{t0}$

$$M_4 = \sqrt{\frac{2}{\gamma - 1}\left(\frac{T_{t4}}{T_4} - 1\right)} \,. \tag{3.1}$$

The equation $M_4 = M_{CJ}$ can be solved analytically for the temperature upstream of the detonation wave T_4. Two solutions are obtained, only one of which is acceptable since M_{CJ} has to be greater than 1. The solution of this equation is

$$T_4 = \frac{2(\gamma - 1)}{\gamma + 1} T_{t4} \left(\frac{1}{\gamma - 1} - \mathcal{Q} - \sqrt{\mathcal{Q}(1 + \mathcal{Q})}\right) \,, \tag{3.2}$$

where $\mathcal{Q}$ is a non-dimensional heat release parameter defined by $\mathcal{Q} = f q_f / (C_p T_{t4})$. Once T_4 is calculated, the properties downstream of the detonation wave can be computed using the one-γ model.

3.2.2 General limitations

Detonations cannot be stabilized for arbitrary values of the governing parameters. In particular, there are restrictions on the allowable values of T_4. Since the flow is accelerated through the nozzle up to a Mach number of about 5, the static temperature drop can become significant and condensation of some components of the mixture can occur in the nozzle. Hence, T_4 has to stay above a limiting temperature T_c corresponding to fuel or oxidizer condensation. Condensation is actually determined by the value of the gas-phase fuel or oxidizer partial pressure relative to its corresponding

liquid-phase vapor pressure, which depends only on temperature. In order to simplify the problem, we assume the fuel or oxidizer condenses below a temperature T_c constant throughout the range of pressures encountered in the nozzle. This simplifying assumption allows the derivation of a zero-order criterion for the establishment of stabilized normal detonation waves: $T_4 > T_c$. This condition imposes a restriction on the total enthalpy of the reservoir. It is directly relevant to liquid fuels, such as Jet A or JP10, which condense below 450 K. However, if hydrogen is used as a fuel, then the oxygen of the air will condense before the fuel at 90 K. The restriction on T_{t0} is, therefore, much less stringent for hydrogen than for liquid hydrocarbon fuels.

Another issue is the location of fuel injection. The flow at the nozzle throat is hot and the fuel-air mixture must be prevented from pre-igniting before the conditions for the stabilized detonation are encountered (Rubins and Bauer, 1994). It is better to locate the fuel injection system further downstream from the throat, where the flow is cooler. However, in practice, there is a compromise with the length necessary for supersonic mixing of the fuel and air. The pre-ignition of the fuel-air mixture can occur if the mixture is at a sufficiently high temperature and its residence time is large enough so that combustion can start. The location of fuel injection is design-dependent and varies with the total enthalpy of the reservoir. However, we can gain some insight into the influence of the upstream conditions on this problem by considering the simple criterion that T_4 be smaller than the auto-ignition temperature of the fuel-air mixture T_{ign}. This is a minimum requirement since the flow upstream of station 4 is always hotter. The residence time is supposed to be long enough so that the only criterion for ignition is the flow static temperature. This criterion allows the determination of an upper boundary on the allowable domain for the upstream conditions, above which no detonation will be possible because of auto-ignition of the fuel-air mixture in the nozzle. Another simplifying assumption is that T_{ign} be independent of pressure in the pressure range considered.

The temperature upstream of the detonation wave T_4 has to be above the condensation temperature T_c and below the fuel-air mixture auto-ignition temperature T_{ign}: $T_c < T_4 < T_{ign}$. This condition can be solved using Eq. 3.2, yielding a criterion

for the upstream total temperature

$$f(T_c) < T_{t0} < f(T_{ign}) \ , \tag{3.3}$$

where $f(T)$ is defined by

$$f(T) = \frac{\gamma+1}{2}T + \frac{\gamma^2-1}{2}\frac{fq_f}{C_p}\left(1+\sqrt{1+\frac{2}{\gamma+1}\frac{C_pT}{fq_f}}\right) \ . \tag{3.4}$$

We applied this criterion to hydrogen-air mixtures, for which $T_c = 90$ K. The auto-ignition temperature T_{ign} for hydrogen-air (Kuchta, 1985) is on the order of 800 K at 1 atmosphere. It is then possible to determine the values of the reservoir total temperature for which a stabilized detonation is obtained as a function of the fuel-air mass ratio (or, equivalently, the total heat release per unit time). Figure 3.2 shows the allowable domain. Below the lower curve, T_{t0} is too low and condensation of the oxygen occurs inside the nozzle; above the upper curve, T_{t0} is too large and the fuel-air mixture will start combusting ahead of the detonation. Comparisons can be made with the open-jet experiments of Nicholls et al. (1959) performed with hydrogen-air. In one case, they reported shock-induced combustion corresponding to a total temperature of the flow of 1194 K, which is within our predicted range for stabilized detonations of 814 K $< T_{t0} <$ 1782 K. In another experiment, burning at the nozzle exit upstream of the detonation was observed, corresponding to a total temperature of the flow of 1172 K. Our criterion predicts that for $T_{t0} >$ 1164 K, pre-ignition of the mixture should occur, which was observed in the experiments of Nicholls et al. (1959).

The restrictions on the allowable domain for liquid hydrocarbon fuels are more severe, since fuel condensation occurs at much higher temperatures, and the auto-ignition temperature is lower than that of hydrogen. Therefore, a much smaller region exists where stabilized detonations can be established using liquid hydrocarbon fuels. This point is illustrated in Table 3.1, which gives boiling points and auto-ignition temperatures for a range of fuels. However, detonations can be obtained

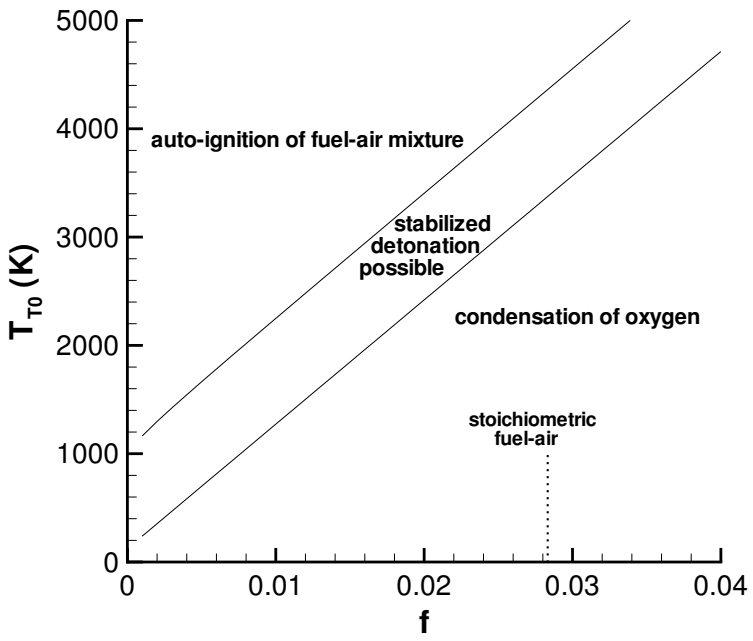

Figure 3.2: Allowable domain for the generation of a stabilized detonation in hydrogen-air as a function of the reservoir total temperature T_{t0} and the fuel-air mass ratio f. $q_f = 120.9$ MJ/kg for hydrogen.

with liquid hydrocarbon fuels at temperatures below their boiling point as long as the vapor pressure of the fuel at the temperature considered is high enough for the given stoichiometry. If the vapor pressure is too low, then too little fuel will be present in the vapor form and detonation will occur in a two-phase mixture. For example, for a stoichiometric mixture of JP10 and air at atmospheric pressure, the temperature has to be above 330 K for complete vaporization of the injected fuel (Austin and Shepherd, 2003).

The presence of liquid fuel in the mixture makes it much harder to detonate compared to a purely vapor phase mixture. In general, low vapor pressure liquid fuel aerosols are characterized by higher ignition energies and larger reaction zones, making it harder to establish self-sustained detonations. Papavassiliou et al. (1993) measured the cell width in heterogeneous phase decane-air detonations and found it to be twice that for decane vapor-air detonations. They concluded that the physical processes for droplet breakup, heat transfer, evaporation, and mixing require a

length scale of the same order of magnitude as that needed for the chemical kinetic processes. They also pointed out that the initiation energy, which scales with the cube of the cell width, is increased by an order of magnitude when detonating a liquid spray (Papavassiliou et al., 1993). Alekseev et al. (1993) showed that it was possible to detonate kerosene in aerosol form. However, the unconfined cloud has to be of significant size, and the cell width for kerosene spray-air was estimated to be on the order of 0.5 m. Hence, condensation (even partial) of the fuel in the combustor can be very penalizing for the establishment of a stabilized detonation wave.

fuel	boiling point (K)	Auto-ignition temperature (K)
hydrogen	20*	793†
ethylene	169*	763†‡, 723*
propane	231*	466‡, 450*†
hexane	342*	496‡, 498*†
decane	447*	481‡, 483*†
Jet A	440–539ϒ	511ϒ
JP10	455ϒ	518ϒ

Table 3.1: Boiling point and auto-ignition temperature of various fuels. *Lide (2001), †Kuchta (1985), ‡Zabetakis (1965), ϒCRC (1983)

3.2.3 Steady detonation stability

In practice, the situation described previously, with a detonation wave stabilized in a nozzle, might be unstable to flow perturbations and the wave might tend to move upstream or downstream. The stability of the detonation wave location is of critical importance in an engine configuration. We consider a CJ detonation stabilized at a location x_0 in a supersonic nozzle. The flow just upstream of the wave moves with a velocity $U_{CJ}(x_0)$ in a fixed reference frame. The wave, when located at x_0, is idle in the fixed reference frame. We study the effect of a flow perturbation that makes the detonation wave move to a position $x_0 + dx$. The perturbed detonation wave is going to move in the fixed reference frame with a velocity $u(x_0 + dx) - U_{CJ}(x_0 + dx)$, where $U_{CJ}(x_0 + dx)$ corresponds to the CJ velocity associated with the initial conditions $P(x_0 + dx)$ and $T(x_0 + dx)$. The sign of the quantity $u(x_0 + dx) - U_{CJ}(x_0 + dx)$ is

going to determine whether the wave is stable or unstable. If $dx > 0$ and $u(x_0 + dx) - U_{CJ}(x_0 + dx) > 0$, then the wave is going to keep moving downstream and is unstable. If $u(x_0 + dx) - U_{CJ}(x_0 + dx) < 0$, then the wave will move back upstream towards its initial position and is stable. So the stability condition for the stabilized detonation wave can be expressed as

$$\frac{d(u - U_{CJ})}{dx} < 0 \, . \tag{3.5}$$

Considering a general area profile for the nozzle $A(x)$, the equations of quasi one-dimensional flow are used to compute the variation of flow properties with position, including the velocity field. The one-γ model is used in combination with the temperature profile in the nozzle to calculate the derivative of the CJ velocity with position.

$$\frac{d(u - U_{CJ})}{dx} = \frac{U_{CJ}}{M_{CJ}^2 - 1} \left[1 + \frac{\gamma - 1}{2} M_{CJ} (\mathcal{H} + 1)^{-1/2} \right] \frac{1}{A(x_0)} \frac{dA}{dx} \tag{3.6}$$

Equation 3.6 shows that a stabilized detonation wave is always unstable in a diverging supersonic nozzle ($dA/dx > 0$) and always stable with respect to flow perturbations in a converging supersonic nozzle ($dA/dx < 0$). The variation of the CJ velocity is only second-order compared to the variation of the flow velocity in the nozzle. This effect was confirmed by computations using realistic thermochemistry (Reynolds, 1986) at various stagnation conditions.

This result is the opposite of that for shock waves, which are only stable in diverging supersonic nozzles (Hill and Peterson, 1992, p. 230). Unlike shock waves, detonation waves have a characteristic velocity determined by the coupling between the upstream flow properties and the heat release. In our analysis, we modeled detonation waves as hydrodynamic discontinuities. However, the intrinsic behavior of shock waves in sections with area change might influence the stability result for detonation waves if the ZND structure of a detonation, consisting of a shock wave coupled to an energy release zone (Section 1.1.2), is considered. A more detailed analysis should take into account the acoustic and entropy waves generated due to shock perturbation, and their respective interactions with the reaction zone. The cel-

lular structure of the wave, its curvature, and the interaction of the transverse waves with the area change also play a role. This problem has many aspects to it that our simplistic analysis does not capture, and we will not consider them any further for the purposes of the present study.

Zhang et al. (1995) studied the stability of a detonation wave passing through opposed supersonic flow in a duct of varying cross section and with friction. They developed a one-dimensional model using a single-step Arrhenius reaction scheme. In their study, detonation stability was expressed in terms of an oscillatory behavior that could potentially lead to failure with the detonation wave being expelled out of the duct. They concluded that the detonation wave was being amplified in a diverging supersonic duct (becoming overdriven) and its stability increased, while it was attenuated in a converging supersonic duct. Similarly, friction was shown to amplify the wave. However, above a certain limit of the friction factor, a stabilized wave configuration could not be reached with a given duct geometry and initial conditions. Adding roughness behind the shock front was proposed as a novel concept to improve detonation front stability.

In practice, efficiently stabilizing a detonation wave will probably require the presence of a stabilizing body, such as a wedge or a rod. The situation will be slightly different with the creation of oblique waves. This situation, however, requires that the flow Mach number be greater than M_{CJ}. For engine applications, the presence of oblique detonation waves would modify the detonation stabilization criterion ($M_4 > M_{CJ}$) and the flowfield downstream of the detonation, but the subsequent performance analysis would still be valid, provided the flow component normal to the wave is used to calculate the CJ properties. The analysis of Pratt et al. (1991) showed that for high enough flow velocities and wedge angles, stable oblique detonation waves can be obtained. At lower wedge angles, incomplete detonation, shock-induced deflagration, or no combustion will occur. At very high wedge angles, the wave will detach and form a normal detonation near the stagnation streamline, similar to the situation studied here. The situation of an oblique detonation stabilized on a body is very similar to the case of projectile-induced detonations. Experiments by Kaneshige

and Shepherd (1996) showed that stable oblique detonations could be obtained on a spherical projectile in a straight channel for projectile speeds greater than U_{CJ}. Propagating oblique detonation waves have also been observed in two-layer detonation experiments (Dabora et al., 1991) in a straight channel. Nevertheless, it is not clear how oblique detonation waves would behave in a converging or diverging channel.

3.2.4 Detonation-related limitations

Up to now, we have modeled detonations as hydrodynamic discontinuities. The simplest model that includes chemical kinetics consists of a shock wave followed by a reaction zone, referred to as the ZND model and described in Section 1.1.2. In this model, the leading shock front is followed by an induction zone, through which the thermodynamic variables remain relatively constant while free radicals, such as OH, are produced. Significant energy release occurs at the end of the induction zone and corresponds to a rapid rise in temperature and a decrease in pressure accompanied by the formation of the major products. The length scale associated with the induction zone, the reaction zone length Δ (Fig. 1.3), is a strong function of the post-shock temperature. It can be used to judge whether a detonation can be obtained, or only shock-induced combustion can be produced. Another length scale associated with detonations is the cell width λ (Fig. 1.5). The cell width is a characteristic length scale corresponding to the intrinsic instability and the structure of propagating detonation waves (Section 1.1.3). Attempts have been made to correlate the cell width with the induction zone length and showed that λ is between 10 and 50 times Δ for stoichiometric mixtures, and between 2 and 100 times Δ for off-stoichiometric mixtures (Westbrook and Urtiew, 1982, Shepherd, 1986, Gavrikov et al., 2000).

Simulations of steady, one-dimensional detonations were performed with a code developed by Shepherd (1986), based on a standard gas-phase chemical kinetics package (Kee et al., 1989). The code solves the one-dimensional, steady reactive Euler equations of the ZND model (Eqs. 1.25–1.28). The chemical reaction model of Konnov

(1998) and standard thermochemistry were used to calculate reaction zone lengths for hydrogen-air mixtures at various initial conditions. Validation of this mechanism against shock tube induction time data is given in Schultz and Shepherd (2000). The reaction zone length was calculated as the distance from the leading shock to the point of maximum temperature gradient. Reaction zone lengths were calculated for hydrogen-air mixtures, for which the kinetics are fairly well understood. The computed reaction zone lengths were then scaled to estimate the cell width. The relationship $\lambda = 50\Delta$ gave the best agreement with the experimental data of Stamps and Tieszen (1991), Ciccarelli et al. (1994), and Guirao et al. (1982), and was used to predict cell widths for hydrogen-air mixtures.

Cell widths were also estimated for JP10-air mixtures, since JP10 is a fuel of interest to propulsion applications because of its high energy density. The reaction zone lengths for JP10-air mixtures were estimated from the ignition time correlation of Davidson et al. (2000), who carried out shock tube measurements of JP10 ignition. The correlation they obtained is

$$\tau_{ign} = 3.06 \cdot 10^{-13}\ P^{-0.56}\ X_{O_2}^{-1}\ \phi^{0.29}\ e^{52150/RT}\ . \tag{3.7}$$

The ignition time was multiplied by the post-shock velocity, which was calculated (Reynolds, 1986) for a non-reactive shock with realistic thermodynamic properties, to obtain the reaction zone length. The relationship $\lambda = 10\Delta$ gave a good estimate of the JP10 cell width data of Austin and Shepherd (2003) and was used to predict JP10-air cell widths.

Cell widths for hydrogen- and JP10-air mixtures are presented in Figs. 3.3, 3.4, and 3.5 versus initial pressure, equivalence ratio, and initial temperature, respectively. Fig. 3.3 shows that the cell width decreases with increasing pressure for both fuels. For JP10 and hydrogen at low pressures (below atmospheric), the cell width is roughly inversely proportional to the initial pressure: $\lambda \propto 1/P_4$ due to the dependence of the reaction rates on the rate of molecular collisions. However, the cell width for hydrogen-air increases for initial pressures between 1 and 6 bar, a behavior similar

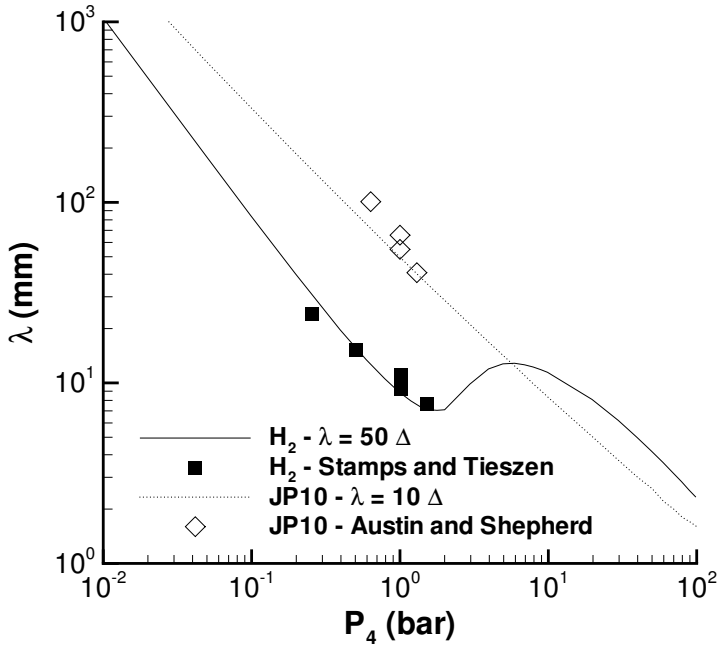

Figure 3.3: Cell width λ as a function of initial pressure P_4 for stoichiometric hydrogen-air at 297 K and JP10-air at 373 K. The lines correspond to cell width predictions using calculated reaction zone lengths (Shepherd, 1986, Kee et al., 1989) for hydrogen and ignition time correlation (Davidson et al., 2000) for JP10. The symbols correspond to experimental data of Stamps and Tieszen (1991) and Austin and Shepherd (2003).

to that observed in the same pressure range by Westbrook and Urtiew (1982), and Stamps and Tieszen (1991). This behavior is attributed to the prevalence of 3-body reactions with increasing pressure (Westbrook and Urtiew, 1982, Stamps and Tieszen, 1991) and is related to the second explosion limit mechanism for the hydrogen-oxygen system (Lewis and von Elbe, 1961, Chap. II.1). As the pressure is further increased, the product of the 3-body recombination reaction, HO_2, is rapidly consumed by other bimolecular reactions favored by high pressures. This effect corresponds to the third limit of the hydrogen-oxygen system (Lewis and von Elbe, 1961, Chap. II.1) and overcomes the inhibiting effect of the recombination reaction, decreasing the reaction zone length and the cell width. A more complete discussion is given in Westbrook and Urtiew (1982).

The cell width in Fig. 3.4 exhibits a U-shaped behavior versus the equivalence

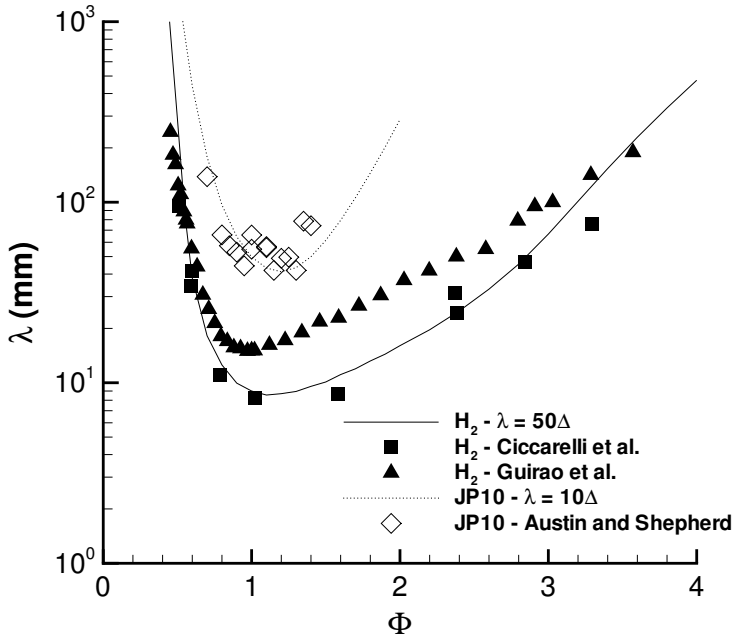

Figure 3.4: Cell width λ as a function of equivalence ratio for hydrogen-air at 297 K and JP10-air at 373 K and 1 bar. The lines correspond to cell width predictions using calculated reaction zone lengths (Shepherd, 1986, Kee et al., 1989) for hydrogen and ignition time correlation (Davidson et al., 2000) for JP10. The symbols correspond to experimental data of Ciccarelli et al. (1994), Guirao et al. (1982), and Austin and Shepherd (2003).

ratio with a minimum around stoichiometry caused by the variation of the post-shock temperature with composition. The cell width at stoichiometry and standard conditions is on the order of 10 mm for hydrogen-air and 60 mm for JP10-air. Finally, λ does not vary significantly for hydrogen when the initial temperature is varied (Fig. 3.5) due to the competing effects of a higher post-shock temperature and a lower density on the reaction rates. The calculated JP10-air cell width decreases with increasing initial temperature due to the larger activation energy for JP10. The JP10 cell widths are shown above a minimum temperature of about 330 K due to vapor pressure considerations (Austin and Shepherd, 2003). In conclusion, the initial pressure and the equivalence ratio are the parameters with the strongest influence on the cell width, since λ varies less than one order of magnitude with initial temperature. These calculations can be used to estimate the characteristic length scales for various

engine configurations.

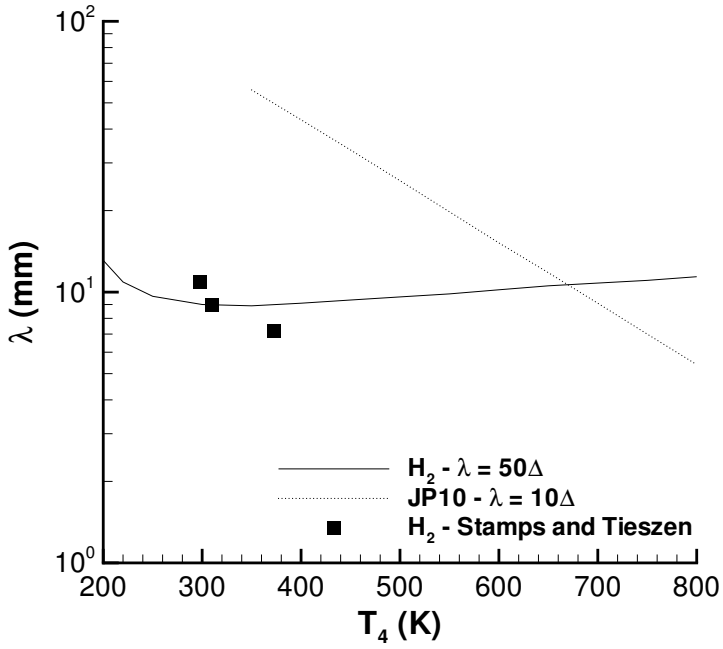

Figure 3.5: Cell width λ as a function of initial temperature T_4 for stoichiometric hydrogen- and JP10-air mixtures at 1 bar. The lines correspond to cell width predictions using calculated reaction zone lengths (Shepherd, 1986, Kee et al., 1989) for hydrogen and ignition time correlation (Davidson et al., 2000) for JP10. The symbols correspond to experimental data of Stamps and Tieszen (1991).

3.2.4.1 Limitations on detonation chamber diameter

The characteristic detonation length scales, which are the reaction zone length and the cell width, impose constraints on the geometry and size of the combustor. The usual rule of thumb for propagating detonations is that the channel width has to be greater than the detonation cell width for the detonation to propagate. The limit for detonation propagation in cylindrical tubes of diameter d is usually taken to be determined by the criterion $\lambda \approx \pi d$, or a velocity deficit of less than 10% of the CJ velocity (Dupre et al., 1986). This criterion corresponds to the onset of single-head spin detonation. Lee (1984) reviewed previous work and pointed out that the limits for circular tubes could be specified by the criterion $\lambda = \pi d$ and for two-dimensional planar channels of width w by $\lambda = w$. Peraldi et al. (1986) found that

the necessary condition for transition to detonation in circular obstacle-laden tubes was $\lambda > d$. However, experiments by Dupre et al. (1990) with standardized initial conditions for detonation propagation, failed to arrive at a definitive λ/d criterion for smooth circular tubes. Unstable detonations with very large velocity fluctuations, such as galloping waves, were obtained for λ/d up to 13. These unstable near-limit phenomena were also observed by Manzhalei (1999) for acetylene-oxygen mixtures. Manzhalei (1999) found that the lower pressure limit for detonation regimes in lean mixtures was an order of magnitude smaller than that corresponding to single-head spin detonation. The problem of detonability limits for propagating detonations does not have a single definitive answer, and, at present, there are no data at all for stabilized detonations. For the purposes of the present study, we adopt the criterion $\lambda = d$ as the detonability limit for a stabilized detonation wave in a given channel.

3.2.4.2 Limitations on detonation chamber length

It has been claimed (Dunlap et al., 1958, Sargent and Gross, 1960, Dabora and Broda, 1993) that using detonations in ramjet-like engines would enable reductions in the combustor length. In practice, the CJ state has to be achieved inside the combustor for maximum efficiency and to isolate the detonation from potential perturbations in the flow downstream of the combustor. If the combustor is too short, the combustion process inside the combustor is incomplete and part of the energy released is lost to the surroundings. The detonation can also become unstable if flow perturbations penetrate the subsonic region between the detonation front and the Chapman-Jouguet plane. Hence, the location of the CJ surface is critical for the design of the detonation chamber. Vasiliev et al. (1972) attempted to determine the location of the CJ surface by photographic observation of a detonation wave propagating from a metal tube into a thin cellophane tube. The velocity decrease observed at lower pressures was associated with the penetration of the rarefaction wave caused by the destruction of the cellophane tube into the subsonic region just behind the front. The upper bound for the location of the CJ surface was found to be within 3.5-10 cell lengths (or $6\lambda - 17\lambda$, assuming a cell width to cell length ratio of 0.6) for hydrogen- and

acetylene-oxygen mixtures diluted with argon. Another method used by Vasiliev et al. (1972) consisted of observing the interaction of a detonation with a thin plate and, more specifically, the detachment of the weak shock formed at the front edge of the plate, corresponding to sonic conditions. These observations yielded a lower bound to the location of the CJ surface, within 1-3 cell lengths ($1.5\lambda - 5\lambda$) behind the front. Edwards et al. (1976) measured the pressure oscillations associated with the transverse waves behind a propagating detonation front for hydrogen- and acteylene-oxygen mixtures. They noticed that the oscillations attenuated in a distance of two to four cell lengths ($3\lambda - 7\lambda$) downstream of the front and suggested that there is a link between the transverse oscillations and the establishment of sonic flow relative to the front. More recently, Weber et al. (2001) reported measurements of the location of the CJ surface using a method similar to Vasiliev's thin plate technique. Their results indicate that the location of the sonic surface is within $0.2\lambda - 0.6\lambda$ behind the detonation front. Although there is a wide range of values for the sonic surface, it apparently lies within 5λ of the front for propagating detonation waves and no measurements have been made for stabilized waves. For the purposes of the present study, we propose to use a criterion for the minimum length of the detonation chamber $L > 5\lambda$.

3.2.4.3 Near-detonability limit effects

The problem of stabilizing a detonation in a channel gets more complicated in configurations close to the detonability limits. It may not be necessary to have $\lambda < d$ if viscous effects can be used to stabilize the flow. The results of detonation propagation in small-diameter tubes or at low pressures (Manzhalei, 1999, Lee et al., 1995) have shown that the detonation velocity can be substantially lower than the CJ velocity for these cases. Manzhalei (1999) and Lee et al. (1995) observed low-velocity detonations in near-limit situations where the detonation velocity was as low as 50% of the CJ velocity. These situations may significantly extend the regime of operation of a steady detonation engine. In these cases, the criterion formulated previously, $M_4 = M_{CJ}$, is no longer valid, and a more specific study is necessary to find the right

parameters for stabilization. The idea of being able to stabilize a detonation wave at a lower velocity than U_{CJ} is attractive, since it reduces the requirements on the total temperature of the flow.

However, propagating detonations at near-limit conditions generally have an unstable behavior. Indeed, the same near-limit detonation studies (Manzhalei, 1999, Lee et al., 1995) have shown that many different behaviors could be observed. Lee et al. (1995) proposed a classification of the six different types of near-limit behavior they observed. In particular, modes characterized by a strong oscillation of the detonation velocity, such as the "stuttering" mode or the galloping waves (where the detonation velocity oscillates between 0.4 and 1.5 U_{CJ}), are characteristic of near-limit behavior. Lee et al. (1995) pointed out that several modes could occur either within a single propagation, or in different experiments at the same initial conditions. It is obvious that such modes would be totally inadequate for detonation stabilization, and even catastrophic in practice if the detonation exits the combustion chamber. We conclude that the possibility of stabilized detonations with velocities substantially less than the CJ value is highly speculative and we will not consider these any further in the present study. For the purposes of the present study, we adopt the requirement $u \geq U_{CJ}$ for stabilizing a detonation in a combustor.

3.2.4.4 Application to hydrogen-air and JP10-air stabilized detonations

The criteria proposed in the previous sections impose some severe restrictions on the dimensions of the detonation chamber of a steady detonation engine. In particular, it is interesting to illustrate these issues with a few representative numbers, corresponding to typical flight conditions. Table 3.2 lists the minimum requirements for the diameter and length of a detonation chamber at various initial conditions, including subatmospheric and superatmospheric pressures and lean mixtures. The CJ parameters corresponding to the mixtures considered are also given. Table 3.2 lists parameters for two different temperatures, 300 K and 500 K. However, vapor pressure considerations (Austin and Shepherd, 2003) indicate that the minimum temperature required for vaporizing all the fuel injected in a stoichiometric JP10-air mixture is

Fuel	T_0 (K)	P_0 (atm)	ϕ	U_{CJ} (m/s)	T_{CJ} (K)	P_{CJ} (bar)	d (mm)	L (mm)
H_2	300	0.1	1	1917.5	2771	1.5	84.9	424.5
H_2	300	1	1	1971	2949	15.7	8.9	44.5
H_2	300	10	1	2014.1	3097	162.5	11.2	56
H_2	300	0.1	0.5	1603.7	2189	1.18	214.5	1072.5
H_2	300	1	0.5	1610.1	2205	11.8	271.5	1357.5
H_2	300	10	0.5	1613.3	2213	118.4	289	1445
H_2	500	0.1	1	1885.2	2777	0.89	98.1	490.5
H_2	500	1	1	1946.5	2977	9.4	10.4	52
H_2	500	10	1	1998.4	3154	98.3	13.1	65.5
H_2	500	0.1	0.5	1605.4	2305	0.73	213	1065
H_2	500	1	0.5	1618	2339	7.4	215.2	1076
H_2	500	10	0.5	1624.5	2356	74.1	247.9	1239.5
JP10	350	0.1	1	1734.4	2693	1.53	369.4	1847
JP10	350	1	1	1779.5	2850	16	55.2	276
JP10	350	10	1	1818.1	2989	165.4	9.2	46
JP10	350	0.1	0.5	1492.8	2092	1.078	8185	40925
JP10	350	1	0.5	1496.6	2101	10.7	2100	10500
JP10	350	10	0.5	1498.2	2105	107.3	561.5	2807.5
JP10	500	0.1	1	1719.6	2706	1.07	165.8	829
JP10	500	1	1	1768.6	2876	11.2	25.5	127.5
JP10	500	10	1	1811.5	3030	116.6	4.3	21.5
JP10	500	0.1	0.5	1500.4	2188	0.78	1557.5	7787.5
JP10	500	1	0.5	1507.6	2206	7.79	384.8	1924
JP10	500	10	0.5	1510.8	2215	77.9	100.8	504

Table 3.2: CJ parameters and minimum detonation chamber length and diameter for a range of initial conditions for hydrogen- and JP10-air. The minimum dimensions are based on the proposed criteria using the computed reaction zone lengths for hydrogen-air (Shepherd, 1986, Kee et al., 1989) and the ignition time correlation for JP10-air of Davidson et al. (2000).

330 K. Hence, the minimum temperature chosen for JP10 was 350 K. The minimum dimensions vary by several orders of magnitude with equivalence ratio and initial pressure. Typical air-breathing engines run at an equivalence ratio substantially less than one in order to limit the maximum temperature in the combustor due to material considerations. The same approach with a steady detonation engine leads to impractical minimum dimensions when the equivalence ratio is decreased to 0.5. A similar behavior is obtained when the pressure is decreased. The claim that using steady detonations in propulsion devices might allow us to reduce the combustor length is not justified, as a careful consideration of the minimum length required shows that the detonation chamber length has to be at least five times the minimum chamber diameter. Finally, Table 3.2 highlights the difficulty associated with detonation stabilization using a liquid hydrocarbon fuel such as JP10. Liquid hydrocarbon fuels are insensitive to detonation and their cell width is much larger than that of hydrogen, yielding stricter constraints on steady detonation engine design.

3.3 Detonation ramjet

A detonation ramjet, or dramjet, is a steady propulsive device using the same principle as a ramjet except that the combustion takes place in the combustor in the form of a steady detonation wave instead of a bluff-body stabilized flame. The ideal ramjet, described in Section 1.2.2, has many components in common with the dramjet, and it will be used as a performance standard. First, we will discuss the portions of the dramjet model which are different from the ramjet. Second, the performance of both engines will be compared. Finally, limitations will be considered due to detonation stabilization requirements, ignition limits, and fuel and oxidizer properties.

3.3.1 Performance analysis

A detonation ramjet has to accommodate a stationary detonation wave in the combustor. The flow must be accelerated or slowed down to a velocity higher than or equal to the CJ detonation velocity. For flow velocities higher than U_{CJ}, overdriven

detonation waves could be stabilized but they are not desirable in order to avoid excessive total pressure loss across the detonation. We consider only Chapman-Jouguet detonation waves. A dramjet has to include a generic nozzle between the inlet diffuser and the combustor inlet in order to bring the flow to the CJ velocity. This is a general situation applicable to various flight Mach numbers. It will be shown later that a converging inlet section is actually more appropriate for most flight Mach numbers. The rest of the engine is similar to the ramjet. A schematic of a dramjet is given in Fig. 3.6. A fluid element going through a dramjet first undergoes a compression through the inlet (station 0 to 2) then an expansion through a nozzle (station 2 to 4) until its velocity is equal to the CJ velocity. The fluid element is then compressed and heated through the detonation wave (station 4 to 5) before undergoing an expansion through the exit nozzle (station 5 to 9).

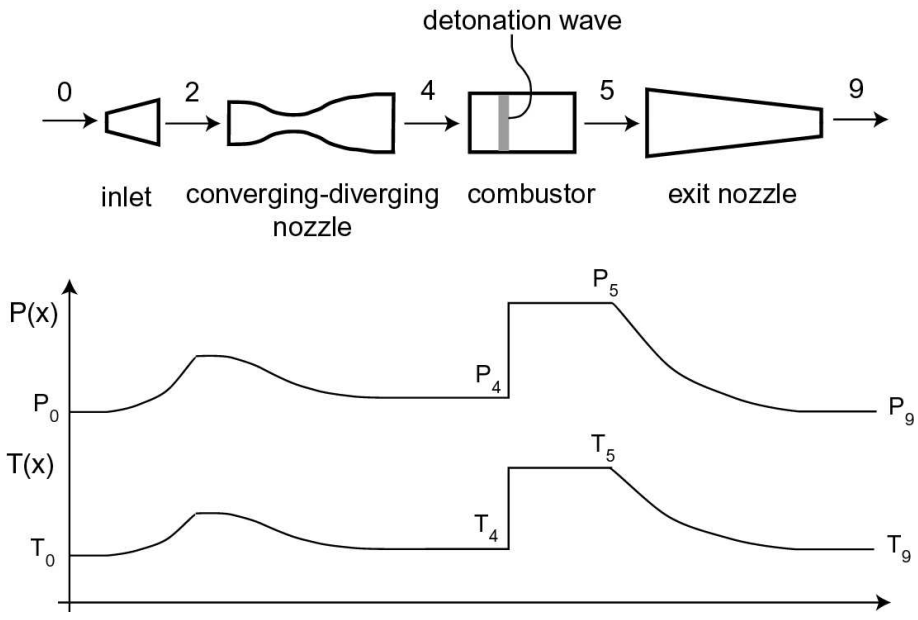

Figure 3.6: Schematic representation of a detonation ramjet (or dramjet). The pressure and temperature profiles through the engine are shown.

In our performance analysis of the dramjet, we assume steady, inviscid and adiabatic flow of an ideal gas. As in the ideal ramjet case, we consider the compression and expansion processes to be isentropic. The dissociation of the combustion products is not taken into account. Products and reactants are assumed to have the same

heat capacity and γ. The stabilization condition for the detonation wave is obtained using Eq. 3.2. The detonation wave is assumed to be stable with respect to flow perturbations. The limitations due to mixture condensation or pre-ignition were not considered in these calculations, nor were the limitations due to reaction zone lengths and detonation cell widths. The performance limits associated with these constraints will be indicated later.

These assumptions are, of course, not realistic due to the presence of irreversible processes such as shocks, mixing, wall friction, and heat transfer. It is possible to make the model much more realistic but for the present purposes, these idealizations are adequate since we are primarily interested in performance comparisons rather than absolute performance. All these assumptions are used to derive simple performance estimates of an ideal dramjet, which can be used as the detonative combustion analog of the ideal ramjet. We apply a limitation on the total temperature at the combustor outlet similar to the ramjet case. The flow evolves isentropically through the inlet and the converging-diverging nozzle. Hence, $T_{t0} = T_{t2} = T_{t4}$ and $P_{t0} = P_{t2} = P_{t4}$. The detonation stabilization condition is that the flow at station 4 must have a Mach number $M_4 = M_{CJ}$.

The fuel-air mass ratio f is determined by the maximum temperature condition (Eq. 1.63) and is assumed to have a value $f \ll 1$, which is typically the case for stoichiometric or lean hydrogen- or hydrocarbon-air mixtures. The flow properties at the combustor outlet are dictated by the Chapman-Jouguet conditions: $M_5 = 1$, $T_{t5} = T_{max}$, P_5 is obtained from Eq. 1.17. The flow through the exit nozzle is considered isentropic and the exit velocity u_9 can be calculated assuming the flow at the nozzle exit is pressure-matched

$$u_9 = \sqrt{2C_pT_{max}\left[1 - \frac{2}{\gamma+1}\frac{T_0}{T_4}\left(\frac{\gamma+1}{1+\frac{2\gamma}{\gamma-1}(\frac{T_{t0}}{T_4}-1)}\right)^{\frac{\gamma-1}{\gamma}}\right]}, \tag{3.8}$$

where T_4 is given by Eq. 3.2. The values of the various performance parameters can be deduced from the value of u_9 and are given in Appendix A.

3.3.2 Performance comparison

The specific thrust (Eq. 1.64), TSFC (Eq. 1.66), and efficiencies (Eqs. 1.58, 1.59, and 1.61) of the dramjet were calculated for a set of initial conditions corresponding to flight at 10,000 m altitude using a fuel of heat release per unit mass $q_f = 45$ MJ/kg (typical of hydrocarbon fuels) and a maximum allowable temperature in the combustor $T_{max} = 2500$ K. These parameters are compared to their ramjet analogs in Figs. 3.7 and 3.10. The only performance parameter that would be modified if hydrogen were used as a fuel would be the TSFC. The heat release per unit time would be unchanged due to the maximum temperature condition, but the fuel-air mass ratio would change and, comparatively, less hydrogen would be consumed.

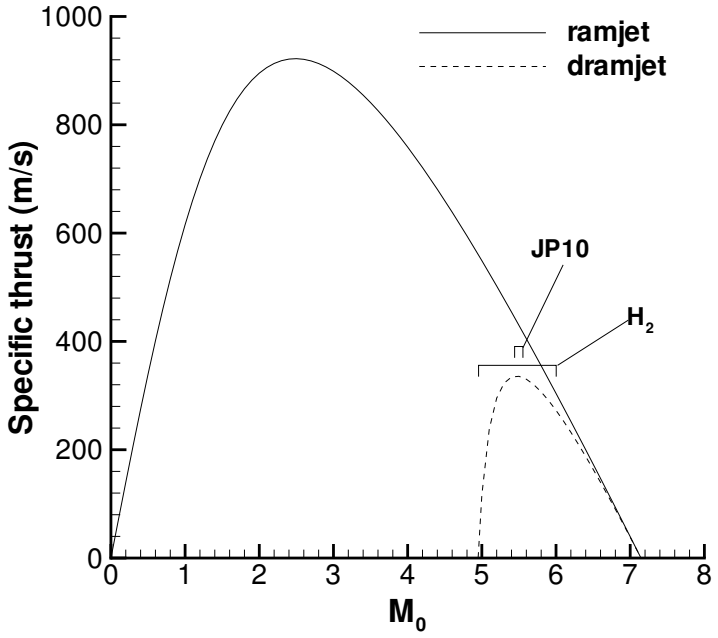

Figure 3.7: Specific thrust of ramjet and dramjet. $T_0 = 223$ K, $P_0 = 0.261$ atm, $q_f = 45$ MJ/kg, $T_{max} = 2500$ K. The limits for effective detonation stabilization are shown for hydrogen and JP10.

The dramjet does not produce any thrust below a flight Mach number of about 5 for the initial conditions considered due to the stabilization condition for a detonation wave. The freestream Mach number is higher than the CJ Mach number for $M_0 > 5.1$. This means that the supersonic flow between stations 2 and 4 has to undergo a

deceleration through the inlet and only a converging section is required, unlike the situation depicted in Fig. 3.6. The pressure and temperature would then increase continuously and isentropically from station 0 to station 4. It also means that the stabilized detonation in the nozzle configuration would be stable with respect to flow perturbations.

The specific thrust for the dramjet (Fig. 3.7) shows a maximum near $M_0 = 5.5$. The performance of the dramjet then decreases with increasing M_0 due to the maximum temperature limitation in the combustor. As M_0 approaches its upper limit, the amount of fuel injected decreases (Eq. 1.63) and the CJ Mach number approaches 1. The combustion process becomes, in theory, closer to a constant-pressure heat addition as in the case of the ramjet, which explains why the two curves match at high Mach numbers. In practice, as the amount of fuel is reduced, the mixture will stop being detonable and only subsonic deflagration will be obtained. Additionally, the reaction zone length will strongly increase until it exceeds the physical dimension of the combustor and incomplete reaction is obtained in the combustor. Below a minimum fuel-air ratio, the mixture will not be flammable and combustion will not be obtained. For this reason, the actual maximum flight Mach number will be lower than the ideal value.

As the flight Mach number decreases, the performance of the dramjet sharply drops. This can be explained by the very substantial total pressure loss across a detonation wave. The total pressure ratio across a CJ detonation was computed as a function of the CJ Mach number and is shown in Fig. 3.8. For reference, the corresponding total pressure ratio across a normal shock wave is also displayed in Fig. 3.8, along with the total pressure ratio across the reaction zone. The dramatic total pressure loss across a CJ detonation is mainly due to the presence of the normal shock wave, although the combustion process can account for up to 14% of the total pressure loss. The total pressure ratio for a detonation decreases rapidly as M_{CJ} increases. CJ detonation waves have very high total pressure losses across them; for example, the total pressure loss across a detonation wave with $M_{CJ} = 4$ is 88%, and the total pressure loss across a wave with $M_{CJ} = 5$ is greater than 94%. In order

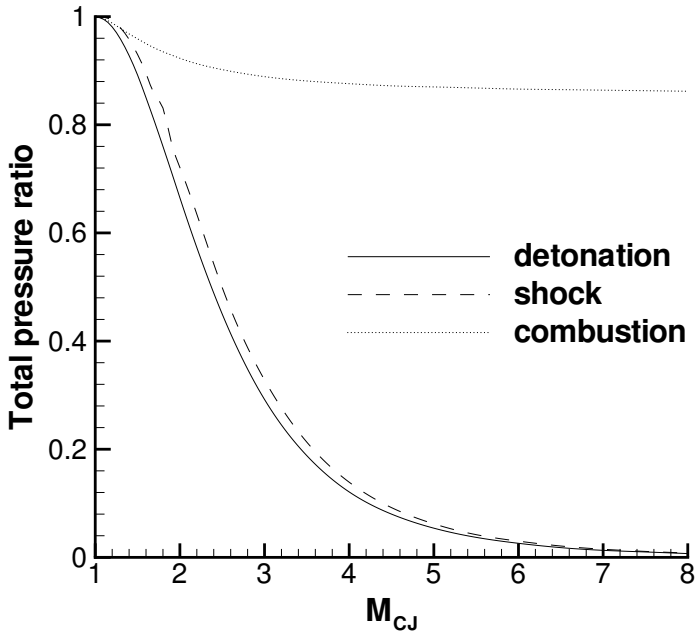

Figure 3.8: Total pressure ratio across a CJ detonation wave, a normal shock, and the reaction zone using the one-γ model. $\gamma = 1.4$.

to maximize the specific thrust, one has to maximize the exit velocity u_9, which is determined by the expansion of the flow from the combustor outlet total pressure P_{t5} to the outside pressure P_0 and increases with P_{t5}. This is why total pressure losses are so penalizing for air-breathing engines. The variation of the CJ Mach number with flight Mach number and the corresponding total pressure ratio across the detonation wave P_{t5}/P_{t4} are shown in Fig. 3.9. As the flight Mach number decreases, the CJ Mach number increases sharply because of the lower static temperature upstream of the detonation. The total pressure ratio across the detonation decreases correspondingly, which causes the sharp drop in the dramjet performance. In the case considered, the specific thrust vanishes at a flight Mach number $M_0 = 4.95$, which corresponds to a total pressure ratio of about 1.5%. If M_0 is further decreased, the drag momentum term $\dot{m}u_0$ then exceeds the thrust momentum term $\dot{m}u_9$ because of the substantial total pressure losses and no net thrust is produced. The high total pressure loss across the detonation strongly penalizes the performance of a dramjet compared to the ideal ramjet, for which there is negligible total pressure loss across the combustor.

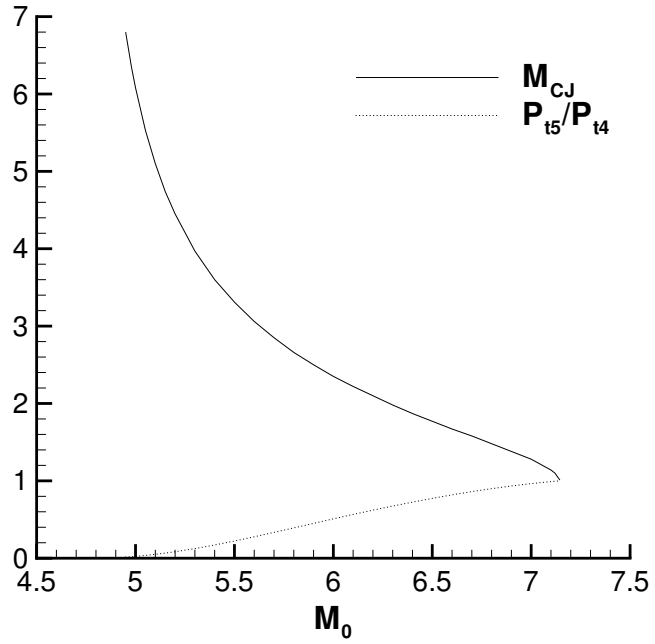

Figure 3.9: Variation of the CJ Mach number and the total pressure ratio across the detonation wave with flight Mach number for the dramjet. $T_0 = 223$ K, $P_0 = 0.261$ atm, $q_f = 45$ MJ/kg, $T_{max} = 2500$ K.

As seen in Fig. 3.10, the TSFC increases sharply for both engines as the flight Mach number decreases. This is due to the decrease in specific thrust while the fuel consumption rate remains finite. At higher Mach numbers, the TSFC remains finite as both the fuel-air mass ratio and the specific thrust decrease, and the process approaches constant-pressure combustion. The thermal efficiency of the ramjet and the dramjet increases as M_0 increases. The freestream total pressure increases with M_0, and adding heat at higher total pressure is thermally more efficient since the exit velocity is higher (see Eq. 1.58). The overall efficiency follows a similar behavior, showing that both engines are more efficient at higher flight speeds. A more realistic approach would take into account irreversible processes such as inlet losses. These losses would, in general, increase with increasing Mach number, making for a more rapid decrease in performance at high Mach numbers for both ramjet and dramjet. However, our goal here is to compare ideal models whose characteristics can be used as performance goals of realistic engines.

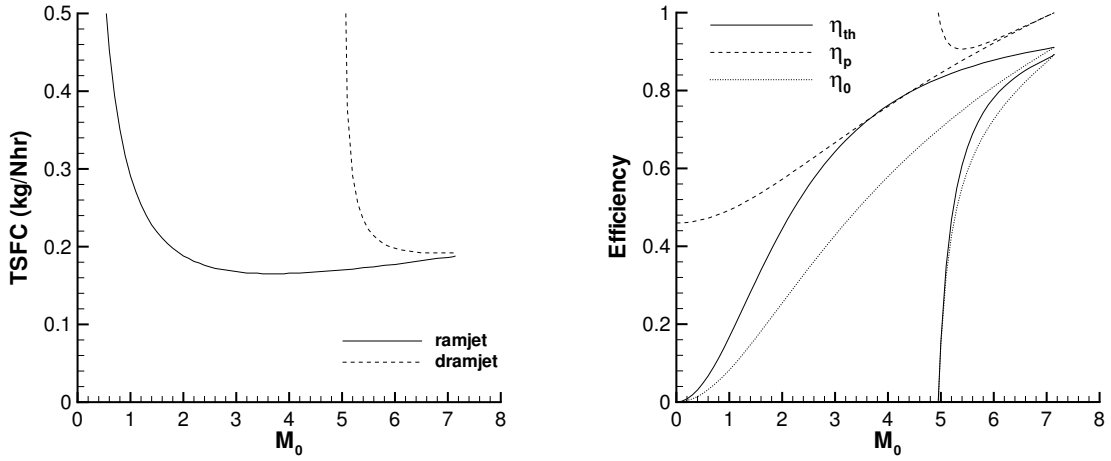

Figure 3.10: Thrust-specific fuel consumption (left) and efficiencies (right) of ramjet and dramjet. $T_0 = 223$ K, $P_0 = 0.261$ atm, $q_f = 45$ MJ/kg, $T_{max} = 2500$ K.

Performance calculations using real gas thermodynamics (Reynolds, 1986) were carried out for JP10 at $M_0 = 5.2$ and $M_0 = 5.4$. The performance calculation methodology for real gas calculations is described in the appendix. These calculations have to be iterated until the stabilization conditions for the detonation wave are found. The use of real gas thermodynamics shows that more fuel would have to be consumed in order to reach the temperature T_{max} at the combustor outlet. The TSFC numbers given in Fig. 3.10 are obtained using the one-γ model and are very optimistic figures if the maximum temperature T_{max} is to be reached at the combustor outlet due to the effect of dissociation. Similarly, the numbers given in Fig. 3.11 are not very representative of real JP10- and hydrogen-air systems. The effect of dissociation on performance was investigated by carrying out real gas calculations at the same operating conditions (including fuel-air mass ratio) as those used in the ideal model. Surprisingly, their results for the specific thrust were very close to those of the ideal model (within 1.5% error) in the case for $M_0 = 5.4$, and even higher (by 15%) in the case for $M_0 = 5.2$. The effect of endothermic dissociation reactions through the detonation wave, which is to decrease the effective energy release, is compensated for by the modified detonation wave stabilization condition, which is satisfied for a lower CJ Mach number than in the ideal case. This lower CJ Mach

number corresponds to a lower total pressure loss across the detonation wave and results in improved performance. The effect of recombination reactions through the nozzle was also considered, since the flow through the nozzle undergoes a substantial expansion due to the high pressure ratios between the combustor and the nozzle exit. However, frozen and equilibrium nozzle calculations resulted in very small differences in terms of specific thrust (less than 1.5%) because of the low CJ temperatures (about 1800 K) due to low fuel input.

3.3.3 Dramjet limitations

Effects such as detonation stability, fuel condensation, mixture pre-ignition, and reaction zone length have to be considered when looking at the dramjet performance curves.

An important issue is the stability of the detonation wave, which has not been assessed experimentally. If the wave is unstable, the consequences can be catastrophic as it might be blown out of the combustor or run back into the fuel lines. Even though the wave appears to be in a stable configuration with respect to flow perturbations for most cases (in a converging nozzle), according to our analysis, a stabilizing body might still be necessary. However, the analysis of Zhang et al. (1995) shows that a detonation wave is attenuated in a converging nozzle and its oscillatory instability increased. Both considerations need to be taken into account when evaluating the overall stability of the wave for practical applications.

As M_0 gets close to the lower limit of the dramjet thrust-producing range, such effects as fuel or oxidizer condensation are going to take place as described in the previous section about standing normal detonation waves. The static temperature at the nozzle outlet is higher than the freestream temperature, but still low because there is very little deceleration required to match the CJ Mach number. This is not an issue for a fuel such as hydrogen, but it is definitely a problem for liquid hydrocarbon fuels, which have boiling points above 450 K (see Table 3.1). On another hand, near the upper limit of the thrust-producing range of M_0, the static temperature T_4

becomes very high because of the strong flow deceleration from a high freestream Mach number to a low M_{CJ} due to low fuel input. Pre-ignition of the fuel-air mixture is expected for $M_0 > 6$. For hydrogen, the condition dictated by Eq. 3.3 corresponds to $5 < M_0 < 6$ for steady detonation generation. For a representative liquid hydrocarbon fuel such as JP10, $5.45 < M_0 < 5.55$ for detonation stabilization. These limits are shown in Fig. 3.7 for mixtures with hydrogen and JP10. If, instead of using the condensation temperature criterion for JP10, we consider vapor pressure requirements so that the amount of fuel injected is totally vaporized, then $5.25 < M_0 < 5.55$ for effective detonation stabilization. The difficulties associated with generating steady detonations using liquid hydrocarbon fuels are readily apparent.

Both the ramjet and dramjet have been modeled so far without considering any total pressure loss other than across the detonation wave. There are obviously total pressure losses across the inlet during supersonic flight, but both engines would suffer a similar decrease in performance. However, the performance of a realistic dramjet is handicapped compared to the ramjet due to the mixing requirements ahead of the combustion chamber. In a ramjet, mixing and combustion occur at $M \ll 1$, where losses are minimal. In a dramjet, mixing has to take place at supersonic speeds, which is one of the key problems for scramjet research (Curran et al., 1996). Supersonic mixing generates total pressure losses because of low residence times and fast mixing rates. Dunlap et al. (1958) modeled the supersonic mixing process for hydrogen-air mixtures and showed that the total pressure loss increases with the flow Mach number. Total pressure losses on the order of 10–40% were predicted for Mach numbers between 2 and 5. Total pressure losses during supersonic mixing were also calculated by Fuller et al. (1992), and Papamoschou (1994) showed that they directly result in thrust losses for a simplified scramjet model. The calculated thrust loss is about 30% for a convective Mach number of 2 and about 50% for a convective Mach number of 3, stressing the importance of minimizing total pressure losses during supersonic mixing. This effect could have a significant impact on the dramjet performance compared to the ramjet.

The limitations associated with detonation reaction zone structure impose further

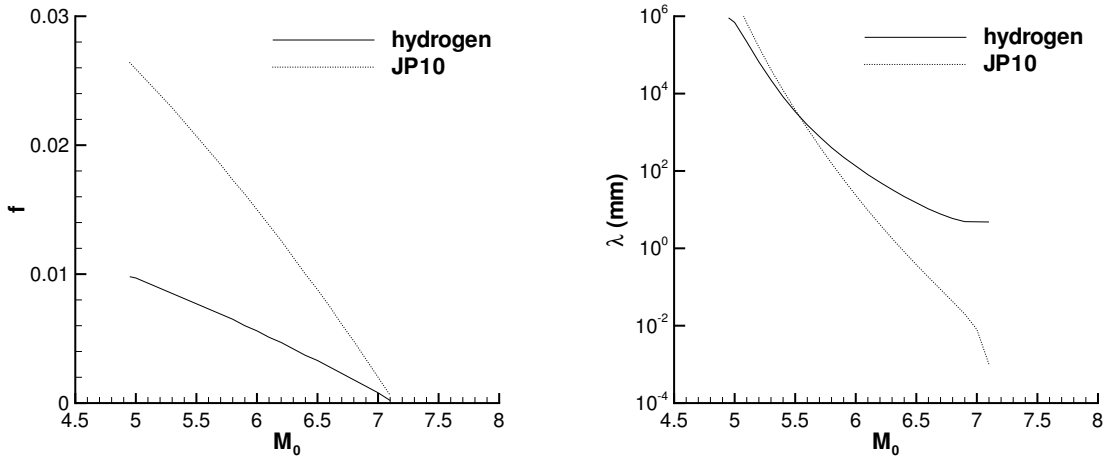

Figure 3.11: Fuel-air mass ratio f (left) and cell width λ (right) versus flight Mach number M_0 for a dramjet operating with hydrogen and JP10. $T_0 = 223$ K, $P_0 = 0.261$ atm, $T_{max} = 2500$ K, $\gamma = 1.4$.

constraints on the performance of the dramjet. The fuel-air mass ratio was calculated for a hydrogen-fueled and a JP10-fueled dramjet as a function of M_0 at flight conditions corresponding to an altitude of 10,000 m ($T_0 = 223$ K, $P_0 = 0.261$ atm) and is plotted in Fig. 3.11. The fuel-air ratio decreases with increasing Mach number because of the fixed combustor outlet total temperature T_{max} until it reaches zero when the freestream total temperature equals T_{max} and no fuel can be injected. Cell width were estimated from the fuel-air mass ratio based on reaction zone length computations (Shepherd, 1986, Kee et al., 1989) for hydrogen and ignition time correlations (Davidson et al., 2000) for JP10, as described previously in Section 3.2.4. Figure 3.11 displays the cell width estimates as a function of the flight Mach number. The computations and correlations used to estimate the cell widths are valid only in a given range of parameters. However, the limits sought for practical engine design (e.g., $\lambda = 1$ m) are usually located within or close to this parameter range. The mixtures are all very lean, but the pressure P_4 and temperature T_4 increase very rapidly with increasing M_0. The cell width is sensitive to the changes in pressure and temperature and decreases by many orders of magnitude with increasing Mach number. For conventional applications, the corresponding cell width λ probably has to be

below 1 m, which requires that $M_0 > 5.6$ for both fuels. The range of applicability of hydrogen-fueled dramjets is now reduced to $5.6 < M_0 < 6$ at the flight conditions considered due to cell width and pre-ignition considerations. For a JP10-fueled dramjet, there is no practical range of applicability due to the lower auto-ignition temperature of the fuel. The influence of flight altitude was also investigated as the variation of the freestream pressure with altitude might result in smaller cell widths at low altitude and, therefore, a wider operating range for the dramjet. However, performance calculations at an altitude of 1,000 m showed that the useful operating range for a hydrogen-fueled dramjet was only $4.9 < M_0 < 5.15$, and there was no practical operating range for JP10. Performance figures similar to the 10,000 m case were obtained for slightly lower flight Mach numbers due to the higher freestream temperature. These results illustrate clearly the strong influence of the fuel properties and the characteristic detonation length scales on the use of detonations in steady-flow engines.

3.4 Detonation turbojet

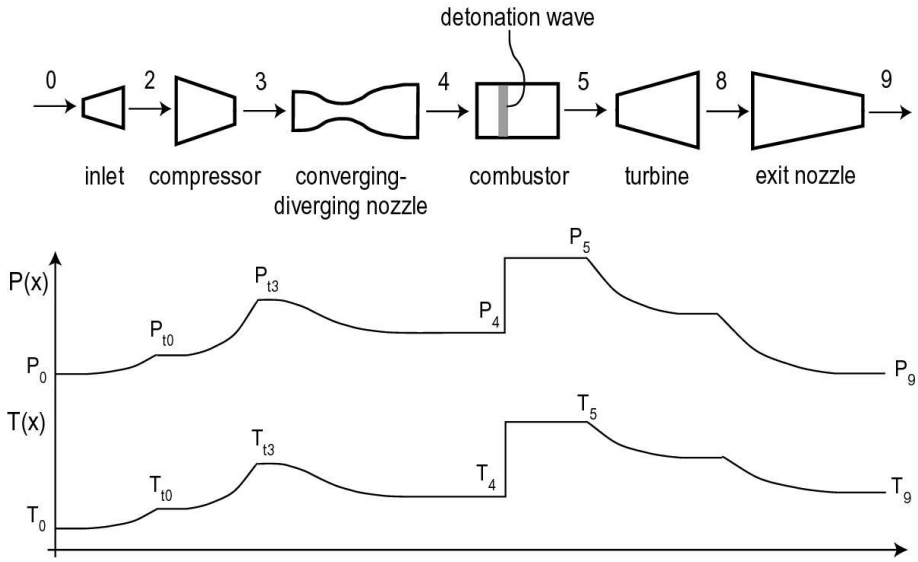

Figure 3.12: Schematic of a detonation turbojet, including the variation of pressure and temperature across the engine.

The principle of a detonation turbojet (or turbodet) is similar to that of the dramjet. The detonation turbojet has the same components as the turbojet engine described in Section 1.2.3, except that it requires an additional nozzle between the compressor and the combustor in order to accelerate the flow to the CJ velocity, as depicted in Fig. 3.12. Unlike the dramjet, the turbodet includes a converging-diverging nozzle to accelerate the subsonic flow exiting the compressor to supersonic in the combustor. This means that a stabilized detonation would be unstable to flow perturbations without the presence of a stabilizing body. The sonic flow exiting the combustor has to be decelerated before entering the turbine in order to minimize losses associated with shock waves. The performance parameters are calculated the same way as for the turbojet, except that the solution for the steady detonation wave is used between the compressor and the combustion chamber. The formulas used to calculate some of the performance parameters are given in the appendix.

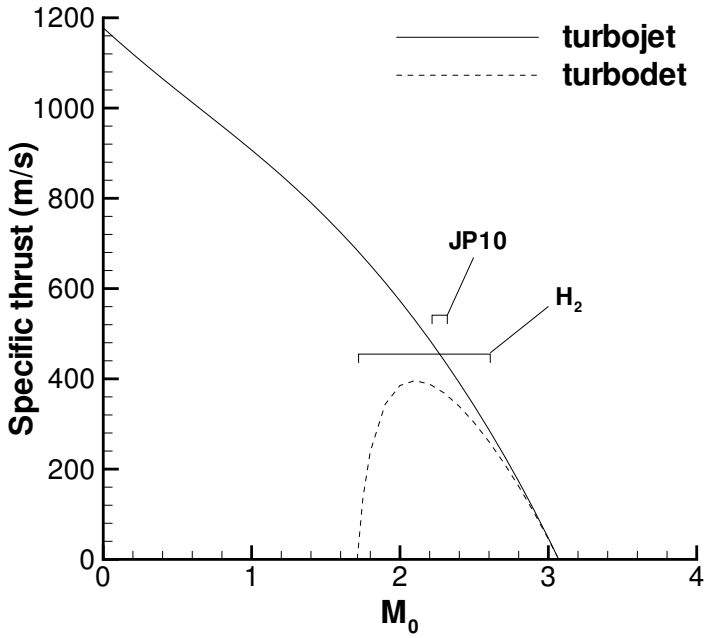

Figure 3.13: Specific thrust of turbojet and turbodet engines. $\pi_c = 30$, $T_0 = 223$ K, $P_0 = 0.261$ atm, $q_f = 45$ MJ/kg, $T_{max} = 1700$ K.

The specific thrust, TSFC, and efficiencies of the turbojet and turbodet engines are plotted in Figs. 3.13 and 3.14, respectively. These plots correspond to a fixed

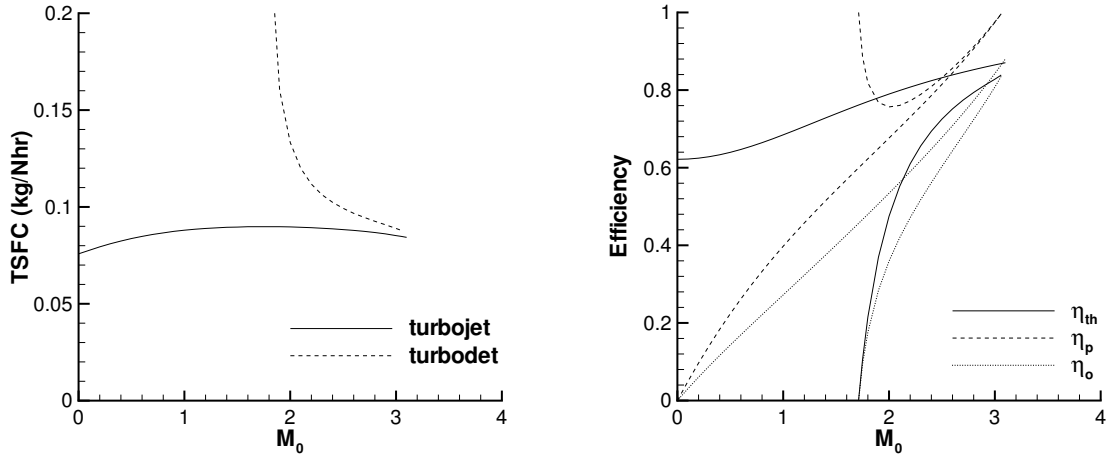

Figure 3.14: Thrust-specific fuel consumption (left) and efficiencies (right) of turbojet and turbodet engines. The efficiency curves for the turbodet are those extending only from $M_0 = 1.75$ to 3. $\pi_c = 30$, $T_0 = 223$ K, $P_0 = 0.261$ atm, $q_f = 45$ MJ/kg, $T_{max} = 1700$ K.

compression ratio of 30, flight conditions at an altitude of 10,000 m, a heat release per unit mass of fuel of 45 MJ/kg, and a maximum turbine inlet temperature $T_{max} = 1700$ K. The turbodet engine shows relatively poor performance compared to the turbojet. It does not produce thrust below a Mach number of 1.75 for the case considered here (the value of the limiting Mach number depends on the compression ratio at fixed flight conditions) due to the detonation wave stabilization condition. The drastic total pressure loss across the steady detonation causes the specific thrust to fall off at lower flight Mach numbers, while the maximum temperature condition causes its decrease at higher flight Mach numbers. The influence of the compression ratio was investigated and the results are presented in Fig. 3.15. The turbodet was found to produce thrust at lower flight Mach numbers as the compression ratio increases due to the requirements on the nozzle total temperature for detonation stabilization. There is a trade-off between ram and mechanical compression through the compressor. The maximum specific thrust increases with increasing compression ratio because the same stagnation conditions are achieved in the combustor at lower flight Mach numbers, hence reducing the momentum drag term and increasing the specific thrust.

The limits corresponding to condensation and pre-ignition conditions are illus-

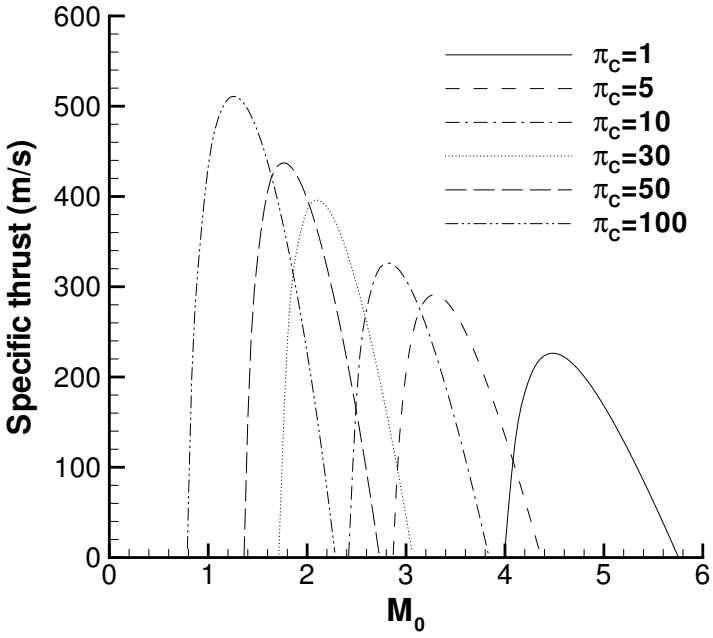

Figure 3.15: Influence of compression ratio π_c on the specific thrust of the turbodet. $T_0 = 223$ K, $P_0 = 0.261$ atm, $q_f = 45$ MJ/kg, $T_{max} = 1700$ K.

trated for one case, corresponding to a compression ratio of 30, on Fig. 3.13 for hydrogen and JP10. Hydrogen can be used for $1.75 < M_0 < 2.6$, and JP10 for $2.2 < M_0 < 2.3$ using the condensation temperature criterion, or $2 < M_0 < 2.3$ using vapor pressure considerations. The TSFC of the turbojet, Fig. 3.14, is about 0.9 kg/N.hr and does not vary much with M_0. The TSFC of the turbodet is higher at all Mach numbers and peaks at low values of the thrust-producing range because the specific thrust vanishes. The thermal efficiency of the turbojet, in Fig. 3.14, increases with the flight Mach number due to the higher efficiency of heat addition at higher stagnation conditions but already has a high value at zero Mach number due to the compression work. The thermal efficiency of the turbodet increases with M_0 but has a lower value than that of the turbojet. The overall efficiency behaves the same way.

Cell width estimates corresponding to the flight conditions are shown in Fig. 3.16. The cell widths obtained are very large due to the low fuel input of a temperature-limited turbodet engine. The scaled cell widths are less than 1 m only for $M_0 > 2.8$. However, the static temperature upstream of the detonation T_4 is already higher than

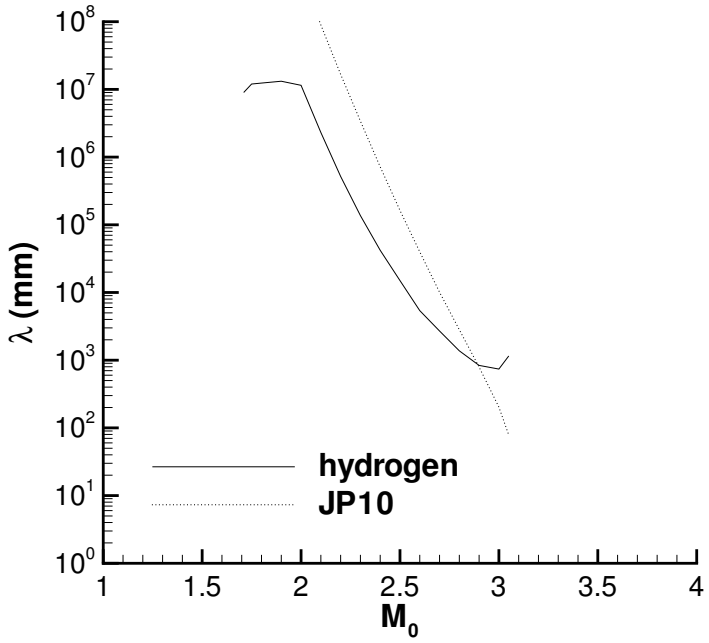

Figure 3.16: Cell width λ versus flight Mach number M_0 for a turbodet operating with hydrogen and JP10. $\pi_c = 30$, $T_0 = 223$ K, $P_0 = 0.261$ atm, $T_{max} = 1700$ K.

the auto-ignition temperature of the mixture for this case for both hydrogen and JP10. Consequently, there is no useful range of Mach numbers for practical applications of the turbodet engine.

3.5 Thermodynamic cycle analysis

An alternative approach to performance calculation for steady propulsion devices is thermodynamic cycle analysis (Section 1.2.4). The thermodynamic cycle for the ramjet and the dramjet is illustrated in Fig. 3.17 in the pressure-specific volume and temperature-entropy planes. The ideal ramjet cycle consists of isentropic ram compression from state 0 to state 4, then constant pressure combustion from state 4 to state 5, and isentropic expansion from state 5 to state 9. The dramjet cycle consists of isentropic compression from state 0' to state 4', detonation from state 4' to state 5', and isentropic expansion to state 9'. The detonation process is represented in Fig. 3.17 by a dashed line, meaning that the process actually corresponds to a jump

from state 4' to state 5'. Both cycles are closed by an imaginary constant pressure process through which heat is removed from the exhaust flow to the surroundings until the fluid element is back to its initial thermodynamic state. Details about how to compute the thermodynamic cycle using more realistic thermochemical properties and efficiencies are given in the appendix.

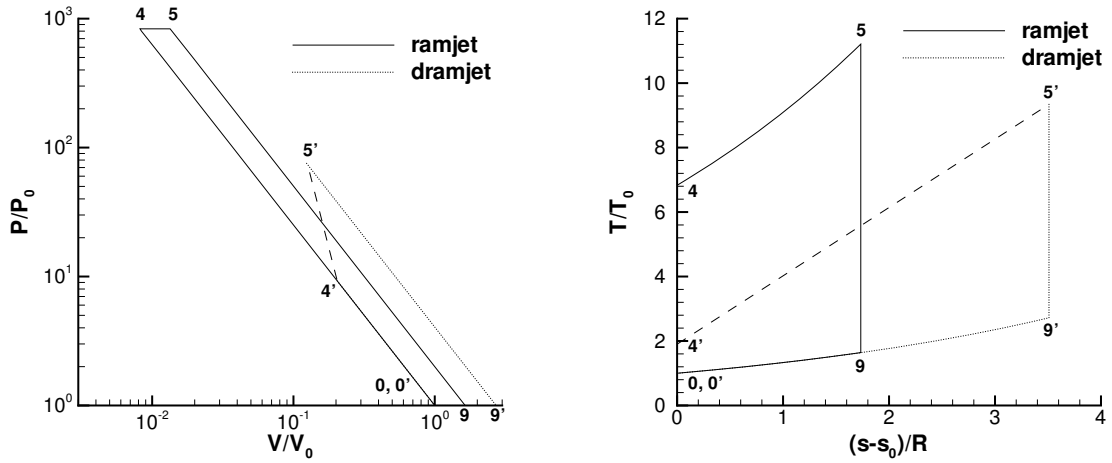

Figure 3.17: Ideal thermodynamic cycle of the ramjet and the dramjet in the (P,V) and (T,s) planes. T_0 = 223 K, P_0 = 0.261 atm, M_0 = 5.4, T_{max} = 2500 K. Primes denote states corresponding to the dramjet case.

Figure 3.18 shows the thermodynamic cycles for the turbojet and the turbodet at the same initial conditions. The turbojet cycle consists of isentropic ram compression from state 0 to 2, isentropic compression due to the compressor from state 2 to 4, constant pressure combustion from 4 to 5, and then isentropic expansion through the turbine from 5 to 8 and through the exit nozzle from 8 to 9. The turbodet cycle is identical to the turbojet cycle from state 0' to 3', but includes an isentropic expansion to the CJ velocity from state 3' to 4', detonation from 4' to 5', isentropic flow deceleration before the turbine from 5' to 6', and then isentropic expansion through the turbine from 6' to 8' and through the exit nozzle from 8' to 9'.

The performance of steady detonation engines has been calculated so far by conducting a flow path analysis, which is based on an open-system control volume analysis that includes the kinetic energy terms associated with the gas motion. The require-

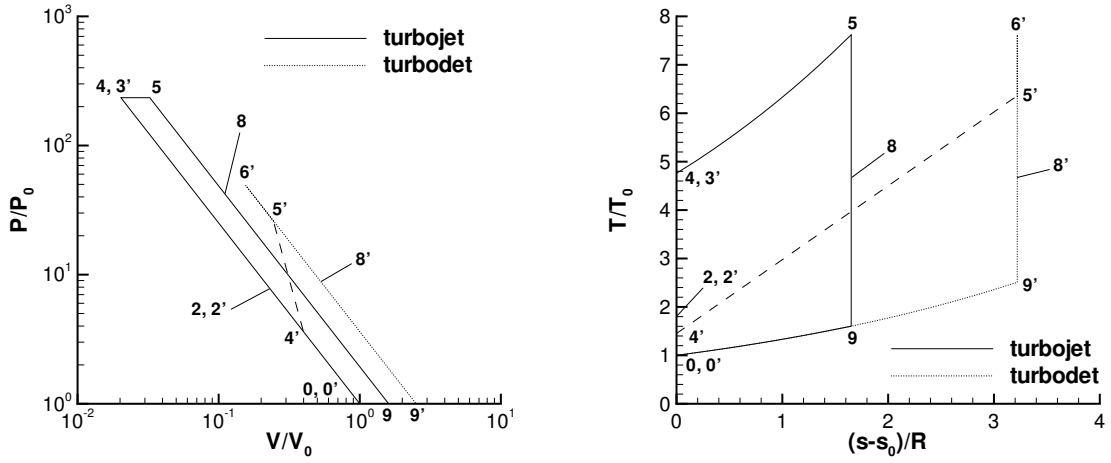

Figure 3.18: Ideal thermodynamic cycle of the turbojet and the turbodet in the (P,V) and (T,s) planes. $T_0 = 223$ K, $P_0 = 0.261$ atm, $M_0 = 2$, $T_{max} = 1700$ K. Primes denote states corresponding to the dramjet case.

ment of a steady detonation process is manifested as the detonation stabilization condition, which, in turn, requires supersonic flow ahead of the detonation wave and (sub)sonic flow behind the detonation wave. However, it is also possible to consider the thermodynamic cycle associated with the detonation process in an engine (Heiser and Pratt, 2002), and to compute the performance based on a notional thermodynamic efficiency of an idealized cycle. The relationship between the flow path analysis and the thermodynamic cycle analysis has been presented in Section 1.2.4.

We can calculate the thermal efficiency directly based on thermodynamic cycle analysis for the dramjet cycle

$$\eta_{th} = 1 - \frac{C_p T_0}{f q_f} \left[\frac{1}{M_{CJ}^2} \left(\frac{1+\gamma M_{CJ}^2}{1+\gamma} \right)^{\frac{\gamma+1}{\gamma}} - 1 \right] , \tag{3.9}$$

which is the exact expression obtained by Heiser and Pratt (2002) when analyzing the detonation cycle. The propulsion performance can be obtained from the thermal efficiency using the entropy method (Eq. 1.83). This is precisely the approach followed by Heiser and Pratt (2002), who proposed that this would apply to pulse detonation engines. In fact, careful examination of their paper shows that it is entirely based

on steady concepts and their formal results are identical to the results of the steady cycle analysis presented above. Although our analysis formally agrees with theirs, our performance predictions (0–1900 s for the dramjet specific impulse) differ dramatically[1] from the values of 3000–5000 s quoted in Heiser and Pratt (2002). This is due to the fact that for a steady-flow engine, the conditions upstream of the detonation wave (state 4) are dictated by the requirements for detonation stabilization. These conditions depend upon the freestream stagnation conditions and the energy release through the wave (Eq. 3.2). On the other hand, the conditions that Heiser and Pratt selected correspond to idealized low-speed combustor inlet conditions of zero velocity for pulsed combustion. Thermodynamic cycle analysis has to account for the fluid mechanics of the specific combustion process in the selection of the possible thermodynamic states.

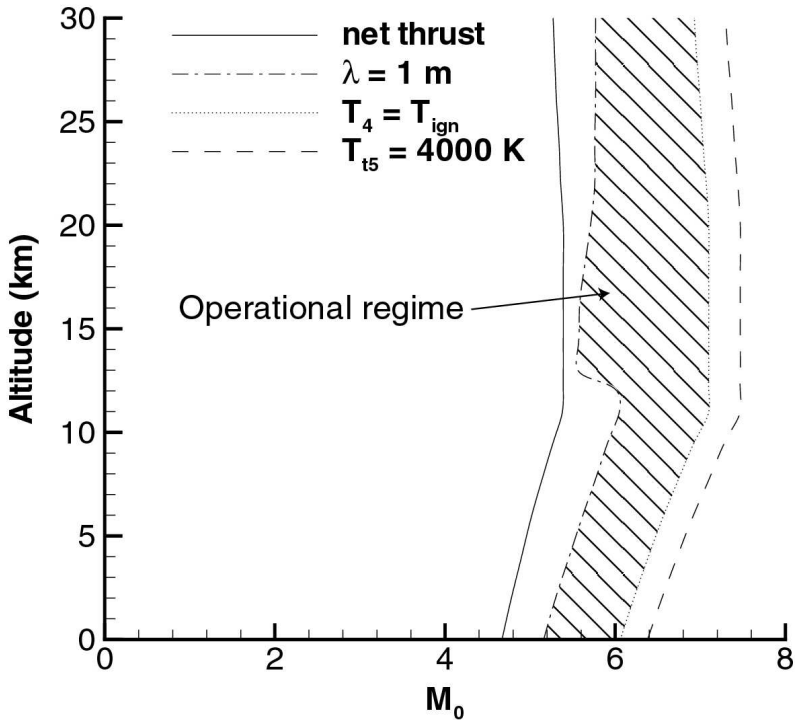

Figure 3.19: Altitude-Mach number diagram for a hydrogen-fueled dramjet. $\phi = 0.4$. The various limitations associated with net thrust production, cell sizes, hydrogen-air auto-ignition, and a very optimistic maximum temperature condition are given.

[1]The reader is referred to our discussion of the analysis of Heiser and Pratt (2002) in Wintenberger et al. (2004).

In our analysis, we find that the performance of the steady detonation-based cycles is always poorer than the Brayton cycle (ramjet or turbojet) and it requires very high compressor pressure ratios (100) to obtain net thrust at flight Mach numbers less than 1. We also find that the thermal efficiency drops off very sharply towards zero as the limiting flight Mach number (associated with the detonation stabilization limit) is reached. We define here the limiting flight Mach number as the lowest Mach number at which net thrust is produced. It does not necessarily correspond to the minimum freestream Mach number for detonation stabilization because at Mach numbers close to their minimum value for stabilization, the momentum drag term in the thrust equation is greater than the thrust term due to the total pressure loss across the detonation, and no net thrust is generated. The limiting flight Mach number is a function of the freestream total enthalpy and the amount of fuel injected. Detonations can, in theory, be stabilized at low supersonic freestream Mach numbers as long as the amount of fuel injected is reduced. However, there are two limitations with this idea: the first one is the limiting flight Mach number for net thrust generation, i.e., if too little fuel is injected, then no thrust is produced. The second and stricter limitation is due to the increase in the cell size of the mixture as the fuel-air mass ratio is decreased. This limitation defines another minimum flight Mach number, which is anticipated to vary with flight altitude due to the dependence of cell size on pressure. Other limitations associated with fuel-air auto-ignition and maximum temperature considerations place an upper bound on the possible design Mach numbers for a dramjet. It is instructive to represent all of these limitations on an altitude-Mach number diagram, which corresponds to the flight envelope of a dramjet for a given fuel-air mass ratio. Figure 3.19 shows the diagram for a very lean hydrogen-air mixture. A very optimistic maximum temperature was selected because the same calculation with our previous maximum temperature of 2500 K did not result in any effective operating range. The operating range of the dramjet in this case is represented by the hatched region in Fig. 3.19.

3.6 Conclusions

The performance of steady detonation engines was estimated and compared with the ideal ramjet and turbojet models. A normal detonation wave ramjet does not appear as an attractive alternative to the conventional ramjet. The performance of the dramjet suffers from two problems: the stabilization of the detonation wave, which reduces the thrust-producing range (between $M_0 = 5$ and 7 for flight conditions at 10,000 m), and the drastic total pressure loss across a normal detonation wave. Moreover, the use of stabilized detonations imposes an additional set of constraints. Although limitations associated with pre-ignition have been pointed out before, this work considers for the first time issues associated with normal detonation stability in a duct, condensation of fuel or oxidizer upstream of the detonation, and characteristic detonation length scales. Additionally, unlike previous work, this analysis places a limitation on the total temperature at the combustor outlet. All these considerations strongly reduce the useful operating range of a dramjet, which is $5.6 < M_0 < 6$ for a hydrogen-fueled dramjet at a flight altitude of 10,000 m. Liquid hydrocarbon fuels such as JP10 have an even smaller range of application due to their lower auto-ignition temperature.

The concept of the detonation turbojet, considered here for the first time, suffers from the same drawbacks as the dramjet and generates thrust only for $1.75 < M_0 < 3.1$ at an altitude of 10,000 m for a compression ratio of 30. Moreover, if the various limitations associated with detonations are taken into account, it turns out that there is no Mach number for which a steady detonation can effectively be stabilized in a reasonable-size combustor without getting pre-ignition. This result may vary with the value of π_c, but it shows that the presence of a compressor and a turbine in the turbodet does not contribute to any performance gain over the dramjet. Finally, a thermodynamic cycle analysis of steady detonation engines shows that, unlike conventional air-breathing engines, their performance model has to explicitly take into account the fluid mechanics of the combustion process.

The implications of our analysis are that using a detonation wave in a steady

engine is not practical, but this clearly does not apply to the unsteady case. In fact, it suggests that unsteady detonation wave engines, such as the pulse detonation engine, are the only useful way to apply detonations to propulsion.

Chapter 4

Single-Cycle Pulse Detonation Tube Performance Modeling

4.1 Introduction

A key issue (Sterling et al., 1995, Bussing and Pappas, 1996, Bussing et al., 1997, Cambier and Tegner, 1998, Kailasanath, 2000) in evaluating pulse detonation engine (PDE) propulsion concepts is reliable estimates of the performance as a function of operating conditions and fuel types. A basic PDE consists of an inlet, a series of valves, a detonation tube (closed at one end and open at the other), and an exit nozzle. It is an unsteady device which uses a repetitive cycle to generate thrust. The engine goes through four major steps during one cycle: the filling of the device with a combustible mixture, the initiation[1] of the detonation near the closed end (thrust surface), the propagation of the detonation down the tube, and finally, the exhaust of the products into the atmosphere. A schematic of the cycle for the detonation tube alone is shown in Fig. 4.1. The pressure differential created by the detonation wave on the tube's thrust surface produces unsteady thrust. If the cycle is repeated at a constant frequency, typically 10 to 100 Hz, an average thrust useful for propulsion is generated.

The goal of the present study is to provide a simple predictive model for detona-

This chapter is based on work presented in Wintenberger et al. (2003).

[1]Initiation at the closed end of the tube is not an essential part of PDE operation but greatly simplifies the analysis and will be used throughout the present study. Zhdan et al. (1994) found that the impulse is essentially independent of the igniter location for prompt initiation.

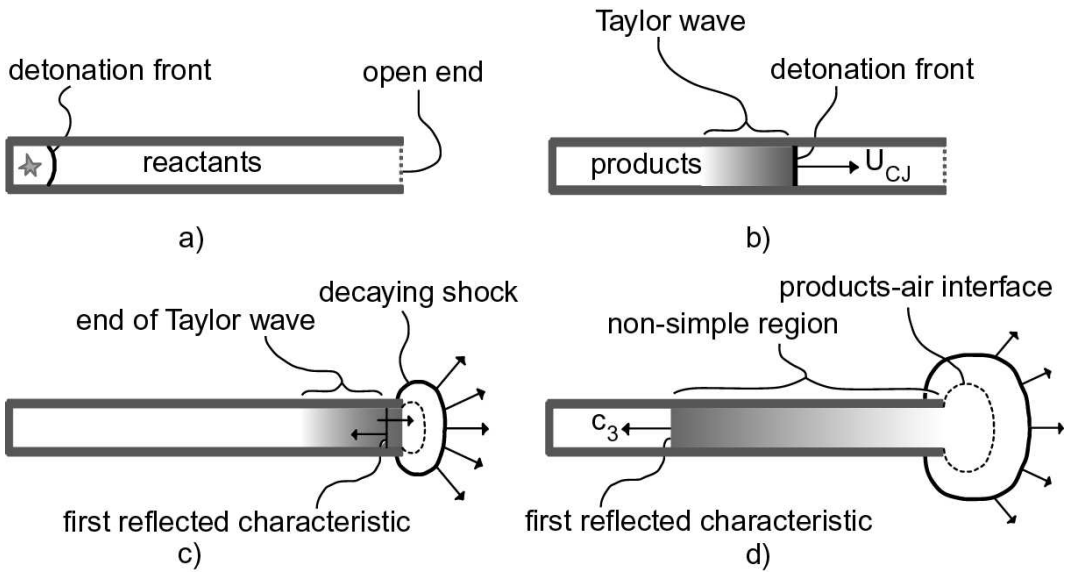

Figure 4.1: Pulse detonation engine cycle: a) The detonation is initiated at the thrust surface. b) The detonation, followed by the Taylor wave, propagates to the open end of the tube at a velocity U_{CJ}. c) An expansion wave is reflected at the mixture-air interface and immediately interacts with the Taylor wave while the products start to exhaust from the tube. d) The first characteristic of the reflected expansion reaches the thrust surface and decreases the pressure at the thrust surface.

tion tube thrust. In order to do that, we have to carry out a fully unsteady treatment of the flow processes within the tube. This is a very different situation from modeling conventional propulsion systems such as turbojets, ramjets, and rockets for which steady-state, steady-flow analyses define performance standards. In those conventional systems, thermodynamic cycle analyses are used to derive simple but realistic upper bounds for thrust, thrust-specific fuel consumption, and other performance figures of merit. Due to the intrinsically unsteady nature of the PDE, the analogous thermodynamic bounds on performance have been elusive.

Unlike some previous (Bussing and Pappas, 1996) and contemporary (Heiser and Pratt, 2002) analyses, we do not attempt to replace the unsteady PDE cycle with a fictitious steady-state, steady-flow cycle. Although these analyses are purported to provide an ideal or upper bound for performance, we find that these bounds are so broad that they are unsuitable for making realistic performance estimates for simple

devices like a detonation tube[2]. This becomes clear when comparing the predicted upper bound values of 2800–3600 s (Heiser and Pratt, 2002) or 4000 s (Bussing et al., 1997) for the fuel-based specific impulse of typical stoichiometric hydrocarbon-air mixtures with the measured values of about 2000 s obtained in detonation tube experiments (Zitoun and Desbordes, 1999, Zhdan et al., 1994, Cooper et al., 2002, Harris et al., 2001). Instead, the present model focuses on the gas dynamic processes in the detonation tube during one cycle. The model is based on a physical description of the flow inside the tube and uses elementary one-dimensional gas dynamics and dimensional analysis of experimental observations. The model computes the impulse delivered during one cycle of operation as the integral of the thrust during one cycle.

It is critical to gain understanding of the single-cycle impulse of a detonation tube before more complex engine configurations are considered. There have been a number of efforts to develop a gas dynamics-based model for single-cycle operation of detonation tubes. The pioneering work on single-cycle impulse was in 1957 by Nicholls et al. (1958) who proposed a very simplified model for the impulse delivered during one cycle. Only the contribution of the constant pressure portion at the thrust surface was considered and the contribution of the pressure decay period was neglected. Consequently, their model predictions are about 20% lower than the results of our model presented here and the values obtained from modern experiments.

Zitoun and Desbordes (1999) proposed a model for the single-cycle impulse and compared this to their experimentally measured data. They showed predictions for stoichiometric mixtures of ethylene, hydrogen and acetylene with oxygen and air. The models of Nicholls et al. (1958), Zitoun and Desbordes (1999), and the more recent work of Endo and Fujiwara (2002) have many features in common with the present model since they are all based on a simple gas dynamic description of the flow field. Zhdan et al. (1994) used both numerical simulations and simple analytical models based on the results of Stanyukovich (1960) to predict the impulse for tubes completely and partially filled with a combustible mixture.

[2]The reader is referred to our discussion of the analysis of Heiser and Pratt (2002) in Wintenberger et al. (2004).

In addition to analytical models, numerous numerical simulations have investigated various aspects of PDEs. Early studies, reviewed by Kailasanath et al. (2001), gave disparate and often contradictory values for performance parameters. Kailasanath (2000) identified how the issue of outflow boundary conditions can account for some of these discrepancies. With the recognition of this issue and the availability of high-quality experimental data, there is now substantial agreement (Kailasanath, 2002) between careful numerical simulation and experimental data, at least in the case of ethylene-air mixtures. However, even with improvements in numerical capability, it is desirable to develop simple analytical methods that can be used to rapidly and reliably estimate the impulse delivered by a detonation tube during one cycle in order to predict trends and to better understand the influence of fuel type, initial conditions, and tube size without conducting a large number of numerical simulations.

An end-to-end performance analysis of a pulse detonation engine has to take into account the behavior of the inlet, the valves, the combustor, and the exit nozzle. However, the ideal performance is mainly dictated by the thrust generation in the detonation tube. In developing our model, we have considered the simplest configuration of a single-cycle detonation tube open at one end and closed at the other. We realize that there are significant issues (Bussing et al., 1997) associated with inlets, valves, exit nozzles, and multi-cycle operation that are not addressed in our approach. However, we are anticipating that our simple model can be incorporated into more elaborate models that will account for these features of actual engines and that the present model will provide a basis for realistic engine performance analysis.

This chapter is organized as follows. First, we describe the flow field for an ideal detonation propagating from the closed end of a tube towards the open end. We describe the essential features of the ideal detonation, the following expansion wave, and the relevant wave interactions. We present a simple numerical simulation illustrating these issues. Second, we formulate a method for approximating the impulse with a combination of analytical techniques and dimensional analysis. Third, the impulse model is validated by comparison with experimental data and numerical simulations.

Fourth, a scaling analysis is performed to study the dependency of the impulse on initial conditions and energy release in the mixture. Fifth, the impulse model is used to compute impulse for a range of fuels and initial conditions. The influence of fuel type, equivalence ratio, initial pressure, and initial temperature are examined in a series of parametric computations.

4.2 Flow field associated with an ideal detonation in a tube

The gas dynamic processes that occur during a single cycle of a PDE can be summarized as follows. A detonation wave is directly initiated and propagates from the thrust surface towards the open end. For the purposes of formulating our simple model, we consider ideal detonations described as discontinuities propagating at the Chapman-Jouguet (CJ) velocity. The detonation front is immediately followed by a self-similar expansion wave (Zel'dovich, 1940a, Taylor, 1950) known as the Taylor wave and described in Section 1.1.4. This expansion wave decreases the pressure and brings the flow to rest. The method of characteristics (Taylor, 1950, Zel'dovich, 1940a) can be used to calculate flow properties within the Taylor wave (see Eqs. 1.42, 1.41, 1.43 in the following section).

There is a stagnant region extending from the rear of the Taylor wave to the closed end of the tube. When the detonation reaches the open end of the tube, a shock is generated and diffracts out into the surrounding air. Because the pressure at the tube exit is higher than ambient, the transmitted shock continues to expand outside of the tube. Since the flow at the tube exit is subsonic, a reflected wave propagates back into the tube. This reflected wave is usually an expansion wave, which reflects from the closed end, reducing the pressure and creating an expansion wave that propagates back towards the open end. After several sequences of wave propagation within the tube, the pressure inside approaches atmospheric. A simplified, but realistic model of the flow field can be developed by using classical analytical methods.

4.2.1 Ideal detonation and Taylor wave

To predict the ideal impulse performance of a pulsed detonation tube, we can consider the detonation as a discontinuity that propagates with a constant velocity (Section 1.1.1). This velocity is a function of the mixture composition and initial thermodynamic state. The reaction zone structure and the associated property variations such as the Von Neumann pressure spike are neglected in this model since the contribution of these features to the impulse is negligible.

The detonation speed is determined by the standard CJ model of a detonation that assumes that the flow just downstream of the detonation is moving at sonic velocity relative to the wave. This special downstream state, referred to as the CJ point, can be found by numerically solving the relations for mass, momentum, and energy conservation across the discontinuity while simultaneously determining the chemical composition. Equilibrium computations (Reynolds, 1986) based on realistic thermochemical properties and a mixture of the relevant gas species in reactants and products are used to calculate the chemical composition.

Alternatively, the conservation equations can be analytically solved for simple models, using an ideal gas equation of state, a fixed heat of reaction, and heat capacities that are independent of temperature. A widely used version of this model, described in Eqs. 1.8-1.14 (Thompson, 1988), uses different properties in the reactants and products, and a fixed value of the energy release, q, within the detonation wave. In the present study we use an even simpler version (Fickett and Davis, 2001), the one-γ model (Eqs. 1.15-1.19), which neglects the differences in specific heat and molar mass between reactants and products.

4.2.2 Interaction of the detonation with the open end

The flow behind a CJ detonation wave is subsonic relative to the tube and has a Mach number $M_2 = u_2/c_2$ of approximately 0.8 for typical hydrocarbon mixtures. Hence, when the detonation wave reaches the open end, a disturbance propagates back into the tube in the form of a reflected wave (Glass and Sislian, 1994). The

interface at the open end of the tube can be modeled in one dimension as a contact surface. When the detonation wave is incident on this contact surface, a transmitted wave will propagate out of the tube while a reflected wave propagates into the tube towards the thrust surface.

The reflected wave can be either a shock or an expansion wave. A simple way to determine the nature of the reflected wave is to use a pressure-velocity diagram (Glass and Sislian, 1994), as the pressure and velocity must be matched across the contact surface after the interaction. In the case of a detonation wave exiting into air, the transmitted wave will always be a shock wave; the locus of solutions (the shock adiabat) is shown in Figs. 4.2 and 4.3. The shock adiabat is computed from the shock jump conditions, which can be written in term of the pressure jump and velocity jump across the wave

$$\frac{\Delta u}{c_1} = \frac{\Delta P / P_1}{\gamma \left(1 + \frac{\gamma+1}{2\gamma}\frac{\Delta P}{P_1}\right)^{\frac{1}{2}}} \,. \tag{4.1}$$

The reflected wave initially propagates back into the products at the CJ state behind the detonation wave. The CJ states for various fuels and equivalence ratios appear in Figs. 4.2 and 4.3. If the CJ point is below the shock adiabat, the reflected wave must be a shock to increase the pressure to match that behind the transmitted shock. Alternatively, if the CJ state is above the shock adiabat, the reflected wave must be an expansion in order to decrease the pressure to match that behind the transmitted shock.

Hydrocarbon fuels all produce a reflected expansion wave at the tube's open end for any stoichiometry. However, a reflected shock is obtained for hydrogen-oxygen at an equivalence ratio $\phi > 0.8$ (Fig. 4.2) and for very rich hydrogen-air mixtures with $\phi > 2.2$ (Fig. 4.3).

Ultimately, following the initial interaction of the detonation wave with the contact surface, the pressure at the exit of the tube will drop as the transmitted shock wave propagates outward. In all cases, since the flow outside the tube is expanding radially

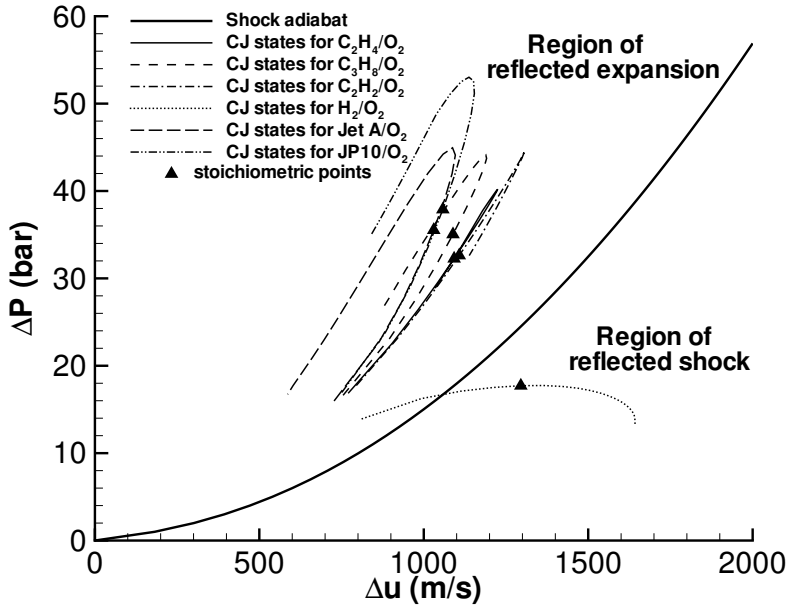

Figure 4.2: Pressure-velocity diagram used to compute wave interactions at the tube open end for fuel-oxygen mixtures.

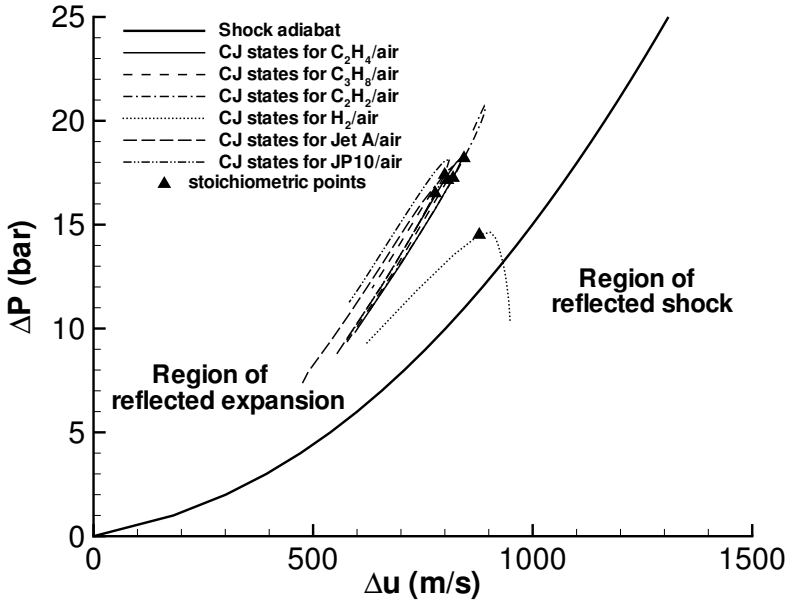

Figure 4.3: Pressure-velocity diagram used to compute wave interactions at the tube open end for fuel-air mixtures.

behind the diffracting shock wave, an expansion wave also exists in the flow external to the tube. The flow in this region can not be modeled as one-dimensional. A numerical simulation (discussed below) is used to illustrate this portion of the flow.

4.2.3 Waves and space-time diagram

A space-time (x–t) diagram, shown in Fig. 4.4, is used to present the important features of the flow inside the tube. The x–t diagram displays the detonation wave propagating at the CJ velocity U_{CJ} followed by the Taylor wave. The first characteristic $\hat{C}^-$ of the wave reflected from the mixture-air interface at the open end of the tube is also shown. The initial slope of this characteristic is determined by the conditions at the mixture-air interface and is then modified by interaction with the Taylor wave. After passing through the Taylor wave, the characteristic $\hat{C}^-$ propagates at the sound speed c_3. The region lying behind this first characteristic is non-simple because of the interaction between the reflected expansion wave and the Taylor wave. Two characteristic times can be defined: t_1 corresponding to the interaction of the detonation wave with the open end, and t_2 corresponding to the time necessary for the characteristic $\hat{C}^-$ to reach the thrust surface. The diffracted shock wave in Fig. 4.4 is shown outside the tube as a single trajectory; however, this is actually a three-dimensional wavefront that can not be fully represented on this simple plot.

4.2.4 A numerical simulation example

In order to further examine the issues related to the interaction of the detonation with the open end of the tube, the flow was investigated numerically (Hornung, 2000) using Amrita (Quirk, 1998). The Taylor wave similarity solution (Zel'dovich, 1940a, Taylor, 1950) was used as an initial condition, assuming the detonation has just reached the open end of the tube when the simulation is started. This solution was calculated using a one-γ model for detonations (Fickett and Davis, 2001, Thompson, 1988) for a non-dimensional energy release $q/RT_1 = 40$ across the detonation and $\gamma = 1.2$ for reactants and products. The corresponding CJ parameters are $M_{CJ} = 5.6$ and

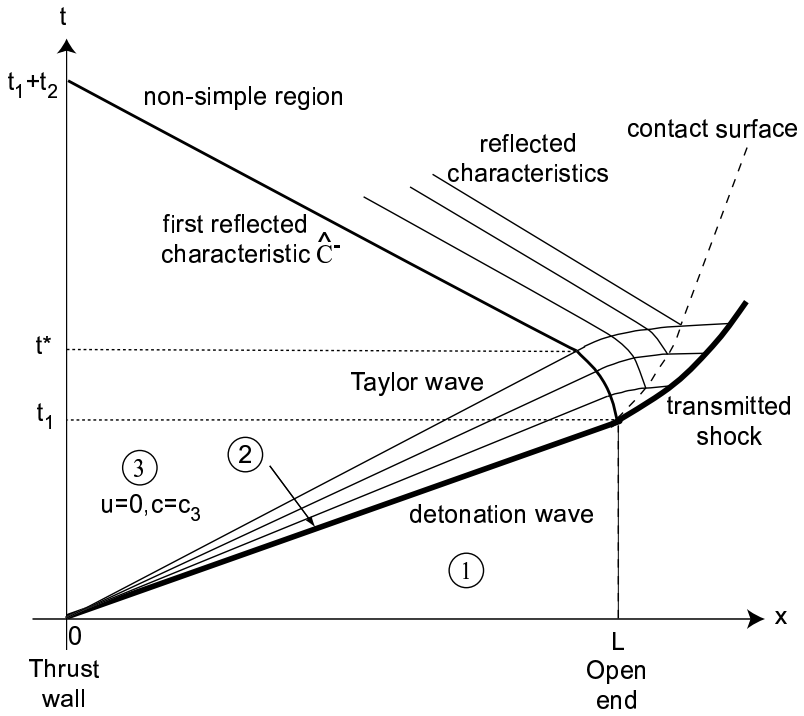

Figure 4.4: Space-time diagram for detonation wave propagation and interaction with the tube open end.

$P_{CJ}/P_1 = 17.5$, values representative of stoichiometric hydrocarbon-air mixtures.

The initial pressure P_1 ahead of the detonation wave was taken to be equal to the pressure P_0 outside the detonation tube. The simulation solved the non-reactive Euler equations using a Kappa-MUSCL-HLLE solver in the two-dimensional (cylindrical symmetry) computational domain consisting of a tube of length L closed at the left end and open to a half-space at the right end. Numerical schlieren images are displayed in Fig. 4.5, and the corresponding pressure and horizontal velocity profiles along the tube centerline are shown on Figs. 4.6 and 4.7, respectively. Only one-half of the tube is shown in Fig. 4.5; the lower boundary is the axis of symmetry of the cylindrical detonation tube. The times given on these figures account for the initial detonation travel from the closed end to the open end of the tube, so that the first frame of Figs. 4.5, 4.6, and 4.7 corresponds to a time $t_1 = L/U_{CJ}$.

The first frame in Figs. 4.5, 4.6, and 4.7 shows the initial condition with the pressure decreasing behind the detonation front from the CJ pressure P_2 to a value

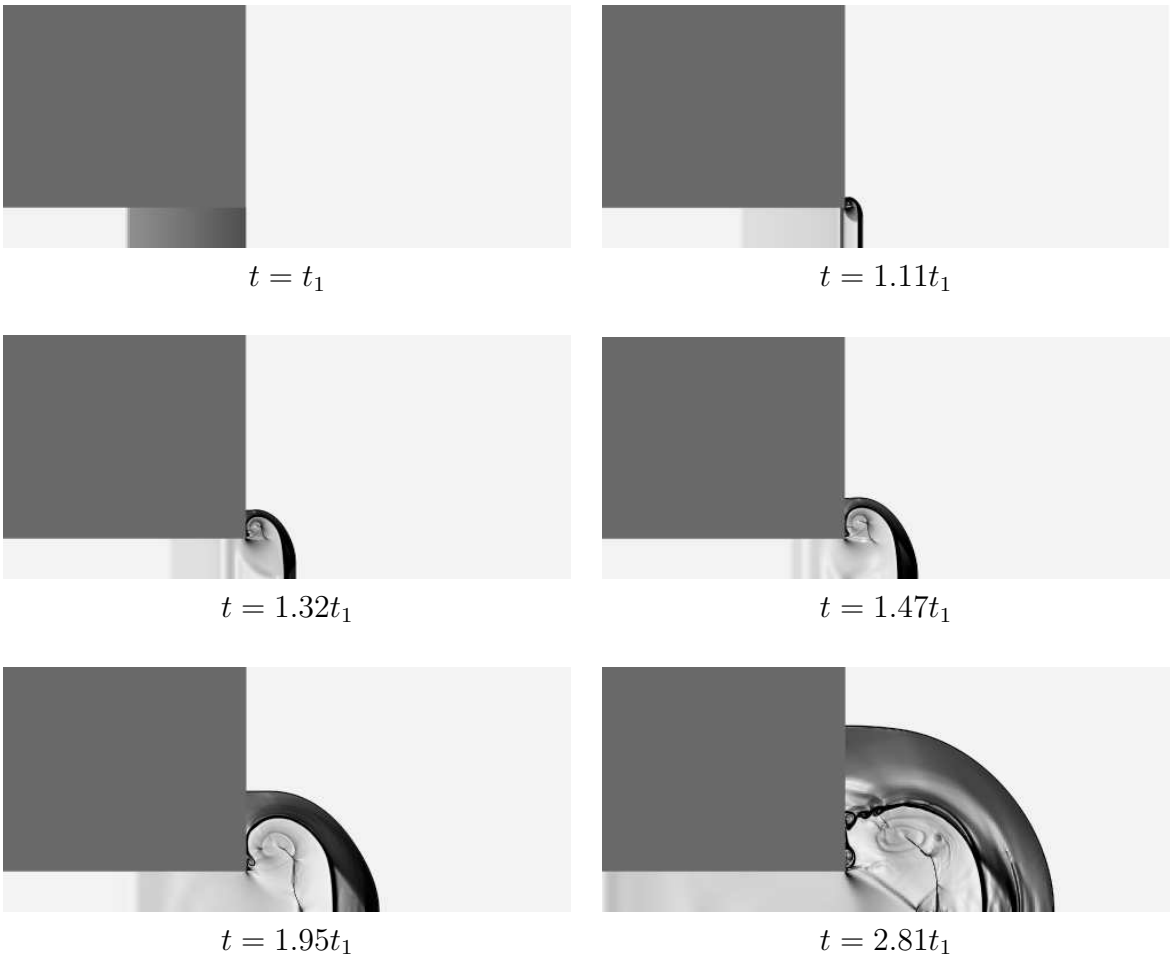

Figure 4.5: Numerical schlieren images of the exhaust process.

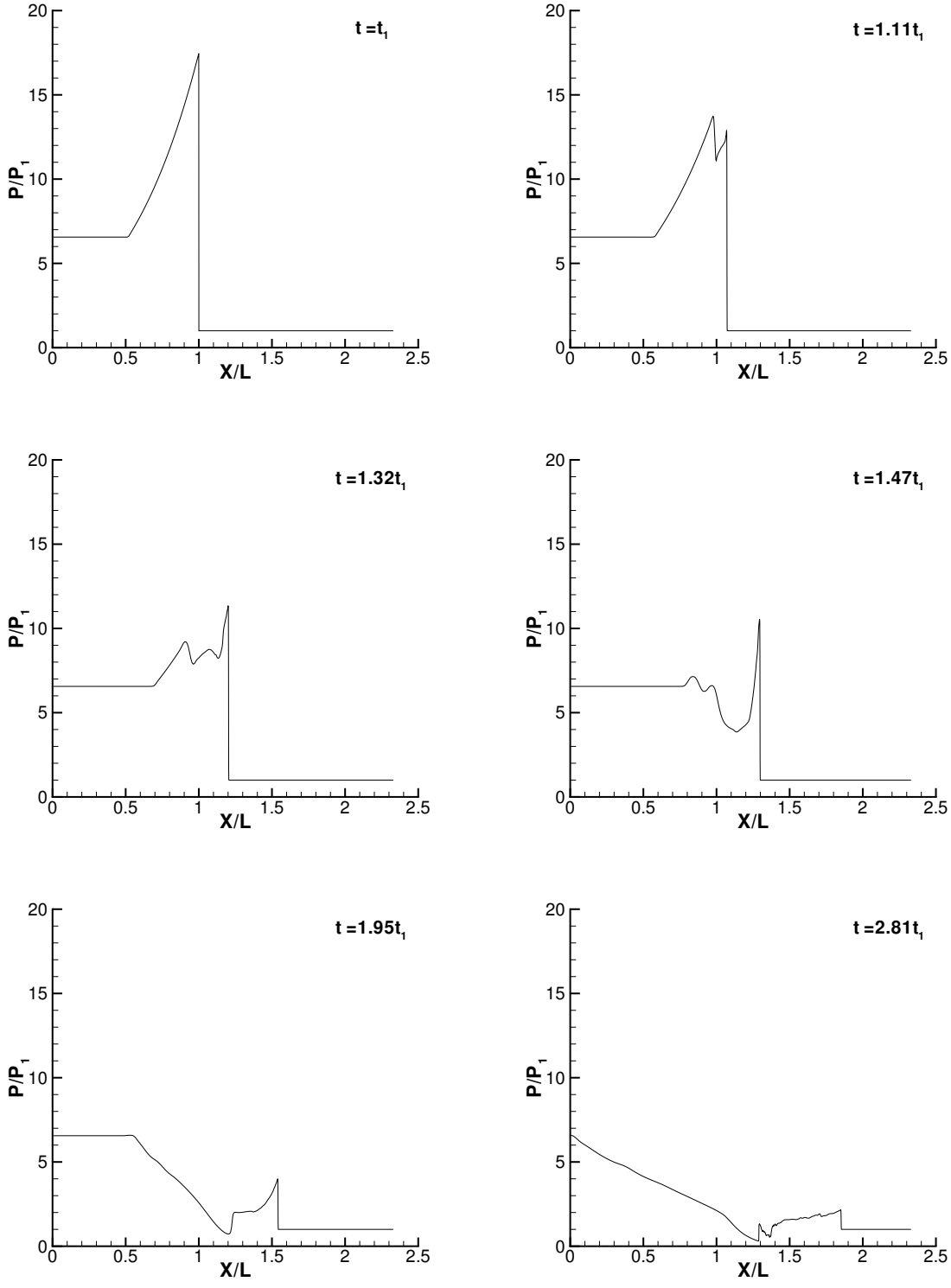

Figure 4.6: Pressure along the tube centerline from numerical simulation. P_1 is the initial pressure inside and outside the tube.

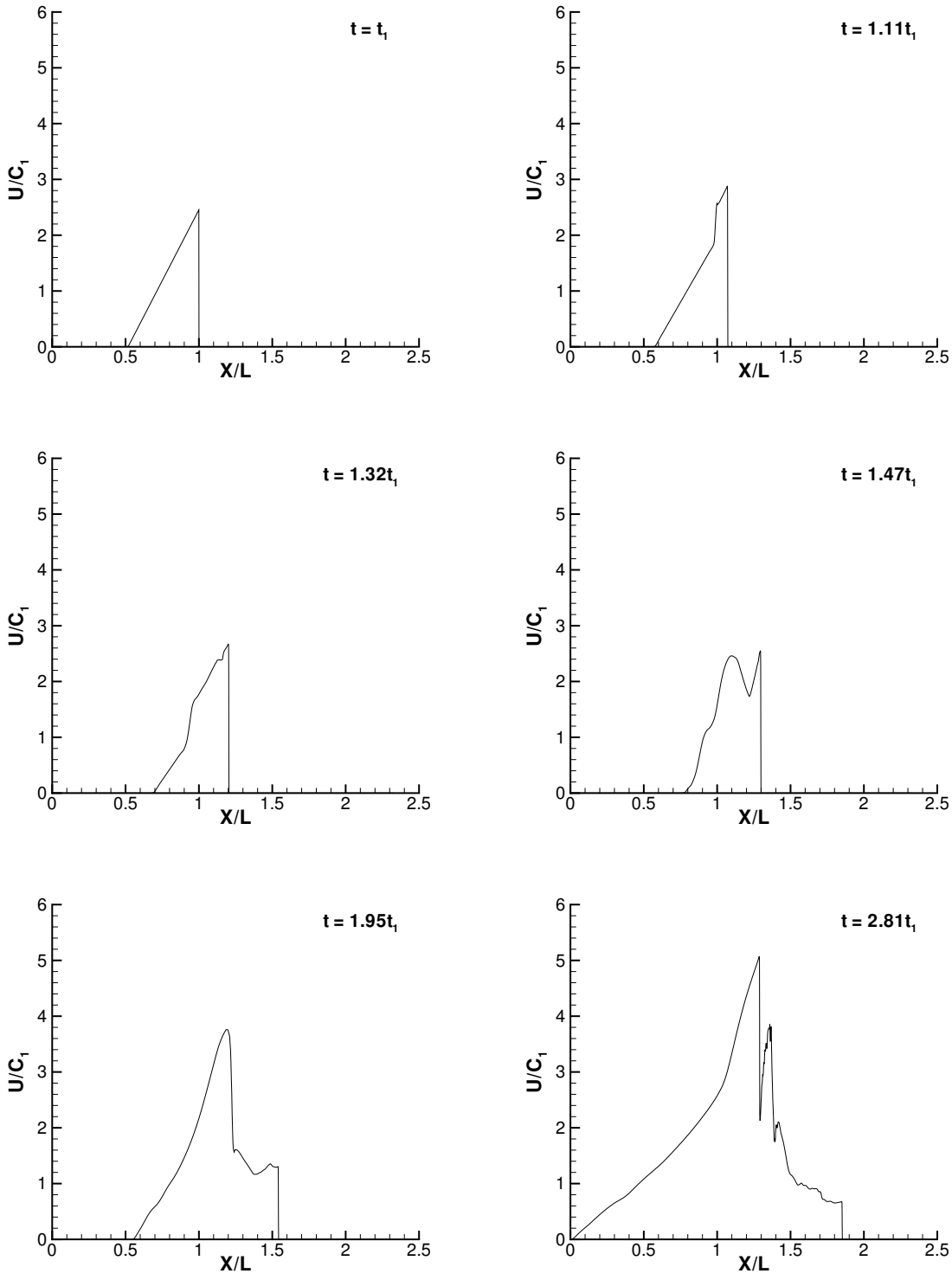

Figure 4.7: Velocity along the tube centerline from numerical simulation. c_1 is the initial sound speed inside and outside the tube.

P_3 at the end of the Taylor wave. The detonation wave becomes a decaying shock as it exits the tube since the region external to the tube is non-reactive, simulating the surrounding atmosphere of most experimental configurations.

This decaying shock is initially planar but is affected by the expansions originating from the corners of the tube and gradually becomes spherical. The pressure profiles show the decay of the pressure behind the leading shock front with time. A very complex flow structure, involving vortices and secondary shocks, forms behind the leading shock. The fluid just outside the tube accelerates due to the expansion waves coming from the corners of the tube. At the same time the leading shock front exits the tube, a reflected expansion wave is generated and propagates back into the tube, interacting with the Taylor wave. This reflected wave propagates until it reaches the closed end of the tube, decreasing the pressure and accelerating the fluid towards the open end. The exhaust process is characterized by low pressure and high flow velocity downstream of the tube exit. A system of quasi-steady shocks similar to those observed in steady underexpanded supersonic jets, and an unsteady leading shock wave, bring the flow back to atmospheric pressure.

One of the most important points learned from this simulation is that the flow inside the tube is one-dimensional except for within one-to-two diameters of the open end. Another is that the pressure at the open end is unsteady, initially much higher than ambient pressure, and decreasing at intermediate times to lower than ambient before finally reaching equilibrium. Despite the one-dimensional nature of the flow within the tube, it is important to properly simulate the multi-dimensional flow in the vicinity of the exit in order to get a realistic representation of the exhaust process. In our simple model, this is accomplished by using a non-dimensional correlation of the experimental data for this portion of the process.

The normalized pressure P/P_1 at the thrust surface as well as the normalized impulse per unit volume $I_V U_{CJ}/P_1$ are shown as a function of normalized time t/t_1 in Fig. 4.8. The impulse per unit volume was computed by integrating the pressure at the thrust surface over time. Note that these plots take into account the initial detonation travel from the closed end to the open end of the tube. The pressure at

the thrust surface remains constant until the reflected wave from the tube's open end reaches the thrust surface at time $t_1 + t_2 \approx 2.81t_1$. The final pressure decay process is characterized by a steep pressure decrease and a region of sub-atmospheric pressure. The integrated impulse consequently increases to a maximum before decreasing due to this region of negative overpressure.

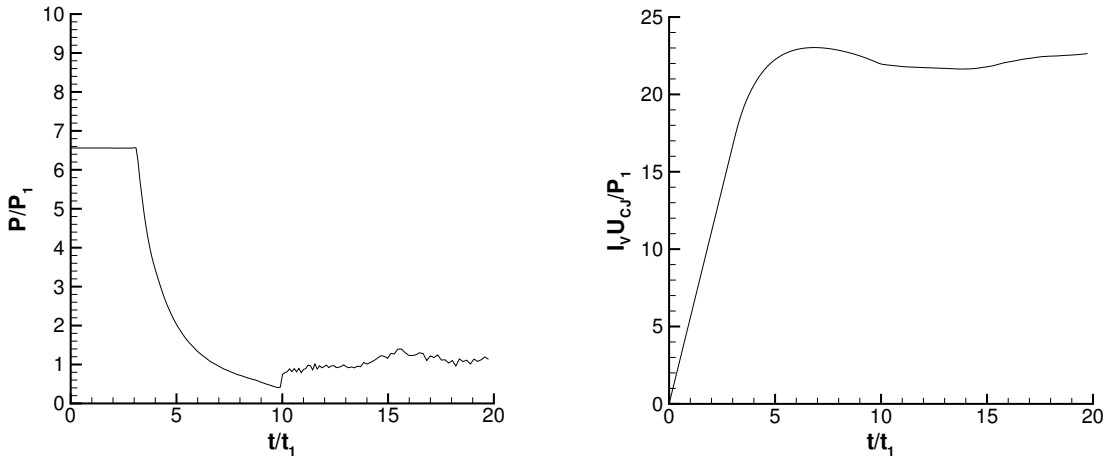

Figure 4.8: Non-dimensionalized thrust surface pressure and impulse per unit volume as a function of non-dimensionalized time for the numerical simulation.

4.3 Impulse model

Our impulse model is based on elementary gas dynamic considerations. We assume one-dimensional, adiabatic flow in a straight unobstructed tube closed at one end and open at the other. The impulse is calculated by considering a control volume around the straight tube as shown in Case (b) of Fig. 4.9. Case (a), which represents the usual control volume used for rocket engine analysis, requires the knowledge of the exit pressure P_e, the exhaust velocity u_e and exhaust density ρ_e (or mass flow rate). Case (b), the control volume considered in the model, requires only the knowledge of the pressure history at the thrust surface. The impulse is obtained by integrating the pressure differential $P_3 - P_0$ across the thrust surface during one cycle, assuming $P_e = P_0$. This approach is rather limited and is certainly not applicable to air-

breathing engines with complex inlets and/or exits. However, it is appropriate for a single tube of constant area and the modeling assumptions eliminate the need for numerical simulations or detailed flow measurements required to evaluate the thrust by integration over the flow properties at the exit plane.

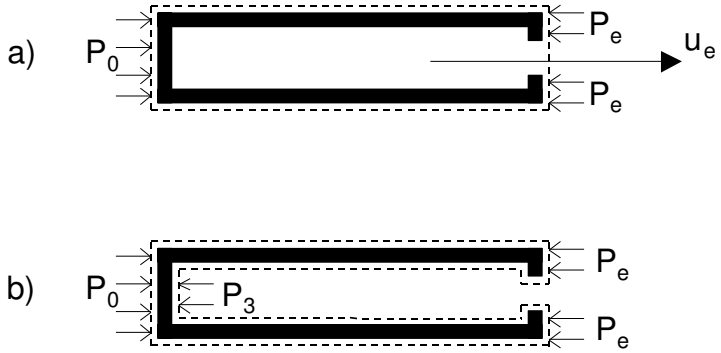

Figure 4.9: Control volumes a) typically used in rocket engine analysis b) used in our analysis.

We have made a number of other simplifying assumptions. Non-ideal effects such as viscosity or heat transfer are not considered. The detonation properties are calculated assuming the ideal one-dimensional CJ profile. Real-gas thermodynamics are used to calculate the CJ detonation properties, and classical gas dynamics for a perfect gas are used to model the flow behind the detonation wave. We assume direct instantaneous initiation of planar detonations at the thrust surface. The effect of indirect initiation is discussed in Cooper et al. (2002) The model assumes that a reflected expansion wave is generated when the detonation wave reaches the open end, which is generally true, as discussed previously. The model is based on analytical calculations except for the modeling of the pressure decay period, which results from dimensional analysis and experimental observations.

4.3.1 Determination of the impulse

Under our model assumptions, the single-cycle impulse is generated by the pressure differential at the thrust surface. A typical experimental pressure history at the thrust surface recorded by Cooper et al. (2002) is given in Fig. 4.10. When the detonation is

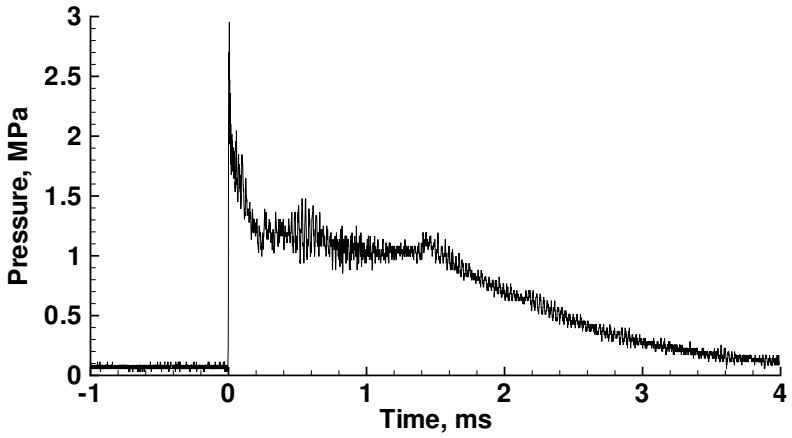

Figure 4.10: Sample pressure recorded at the thrust surface (Cooper et al., 2002) for a mixture of stoichiometric ethylene-oxygen at 1 bar and 300 K initial conditions.

initiated, the CJ pressure peak is observed before the pressure decreases to P_3 by the passage of the Taylor wave. The pressure at the thrust surface remains approximately constant until the first reflected characteristic reaches the thrust surface and the reflected expansion wave decreases the pressure. The pressure is decreased below atmospheric for a period of time before ultimately reaching the atmospheric value (Fig. 4.8).

For our modeling, the pressure-time trace at the thrust surface has been idealized (Fig. 4.11). The CJ pressure peak is considered to occur during a negligibly short time. The pressure stays constant for a total time $t_1 + t_2$ at pressure P_3. Then the pressure is affected by the reflected expansion and eventually decreases to the atmospheric value.

Using the control volume defined in Case (b) of Fig. 4.9, the single-cycle impulse is the integral of the pressure differential over the detonation tube cross-sectional area A,

$$I = A \int_0^\infty \Delta P(t)\, dt \quad , \tag{4.2}$$

where ignition is assumed to occur at $t = 0$. From the idealized pressure-time trace, the impulse can be decomposed into three terms

$$I = A \left[\Delta P_3\, t_1 + \Delta P_3\, t_2 + \int_{t_1+t_2}^\infty \Delta P(t)\, dt \right] . \tag{4.3}$$

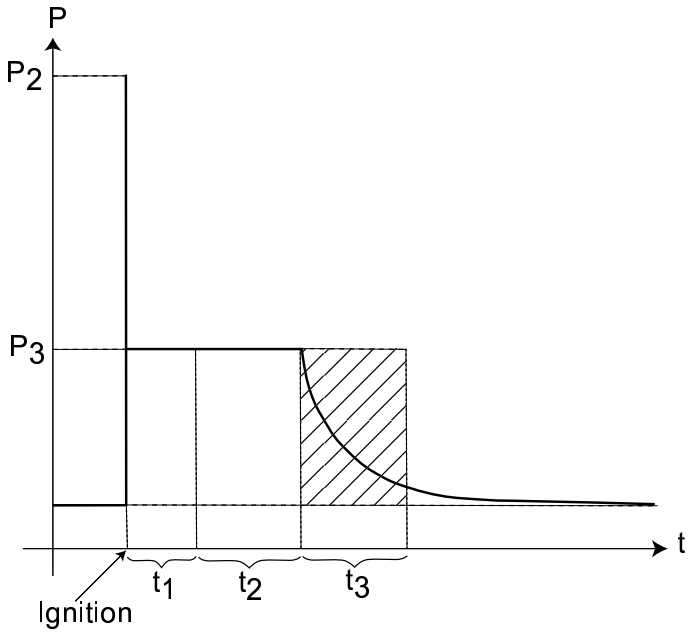

Figure 4.11: Idealized model of the thrust surface pressure history.

The first term on the right-hand side of Eq. 4.3 represents the contribution to the impulse associated with the detonation propagation during time $t_1 = L/U_{CJ}$, the second term is the contribution associated with the time t_2 required for expansion wave propagation from the open end to the thrust surface, and the third term is associated with the pressure decay period.

The time t_2 depends primarily on the length of the tube and the characteristic sound speed c_3 behind the expansion wave which suggests the introduction of a non-dimensional parameter α defined by

$$t_2 = \alpha L/c_3 \; . \tag{4.4}$$

Dimensional analysis will be used to model the third term on the right-hand side of Eq. 4.3. The inviscid, compressible flow equations can always be non-dimensionalized using reference parameters, which are a sound speed, a characteristic length, and a reference pressure. Thus, we non-dimensionalize our pressure integral in terms of c_3, L, and P_3

$$\int_{t_1+t_2}^{\infty} \Delta P(t)\, dt = \frac{\Delta P_3 L}{c_3} \int_{t_1'+t_2'}^{\infty} \Pi(t')\, dt' \; . \tag{4.5}$$

The non-dimensional integral on the right-hand side of Eq. 4.5 can depend only on the remaining non-dimensional parameters of the flow, which are the ratio of specific heats in the products γ, the pressure ratio between the constant pressure region and the initial pressure P_3/P_1, and the non-dimensional energy release during the detonation process q/RT_1. We will define the value of this integral to be β, which has a definite value for a given mixture

$$\beta(\gamma, P_3/P_1, q/RT_1) = \int_{t_1'+t_2'}^{\infty} \Pi(t')\, dt' \ . \tag{4.6}$$

For fuel-air detonations over a limited range of compositions close to stoichiometric, the parameters in Eq. 4.6 vary by only a modest amount and we will assume that β is approximately constant. This assumption is not crucial in our model and a more realistic expression for β can readily be obtained by numerical simulation. For the present purposes, this assumption is justified by the comparisons with the experimental data shown subsequently.

The dimensional integral on the left-hand side of Eq. 4.5 can be used to define a characteristic time t_3, which is related to β

$$\int_{t_1+t_2}^{\infty} \Delta P(t)\, dt = \Delta P_3\, t_3 = \Delta P_3 \beta \frac{L}{c_3} \ . \tag{4.7}$$

In Fig. 4.11, the time t_3 can be interpreted as the width of the hatched zone representing the equivalent area under the decaying part of the pressure-time trace for $t > t_1 + t_2$. The impulse of Eq. 4.3 can now be rewritten to include the non-dimensional parameters α and β

$$I = A\Delta P_3 \left[\frac{L}{U_{CJ}} + (\alpha + \beta)\frac{L}{c_3} \right] \ . \tag{4.8}$$

4.3.2 Determination of α

We have determined α by considering the interaction of the reflected wave and the Taylor wave. The method of characteristics is used to derive a similarity solution for the leading characteristic of the reflected expansion. This technique will also work

for reflected compressions as long as the waves are sufficiently weak.

The derivation of the expression for α begins by considering the network of characteristics within the Taylor wave, shown in Fig. 4.4. As in Section 1.1.4, we model the detonation products as a perfect gas with a constant value of the polytropic exponent γ. The Riemann invariant J^- is conserved along a C^- characteristic going through the Taylor wave

$$J^- = u_2 - \frac{2c_2}{\gamma - 1} = -\frac{2c_3}{\gamma - 1} = u - \frac{2c}{\gamma - 1} \; . \tag{4.9}$$

Inside the Taylor wave, the C^+ characteristics are straight lines with a slope given by $x/t = u + c$. Using the Riemann invariant J^- to relate u and c to the flow parameters in state 2, we find that

$$\frac{x}{c_2 t} = \frac{u + c}{c_2} = \frac{u_2}{c_2} + \frac{\gamma + 1}{\gamma - 1}\frac{c}{c_2} - \frac{2}{\gamma - 1} \; . \tag{4.10}$$

Considering the interaction of the reflected expansion wave with the Taylor wave, the slope of the first reflected characteristic $\hat{C}^-$ can be calculated as

$$\frac{dx}{dt} = u - c = \frac{x}{t} - 2c \; . \tag{4.11}$$

Substituting for x/t from Eq. 4.10, we find that

$$\frac{1}{c_2}\frac{dx}{dt} - \frac{2(\gamma - 1)}{\gamma + 1}\left[\frac{u_2}{c_2} - \frac{2}{\gamma - 1} + \frac{3 - \gamma}{2(\gamma - 1)}\frac{x}{c_2 t}\right] = 0 \; . \tag{4.12}$$

The form of Eq. 4.12 suggests the introduction of a similarity variable $\eta = x/c_2 t$. Making the change of variables, we obtain an ordinary differential equation for η

$$t\frac{d\eta}{dt} + \frac{2(\gamma - 1)}{\gamma + 1}\left[\eta - \frac{u_2}{c_2} + \frac{2}{\gamma - 1}\right] = 0 \; . \tag{4.13}$$

The solution to this equation is

$$\eta(t) = \frac{u_2}{c_2} - \frac{2}{\gamma - 1} + \frac{\gamma + 1}{\gamma - 1}\left(\frac{L}{U_{CJ} t}\right)^{\frac{2(\gamma-1)}{\gamma+1}} \; , \tag{4.14}$$

where we have used the initial condition $\eta(t_1) = U_{CJ}/c_2$. The last characteristic of the Taylor wave has a slope $x/t = c_3$. Hence, the first reflected characteristic exits the Taylor wave at time t^* determined by $\eta(t^*) = c_3/c_2$. Solving for t^*, we have

$$t^* = \frac{L}{U_{CJ}} \left[\left(\frac{\gamma - 1}{\gamma + 1} \right) \left(\frac{c_3 - u_2}{c_2} + \frac{2}{\gamma - 1} \right) \right]^{-\frac{\gamma+1}{2(\gamma-1)}} . \tag{4.15}$$

For $t^* < t < t_1 + t_2$, the characteristic $\hat{C}^-$ propagates at constant velocity equal to the sound speed c_3. From the geometry of the characteristic network shown in Fig. 4.4, $\hat{C}^-$ reaches the thrust surface at time $t_1 + t_2 = 2t^*$. Thus, $t_2 = 2t^* - t_1 = \alpha L/c_3$. Solving for α, we obtain

$$\alpha = \frac{c_3}{U_{CJ}} \left[2 \left(\frac{\gamma - 1}{\gamma + 1} \left[\frac{c_3 - u_2}{c_2} + \frac{2}{\gamma - 1} \right] \right)^{-\frac{\gamma+1}{2(\gamma-1)}} - 1 \right] . \tag{4.16}$$

The quantities involved in this expression essentially depend on two non-dimensional parameters: γ and the detonation Mach number $M_{CJ} = U_{CJ}/c_1$. These can either be computed numerically with realistic thermochemistry or else analytically using the ideal gas one-γ model for a CJ detonation (Section 1.1.1). Numerical evaluations of this expression for typical fuel-air detonations show that $\alpha \approx 1.1$ for a wide range of fuel and compositions. Using the one-γ model, the resulting expression for $\alpha(\gamma, M_{CJ})$ is

$$\frac{1}{2} \left(1 + \frac{1}{M_{CJ}^2} \right) \left(2 \left[\frac{\gamma - 1}{\gamma + 1} \left(\frac{\gamma + 3}{2} + \frac{2}{\gamma - 1} - \frac{(\gamma + 1)^2}{2} \quad \frac{M_{CJ}^2}{1 + \gamma M_{CJ}^2} \right) \right]^{-\frac{\gamma+1}{2(\gamma-1)}} - 1 \right) . \tag{4.17}$$

4.3.3 Determination of β

The region between the first reflected characteristic and the contact surface in Fig. 4.4 is a non-simple region created by the interaction of the reflected expansion wave with the Taylor wave. The multi-dimensional flow behind the diffracting shock front also plays a significant role in determining the pressure in this region. For these reasons,

it is impossible to derive an analytical solution for the parameter β. It is, however, possible to use experimental data and Eq. 4.6 to calculate β. We considered data from Zitoun and Desbordes (1999), who carried out detonation tube experiments and measured impulse using tubes of different lengths. They showed that the impulse scales with the length of the tube, as expected from Eq. 4.8.

Zitoun and Desbordes used an exploding wire to directly initiate detonations, which is representative of the idealized conditions of our model. They determined impulse for stoichiometric ethylene-oxygen mixtures by integrating the pressure differential at the thrust surface. The analysis of their pressure-time traces reveals that the overpressure, after being roughly constant for a certain period of time, decreases and becomes negative before returning to zero. The integration of the decaying part of the pressure-time trace was carried out up to a time late enough (typically greater than $20t_1$) to ensure that the overpressure has returned to zero. This integration gave a value of $\beta = 0.53$.

4.3.4 Determination of P_3 and c_3

The properties in the stagnant region near the closed end of the tube are determined by the gas expansion in the Taylor wave following the detonation front. This expansion is modeled analytically in Section 1.1.4 for the ideal case of a perfect gas with a constant value of γ. However, the value of γ in a dissociating gas is not unique and changes with temperature and composition.

In the classical thermodynamic model of detonation, the speed of sound behind the detonation front c_2 is the equilibrium speed of sound, computed as

$$c_{eq}^2 = \left(\frac{\partial P}{\partial \rho}\right)_{s,Y_i=Y_i^{eq}} \tag{4.18}$$

where the superscript eq means that the derivative is taken at conditions of chemical equilibrium. As the state variable ρ is varied, the composition also changes so that the mixture of species remains in chemical equilibrium. This is what standard thermochemical programs such as STANJAN (Reynolds, 1986) use to compute the

CJ state. The equilibrium speed of sound is distinct from the frozen speed of sound, which is defined by differentiating for fixed species amounts.

$$c_{fr}^2 = \left(\frac{\partial P}{\partial \rho}\right)_{s,Y_i} \tag{4.19}$$

The frozen speed of sound is always higher than the equilibrium speed of sound and the two are related by the equilibrium constraints and thermodynamic properties of the species (Fickett and Davis, 2001).

Two distinct values of γ can be calculated from the frozen and equilibrium speeds of sound by writing $\gamma = \rho c^2/P$. The frozen γ_{fr} is also the ratio of the specific heats. The value of γ_{eq} is smaller than γ_{fr} by an amount that depends on the degree of dissociation in the gas and the Gibbs energy associated with the dissociation and recombination reactions. The differences between γ_{fr} and γ_{eq} are much more significant for high-temperature, low-pressure mixtures of detonation products of fuel-oxygen mixtures used in laboratory experiments than for fuel-air mixtures at high pressure used in engine combustors. Both γ_{fr} and γ_{eq} are functions of the thermodynamic state and their values change as the combustion products expand in the Taylor wave.

In a dissociating gas such as detonation products, the role of chemical kinetics has to be considered. The effective value of γ is determined by the competition between the chemical reaction rates and the rate of pressure change along a particle path. If the rate of pressure change is much larger than the chemical reaction rates, the flow expansion occurs much faster than the chemical reactions and the species composition is essentially unchanged and it is adequate to use γ_{fr}. If the chemical reaction rates are much larger than the rate of pressure change, the detonation products are essentially in equilibrium during the flow expansion and γ_{eq} should be used. The self-similarity of the flow in the Taylor wave implies that particles initially located near the closed end of the tube spend less time in the Taylor wave than particles located further away from the closed end, and are, therefore, subject to higher temporal pressure gradients. It is shown in Wintenberger et al. (2002), using numerical solutions with detailed chemical kinetics, that for conditions representative of typical laboratory

straight-tube PDE experiments, the flow in the Taylor wave can be approximated as being in chemical equilibrium. Since the chemical reaction rates are a strong function of temperature, departures from equilibrium will occur at low initial pressures or if additional flow expansion is obtained through an exit nozzle. In particular, freezing of the composition is likely to occur in exit nozzles at sufficiently high pressure ratios.

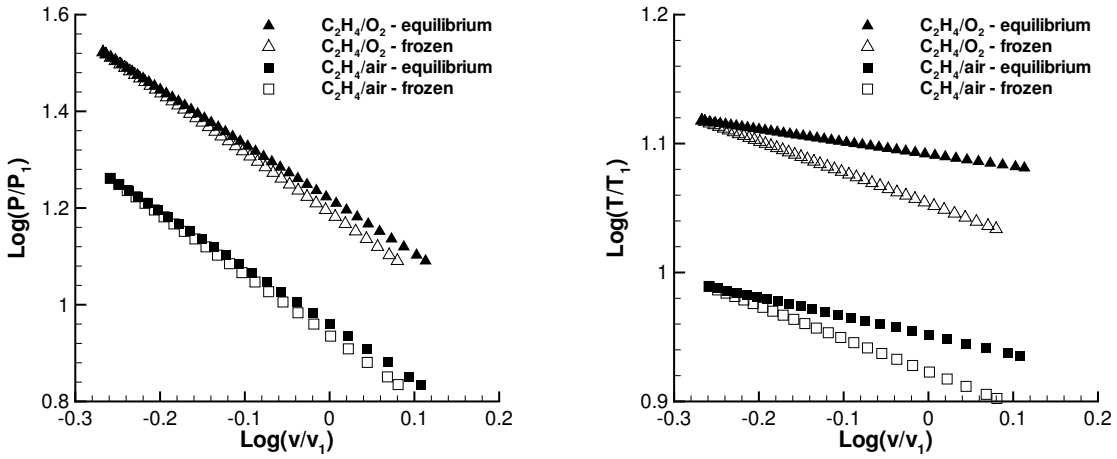

Figure 4.12: Logarithm of pressure (left) and temperature (right) versus logarithm of specific volume along the CJ equilibrium and frozen isentropes for ethylene-oxygen and -air mixtures.

The classical model of gas dynamics in the detonation products presented in Section 1.1.4 uses a simple polytropic model for the gas expansion: $P\rho^{-\gamma} = \text{constant}$. Characterizing the detonation products with a single value of γ is an approximation that can result in substantial differences depending on whether the flow is in chemical equilibrium or frozen and the corresponding value of γ (Fig. 4.12). For example, the value calculated for P_3 using this analytical treatment for ethylene-oxygen mixtures at standard conditions is about 10% lower when assuming frozen flow and using $\gamma_{fr} = 1.2356$ rather than when assuming chemical equilibrium with $\gamma_{eq} = 1.1397$ evaluated at the CJ point (Radulescu and Hanson, 2004). For most laboratory-scale experiments, the flow through the Taylor wave is in chemical equilibrium and an effective value of γ can be calculated by fitting the equilibrium isentrope with the polytropic relationship (Fig. 4.12). However, attempts at fitting the equilibrium isentrope showed that the effective value of γ obtained varied depending on the thermodynamic

variables selected for the fit. Table 4.1 illustrates this point for ethylene-oxygen and ethylene-air mixtures. The pressure-specific volume fit seems to yield the best agreement with the equilibrium γ at the CJ point. These variations can result in significant errors in the calculation of c_3 and P_3.

γ	C_2H_4+3O_2	C_2H_4+3O_2+11.28N_2
CJ frozen	1.2356	1.1717
CJ equilibrium	1.1397	1.1611
$P-v$ fit	1.1338	1.1638
$T-v$ fit	1.0967	1.1466

Table 4.1: Frozen and equilibrium values of γ evaluated at the CJ point for stoichiometric ethylene-oxygen and ethylene-air at 1 bar and 300 K initial conditions compared with results from fitting the isentrope based on the polytropic relationship using pressure and specific volume or temperature and specific volume.

The correct way to calculate the properties at state 3 is to use the original form of the Riemann invariant (Eq. 1.39). The exact value of P_3 is the solution to the following equation

$$\int_{P_3}^{P_2} \frac{dP}{\rho c} = u_2 \ . \tag{4.20}$$

This equation is solved numerically by integrating along the equilibrium isentrope until the integral of $dP/\rho c$ satisfies Eq. 4.20. In general, using a polytropic approximation with the equilibrium γ evaluated at the CJ point predicted fairly well the values of c_3 (within 1% error) and P_3 (within 2% error) but could result in more substantial errors on the impulse (up to 6% at high nitrogen dilution), which was calculated based on Eqs. 4.8 and 4.16. The numerical solution of Eq. 4.20 was used to calculate the values of P_3 and c_3 in all the subsequent impulse calculations. An effective value of γ is still required in order to calculate the parameter α from the self-similarity solution of Eq. 4.16. However, as long as c_3 is calculated from Eq. 4.20, α is relatively insensitive to the value of γ. For an ethylene-oxygen mixture at 300 K and 1 bar initial conditions, varying γ between 1.05 and 1.25 resulted in variations of α less than 1.6% and a resulting impulse variation less than 0.8% from their values calculated with $\gamma_{eq} = 1.1397$. Based on these observations and the results presented in Wintenberger et al. (2002), the equilibrium value γ_{eq} evaluated at the CJ point

was chosen as the effective value of γ in the Taylor wave.

4.4 Validation of the model

The model was validated against experimental data, and comparisons were made in terms of impulse per unit volume and specific impulse. The impulse per unit volume is defined as

$$I_V = I/V_{dt} \; . \tag{4.21}$$

The mixture-based specific impulse I_{sp} is defined as

$$I_{sp} = \frac{I}{\rho_1 V_{dt} g} = \frac{I_V}{\rho_1 g} = \frac{I}{\mathcal{M} g} \; . \tag{4.22}$$

The fuel-based specific impulse I_{spf} is defined with respect to the fuel mass instead of the mixture mass

$$I_{spf} = \frac{I}{\rho_1 X_F V_{dt} g} = \frac{I_{sp}}{X_F} = \frac{I}{\mathcal{M}_f g} \; . \tag{4.23}$$

4.4.1 Comparisons with single-cycle experiments

The calculation of the parameter α was validated by comparing the arrival time of the reflected expansion wave from experimental pressure histories at the thrust surface with the time calculated from the similarity solution. For a mixture of stoichiometric ethylene-air at 1 bar initial pressure, the time in an experimental pressure history (Cooper et al., 2002) between detonation initiation and the arrival of the reflected expansion wave was 1.43 ms from a 1.016 m long tube. The corresponding calculated time was 1.37 ms, within 4% of the experimental value. Similarly, comparing with data (Zitoun and Desbordes, 1999) for a tube of length 0.225 m, excellent agreement (within 3.8%) is obtained between our calculated value (303 μs) and experiment (315 μs).

The value of β was also computed using data from our experiments (Cooper et al., 2002) with stoichiometric ethylene-oxygen. Because these experiments used indirect

detonation initiation (DDT), we were able to compare with only two cases using an unobstructed tube and an initial pressure of 1 bar for which there was very rapid onset of detonation. These cases correspond to values of β equal to 0.53 and 0.63. Note that these values are sensitive to the time at which the integration is started. We computed this time using our theoretical values of t_1 and t_2.

Model predictions of impulse per unit volume were compared with data from Cooper et al. (2002). Direct experimental impulse measurements were obtained with a ballistic pendulum and detonation initiation was obtained via DDT. Obstacles were mounted inside the detonation tube in some of the experiments in order to enhance DDT. A correlation plot showing the impulse per unit volume obtained with the model versus the experimental values is displayed in Fig. 4.13. The values displayed here cover experiments with four different fuels (hydrogen, acetylene, ethylene, and propane) over a range of initial conditions and compositions. The solid line represents perfect correlation between the experimental data and the model. The filled symbols represent the data for unobstructed tubes, while the open symbols correspond to cases for which obstacles were used in the detonation tube.

The analytical model predictions were close to the experimental values of the impulse as shown on Fig. 4.13. The model assumes direct initiation of detonation, so it does not take into account any DDT phenomenon. The agreement is better for cases with high initial pressure and no nitrogen dilution, since the DDT time (time it takes the initial flame to transition to a detonation) is the shortest for these mixtures. For the unobstructed tube experiments, the model almost systematically underpredicts the impulse by up to 13%, except for the acetylene case, where it is about 19% too low. When obstacles are used, the experimental values are up to 73% lower than the model predictions. The differences are larger for low-pressure cases, for which the DDT time is higher. High-pressure cases yielded lower discrepancies of up to 21%. The lower experimental values for cases with obstacles are apparently caused by the additional form drag associated with the separated flow over the obstacles (Cooper et al., 2002). In general, the discrepancy between model and experiment is less than or equal to $\pm 15\%$. This conclusion is supported in Fig. 4.13 by the $\pm 15\%$ deviation

lines which encompass the experimental data.

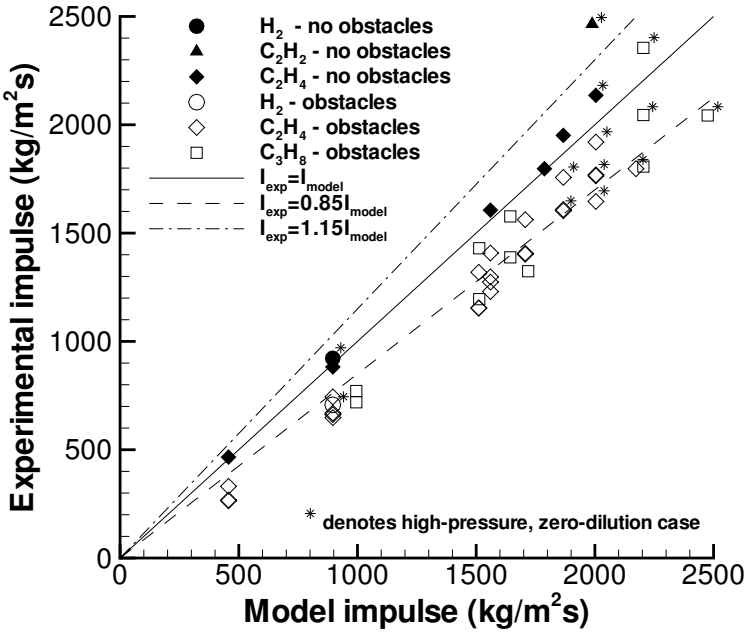

Figure 4.13: Model predictions versus experimental data (Cooper et al., 2002) for the impulse per unit volume. Filled symbols represent data for unobstructed tubes, whereas open symbols show data for cases in which obstacles were used. Lines corresponding to +15% and -15% deviation from the model values are also shown. * symbols denote high-pressure (higher than 0.8 bar), zero-dilution cases.

The model parameters are relatively constant, $1.07 < \alpha < 1.12$ and $0.53 < \beta < 0.63$, for all the mixtures studied here. A reasonable estimate for α is 1.1 and for β is 0.53. The ratio U_{CJ}/c_3 for fuel-oxygen-nitrogen mixtures is approximately 2 (see Eq. 1.44). For quick estimates of the impulse, these values can be used in Eq. 4.8 to obtain the approximate model prediction formula

$$I = 4.3\frac{\Delta P_3}{U_{CJ}}AL = 4.3\frac{\Delta P_3}{U_{CJ}}V_{dt} \; . \tag{4.24}$$

The approximate formula overpredicts the exact expressions by 4.1% for fuel-oxygen mixtures, and by 8.3% for fuel-air mixtures. The discrepancy between exact expression and approximate formula increases with decreasing pressure and increasing nitrogen dilution. The approximate formula reproduces the exact expressions for

stoichiometric fuel-oxygen mixtures at 1 bar initial pressure within 2.6%, and for stoichiometric fuel-air mixtures within 3.9%.

Zitoun and Desbordes (1999) calculated the single-cycle specific impulse for various reactive mixtures based on a formula developed from their experimental data for ethylene-oxygen mixtures: $I_{sp} = K\Delta P_3/(g\rho_1 U_{CJ})$. The coefficient K is estimated to be 5.4 in their study (although it was later corrected to 5.15 by Daniau (2001)), whereas we obtained an estimate of 4.3. This accounts for the systematic difference in the specific impulse results presented in Table 4.2. The present analytical model impulse is between 16% and 18% lower than Zitoun's predictions. This difference can be explained by the fact that Zitoun and Desbordes (1999) considered only the region of positive overpressure, which extends to about $9t_1$, in their integration of the pressure differential. They based this on the assumption that the following region of negative overpressure would be used for the self-aspiration of air in a multi-cycle air-breathing application. However, since we were interested in comparing with ballistic pendulum measurements, we performed the integration until the overpressure was back to zero, which occurs at about $20t_1$. The region of negative overpressure between 9 and $20t_1$ results in an impulse decrease. If we calculate the value of β by limiting the integration to the time of positive overpressure, we obtain a value of K = 4.8.

Mixture	Model I_{sp}	Zitoun and Desbordes (1999)
C_2H_4+3O_2	164.3	200
C_2H_4+3(O_2+3.76N_2)	117.7	142
C_2H_2+2.5O_2	166.8	203
C_2H_2+2.5(O_2+3.76N_2)	122.2	147
H_2+0.5O_2	189	226
H_2+0.5(O_2+3.76N_2)	123.9	149

Table 4.2: Comparison of the model predictions for the mixture-based specific impulse.

4.4.2 Comparisons with multi-cycle experiments

Calculations of specific impulse and thrust were compared to experimental data from Schauer et al. (2001). Their facility consisted of a 50.8 mm diameter by 914.4 mm long tube mounted on a damped thrust stand. Impulse and thrust measurements were made in hydrogen-air and propane-air mixtures with varying equivalence ratio. Data were collected during continuous multi-cycle operation and the thrust was averaged over many cycles. To compare with our model predictions, we assume multi-cycle operation is equivalent to a sequence of ideal single cycles. In multi-cycle operation, a portion of the cycle time is used to purge the tube and re-fill with reactants. The expulsion of gas from the tube can result in a contribution to the impulse which is not accounted for in our simple model. To estimate the magnitude of the impulse during refilling, we assumed that the detonation and exhaust phase had a duration of about $10t_1$ and that the remaining portion of the cycle is used for the purging and filling processes. We found that the contribution of the purge and fill portion to the thrust was less than their stated experimental uncertainty of 6% (Schauer et al., 2001).

Comparisons of specific impulse are presented in Fig. 4.14 for hydrogen-air and in Fig. 4.15 for propane-air. For comparison, predictions and one single-cycle measurement for hydrogen-oxygen are shown in Fig. 4.14. Two sets of data are shown for propane: data labeled "det" are from runs in which the average detonation wave velocity was about 80% of the CJ value, and data labeled "no det?" are from runs in which detonations were unstable or intermittent. The impulse model predictions are within 10% of the experimental data for hydrogen-air at $\phi > 0.8$, and within 16% for most stable propane-air cases. Figure 4.14 also includes an experimental hydrogen-oxygen single-cycle data point from our own experiments (Cooper et al., 2002). The vertical dashed line on Fig. 4.14 denotes a limit of the model validity. For richer mixtures, a reflected shock is calculated (Figs. 4.2, 4.3). The fact that the model still correctly predicts the impulse beyond this limit suggests that the reflected shock is weak and does not significantly affect the integrated pressure. Indeed, a ballistic pendulum experiment (Cooper et al., 2002) carried out with hydrogen-oxygen

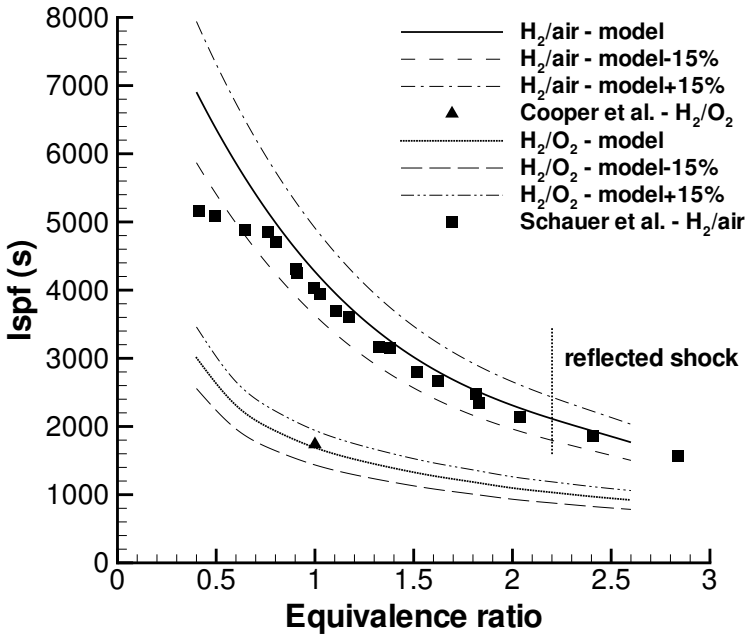

Figure 4.14: Comparison of specific impulse between model predictions and experimental data for hydrogen-air (Schauer et al., 2001) with varying equivalence ratio and stoichiometric hydrogen-oxygen (Cooper et al., 2002). Nominal initial conditions are $P_1 = 1$ bar, $T_1 = 300$ K. Lines corresponding to +15% and -15% deviation from the model values are also shown.

resulted in the directly measured impulse being within 2.9% of the value predicted by the model (Fig. 4.14). Figures 4.14 and 4.15 also include ±15% deviation lines from the model predictions.

In Fig. 4.15, the significantly lower impulse of the experimental point at $\phi = 0.59$ in propane mixtures is certainly due to cell size effects. At the lower equivalence ratios, the cell size (Shepherd and Kaneshige, 1997) of propane-air (152 mm at $\phi = 0.74$) approaches π times the diameter of the tube which is the nominal limit for stable detonation propagation (Zel'dovich et al., 1956, Lee, 1984).

In the case of hydrogen-air, Fig. 4.14, the cell size (Shepherd and Kaneshige, 1997) at $\phi = 0.75$ is 21 mm so the decrease in the experimental impulse data at low equivalence ratios can not be explained by cell size effects. Following the work of Dorofeev et al. (2001), the magnitude of the expansion ratio was examined for these mixtures. However, calculations for lean hydrogen-air showed that the expansion ratio

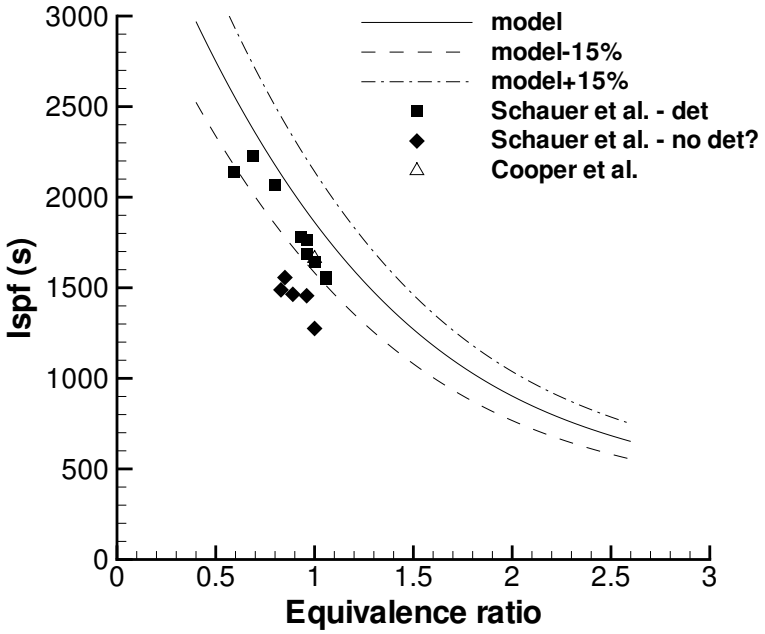

Figure 4.15: Comparison of specific impulse between model predictions and experimental data (Cooper et al., 2002, Schauer et al., 2001) for propane-air with varying equivalence ratio. Nominal initial conditions are $P_1 = 1$ bar, $T_1 = 300$ K. Lines corresponding to +15% and -15% deviation from the model values are also shown.

is always higher than the critical value defined (Dorofeev et al., 2001) for hydrogen mixtures. Instead, the results may be explained by the transition distance of the mixtures. Dorofeev et al. (2000) studied the effect of scale on the onset of detonations. They proposed and validated a criterion for successful transition to detonation: $\mathcal{L} > 7\lambda$, where $\mathcal{L}$ is the characteristic geometrical size (defined to account for the presence of obstacles) and λ the cell size of the mixture. Schauer et al. (2001) used a 45.7 mm pitch Shchelkin spiral constructed of 4.8 mm diameter wire to initiate detonations in their detonation tube. As defined by Dorofeev et al. (2000), this results in a characteristic geometrical size of 257 mm, comparable to $7\lambda = 217$ mm for a value of $\phi = 0.67$. The cell size increases with decreasing equivalence ratio for lean mixtures, so mixtures with equivalence ratios smaller than 0.67 will not transition to detonation within the spiral or possibly even the tube itself. This is consistent with the data shown on Fig. 4.14; hydrogen-air tests with $\phi \leq 0.67$ have experimental specific

impulse values significantly lower than the model prediction. Similar reductions in I_{sp} were also observed by Cooper et al. (2002) in single-cycle tests of propane-oxygen-nitrogen and ethylene-oxygen-nitrogen mixtures with greater than a critical amount of nitrogen dilution.

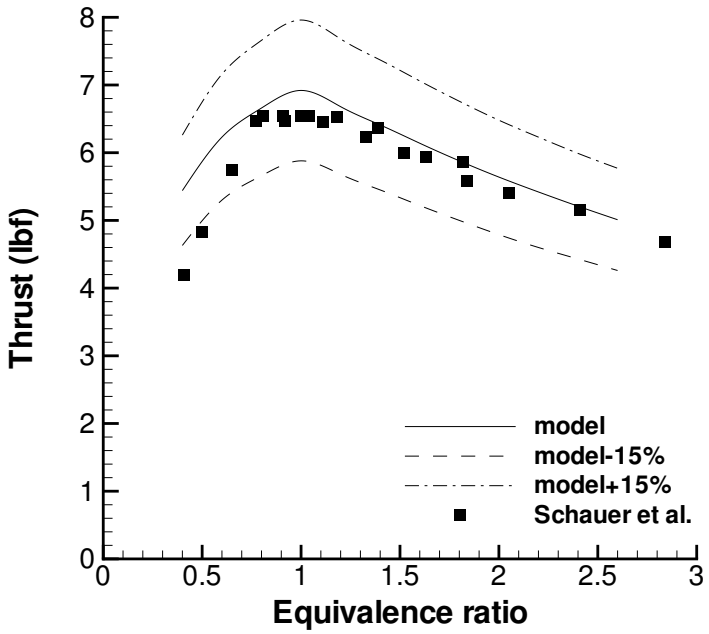

Figure 4.16: Thrust prediction for a 50.8 mm diameter by 914.4 mm long hydrogen-air PDE operated at 16 Hz. Comparison with experimental data of Schauer et al. (2001). Nominal initial conditions are $P_1 = 1$ bar, $T_1 = 300$ K. Lines corresponding to +15% and -15% deviation from the model values are also shown.

Average thrust for multi-cycle operation can be calculated from our single-cycle impulse model predictions, assuming a periodic sequence of individual pulses that do not interact. For a given single-cycle performance and tube size, the average thrust is proportional to the frequency (which is the inverse of the cycle time τ)

$$F = \frac{I_V V_{dt}}{\tau} \ . \tag{4.25}$$

Schauer et al. (2001) measured the average thrust in multi-cycle operation with hydrogen-air over a range of frequencies between 14 and 40 Hz and verified the linear dependence on frequency. Although this simple model suggests that thrust can be

increased indefinitely by increasing the cycle frequency, there are obvious physical constraints (Chao et al., 2001) that limit the maximum frequency for given size tube. The maximum cycle frequency is inversely proportional to the sum of the minimum detonation, exhaust, fill, and purge times. The purge and fill times are typically much longer than the detonation and exhaust time and therefore are the limiting factors in determining the maximum cycle frequency. Figure 4.16 compares measurements (Schauer et al., 2001) and model predictions for operation at a fixed frequency of 16 Hz. The computation of the thrust with the model is within 5.8% of the experimental data for $\phi > 0.8$. The discrepancies at low equivalence ratios are due to the increased transition distance discussed above.

4.4.3 Comparisons with numerical simulations

Data from the numerical simulation presented in Section 4.2.4 were used to compute the impulse per unit volume. The pressure at the thrust surface (Fig. 4.8) was integrated over time to obtain the impulse per unit area. Since the simulation was carried out for non-reactive flow and started as the detonation front exited the tube, the initial time corresponding to the detonation travel from the closed end to the open end of the tube was not simulated but was taken to be L/U_{CJ}. The integration was performed up to a time corresponding to $20t_1$ and the impulse per unit volume was

$$I_V = 22.6\frac{P_1}{U_{CJ}} \; . \tag{4.26}$$

This result is within 0.1% of the approximate model formula of Eq. 4.24. The simulation results are valid only for cases where the initial pressure P_1 is equal to the pressure outside the detonation tube P_0.

Comparisons with numerical computations of specific impulse by other researchers can also be made. Numerical simulations are very sensitive to the specification of the outflow boundary condition at the open end, and the numerical results vary widely when different types of boundary conditions are used. Sterling et al. (1995) obtained an average value of 5151 s for the fuel-based specific impulse of a stoichiometric

hydrogen-air mixture in a multi-cycle simulation using a constant pressure boundary condition. Bussing et al. (1997) obtained a range of values of 7500–8000 s. Other predictions by Cambier and Tegner (1998), including a correction for the effect of the initiation process, gave values between 3000 and 3800 s. More recently, Kailasanath (2000) tried to reconcile these different studies for hydrogen-air by highlighting the effect of the outflow boundary condition. They varied the pressure relaxation rate at the exit and obtained a range of values from 4850 s (constant pressure case) to 7930 s (gradual relaxation case). Our analytical model predicts 4344 s for the fuel-based specific impulse of stoichiometric hydrogen-air and the experimental value of Schauer et al. (2001) is 4024 s.

4.5 Impulse scaling relationships

From Eq. 4.24, the impulse can be written as

$$I = K \cdot V_{dt} \frac{\Delta P_3}{U_{CJ}} \,, \tag{4.27}$$

where K has a weak dependence on the properties of the mixture, $K(\gamma, q/RT_1)$. For the purposes of predicting how the impulse depends on the mixture properties and tube size, the principal dependencies are explicitly given in Eq. 4.27 with $K =$ constant. The dependence of impulse on the mixture properties comes in through the thermodynamic quantities U_{CJ} and ΔP_3. The CJ velocity is a function of composition only and independent of initial pressure as long as it is not so low that dissociation of the detonation products is significant. For the case of $P_1 = P_0$, the impulse can be written

$$I = K \frac{V_{dt} P_1}{U_{CJ}} \left(\frac{P_2}{P_1} \frac{P_3}{P_2} - 1 \right) \,. \tag{4.28}$$

For a perfect gas with a constant value of γ, Eq. 1.43 implies that

$$\frac{P_3}{P_2} = \left[1 - \left(\frac{\gamma - 1}{\gamma + 1} \right) \left(1 - \frac{U_{CJ}}{c_3} \right) \right]^{-\frac{2\gamma}{\gamma - 1}} \,. \tag{4.29}$$

Equilibrium computations with realistic thermochemistry indicate that $U_{CJ}/c_3 \approx 2$ and $0.353 \leq P_3/P_2 \leq 0.382$ with an average value of 0.37 for a wide range of compositions and initial conditions. Under these conditions, the pressure ratio is approximately constant

$$\frac{P_3}{P_2} \approx \left(\frac{2\gamma}{\gamma+1}\right)^{-\frac{2\gamma}{\gamma-1}} . \tag{4.30}$$

The approximate value of Eq. 4.30 is within 6% of the exact value of Eq. 4.29 for a range of mixtures including hydrogen, acetylene, ethylene, propane, and JP10 with air and oxygen varying nitrogen dilution (0 to 60%) at initial conditions $P_1 = 1$ bar and $T_1 = 300$ K. This indicates that the impulse will be mainly dependent on the CJ conditions and the total volume of explosive mixture

$$I \propto \frac{V_{dt} P_2}{U_{CJ}} . \tag{4.31}$$

Values of the CJ parameters and model impulses for several stoichiometric fuel-oxygen-nitrogen mixtures are given in Table 4.3.

4.5.1 Dependence of impulse on energy content

In order to explicitly compute the dependence of impulse on energy content, the approximate one-γ model of a detonation can be used. The CJ Mach number can be written

$$M_{CJ} = \sqrt{1+\mathcal{H}} + \sqrt{\mathcal{H}} \qquad \text{where} \qquad \mathcal{H} = \frac{\gamma^2-1}{2\gamma}\frac{q}{RT_1} . \tag{4.32}$$

The effective specific energy release q is generally less than the actual heat of combustion q_c due to the effects of dissociation, specific heat dependence on temperature, and the difference in average molar mass of reactants and products. Values of γ, q_c, and q are given for selected fuel-oxygen-nitrogen mixtures in Table 4.3 and the computation of q is discussed subsequently. For large values of the parameter $\mathcal{H}$, we can approximate the CJ velocity as

$$M_{CJ} \approx 2\sqrt{\mathcal{H}} \qquad \text{or} \qquad U_{CJ} \approx \sqrt{2(\gamma^2-1)q} . \tag{4.33}$$

Mixture	q_c (MJ/kg)	γ	P_2 (bar)	T_2 (K)	U_{CJ} (m/s)	M_{CJ}	I_{sp} (s)	q (MJ/kg)
H_2-O_2	13.29	1.1292	18.72	3679	2840	5.26	189	10.96
H_2-O_2-20% N_2	8.39	1.1313	17.98	3501	2474	5.16	164.4	8.16
H_2-O_2-40% N_2	5.20	1.141	16.95	3256	2187	5.01	142.3	5.93
H_2-air	3.39	1.1633	15.51	2948	1971	4.81	123.9	4.17
C_2H_2-O_2	11.82	1.1527	33.63	4209	2424	7.32	166.8	7.45
C_2H_2-O_2-20% N_2	9.60	1.1503	30.17	4051	2311	6.89	157.4	6.69
C_2H_2-O_2-40% N_2	7.31	1.1497	26.53	3836	2181	6.42	147.8	5.95
C_2H_2-O_2-60% N_2	4.95	1.1523	22.46	3505	2021	5.87	134.3	4.93
C_2H_2-air	3.39	1.1631	19.20	3147	1879	5.42	122.2	3.93
C_2H_4-O_2	10.67	1.1397	33.27	3935	2376	7.24	164.2	7.74
C_2H_4-O_2-20% N_2	8.70	1.1366	29.57	3783	2258	6.79	156.1	7.05
C_2H_4-O_2-40% N_2	6.66	1.1372	25.89	3589	2132	6.32	145.6	6.16
C_2H_4-O_2-60% N_2	4.53	1.143	21.82	3291	1977	5.77	131.5	4.99
C_2H_4-air	3.01	1.161	18.25	2926	1825	5.27	117.7	3.73
C_3H_8-O_2	10.04	1.1345	36.04	3826	2360	7.67	164.7	8.24
C_3H_8-O_2-20% N_2	8.33	1.133	31.73	3688	2251	7.14	155.6	7.44
C_3H_8-O_2-40% N_2	6.48	1.1342	27.45	3513	2131	6.58	146.3	6.47
C_3H_8-O_2-60% N_2	4.49	1.1411	22.79	3239	1980	5.95	132.6	5.18
C_3H_8-air	2.80	1.1655	18.15	2823	1801	5.29	115.6	3.57
JP10-O_2	9.83	1.1378	38.89	3899	2294	7.99	160.8	7.67
JP10-O_2-20% N_2	8.34	1.1351	34.00	3759	2204	7.41	153	7.08
JP10-O_2-40% N_2	6.65	1.1353	29.18	3585	2103	6.81	145.2	6.28
JP10-O_2-60% N_2	4.73	1.1398	24.06	3316	1972	6.12	133.1	5.21
JP10-air	2.79	1.1637	18.40	2843	1784	5.32	114.9	3.55

Table 4.3: Detonation CJ parameters and computed impulse for selected stoichiometric mixtures at 1 bar initial pressure and 300 K initial temperature.

The pressure ratio $\Delta P_3/P_1$ is also a function of composition only as long as the initial pressure is sufficiently high. The one-γ model can be used to compute the CJ pressure as

$$\frac{P_2}{P_1} = \frac{\gamma M_{CJ}^2 + 1}{\gamma + 1} \, . \tag{4.34}$$

For large values of the parameter $\mathcal{H}$, equivalent to large M_{CJ}, this can be approximated as

$$P_2 \approx \frac{1}{\gamma + 1} \rho_1 U_{CJ}^2 \, . \tag{4.35}$$

In the same spirit, we can approximate, assuming $P_1 = P_0$,

$$\Delta P_3/P_1 = \frac{P_2}{P_1}\frac{P_3}{P_2} - 1 \approx \frac{P_2}{P_1}\frac{P_3}{P_2} \tag{4.36}$$

and the impulse can be approximated as

$$I \approx \frac{1}{\gamma + 1} \mathcal{M} U_{CJ} K \frac{P_3}{P_2} \, . \tag{4.37}$$

where $\mathcal{M} = \rho_1 V_{dt}$ is the mass of explosive mixture in the tube. Using the approximation of Eq. 4.33, this can be written

$$I \approx \mathcal{M}\sqrt{q} \left[\sqrt{2\frac{\gamma - 1}{\gamma + 1}} K \frac{P_3}{P_2} \right] \, . \tag{4.38}$$

The term in the square brackets is only weakly dependent on the mixture composition. Using Eq. 4.30, the impulse can be approximated as

$$I \approx \mathcal{M}\sqrt{q} K \sqrt{2\frac{\gamma - 1}{\gamma + 1}} \left(\frac{2\gamma}{\gamma + 1} \right)^{-\frac{2\gamma}{\gamma - 1}} \, . \tag{4.39}$$

This expression indicates that the impulse is directly proportional to the product of the total mass of explosive mixture in the tube and the square root of the specific energy content of the mixture.

$$I \propto \mathcal{M}\sqrt{q} \tag{4.40}$$

4.5.2 Dependence of impulse on initial pressure

At fixed composition and initial temperature, the values of q, γ, and R are constant. Equilibrium computations with realistic thermochemistry show that for high enough initial pressures, U_{CJ}, P_3/P_2, and P_2/P_1 are essentially independent of initial pressure. From Eq. 4.39, we conclude that the impulse (or impulse per unit volume) is directly proportional to initial pressure under these conditions, since $\mathcal{M} = \rho_1 V_{dt} = P_1 V_{dt}/RT_1$.

$$I \propto V_{dt} P_1 \tag{4.41}$$

4.5.3 Dependence of impulse on initial temperature

At fixed composition and initial pressure, the impulse decreases with increasing initial temperature. This is because the mass in the detonation tube varies inversely with initial temperature when the pressure is fixed. From Eq. 4.39, we have

$$I \propto \frac{V_{dt}}{T_1} \,. \tag{4.42}$$

4.5.4 Mixture-based specific impulse

At fixed composition, the mixture-based specific impulse is essentially independent of initial pressure and initial temperature:

$$I_{sp} = \frac{I}{\mathcal{M} g} \approx \frac{\sqrt{q}}{g} K \sqrt{2 \frac{\gamma - 1}{\gamma + 1}} \left(\frac{2\gamma}{\gamma + 1} \right)^{-\frac{2\gamma}{\gamma - 1}} \,. \tag{4.43}$$

This also holds for the fuel-based specific impulse since at fixed composition, the fuel mass is a fixed fraction of the total mass. More generally, Eq. 4.43 shows that the specific impulse is proportional to the square root of the specific energy content of the explosive mixture

$$I_{sp} \propto \sqrt{q} \,. \tag{4.44}$$

The coefficient in Eq. 4.43 can be numerically evaluated using our value of the coefficient K of 4.3 and a value of γ obtained from equilibrium computations (Reynolds, 1986). The range of γ for the mixtures considered (Table 4.3) was $1.133 < \gamma < 1.166$. The resulting coefficient of proportionality in Eq. 4.44 is between 0.054 and 0.061 with an average value of 0.058 when q is expressed in J/kg, so that $I_{sp} \approx 0.058\sqrt{q}$.

The value of q is calculated with Eq. 4.32 and the results (Table 4.3) of equilibrium computations of M_{CJ} and γ. Eq. 4.32 can be rearranged to give q explicitly

$$q = \frac{\gamma R T_1}{2(\gamma^2 - 1)} \left(M_{CJ} - \frac{1}{M_{CJ}} \right)^2 . \tag{4.45}$$

Values of q given in Table 4.3 were computed using this expression with a gas constant based on the reactant molar mass. Note that the values of q computed in this fashion are significantly less than the heat of combustion q_c when the CJ temperature is above 3500 K. This is due to dissociation of the major products reducing the temperature and the effective energy release. The values of q in Table 4.3 calculated for highly diluted mixtures can be higher than q_c because of the approximations made in using the one-γ model to calculate q. In general, the ratio of the effective energy release to the heat of combustion q/q_c decreases with increasing CJ temperature due to the higher degree of dissociation.

The scaling relationship of Eq. 4.44 is tested in Fig. 4.17 by plotting the model impulse I_{sp} versus the effective specific energy release q for all of the cases shown in Table 4.3. The approximate relationship $I_{sp} \approx 0.058\sqrt{q}$ is also shown. In general, higher values of the specific impulse correspond to mixtures with a lower nitrogen dilution and, hence, a higher energy release, for which the CJ temperature is higher and dissociation reactions are favored. There is reasonable agreement between the model I_{sp} and the approximate square root scaling relationship with a fixed coefficient of proportionality. There is some scatter about the average trend due to the dependence of γ on the mixture composition and temperature, but the predictions of Eq. 4.43 are within 6% of the values computed by Eq. 4.8.

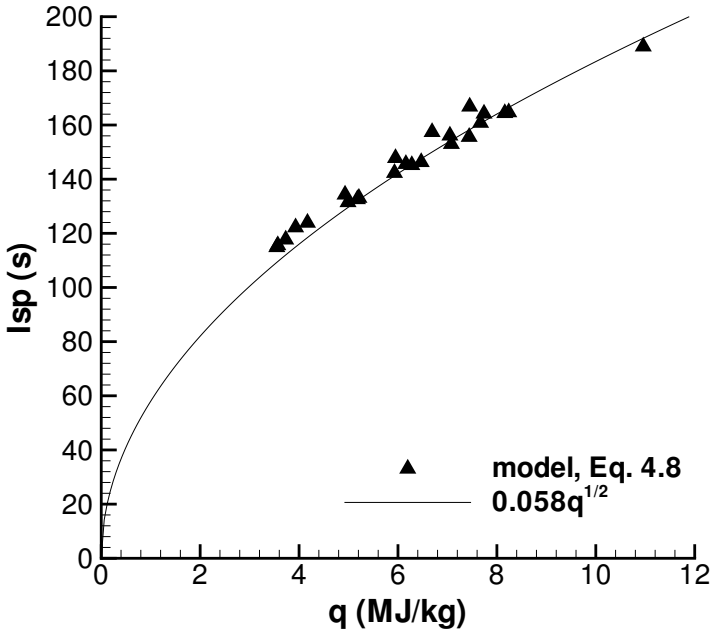

Figure 4.17: Specific impulse scaling with energy content. Model predictions (Eq. 4.8) versus effective specific energy content q for hydrogen, acetylene, ethylene, propane, and JP10 with air and oxygen including 0, 20%, 40%, and 60% nitrogen dilution at $P_1 = 1$ bar and $T_1 = 300$ K.

4.6 Impulse predictions – Parametric studies

Impulse calculations were carried out for different mixtures, equivalence ratios, initial pressures, and nitrogen dilutions. Unless otherwise mentioned, all calculations were performed with an initial temperature of 300 K.

The model input parameters consist of the external environment pressure P_0, the detonation velocity U_{CJ}, the equilibrium speed of sound behind the detonation front c_2, the CJ pressure P_2, and the equilibrium polytropic exponent in the products γ. All parameters were computed using equilibrium calculations (Reynolds, 1986) performed with a realistic set of combustion products. The properties at state 3 were calculated based on Eq. 4.20. These parameters were then used in Eq. 4.16 and 4.8 to obtain the impulse.

The impulse is calculated for the following fuels: ethylene, propane, acetylene, hydrogen, Jet A, and JP10 with varying initial pressure (Figs. 4.18, 4.21, 4.24),

equivalence ratio (Figs. 4.19, 4.22, 4.25), and nitrogen dilution (Figs. 4.20, 4.23, 4.26). Results are expressed in terms of impulse per unit volume of the tube, specific impulse, and fuel-based specific impulse. Results for hydrogen-oxygen mixtures are strictly valid for equivalence ratios less than 0.8 and for hydrogen-air mixtures with equivalence ratios less than 2.2. In these cases, the calculations are probably reasonable estimates but the reader should keep in mind that the underlying physical assumption is no longer justified. The results for Jet A and JP10 assume that these fuels are in completely vaporized form for all initial conditions. While unrealistic at low temperatures, this gives a uniform basis for comparison of all fuels.

4.6.1 Impulse per unit volume

The impulse per unit volume is independent of the tube size and is linearly dependent on the initial pressure, as indicated by Eq. 4.41. The variation of I_V with P_1, ϕ, and $N_2\%$ is shown in Figs. 4.18, 4.19, and 4.20. Hydrogen cases are very different from hydrocarbons. The impulse per unit volume is much lower due to the lower molecular mass of hydrogen, which results in lower density and CJ pressure. Eq. 4.40 shows that the impulse per unit volume is proportional to the density of the explosive mixture and the square root of the specific energy release. The specific energy release of hydrogen mixtures is of the same order as that obtained with other fuels, but the density of hydrogen mixtures is much lower, resulting in a lower impulse per unit volume.

Impulse per unit volume versus equivalence ratio is shown in Fig. 4.19. The impulse is expected to be maximum at stoichiometric conditions from Eq. 4.40 if we consider only the major products of combustion. However, examining the plot, we see that, with the exception of hydrogen, the maximum values of I_V occur for rich ($\phi \sim 2$) fuel-oxygen mixtures and slightly rich ($\phi \sim 1.1$–1.2) fuel-air mixtures. Equilibrium computations reveal that the maximum detonation velocity and pressure also occur for rich mixtures. Even though the nominal heat of reaction of the mixture based on major products is maximum at stoichiometry, the detonation velocity is not

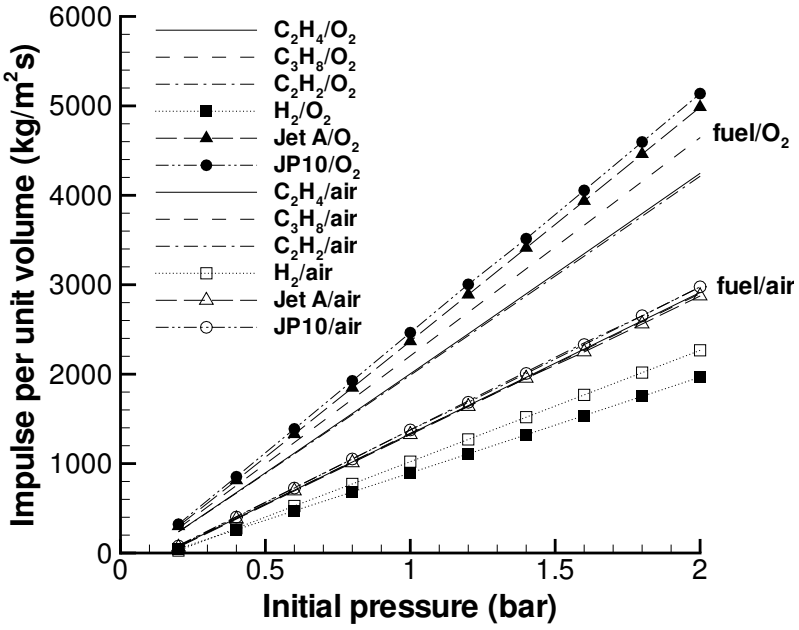

Figure 4.18: Variation of impulse per unit volume with initial pressure. Nominal initial conditions are $T_1 = 300$ K, stoichiometric fuel-oxygen ratio.

a maximum at stoichiometric because of the product species distribution for rich combustion. Increasing amounts of CO and H_2 in increasingly rich mixtures results in a larger number of products, effectively increasing the heat of reaction and shifting the peak detonation velocity and pressure to a rich mixture. The effect is much stronger in fuel-oxygen mixtures than in fuel-air mixtures since the nitrogen in the air moderates the effect of the increasing number of products in rich mixtures. A similar effect is observed in flames.

In the case of hydrogen, the product distribution effect is not as prominent since the number of major products is always less than reactants, independent of stoichiometry. For hydrogen-air mixtures, the maximum I_V is obtained for an equivalence ratio close to 1. The impulse of hydrogen-oxygen mixtures decreases monotonically with increasing equivalence ratio. Unlike hydrocarbon fuels, which have a molecular mass comparable to or higher than oxygen and air, hydrogen has a much lower molecular mass. Thus, increasing the equivalence ratio causes a sharp decrease in the mixture density. The linear dependence of the impulse per unit volume with mixture density

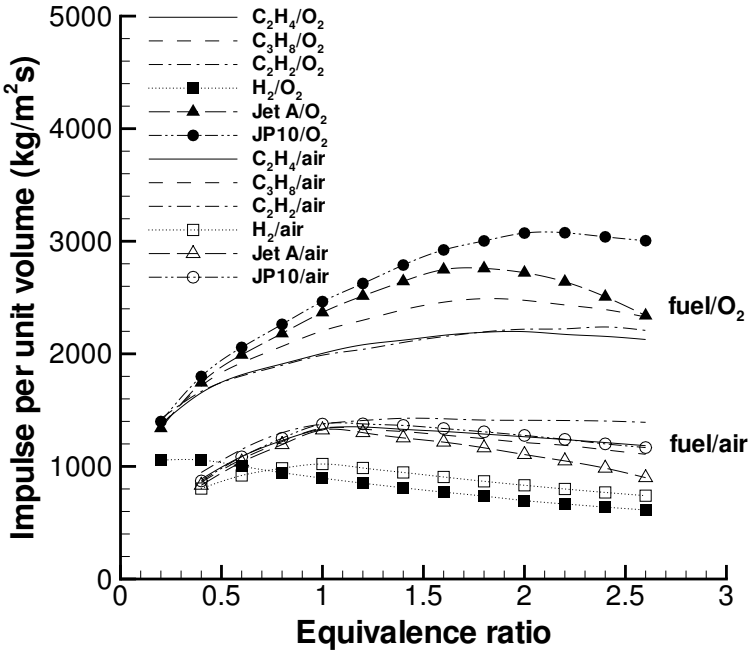

Figure 4.19: Variation of impulse per unit volume with equivalence ratio. Nominal initial conditions are $P_1 = 1$ bar, $T_1 = 300$ K.

dominates over its square root variation with effective energy release (Eq. 4.40), resulting in a decreasing impulse with increasing equivalence ratio for hydrogen-oxygen mixtures.

The impulse per unit volume generated by the different fuels with oxygen can be ranked in all cases as follows from lowest to highest: hydrogen, acetylene, ethylene, propane, Jet A, and JP10. The impulse is generated by the chemical energy of the mixture, which depends on a combination of bond strength and hydrogen to carbon ratio. The results obtained for the impulse per unit volume versus the equivalence ratio are presented for an equivalence ratio range from 0.4 to 2.6. The results of calculations at higher equivalence ratios were considered unreliable because carbon production, which is not possible to account for correctly in equilibrium calculations, occurs for very rich mixtures, in particular for Jet A and JP10.

The nitrogen dilution calculations (Fig. 4.20) show that the impulse decreases with increasing nitrogen dilution for hydrocarbon fuels. However, as the dilution increases, the values of the impulse for the different fuels approach each other. The presence of

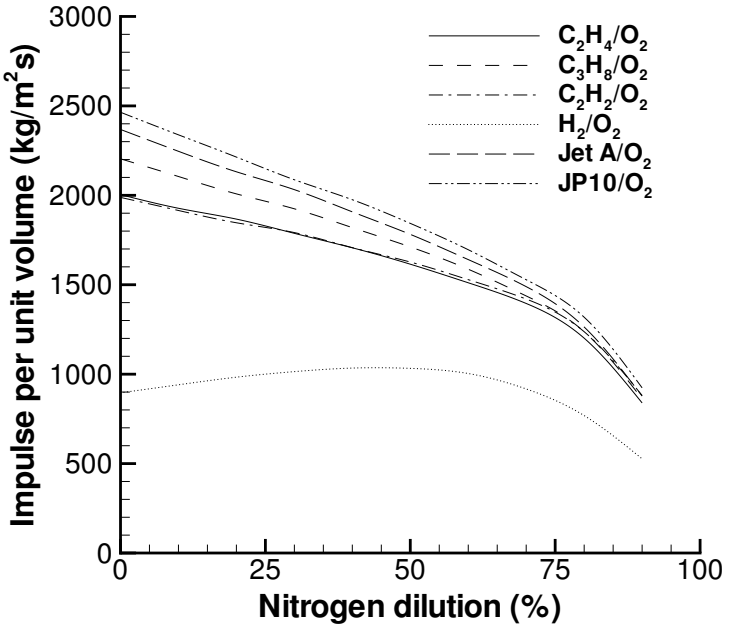

Figure 4.20: Variation of impulse per unit volume with nitrogen dilution. Nominal initial conditions are $P_1 = 1$ bar, $T_1 = 300$ K, stoichiometric fuel-oxygen ratio.

the diluent masks the effect of the hydrogen to carbon ratio. The hydrogen curve is much lower due to the lower CJ pressures caused by the lower molecular mass and heat of combustion of hydrogen. Unlike for hydrocarbons, this curve has a maximum. The presence of this maximum can be explained by the two competing effects of nitrogen addition: one is to dilute the mixture, reducing the energy release per unit mass (dominant at high dilution), while the other is to increase the molecular mass of the mixture (dominant at low dilution). Note that the highest value of the impulse is obtained close to 50% dilution, which is similar to the case of air (55.6% dilution).

4.6.2 Mixture-based specific impulse

The mixture-based specific impulse I_{sp} is plotted versus initial pressure, equivalence ratio, and nitrogen dilution in Figs. 4.21, 4.22, and 4.23, respectively. The specific impulse decreases steeply as the initial pressure decreases due to the increasing importance of dissociation at low pressures (Fig. 4.21). Dissociation is an endothermic

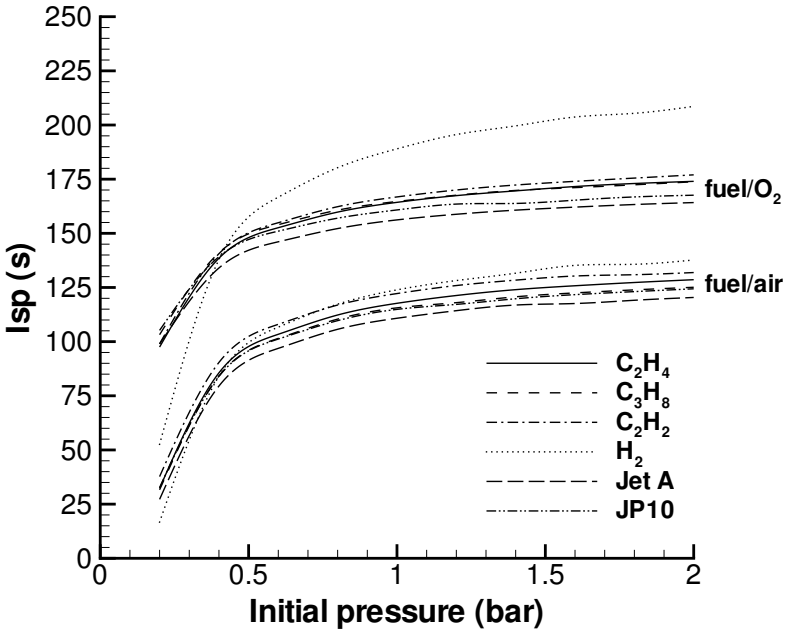

Figure 4.21: Variation of mixture-based specific impulse with initial pressure. Nominal initial conditions are $T_1 = 300$ K, stoichiometric fuel-oxygen ratio.

process and the effective energy release q decreases with decreasing initial pressure.

Recombination of radical species occurs with increasing initial pressure. At sufficiently high initial pressures, the major products dominate over the radical species and the CJ detonation properties tend to constant values. The mixture-based specific impulse tends to a constant value at high pressures, which is in agreement with the impulse scaling relationship of Eq. 4.43 if the values of q and γ reach limiting values with increasing initial pressure. Additional calculations for ethylene and propane with oxygen and air showed that the specific impulse was increased by approximately 7% between 2 and 10 bar and by less than 2% between 10 and 20 bar, confirming the idea of a high-pressure limit.

The specific impulses of hydrocarbon fuels varying the equivalence ratio (Fig. 4.22) have a similar behavior to that of the impulse per unit volume. This is expected since the only difference is due to the mixture density. Most hydrocarbon fuels have a heavier molecular mass than the oxidizer, but the fuel mass fraction for heavier fuels is smaller. The overall fuel mass in the mixture does not change much with

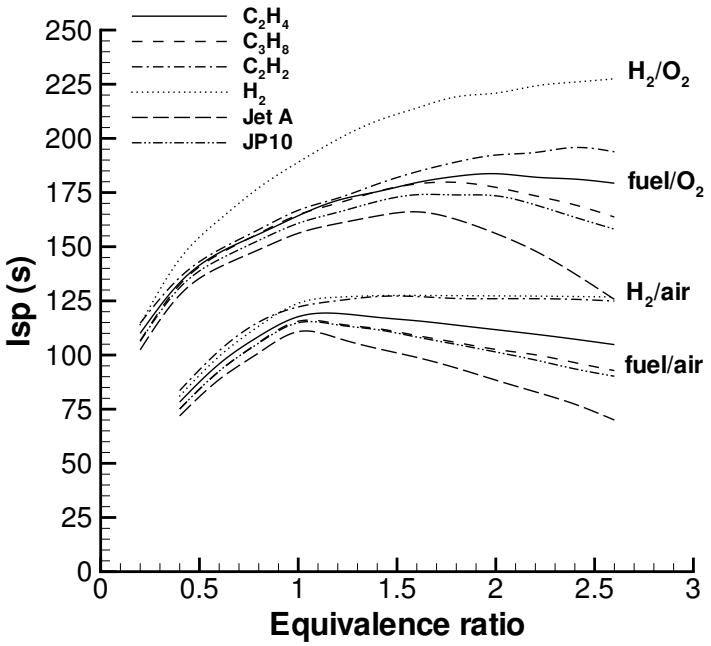

Figure 4.22: Variation of mixture-based specific impulse with equivalence ratio. Nominal initial conditions are $P_1 = 1$ bar, $T_1 = 300$ K.

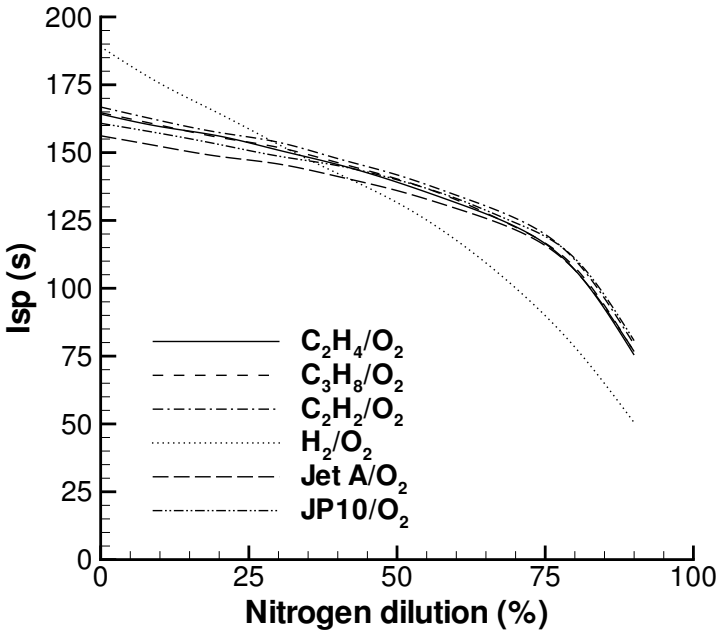

Figure 4.23: Variation of mixture-based specific impulse with nitrogen dilution. Nominal initial conditions are $P_1 = 1$ bar, $T_1 = 300$ K, stoichiometric fuel-oxygen ratio.

the equivalence ratio, so the mixture density does not vary significantly. However, this effect is important in the case of hydrogen, where the mixture density decreases significantly as the equivalence ratio increases. This accounts for the monotonic increase of the hydrogen-oxygen curve. In the case of hydrogen-air, the mixture density effect is masked because of the nitrogen dilution, which explains the nearly constant portion of the curve on the rich side. The variation of the I_{sp} with nitrogen dilution, Fig. 4.23, is the same for all fuels including hydrogen. The mixture-based specific impulse decreases as the nitrogen amount in the mixture increases.

4.6.3 Fuel-based specific impulse

The fuel-based specific impulse I_{spf} is plotted versus initial pressure, equivalence ratio, and nitrogen dilution in Figs. 4.24, 4.25, and 4.26, respectively. The variation of I_{spf} with initial pressure, Fig. 4.24, is very similar to the corresponding behavior of I_{sp}. The curves are individually shifted by a factor equal to the fuel mass fraction. Note the obvious shift of the hydrogen curves because of the very low mass fraction of hydrogen. The fuel-based specific impulse is about three times higher for hydrogen than for other fuels.

The plots on Fig. 4.25 show a monotonically decreasing I_{spf} with increasing equivalence ratio. This is due to the predominant influence of the fuel mass fraction, which goes from low on the lean side to high on the rich side. The hydrogen mixtures again have much higher values compared to the hydrocarbon fuels due to the lower molar mass of hydrogen as compared to the hydrocarbon fuels. The values of I_{spf} shown in Fig. 4.26 exhibit a monotonically increasing behavior with increasing nitrogen dilution, due to the decrease in fuel mass fraction as the nitrogen amount increases.

4.6.4 Influence of initial temperature

Temperature is an initial parameter that may significantly affect the impulse, especially at values representative of stagnation temperature for supersonic flight or temperatures required to vaporize aviation fuels. The results shown in previous figures

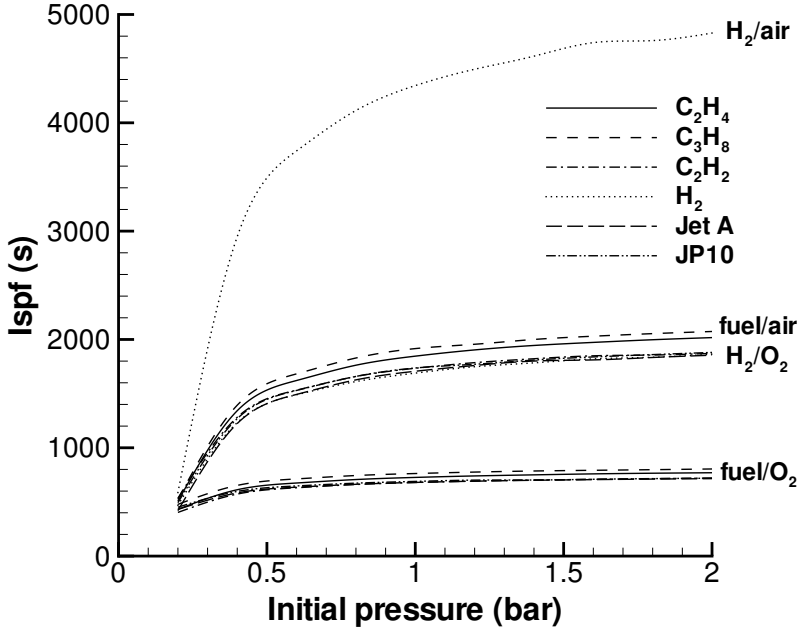

Figure 4.24: Variation of fuel-based specific impulse with initial pressure. Nominal initial conditions are $T_1 = 300$ K, stoichiometric fuel-oxygen ratio.

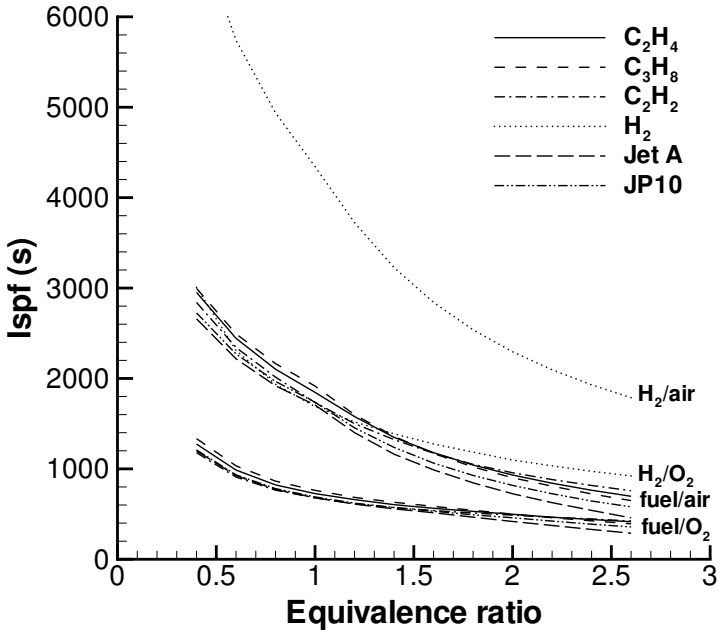

Figure 4.25: Variation of fuel-based specific impulse with equivalence ratio. Nominal initial conditions are $P_1 = 1$ bar, $T_1 = 300$ K.

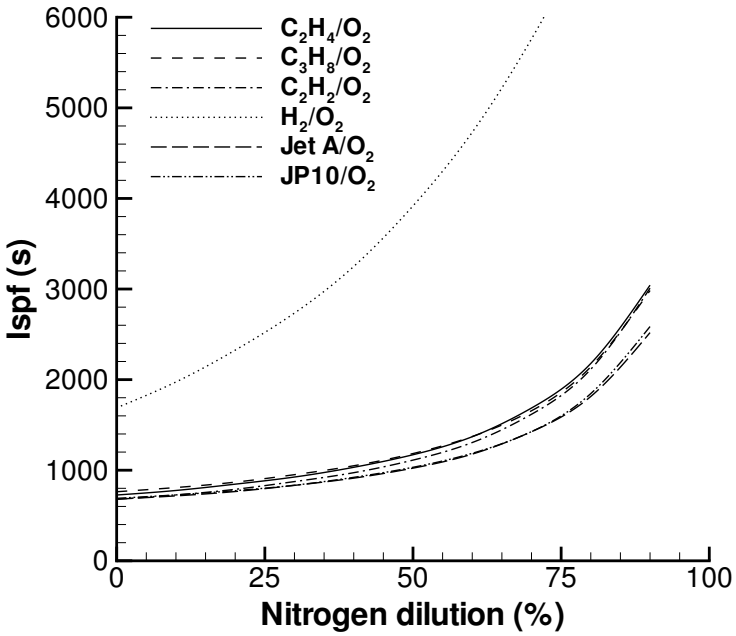

Figure 4.26: Variation of fuel-based specific impulse with nitrogen dilution. Nominal initial conditions are $P_1 = 1$ bar, $T_1 = 300$ K, stoichiometric fuel-oxygen ratio.

were for an initial temperature of 300 K. Calculations with initial temperatures from 300 to 600 K were carried out for stoichiometric JP10-air; JP10 is a low vapor pressure liquid ($C_{10}H_{16}$) at room temperature. The impulse per unit volume (Fig. 4.27) and the mixture-based specific impulse (Fig. 4.28) were calculated as a function of the initial temperature for different pressures representative of actual stagnation pressure values in a real engine.

The impulse per unit volume decreases with increasing initial temperature, as predicted by Eq. 4.42. At fixed pressure and composition, this decrease is caused by the decrease of the initial mixture density. The mixture-based specific impulse is found to be approximately constant when initial temperature and initial pressure are varied (Fig. 4.28). The scaling predictions of Eq. 4.43 are verified for constant composition. The slight decrease of the specific impulse observed with increasing temperature and decreasing pressure can be attributed to the promotion of dissociation reactions under these conditions. Specific impulse is a useful parameter for estimating performance since at high enough initial pressures, it is almost independent of initial pressure and

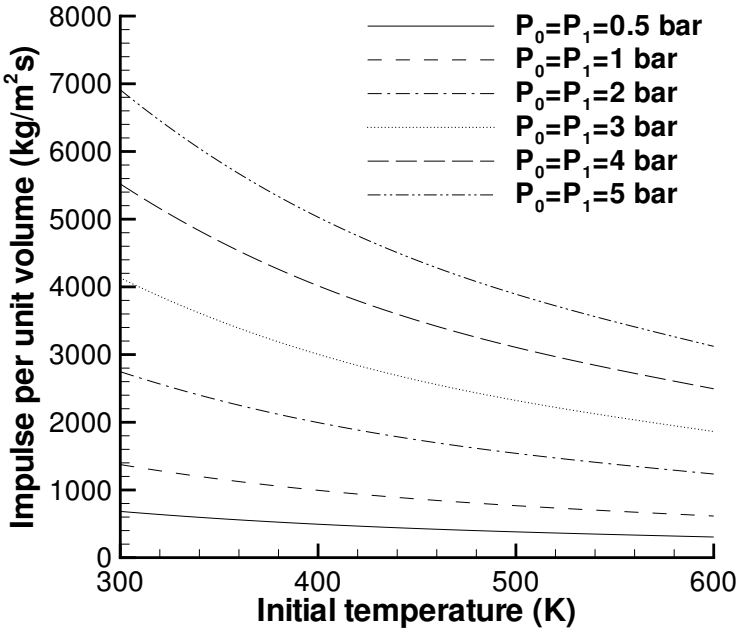

Figure 4.27: Variation of impulse per unit volume with initial temperature for different values of the stagnation pressure.

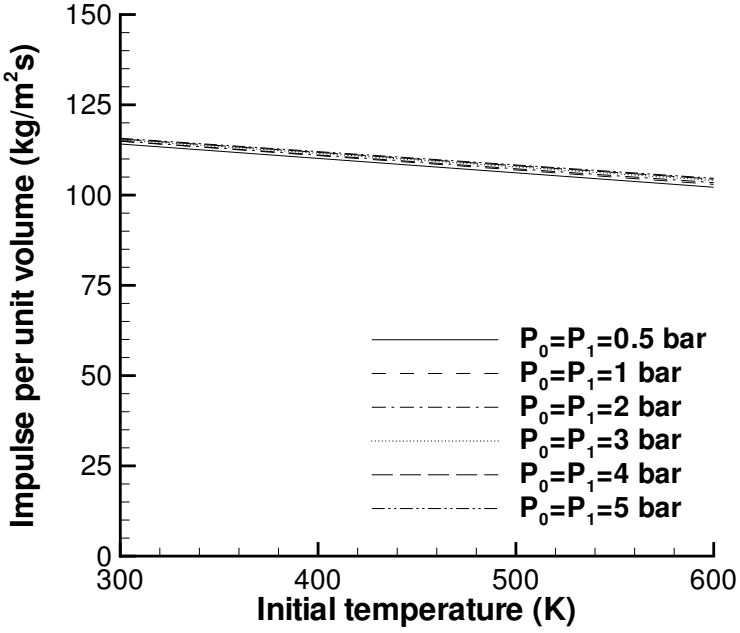

Figure 4.28: Variation of mixture-based specific impulse with initial temperature for different values of the stagnation pressure.

temperature.

4.7 Conclusions

An analytical model for the impulse of a pulse detonation tube has been developed using a simple one-dimensional gas dynamic analysis and empirical observations. This model is one of the first tools available to the propulsion community to quickly and reliably evaluate the performance of the most basic form of a pulse detonation engine, consisting of a straight tube open at one end. The model predictions were compared with various experimental results, from direct single-cycle impulse measurements (Zitoun and Desbordes, 1999, Cooper et al., 2002) to multi-cycle thrust measurements (Schauer et al., 2001), and also numerical simulations. These show reasonable agreement (within $\pm 15\%$ or better in most cases) for comparisons of impulse per unit volume, specific impulse, and thrust. This work investigates for the first time the dependence of the impulse on a wide range of initial conditions including fuel type, initial pressure, equivalence ratio, and nitrogen dilution.

We found that the impulse of a detonation tube scales directly with the mass of the explosive mixture in the tube and the square root of the effective energy release per unit mass of the mixture. A procedure was given to account for product dissociation in determining the effective specific energy release. Based on a scaling analysis and the results of equilibrium computations, we reached the following conclusions:

a) At fixed composition and initial temperature, the impulse per unit volume varies linearly with initial pressure.

b) At fixed composition and initial pressure, the impulse per unit volume varies inversely with initial temperature.

c) At fixed composition and sufficiently high initial pressure, the specific impulse is approximately independent of initial pressure and initial temperature. This makes specific impulse the most useful parameter for estimating pulse detonation tube performance over a wide range of initial conditions.

The predicted values of the mixture-based specific impulse are on the order of 155 to 165 s for hydrocarbon-oxygen mixtures, 190 s for hydrogen-oxygen, and on the order of 115 to 125 s for fuel-air mixtures at initial conditions of 1 bar and 300 K. These values are lower than the maximum impulses possible with conventional steady propulsion devices (Sutton, 1986, Hill and Peterson, 1992). As mentioned in the introduction, there are many other factors that should be considered in evaluating PDE performance and their potential applications. The present study provides some modeling ideas that are used in the next chapter as a basis for the development of a performance model for air-breathing pulse detonation engines.

Chapter 5

Air-Breathing Pulse Detonation Engine Performance Modeling

5.1 Introduction

PDE performance analysis has followed several different approaches, starting with attempts to measure and model the static performance of single-cycle detonation tubes. The research efforts focused on the single-cycle performance of detonation tubes are reviewed in Section 4.1. In parallel, researchers have also experimentally investigated the static multi-cycle performance of single (Zitoun and Desbordes, 1999, Kasahara et al., 2002, Brophy et al., 2003) and multiple (Schauer et al., 2001) detonation tubes. Although good agreement has been obtained between the experimental multi-cycle data of Schauer et al. (2001) and the single-cycle estimates presented in Chapter 4, the numerical simulations of Cambier and Tegner (1998) also showed that the multi-cycle performance can be substantially different from the single-cycle performance. The fuel injection, ignition, and refilling strategies highlighted by Cambier and Tegner (1998) as well as the assumptions made for detonation initiation discussed by Kailasanath (2002) play a crucial role in estimating the multi-cycle performance.

Although PDE static performance has been studied extensively, very few efforts have focused on estimating the performance of an air-breathing PDE. The difficulties associated with coupling the inlet flow to the unsteady flow inside the deto-

This chapter is based on work presented in Wintenberger and Shepherd (2003a).

nation tube(s) and the lack of understanding about the influence of an exit nozzle (Kailasanath, 2001) are two significant modeling challenges. Bratkovich and Bussing (1995) presented a performance model for air-breathing PDEs, which considers contributions from an inlet, a mixer, a combustor, and a nozzle. The code is based on a control volume analysis and a time averaging methodology for the unsteady components. It allows for the selection of various inlet types and single- or multiple-tube detonation chambers. Kaemming (2001) conducted a mission analysis showing that an air-breathing PDE can present performance advantages over the turbo-ramjet, without providing any absolute performance values. Because of the proprietary nature of the work and the lack of details about these commercial codes (Bratkovich and Bussing, 1995, Kaemming, 2001), the accuracy of these performance predictions is difficult to assess.

Wu et al. (2003) have presented what is so far the most comprehensive system performance analysis for an air-breathing PDE. Their work is based on a modular approach, including supersonic inlet dynamics and detonation in single and multiple tubes. They carried out detailed numerical simulations for a hydrogen-fueled air-breathing PDE flying at 9.3 km altitude and a Mach number of 2.1. A series of parametric studies showed that the system performance decreased with increasing ignition delay and increasing refilling period for a fixed blowdown time. Investigations of nozzle design concluded that a limited performance gain was obtained for non-choked nozzles, but that choked converging-diverging nozzles could considerably improve performance. Maximum fuel-based specific impulses on the order of 3500 s were obtained for stoichiometric hydrogen-air. More recently, Ma et al. (2003) presented numerical results showing the thrust chamber dynamics of multiple-tube PDEs. They showed that the multiple-tube design improves the performance by reducing the degree of unsteadiness in the flow. Specific impulses as high as 3800 s at a flight Mach number of 2.1 were obtained with a single converging-diverging exit nozzle.

Other PDE performance estimates have been based on thermodynamic cycle analysis. Heiser and Pratt (2002) proposed a thermodynamic cycle based on the ZND

model of detonation and used the entropy method (Eq. 1.83) to predict performance. The constant volume combustion cycle has also been used as a surrogate for the detonation cycle (Bussing and Pappas, 1996, Kentfield, 2002). Performance models based on gas dynamics have been proposed. Talley and Coy (2002) developed a blow-down model assuming quasi-steady isentropic one-dimensional nozzle flow following constant volume combustion. The performance results were compared to constant pressure propulsion devices. Harris et al. (2002) evaluated the respective performance of zero-, one-, and two-dimensional models for the PDE cycle showing that the model of Talley and Coy (2002) offers a good approximation of the time-averaged performance. Harris et al. (2002) also concluded that the Heiser and Pratt (2002) analysis was overly optimistic in its maximum performance predictions.

Based on comparison with detonation tube experiments, the most realistic performance models (Zitoun and Desbordes, 1999, Wintenberger et al., 2003, Talley and Coy, 2002) have so far been based on unsteady gas dynamics because of the inherent unsteadiness in the flow. Our goal is to develop a simple predictive model that can be used to evaluate engine performance at various operating conditions. We present a fully unsteady one-dimensional control volume analysis of a single-tube air-breathing PDE, taking into account the kinetic energy of the flow, which is critical in analyzing high-speed propulsion systems. The flow field inside the engine is investigated using gas dynamics. The performance of the air-breathing PDE is calculated from the conservation equations and compared with that of a conventional propulsion system, the ideal ramjet.

5.2 Single-tube air-breathing PDE

We consider a supersonic single-tube air-breathing PDE that consists of an inlet, an acoustic cavity (or plenum), a valve, and a straight detonation tube. A schematic is given in Fig. 5.1. We assume a steady inlet because of its well-known performance characteristics. Installing a steady inlet in an unsteady air-breathing engine is possible as long as quasi-steady flow downstream of the inlet is achieved by one of two ways.

The first way uses multiple detonation tubes operating out of phase so that the flow upstream of the detonation tubes decouples from the unsteady flow inside the tubes, becoming quasi-steady. The second way is to have a plenum downstream of the inlet that is large enough to dampen pressure transients generated by the pulsed operation of the engine (Bussing and Pappas, 1996). This second approach increases the engine total volume and may not be practical, but we adopt it in our one-dimensional modeling due to its simplicity. Other types of inlets for PDEs include unsteady valveless (Foa, 1960, Lynch and Edelman, 1996, Brophy et al., 2003) and valved (Foa, 1960, Bussing and Pappas, 1996) inlets such as those used in pulsejet applications. However, large external losses for valveless inlets and leakage problems and poor off-design performance for valved inlets are serious handicaps for unsteady inlets (Bussing and Pappas, 1996).

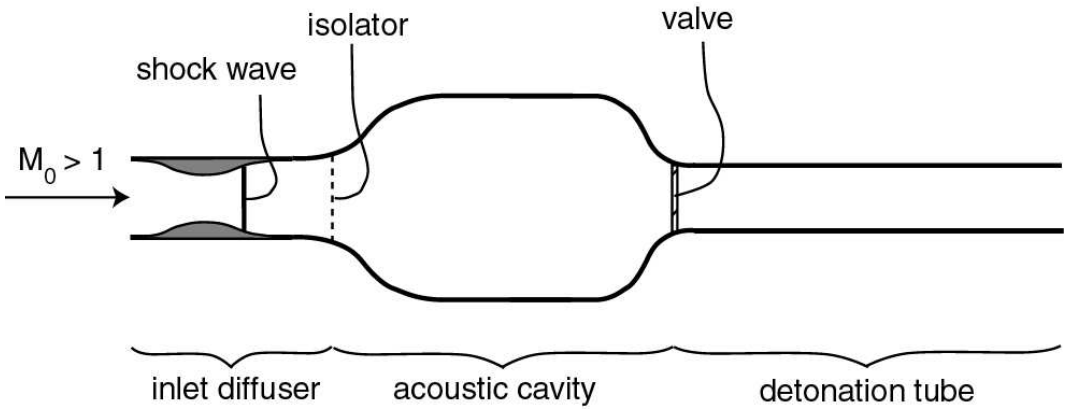

Figure 5.1: Schematic representation of a single-tube PDE.

The steady inlet is separated from the plenum by an isolator (a grid or screen similar to what is used in ramjets). Flow perturbations generated by combustion or valve motion are assumed to be isolated within the plenum. The inlet flow is unaffected by these flow perturbations and remains started. Hence, the single-tube PDE considered has a steady inflow entering the plenum and an unsteady outflow at the detonation tube exit. This is true in practice when the inlet flow is choked during supersonic flight. The valve is located at the upstream end of the detonation tube, separating it from the plenum. We assume that the valve opens and closes instantaneously.

Although there are transients associated with finite opening and closing times, they must be modeled by more complex multi-dimensional numerical simulations and are outside the scope of this one-dimensional model. The fuel injection system is located downstream of the valve. Fuel is injected only during the filling process and is assumed to mix instantaneously with the flowing air. As there is no wide agreement on the influence of nozzles on PDE performance, the effect of exit nozzles on detonation tube performance is not considered in this study and the detonation tube is assumed to be straight.

5.3 Control volume analysis

The performance of the air-breathing PDE is determined by performing an unsteady open-system control volume analysis. The control volume Ω considered, displayed in Fig. 5.2, is stationary with respect to the engine. The engine is attached to the vehicle through a structural support. The control surface Σ passes through the engine valve plane and encompasses the detonation tube, extending far upstream of the inlet plane. The side surfaces are parallel to the freestream velocity. We consider the equations for mass, energy, and momentum for this control volume.

5.3.1 Mass conservation

The general unsteady conservation equation for mass in the control volume Ω bounded by the surface Σ can be written

$$\frac{d}{dt}\int_{\Omega}\rho dV + \int_{\Sigma}\rho(\mathbf{u}\cdot\mathbf{n})dS = 0\ . \tag{5.1}$$

Note that the velocities are given in the engine reference frame. The first integral is equal to the mass $\mathcal{M}$ of fluid in the control volume. Due to the unsteady operation of the engine, there is temporary mass storage through a cycle so that $d\mathcal{M}/dt \neq 0$, but the average mass storage must equal zero for cyclic operation. Assuming reversible external flow, the pressure and velocity are constant over the entire control surface,

except inside the detonation tube. Evaluating the surface integrals results in

$$\frac{d\mathcal{M}}{dt} + \dot{m}_V(t) - \rho_0 u_0 A_V + \dot{m}_s = 0 \ . \tag{5.2}$$

As mentioned previously, there is no average mass storage in the engine during steady flight, so we integrate the mass conservation equation between the inlet and the valve plane over a cycle.

$$\int_0^\tau \dot{m}_V(t)dt = \tau \dot{m}_0 \tag{5.3}$$

Integrating Eq. 5.2 over a cycle, we can calculate the mass flow of air through the side surfaces of Ω.

$$\dot{m}_s = \rho_0 u_0 (A_V - A_0) \tag{5.4}$$

5.3.2 Momentum conservation

The general unsteady conservation equation for momentum in the control volume is

$$\frac{d}{dt}\int_\Omega \rho \mathbf{u} dV + \int_\Sigma \rho \mathbf{u}(\mathbf{u}\cdot\mathbf{n})dS = \Sigma \mathbf{F} \ . \tag{5.5}$$

The forces to consider for our engine are the pressure forces and the reaction to the thrust carried through the structural support. If we assume that the top and bottom sides of the control volume are sufficiently distant from the engine, then the flow crosses them with an essentially undisturbed velocity component in the flight direction. Applying the previous equation in the flight direction, we obtain

$$\frac{d}{dt}\int_\Omega \rho u dV + \dot{m}_V(t)u_V(t) - \rho_0 u_0^2 A_V + \dot{m}_s u_0 = -A_V(P_V(t) - P_0) + F(t) \ . \tag{5.6}$$

Using Eq. 5.4, we obtain an expression for the instantaneous thrust (Hill and Peterson, 1992)

$$F(t) = \dot{m}_V(t)u_V(t) - \dot{m}_0 u_0 + A_V(P_V(t) - P_0) + \frac{d}{dt}\int_\Omega \rho u dV \ . \tag{5.7}$$

The last term represents the unsteady variation of momentum inside the control volume.

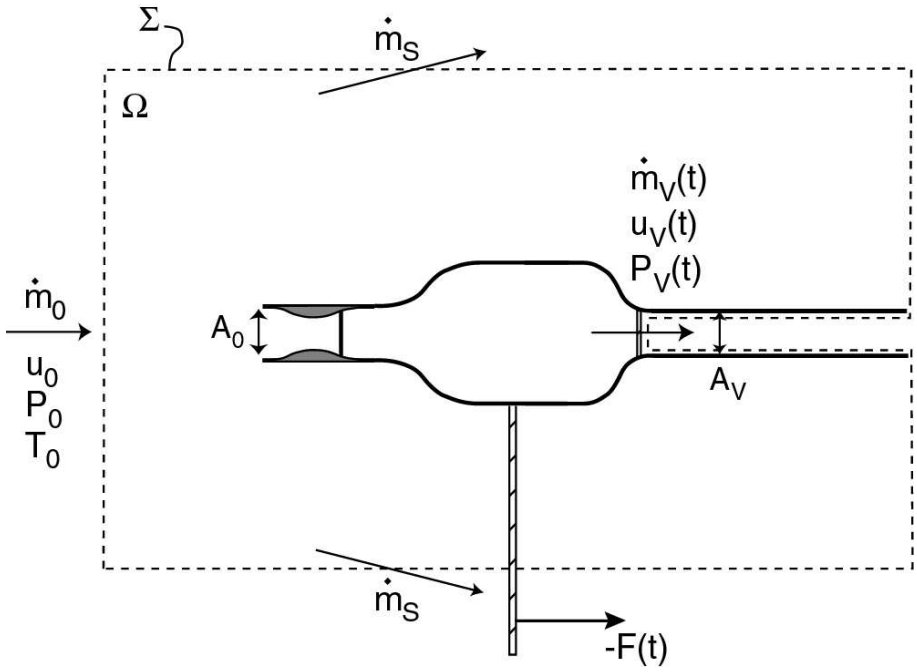

Figure 5.2: Control volume considered for analysis of single-tube PDE.

5.3.3 Energy conservation

In the absence of body forces or heat release, the general unsteady conservation equation for energy in the control volume Ω is

$$\frac{d}{dt}\int_{\Omega}\rho(e+u^2/2)dV+\int_{\Sigma}\rho(e+u^2/2)(\mathbf{u}\cdot\mathbf{n})dS=-\int_{\Sigma}P(\mathbf{u}\cdot\mathbf{n})dS\ . \tag{5.8}$$

Heat is released only in the detonation tube, which is outside our control volume Ω. Evaluating each term leads to

$$\frac{d}{dt}\int_{\Omega}\rho(e+u^2/2)dV+\dot{m}_V(t)(e+u^2/2)_V-\rho_0u_0A_V(e+u^2/2)_0+\dot{m}_s(e+u^2/2)_0= P_0u_0A_V-P_V(t)u_V(t)A_V-\frac{P_0}{\rho_0}\dot{m}_s\ . \tag{5.9}$$

Simplifying these terms using Eq. 5.4, we obtain the usual form of the unsteady energy equation for an adiabatic system with no external work.

$$\frac{d}{dt}\int_{\Omega}\rho(e+u^2/2)dV+\dot{m}_V(t)h_{tV}(t)-\dot{m}_0h_{t0}=0 \tag{5.10}$$

Integrating over a cycle, the first term vanishes because there is no average energy storage in the control volume.

$$\int_o^{\tau}\dot{m}_V(t)h_{tV}(t)dt=\tau\dot{m}_0h_{t0} \tag{5.11}$$

The energy conservation equation requires that the flux of stagnation enthalpy has to be conserved during a cycle between the inlet and the valve plane.

5.3.4 Thrust calculation

The average thrust is calculated by integrating Eq. 5.7 over a complete cycle

$$\begin{aligned}\overline{F}&=\frac{1}{\tau}\int_0^{\tau}F(t)dt\\&=\frac{1}{\tau}\int_0^{\tau}\dot{m}_V(t)u_V(t)dt+\frac{1}{\tau}\int_0^{\tau}A_V(P_V(t)-P_0)dt+\frac{1}{\tau}\int_0^{\tau}\frac{d}{dt}\int_{\Omega}\rho udVdt-\dot{m}_0u_0\end{aligned}$$

.

(5.12)

The unsteady term can be integrated and corresponds to the variation of total momentum in the control volume during a cycle.

$$\frac{1}{\tau}\int_0^{\tau}\frac{d}{dt}\int_{\Omega}\rho udVdt=\frac{1}{\tau}\left[\int_{\Omega}\rho udV\right]_0^{\tau} \tag{5.13}$$

During steady flight, the total momentum in the control volume has a periodic behavior so the unsteady term vanishes when averaged over one period. The only situation in which the mass, momentum, and energy storage terms lead to nonzero cycle-averaged contributions are during unsteady flight conditions such as acceler-

ation or deceleration. Even under these conditions, significant unsteady terms will occur only if the accelerations are extremely large, on the order of u_0^2/L_E, where L_E is the engine size. For this study, we restrict ourselves to performance calculations during steady flight conditions.

During a cycle, the valve is closed from time 0 to t_{close} and open from t_{close} to τ. During the closed part of the cycle, the momentum contribution in Eq. 5.12 (first term on right-hand side) vanishes. The pressure contribution (second term on right-hand side) corresponds to the conventional detonation tube impulse I_{dt}.

$$\int_0^{t_{close}} A_V(P_V(t) - P_0)dt = I_{dt} \tag{5.14}$$

Hence, the average thrust is given by

$$\overline{F} = \frac{1}{\tau} I_{dt} + \frac{1}{\tau}\int_{t_{close}}^{\tau} \dot{m}_V(t)u_V(t)dt + \frac{1}{\tau}\int_{t_{close}}^{\tau} A_V(P_V(t) - P_0)dt - \dot{m}_0 u_0 \; . \tag{5.15}$$

The average thrust is the sum of contributions from the detonation tube impulse, the momentum and pressure at the valve plane during the open part of the cycle, and the ram momentum. In order to evaluate this thrust, we need an estimate of the detonation tube impulse and of the momentum and pressure contributions at the valve plane during the part of the cycle when the valve is open. These terms have to be estimated by modeling the filling process, which requires a detailed investigation of the gas dynamics.

5.4 Detonation tube dynamics

In order to estimate the different terms in the PDE thrust equation (Eq. 5.15), it is instructive to study the dynamics of the detonation tube during one cycle. This cycle has three main components, which are illustrated in detail in Fig. 5.3: detonation and blowdown of the burned gases, purging of the expanded burned products, and refilling of the tube with fresh reactants. The detonation/blowdown process was studied in detail in Chapter 4, and occurs when the valve is closed (from 0 to t_{close}). The purging

and filling processes occur when the valve is open (from t_{close} to τ). The cycle time is the sum of the valve close and open times, the latter being the sum of the fill and purging times.

$$\tau = t_{close} + t_{open} = t_{close} + t_{fill} + t_{purge} \tag{5.16}$$

Experiments have shown that purging the burned gases (usually with air) is necessary to avoid pre-ignition of the fresh mixture before the detonation initiation. Because the air entering the plenum is decelerated and compressed through the inlet due to the ram effect, the plenum acts as a high-pressure air reservoir that periodically fills the detonation tube. Although the unsteady flow in the detonation tube is complex and involves many wave interactions, the main physical processes occurring during a cycle have been well documented in previous studies.

5.4.1 Detonation/blowdown process

A detonation is assumed to be instantaneously initiated at the closed end of the tube. The detonation propagates to the open end of the tube, starting the blowdown process. The specific gas dynamics during this process are described in detail in Section 4.2 for a static detonation tube. It was shown that as the detonation exits the tube, a reflected wave propagates back towards the closed valve. This reflected wave is an expansion wave for hydrocarbon-air mixtures as well as for lean and slightly rich hydrogen-air mixtures. After interacting with the Taylor wave, this reflected expansion accelerates the fluid towards the tube's open end and decreases the pressure at the closed end of the tube. The exhaust gas is characterized by low pressure and high flow velocity downstream of the tube exit. The pressure inside the tube typically decreases below the ambient pressure (Zitoun and Desbordes, 1999) at the end of the blowdown process before returning to ambient pressure after about $20t_1$. Zitoun and Desbordes (1999) suggested to use the sub-ambient pressure part of the cycle for the self-aspiration of air in an air-breathing PDE configuration. This suggests that the valve for a given tube must be closed for at least $10t_1$ to maximize the impulse per cycle.

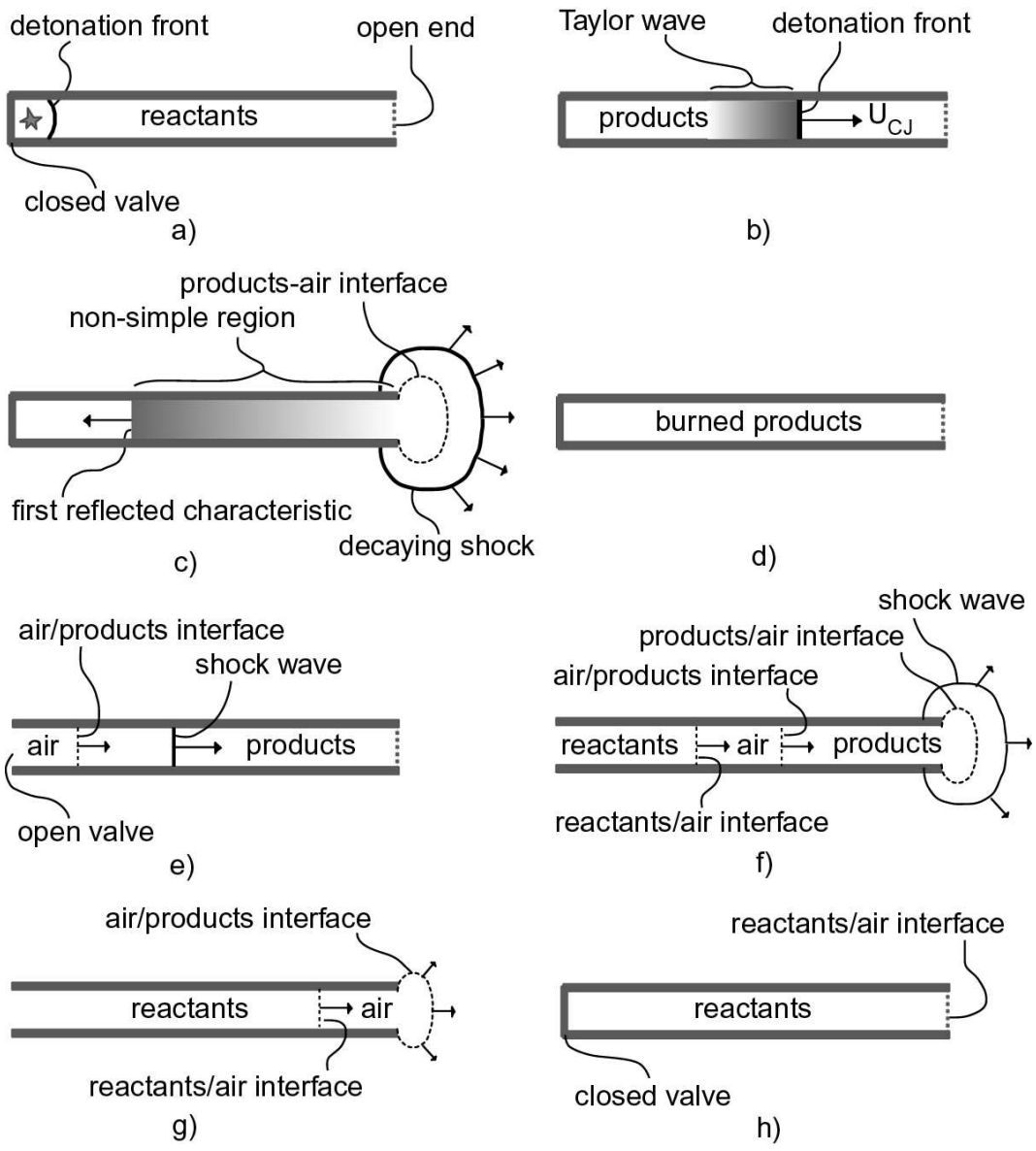

Figure 5.3: PDE cycle schematic for a detonation tube. a) The detonation is initiated at the closed end of the tube and b) propagates towards the open end. c) It diffracts outside as a decaying shock and a reflected expansion wave propagates to the closed end, starting the blowdown process. d) At the end of the blowdown process, the tube contains burned products at rest. e) The purging/filling process is triggered by the opening of the valve, sending a shock wave in the burned gases, followed by the air-products contact surface. f) A slug of air is injected before the reactants for purging. g) The purging air is pushed out of the tube by the reactants. h) The reactants eventually fill the tube completely and the valve is closed.

In an air-breathing PDE, the flow in the detonation tube differs from the static case because of the interaction between the detonation and filling processes. The

detonation propagation is affected by the flow following the filling process. The valve is assumed to close instantaneously prior to the detonation initiation. Closing the valve sends an expansion wave through the tube to decelerate the flow created by the filling process. This expansion wave decreases the pressure and density inside the tube, causing a reduction in detonation pressure and thrust. However, a detonation that is initiated immediately after valve closing will overtake the expansion wave within the tube. After this interaction, the detonation will propagate into the uniform flow produced by the filling process. The thrust for this situation will be different from the case of a detonation propagating into a stationary mixture but can be calculated if we assume ideal valve closing and detonation initiation. When the detonation propagates into a non-uniform moving flow, the subsequent gas dynamic processes are similar to the static case, although the strength of the various waves generated is a function of the moving flow velocity.

5.4.2 Purging/filling process

At the end of the detonation/blowdown process, the valve at the upstream end of the tube opens instantaneously. This valve separates high-pressure air that was compressed due to the ram effect through the inlet, and burned gases at ambient pressure and elevated temperature. Opening the valve causes the high-pressure air to expand into the detonation tube. A shock wave is generated and propagates into the detonation tube, followed by a contact surface between the fresh air and the burned products. Fuel is not injected until after the burned gases have been purged. This prevents pre-ignition of the fresh mixture as mentioned before. An unsteady expansion wave propagates upstream of the valve inside the plenum, setting up a steady expansion of the plenum air into the detonation tube. Thus, the filling process is characterized by a combination of unsteady and steady expansions.

The gas dynamics of the flow are complex and involve multiple wave interactions, but in the interest of simplicity, we will attempt to characterize the filling process with a few key quantities. In order to do so, we analyzed the problem numerically using

Amrita (Quirk, 1998). The simulations employed the non-reactive Euler equations in an axisymmetric domain using a Kappa-MUSCL-HLLE solver. The configuration tested appears in Fig. 5.4, and consists of a large cavity connected by a smooth area change to a straight tube open to a half-space. The simulation was started with high-pressure air in the cavity at conditions given by $P_C/P_0 = P_R$ and $T_C/T_0 = P_R^{(\gamma-1)/\gamma}$. The burned gases in the tube were at pressure P_0 and elevated temperature $T_f = 7.69T_0$. The value used for T_f, on the order of 1700 K for a hydrogen-fueled PDE flying at 10,000 m altitude, is representative of the burned gas temperature at the end of the blowdown process. The air outside the detonation tube is at pressure P_0 and temperature T_0. The problem has two contact surfaces. One contact surface is the inlet air-burned gas interface at the valve end, and the second is the burned gas–outside air interface at the tube exit. Numerical schlieren images of the filling process are given in Fig. 5.4.

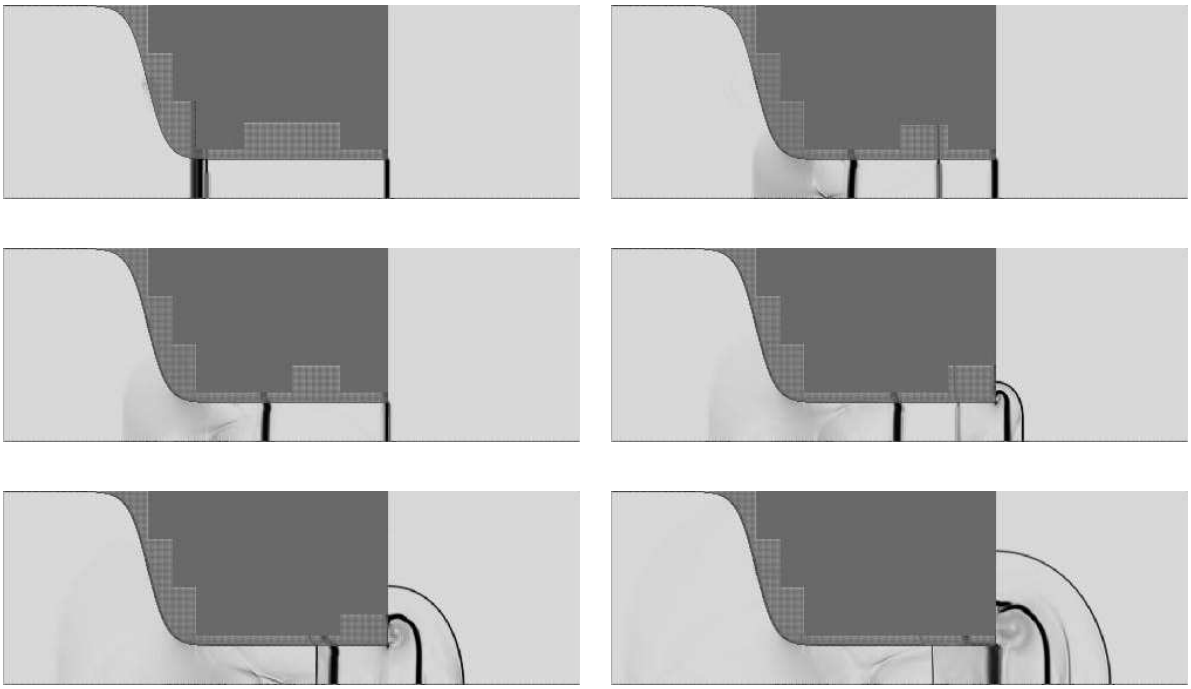

Figure 5.4: Numerical schlieren images of the filling process. $P_R = 8$, $T_f/T_0 = 7.69$, $\gamma = 1.4$.

When the shock wave formed by opening the valve reaches the open end of the detonation tube, it diffracts outwards and eventually becomes a decaying spherical

shock. This diffraction process is similar to that of the shock wave resulting from the detonation and is characterized by low pressure and high flow velocity downstream of the tube exit. When interacting with the area change at the open end, a reflected shock is generated, since the detonation tube contains hot burned products at the same pressure but with a lower density than the outside air (soft-hard interaction). The reflected shock propagates upstream and decelerates the flow that is moving towards the open end. However, this reflected shock interacts with the expansion waves that propagate back into the tube from the corners and accelerate the flow towards the open end, causing a decrease in pressure. This weakened shock now interacts with the inlet air-burned gas contact surface. This soft-hard shock-contact surface interaction generates a transmitted shock and a reflected expansion wave that propagates towards the tube's open end. When the flow behind the inlet air-burned gas contact surface is supersonic (for $P_R > 5$), the transmitted shock can either be steady or be convected by the flow towards the open end. The reflected expansion reflects again off the burned gas-outside air contact surface, diffracting outside the tube to generate a shock wave located downstream of the tube exit.

For low pressure ratios ($P_R < 5$), the simulations show that the initial flow and subsequent wave interactions inside the tube are essentially one-dimensional. Multi-dimensional effects are observed only within one tube diameter of the tube exit, just after the exhaust of the incident shock. The multi-dimensional corner expansion waves propagate back into the tube and quickly catch up to merge with the reflected shock. The same behavior is observed at higher pressure ratios, although two-dimensional waves are generated when the valve opens and closely follow the inlet air-burned gas contact surface (Fig. 5.4). In practice, due to the finite time allowed for the detonation and blowdown processes, the flow in the tube before valve opening will not be quite uniform. It may contain residual waves still propagating in the tube, which can only be captured by multi-cycle numerical simulations that model the moving components and reacting gas chemistry of PDE operation. After this description of the main processes occurring in a cycle, we discuss in detail how each was modeled.

5.5 Modeling of the filling process

We now discuss our modeling of the filling process, which is critical to determining the momentum and pressure contributions at the valve plane necessary to computing the thrust (Eq. 5.15). Moreover, the filling process also determines the conditions in the tube prior to detonation initiation, and so strongly influences the resulting impulse. The plenum connects the steady inlet to the unsteady valve so the flow between the plenum and the detonation tube is coupled. Thus, the average conditions in the plenum must be modeled accurately.

5.5.1 Plenum/detonation tube coupling

The average plenum conditions can be estimated by analyzing the control volume shown in Fig. 5.5. The cycle time is assumed to be much larger than the characteristic acoustic transit time in the plenum so the plenum properties are assumed to be spatially uniform. The plenum has a constant incoming mass flow rate equal to $\dot{m}_0$ because of choked flow through the inlet, and an outgoing mass flow rate when the valve is open. The outgoing mass flow rate is defined as the flow rate at the valve plane $\dot{m}_V(t)$. Since the plenum is located downstream of the inlet, its inflow is assumed to have a low velocity. We start with the mass, momentum, and energy conservation equations for the control volume V_C defined in Fig. 5.5:

$$V_C \frac{d\rho_C}{dt} = \dot{m}_0 - \dot{m}_V(t) \ , \tag{5.17}$$

$$\frac{d}{dt}\int_{V_C} \rho u dV + \dot{m}_V(t) u_V(t) = A_2 P_{t2} - A_V P_V(t) + (A_V - A_2) P_C(t) \ , \tag{5.18}$$

$$\frac{dE_C}{dt} = \dot{m}_0 h_{t2} - \dot{m}_V(t) h_{tV}(t) \ . \tag{5.19}$$

In order to determine the average plenum conditions, we average the previous equations over a cycle. Although the mass, momentum, and energy in the control volume

will vary, there can be no accumulation in the plenum over a cycle during periodic operation. This yields

$$\overline{\dot{m}_V(t)} = \dot{m}_0 \ , \tag{5.20}$$

$$\overline{\dot{m}_V(t)u_V(t)} = A_2 P_{t2} - A_V \overline{P_V(t)} + (A_V - A_2)\overline{P_C(t)} \ , \tag{5.21}$$

$$\overline{\dot{m}_V(t)h_{tV}(t)} = \dot{m}_0 h_{t2} \ . \tag{5.22}$$

where $\overline{()}$ indicates temporal averaging over a cycle.

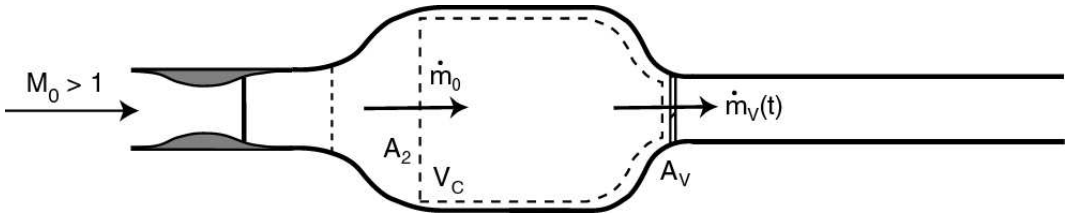

Figure 5.5: Control volume V_C considered for analysis of flow in the plenum.

Based on our numerical simulations of the filling process, we model some of the properties at the valve plane as piecewise constant functions of time. The velocity $u_V(t)$ and mass flow rate $\dot{m}_V(t)$ are equal to zero when the valve is closed and take on values u_V^o and $\dot{m}_V^o$ when the valve is open. The mass conservation equation yields

$$t_{open}\dot{m}_V^o = \tau \dot{m}_0 \ . \tag{5.23}$$

Assuming that the plenum volume is much larger than the detonation tube volume, the plenum pressure will be approximately constant throughout a cycle. Deviations from this are discussed further in Section 5.6.1. The pressure at the valve plane equals the average pressure in the plenum $\overline{P_C}$ when the valve is closed and equals P_V^o when the valve is open. The momentum equation becomes

$$\dot{m}_0 u_V^o = A_2(P_{t2} - \overline{P_C}) - \frac{t_{open}}{\tau} A_V(\overline{P_C} - P_V^o) \ . \tag{5.24}$$

The total temperature at the valve plane equals the average total temperature in the plenum $\overline{h_{tC}}$ when the valve is closed and equals h^o_{tV} when the valve is open. Rewriting the averaged energy equation in terms of the temperature yields

$$T^o_{tV} = T_{t2} \; . \tag{5.25}$$

The average conditions in the plenum, described by Eqs. 5.23, 5.24, and 5.25, must be evaluated by considering the flow in the detonation tube when the valve is open. Because the valve plane corresponds to a geometrical throat, either subsonic or sonic flow at the valve plane may exist.

5.5.1.1 Subsonic flow at the valve plane

When the valve opens, the pressure differential at the valve plane generates an unsteady expansion wave that propagates upstream in the plenum (Fig. 5.4). This unsteady expansion sets up a steady expansion through the area change between the plenum and the detonation tube, and decays when propagating through the area change. We assume that its propagation time through the area change is much smaller than the time necessary to fill the detonation tube. Thus, we neglect the initial transient corresponding to the unsteady expansion propagation through the area change.

The flow configuration consists of a left-facing unsteady expansion in the plenum, a steady expansion through the area change, and a right-facing shock wave propagating in the tube followed by the burned gases-fresh air contact surface. This flow configuration is identical to that encountered in shock tubes with positive chambrage (Glass and Sislian, 1994). The unsteady expansion in the plenum is very weak after its propagation through the area change. For example, for an area ratio of 10, it modifies the plenum stagnation temperature by less than 2.3% and the stagnation pressure by less than 0.3%. Thus, we assume a large area ratio between the plenum and the valve and we ignore it in our calculations.

Based on the previous assumptions, we model the flow during the filling process with the flow configuration shown in Fig. 5.6. The interactions of the shock wave with

the open end and any subsequent reflected waves are ignored. These assumptions are discussed further with respect to the results of numerical simulations of the filling process.

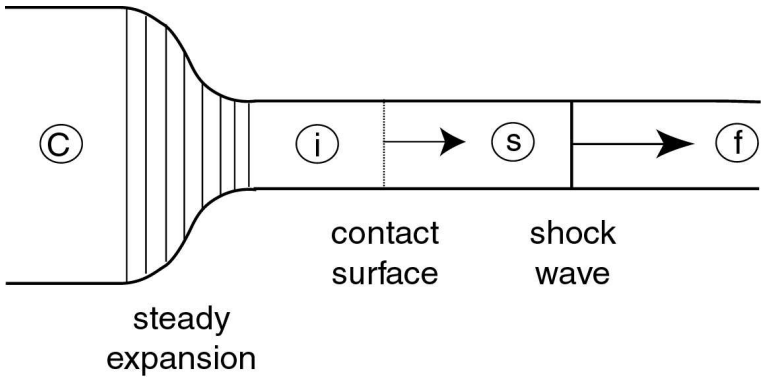

Figure 5.6: Flow configuration used to model the filling process in the case of subsonic flow at the valve plane.

Since the filling process is modeled with a steady expansion between the plenum and the valve plane (Fig. 5.6), the stagnation temperature is constant across it and the average temperature in the plenum is estimated as $\overline{T_C} \approx \overline{T_{tC}} = \overline{T_{tV}} = T_{t2}$ from Eq. 5.25. Hence, the average temperature inside the plenum is equal to the total temperature downstream of the inlet. The conditions at the valve plane are determined from the average plenum conditions as a function of the velocity u_V^o, using the isentropic flow relationships through a steady expansion wave. The ratio between the open time and the cycle time is equal to the ratio of the mass flow rate at the valve plane and $\dot{m}_0$: $t_{open}/\tau = \dot{m}_0/\dot{m}_V$. After some algebra, Eq. 5.24 yields the following result for the average plenum pressure as a function of the velocity at the valve plane.

$$\overline{P_C} = P_{t2} - \frac{\dot{m}_0 u_V^o}{A_2} + \frac{\dot{m}_0 R \overline{T_C}}{A_2 u_V^o} \left(1 - \frac{{u_V^o}^2}{2C_p \overline{T_C}}\right)^{-\frac{1}{\gamma-1}} \left[1 - \left(1 - \frac{{u_V^o}^2}{2C_p \overline{T_C}}\right)^{\frac{\gamma}{\gamma-1}}\right] \quad (5.26)$$

The velocity at the valve plane is determined by matching the flow in the plenum with the downstream conditions in the detonation tube. Before the valve opens, the detonation tube contains burned gases at atmospheric pressure. The initial pressure ratio across the valve determines the shock Mach number and the velocity at the valve

plane (also the velocity of the contact surface). Matching the interface conditions yields the classical solution for the shock tube problem with positive chambrage (Glass and Sislian, 1994).

$$\overline{P_C} = P_0 \frac{1 + \frac{2\gamma_b}{\gamma_b+1}(M_S^2 - 1)}{\left[1 - \frac{2(\gamma-1)}{(\gamma_b+1)^2}\left(\frac{c_f}{\overline{c_C}}\right)^2 (M_S - 1/M_S)^2\right]^{\frac{\gamma_b}{\gamma_b-1}}} \tag{5.27}$$

The velocity at the valve plane is equal to the post-shock velocity in the burned gases

$$\frac{u_V^o}{c_f} = \frac{2}{\gamma_b + 1}\left(M_S - \frac{1}{M_S}\right) . \tag{5.28}$$

We solve for M_S by equating Eqs. 5.26 and 5.27, substituting Eq. 5.28 for u_V^o. Once M_S is known, all other variables of the system are determined using the relationships across the shock and the expansion wave.

5.5.1.2 Sonic flow at the valve plane

The velocity at the valve plane becomes sonic when the pressure ratio across the valve exceeds a critical value, given by $\overline{P_C}/P_V = ((\gamma+1)/2)^{\frac{\gamma}{\gamma-1}}$. The flow configuration (Fig. 5.7) includes an additional unsteady expansion between the valve plane and the fresh air-burned gases contact surface. This unsteady expansion accelerates the flow from sonic at the valve plane to supersonic behind the contact surface and decouples the plenum flow from the flow in the detonation tube. The velocity at the valve plane equals the speed of sound

$$u_V^o = c^* = \sqrt{\frac{2\gamma}{\gamma+1} R \overline{T_C}} . \tag{5.29}$$

Using the relationships for choked flow at the valve plane, it is possible to directly estimate the average plenum pressure from Eq. 5.24.

$$\overline{P_C} = P_{t2} - \frac{\dot{m}_0 c^*}{\gamma A_2}\left[\gamma + 1 - \left(\frac{\gamma+1}{2}\right)^{\frac{\gamma}{\gamma-1}}\right] \tag{5.30}$$

The properties at the valve plane are given by the standard isentropic relations and the sonic condition.

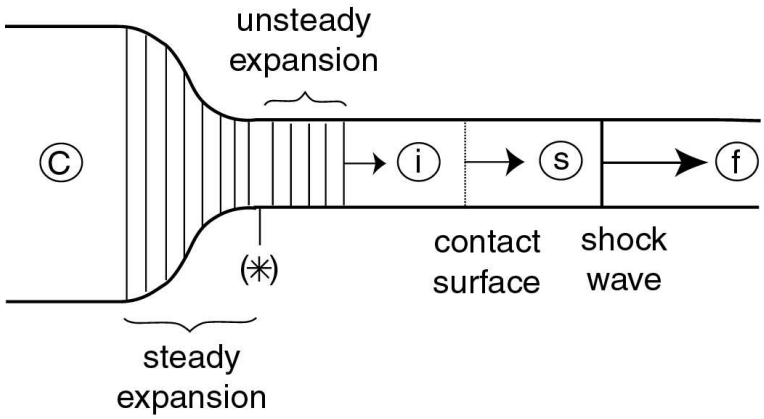

Figure 5.7: Flow configuration used to model the filling process in the case of sonic flow at the valve plane.

The flow in the detonation tube is calculated from a pressure-velocity diagram by matching conditions across the interface and solving for the shock Mach number (Glass and Sislian, 1994).

$$\frac{\overline{P_C}}{P_0} = \frac{1 + \frac{2\gamma_b}{\gamma_b+1}(M_S^2 - 1)}{\left[\sqrt{\frac{\gamma+1}{2}} - \frac{\gamma-1}{\gamma_b+1}\frac{c_f}{\overline{c_C}}\left(M_S - 1/M_S\right)\right]^{\frac{2\gamma}{\gamma-1}}} \tag{5.31}$$

The velocity of the contact surface equals the post-shock velocity.

5.5.1.3 Average plenum conditions

The coupled flow between the plenum and the detonation tube results in average plenum conditions that are different from the stagnation conditions downstream of the inlet. Although the average plenum stagnation temperature equals the inlet stagnation temperature, the average plenum pressure is lower than the stagnation pressure downstream of the inlet due to the flow unsteadiness. Opening the valve generates an unsteady expansion that propagates into the plenum, while closing the valve generates a shock wave. The entropy increase associated with these unsteady waves results in losses in the plenum stagnation pressure as compared with the ideal steady-flow

case in which the stagnation pressure remains constant. Although the actual waves are not represented in our averaged model, the average unsteady losses associated with them are taken into account through the momentum equation (Eq. 5.24). The ratio of the average plenum pressure to the stagnation pressure downstream of the inlet is shown as a function of the flight Mach number in Fig. 5.8. Values are given only for $M_0 \geq 1$ because of the assumption of choked inlet flow and constant inflow in the plenum. For subsonic flight, the constant inflow assumption is not valid since propagating pressure waves can modify the inlet flow. In particular, the incoming mass flow rate in the plenum can vary over time and does not equal a constant $\dot{m}_0$.

The ratio $\overline{P_C}/P_{t2}$ decreases with increasing flight Mach number when the flow at the valve plane is subsonic and increases when the flow becomes sonic. For subsonic flow, increasing losses occur as the flight Mach number increases. However, for sonic flow, the decoupling of the plenum flow from the detonation tube flow limits the losses. In this case, the ratio $\overline{P_C}/P_{t2}$ increases with increasing flight Mach number because the stagnation pressure increases faster than the velocity at the throat (second term of Eq. 5.30). In the worst case of Fig. 5.8, $\overline{P_C}$ is only 2.6% lower than P_{t2}. However, this value can become significant (greater than 10%) if the ratio of the plenum area to the inlet capture area A_2/A_0 is decreased.

In our calculations, we assumed fixed valve area A_V and valve close time t_{close}. Other parameters such as valve open time and detonation tube length are determined by the periodicity of the system. The open time is determined by the mass balance in the plenum (Eq. 5.23)

$$t_{open} = \frac{t_{close}}{\frac{\dot{m}_V^o}{\dot{m}_0} - 1} \, . \tag{5.32}$$

Another option would be to fix the open time and vary the valve area in order to satisfy Eq. 5.23. As shown in Fig. 5.8, the open time increases with decreasing flight Mach number because of the decrease in the mass flow rate at the valve plane. The fixed valve area limits $\dot{m}_V^o$. There is a critical value of the flight Mach number at which $\dot{m}_V^o$ equals $\dot{m}_0$, corresponding to an infinite open time (Eq. 5.32) . This critical value depends on the ratio of the valve area to the inlet capture area and increases with

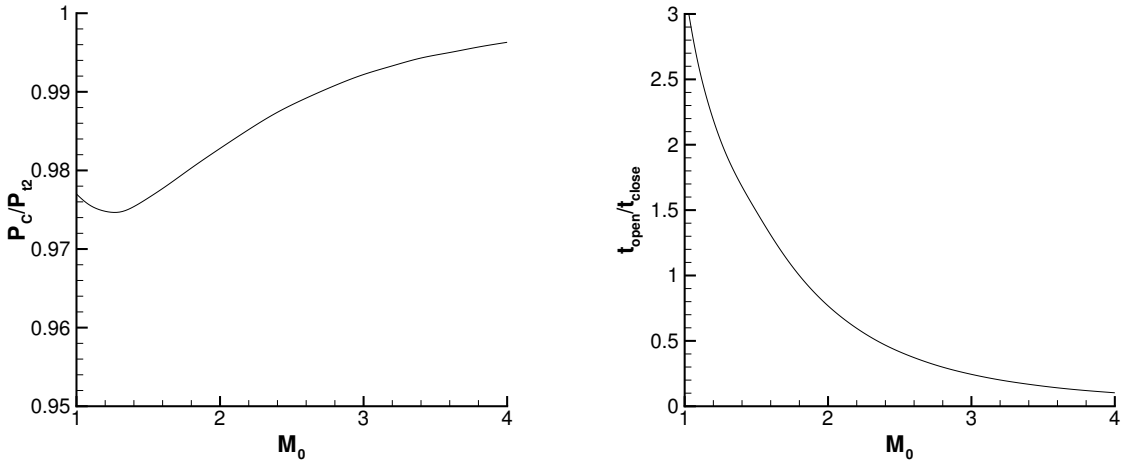

Figure 5.8: Ratio of the average pressure in the plenum to the total pressure downstream of the inlet (left) and ratio of the open time to the close time (right) as a function of the flight Mach number. $P_0 = 0.265$ bar, $T_0 = 223$ K, $A_0 = 0.004$ m^2, $A_2 = 0.04$ m^2, $A_V = 0.006$ m^2.

decreasing A_V/A_0. For realistic values of this parameter, this behavior is observed at subsonic flight conditions. In subsonic flight, the inlet flow is strongly affected by the unsteady flow in the plenum and our model is no longer valid. In practice, when $\dot{m}_V^o$ approaches $\dot{m}_0$, the system will adjust by sending pressure waves upstream in order to modify the inlet flow. These pressure waves decrease the inlet mass flow rate and keep the open time finite. Although our model does not capture this phenomenon, it shows that there is a strong coupling between the mass flow rate at the valve plane and the open time. This coupling and its associated limitations have to be taken into account.

It is also possible to constrain the system by prescribing the valve area, the close time and the open time. After some transient, the system will eventually reach a cyclic limit corresponding to average conditions that are different from those for the free system we calculated. However, there are limitations to this forced system. If the open time or the valve area prescribed are too small, the plenum will accumulate mass during the transient. The resulting plenum pressure may exceed the stagnation pressure downstream of the inlet, and cause it to unstart. This behavior has been observed by Wu et al. (2003), who prescribe the geometry, t_{close} and t_{open} in their

numerical simulations. It is very important to be aware of these limitations when constraining the system. They can be predicted only by multi-dimensional numerical simulations of the coupled system, including the moving valve.

5.5.2 Comparison with numerical simulations of the filling process

The model predictions of the filling process are compared with the results of the numerical simulations with Amrita (Quirk, 1998) described previously. The quantities of interest are the average velocity and pressure at the valve plane and the average filling velocity. The valve plane velocity and pressure were calculated from the two-dimensional simulations by spatially and temporally averaging these quantities along the valve plane. The average filling velocity was calculated as the average velocity of the inlet air-burned gases contact surface between the valve plane and the tube exit. These quantities are shown in Fig. 5.9 as a function of the initial pressure ratio P_R for both model and simulations.

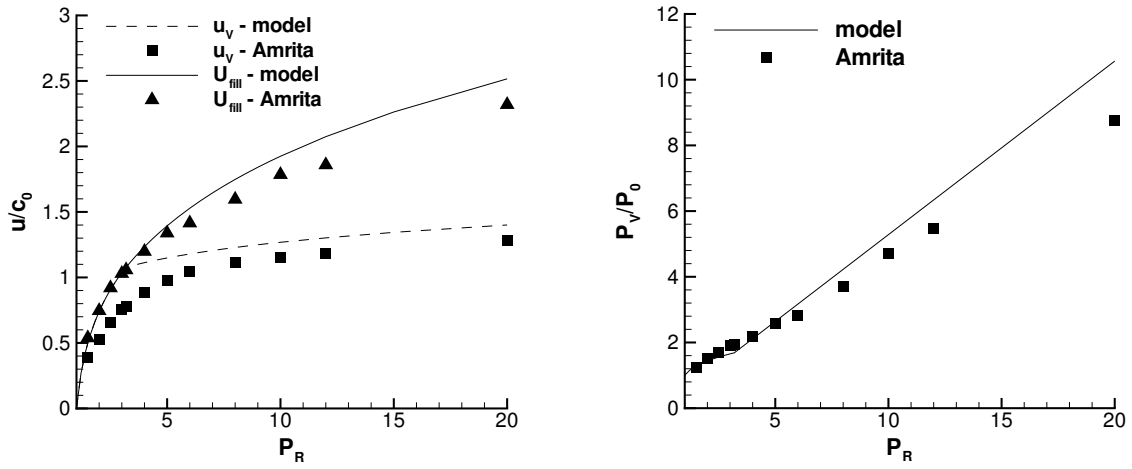

Figure 5.9: Comparison of model predictions and numerical simulations with Amrita (Quirk, 1998) for the velocity at the valve plane, the average filling velocity, and the pressure at the valve plane. $T_f/T_0 = 7.69$, $\gamma = 1.4$.

According to our one-dimensional model, the flow at the valve plane is expected to become sonic above a critical pressure ratio equal to 3.19. For pressure ratios

below this value, the flow configuration is that of Fig. 5.6, and the velocity at the valve plane is equal to the velocity of the contact surface: $u_V = U_{fill}$. For higher values of P_R, the flow configuration is that of Fig. 5.7; the flow is sonic at the valve plane and an unsteady expansion accelerates the flow to supersonic downstream of the valve plane. Thus, the values of u_V and U_{fill} are different. The velocity at the valve plane is predicted by the speed of sound at the throat c^*, while the filling velocity is predicted by the post-shock velocity. The two curves in Fig. 5.9 correspond to these two cases. The pressure at the valve plane P_V is predicted by the post-shock pressure for subsonic flow at the valve plane ($P_R < 3.19$) and by the pressure at the throat P^* for sonic flow ($P_R > 3.19$).

The model predictions for U_{fill} and P_V are in reasonable agreement with the results of the numerical simulations, with a maximum deviation of 11% and 20%, respectively. The model predictions for u_V are systematically higher than the numerical results by up to 40% near choking. The discrepancies between the model and the numerical simulations can be attributed to two factors. First, the model neglects the transient before the steady expansion is set up. The initial unsteady expansion that we ignore in our model generates a lower flow velocity than the steady expansion it sets up in the area change. Indeed, velocity profiles at the valve plane show that the velocity increases significantly while the steady expansion is being set up and reaches a value lower than that obtained from the model. This effect is expected to be stronger at lower values of the pressure ratio, as is observed in the numerical simulations. The second discrepancy between the model and the simulations is caused by the model not accounting for two-dimensional flow at the valve plane. Oblique waves are generated after valve opening and propagate back and forth between the tube walls behind the contact surface. These waves are strongest at the valve plane and may affect the average flow velocity and pressure. However, their influence is weaker far from the valve plane, and the contact surface velocity is in good agreement with our one-dimensional predictions. To investigate the effect of the reflected waves at the open end, we conducted simulations with an infinitely long tube with only minimal differences observed. This indicates that the discrepancies between the model and the

numerical simulations observed in Fig. 5.9 are primarily the result of the unsteady two-dimensional nature of the flow field associated with the valve opening.

The values of the flow properties at the end of the filling process determine the amount of mass and energy in the detonation tube prior to detonation initiation. Knowledge of these values is critical to accurately predicting the detonation tube impulse. The model assumes that the flow in the detonation tube is uniform, moves at a velocity U_{fill}, and has a pressure equal to the post-shock pressure. This crude approximation is based on one-dimensional considerations. The unsteady transient occurring when the valve opens, any reflected waves from the open end and further wave interaction, as well as the two-dimensional nature of the flow are neglected. In order to test the validity of this approximation, the pressure and velocity profiles along the centerline from our numerical simulations are plotted in Fig. 5.10 for $P_R = 8$. These profiles indicate that the flow inside the detonation tube, including a quasi-steady left-facing shock followed by a steady expansion near the open end, is relatively uniform in the upstream half of the tube but quite non-uniform in the downstream half. The quasi-steady shock is the result of the interaction of the reflected shock from the open end with the inlet air-burned gases contact surface. Our model tries to suitably represent the conditions in the tube at the end of the filling process by uniform average conditions that can then be used to estimate detonation tube impulse and engine performance. We calculated the spatial average of the pressure and velocity in the detonation tube at the end of the filling process from the numerical simulations and compared these values with our model predictions. The model predicts a pressure between 5.8% and 22.7% higher than that of the numerical simulations for values of P_R between 2 and 10. For the same pressure ratios, the model velocity is between -11.3% and +23.5% of the numerical results. These numbers are helpful to understand the influence of our approximations on the accuracy of our predictions and their potential consequence on performance parameters.

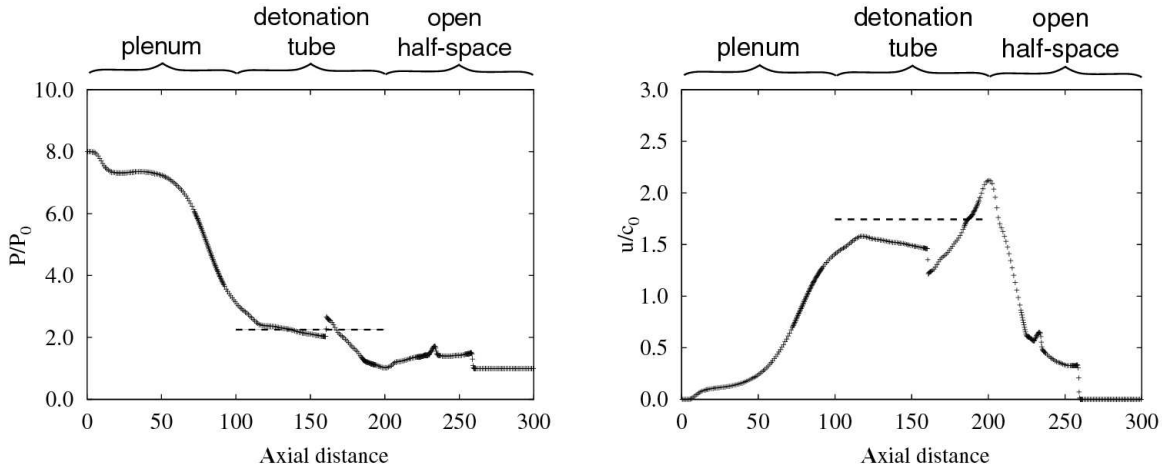

Figure 5.10: Pressure and velocity profiles along the centerline from the numerical simulations with Amrita (Quirk, 1998). The valve is located at an axial distance of 100 and the detonation tube exit is located at 200. The dashed line shows the value of the model prediction. $P_R = 8$, $T_f/T_0 = 7.69$, $\gamma = 1.4$.

5.6 Flow fluctuations in the engine

The unsteady pressure waves generated by valve closing and opening strongly affect the coupled flow in the plenum and the inlet. Since conventional steady inlets are sensitive to downstream pressure fluctuations, it is critical to be able to model these flow fluctuations in the engine. In the previous section, the averaging process was useful to determine the average values of the plenum properties. We now proceed to estimate the magnitude of the fluctuations during a cycle and how they influence the inlet flow.

5.6.1 Unsteady flow in the plenum

In order to model the unsteady flow in the plenum, we solve the unsteady mass and energy equations (Eqs. 5.17 and 5.19). These equations are not averaged as in the previous section but solved as a function of time. The flow downstream of the inlet has a low Mach number so we neglect the kinetic energy term when calculating the total energy and the total enthalpy in the plenum. The flow from the plenum into the detonation tube is modeled with a steady expansion in the area change. Hence, the total enthalpy is conserved between the plenum and the valve plane. Rewriting

the energy equation (Eq. 5.19) as an equation for temperature leads to the following system of equations

$$V_C \frac{d\rho_C}{dt} = \dot{m}_0 - \dot{m}_V(t) \ , \tag{5.33}$$

$$V_C \rho_C(t) \frac{dT_C}{dt} = \gamma \dot{m}_0 T_{t2} - \left[\dot{m}_0 + (\gamma - 1)\dot{m}_V(t)\right] T_C(t) \ . \tag{5.34}$$

This system of equations has to be solved separately for the closed part of the cycle [0, t_{close}], where $\dot{m}_V(t) = 0$ and for the open part of the cycle [t_{close}, τ] where $\dot{m}_V(t) \neq 0$. We approximate $\dot{m}_V(t)$ as constant during the open part of the cycle, as in the previous section, by assuming small variations in the plenum properties. For sufficiently large supersonic flight Mach numbers in which the flow at the valve plane during the filling process is choked, this approximation is justified. We seek the limit cycle solution corresponding to periodic behavior for this system of equations.

The solution for the density is straightforward within the assumptions of constant inflow and piecewise constant outflow in the plenum. The density varies linearly around its average value $\overline{\rho_C}$.

$$\rho_C(t) = \overline{\rho_C} + \frac{\dot{m}_0 t_{close}}{V_C}(t/t_{close} - 1/2) \quad \text{for} \quad 0 < t < t_{close} \tag{5.35}$$

$$\rho_C(t) = \overline{\rho_C} - \frac{\dot{m}_0 t_{close}}{2V_C} + \frac{\dot{m}_0 t_{close}}{V_C(1 - t_{close}/\tau)}(1 - t/\tau) \quad \text{for} \quad t_{close} < t < \tau \tag{5.36}$$

The limit cycle solution for the temperature has to satisfy the averaged energy equation, Eq. 5.22. Taking into account the temporal variation of the temperature in the plenum and using the conservation of total energy through a steady expansion, Eq. 5.25 can be expressed as

$$\frac{1}{t_{open}} \int_{t_{close}}^{\tau} T_C(t) dt = T_{t2} = \overline{T_C} \ . \tag{5.37}$$

Calculations were carried out for conditions corresponding to a PDE flying at 10,000 m and Mach 2 and operating at a frequency of 56.5 Hz (corresponding to the area

values given in Fig. 5.11). The solution for the temperature evolution was obtained numerically. An initial value of 350 K was prescribed for the temperature, and the calculation was run for several cycles. The solution converges to a periodic behavior after a few cycles (about five for the case shown in Fig. 5.11). The evolution of the density and temperature inside the plenum is represented in Fig. 5.11. After ten cycles, the average value of the temperature in the plenum during a cycle was found to be within 0.35% of $\overline{T_C}$. The average temperature during the open part of the cycle, corresponding to Eq. 5.37, was found to be within 0.14% of $\overline{T_C}$. This means that the unsteady analysis of the flow in the plenum is consistent with the averaged conservation equations. The characteristic acoustic time in this case was estimated as $V_C^{1/3}/\overline{c_C}$ and was found to be an order of magnitude lower than t_{close}, which justifies our assumption of uniform flow properties in the plenum.

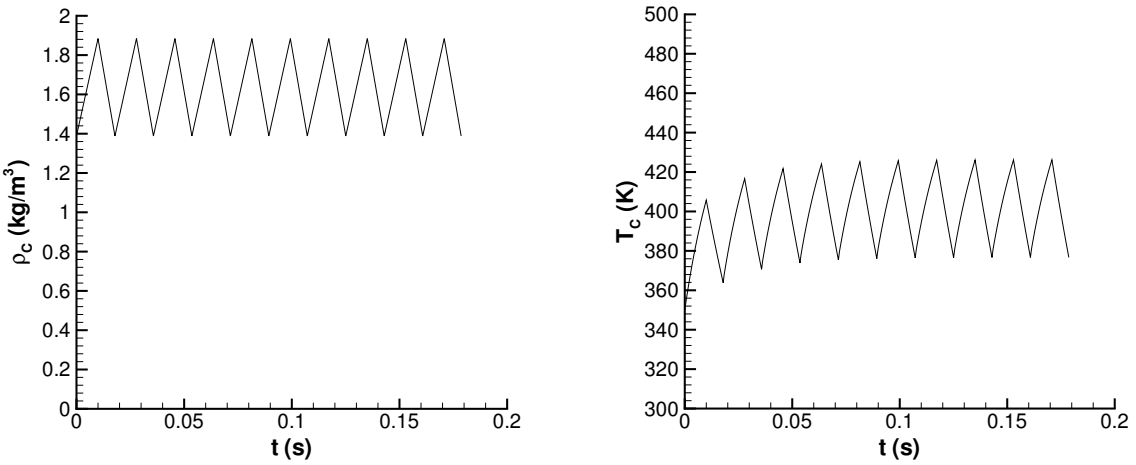

Figure 5.11: Evolution of flow properties in the plenum. $A_0 = 0.004$ m^2, $A_2 = 0.04$ m^2, $A_V = 0.006$ m^2, $V_C = 0.02$ m^3, $\dot{m}_0 = 0.9915$ kg/s, $\overline{P_C} = 1.885$ bar, $\overline{T_C} = 401.4$ K, $t_{close} = 0.01$ s, $t_{open} = 0.007865$ s.

It is also possible to derive an analytical solution for the limit temperature in the plenum,

$$T_C(t) = \gamma\overline{T_C} + \frac{T_C(0) - \gamma\overline{T_C}}{1 + \dfrac{t/t_{close}}{V_C\overline{\rho_C}/(\dot{m}_0 t_{close}) - 1/2}} \quad \text{for} \quad 0 < t < t_{close} \tag{5.38}$$

where $T_C(0)$ satisfies the limit cycle condition given in Eq. 5.37. The solution for T_C during the open part of the cycle can also be derived analytically but is rather involved and is not given here. Equations 5.35 and 5.38 can be used to determine the amplitude of the fluctuations in density, temperature, and pressure in the plenum.

$$\frac{\Delta\rho_C}{\overline{\rho_C}} = \frac{\dot{m}_0 t_{close}}{2V_C\overline{\rho_C}} \tag{5.39}$$

$$\frac{\Delta T_C}{\overline{T_C}} = \frac{\gamma-1}{2}\cdot\frac{\dot{m}_0 t_{close}}{V_C\overline{\rho_C}} \tag{5.40}$$

$$\frac{\Delta P_C}{\overline{P_C}} = \frac{\dot{m}_0 t_{close}}{V_C\overline{\rho_C}}\left(\frac{\gamma}{2}+\frac{\gamma-1}{4}\cdot\frac{\dot{m}_0 t_{close}}{V_C\overline{\rho_C}}\right) \tag{5.41}$$

The amplitudes of the fluctuations in density, temperature, and pressure for the case shown in Fig. 5.11 are 15.2%, 6.1%, and 22.1%, respectively. These amplitudes are all controlled by the same non-dimensional parameter, $\dot{m}_0 t_{close}/(V_C\overline{\rho_C})$. This parameter represents the ratio of the amount of mass added to the system during the closed part of the cycle to the average mass in the plenum. The amplitude of the oscillations is reduced for a lower inlet mass flow rate (corresponding to a lower flight Mach number or a higher altitude), a lower close time, a larger plenum volume, or a higher average plenum density.

5.6.2 Inlet response to flow fluctuations

The pressure oscillations in the plenum induce unsteady flow in the inlet. This unsteady behavior has been previously studied in the context of longitudinal pressure fluctuations generated by combustion instabilities in ramjets. The effect of pressure oscillations on the inlet may be regarded as an equivalent loss of pressure margin possibly resulting in inlet unstart.

The response of the shock wave in an inlet diffuser, such as that represented in Fig. 5.1, was modeled by Culick and Rogers (1983). They analyzed the problem of small-amplitude motions of a normal shock in one-dimensional inviscid flow and

incorporated a simplified model for flow separation. Their analysis treats the acoustic field only, consisting of a perturbing acoustic wave propagating upstream to the shock and a reflected wave propagating downstream. One of their main findings is that the shock response depends strongly on the following non-dimensional frequency

$$\Phi = \frac{\omega/c_2}{\frac{1}{A}\frac{dA}{dx}} \ . \tag{5.42}$$

The response of the shock was shown to increase if Φ decreases (corresponding to lower frequency oscillations or an area increase in the inlet diffuser). Thus, low-frequency oscillations are potentially more dangerous than high-frequency oscillations.

Yang and Culick (1985) numerically studied the response of the diffuser shock to finite-amplitude perturbations. Their analysis takes into account the fluctuations of entropy and mass flow rate induced by the shock motion. The conclusions drawn from the acoustic theory (Eq. 5.42) were confirmed as lower frequencies and higher amplitudes displaced the shock toward the throat. However, unlike the predictions of acoustic theory, the amplitude of the mass flow oscillations was found to be smaller for disturbances with a higher amplitude. This was attributed to non-linear effects, which tend to displace the shock toward the throat and reduce its strength. Pressure oscillations at a frequency of 300 Hz and an amplitude of 10% caused the mass flow rate to fluctuate by about 3%. No resonance phenomena due to the coupling of the shock motion and initial flow perturbations were observed. Similar observations were made based on the experiments of Sajben et al. (1984).

The strength of the diffuser shock plays an important role in the stability of the inlet flow field to flow perturbations. The boundary layer at the wall may separate and significantly alter the flow field in the strong shock case (Sajben et al., 1984). Separation results in a reduced effective flow area and it is possible to use asymptotic methods to analyze the unsteady flow through the diffuser (Biedron and Adamson, 1988). Recent experiments have focused on inlets specifically for PDEs. Mullagiri et al. (2003) studied a supersonic inlet at Mach 2.5 with back pressure excitation due to varying blockage at the exit plane. They observed that increasing the exci-

tation frequency decreased the amplitude of pressure perturbations. Increasing the excitation amplitude was found to increase the upstream distance over which the perturbation was sensed. Nori et al. (2003) produced pressure oscillations by injecting air at the supersonic inlet exit in a Mach 3.5 air flow. Their results showed that even when a substantial amount of the inlet capture mass was injected (40%), the inlet remained started. For a given injection mass flow, lower back pressure excitation frequencies produced larger pressure oscillations, confirming the predictions of Culick and Rogers (1983).

The problem of the inlet response to pressure oscillations generated by valve closing and opening in a PDE is complex. However, the results of previous researchers have given us some insight into what parameters exert a critical influence on the inlet response in a PDE. Higher frequency oscillations tend to stabilize the diffuser shock (Culick and Rogers, 1983, Yang and Culick, 1985, Nori et al., 2003). The frequency of the oscillations in the plenum is given by $1/\tau$. Thus, reducing the cycle time is going to benefit inlet stability. For a given inlet configuration and flight condition, the amplitude of the pressure oscillations in the plenum and the inlet response decrease with decreasing close time and increasing plenum volume (Eq. 5.41). Other factors obviously have to be taken into account in determining the unsteady behavior of the system, but this analysis gives some general ideas about the unsteady response of the inlet. A more detailed investigation of this problem requires careful numerical simulations and experiments based on a specific inlet design.

5.7 PDE performance calculation

The filling process modeling is used to estimate the momentum and pressure integrals in the thrust equation (Eq. 5.15). Recall that the velocity and mass flow rate at the valve plane are modeled as piecewise constant functions of time. The pressure at the valve plane is assumed to be constant during the open part of the cycle, and time-varying during the closed part due to the detonation process. The behavior of the pressure and mass flow rate at the valve plane is illustrated schematically in

Fig. 5.12. This section describes the thrust and specific impulse calculation for our air-breathing PDE.

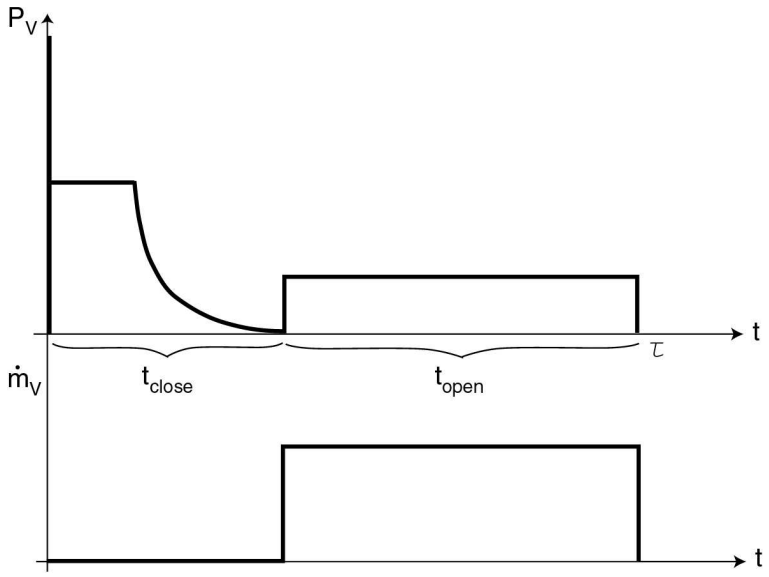

Figure 5.12: Modeling of pressure and flow velocity at the valve plane during a cycle.

5.7.1 PDE thrust equation

Before calculating the thrust from the momentum equation, we must verify that our model satisfies the averaged energy equation, Eq. 5.11. Within the approximations of our model, the stagnation temperature at the valve plane is constant during the open part of the cycle. Using Eq. 5.23, Eq. 5.11 is equivalent to $h_{tV}^{o} = h_{t0}$. The averaged energy conservation equation states that the stagnation enthalpy has to be conserved between the freestream and the valve plane during the open part of the cycle. The stagnation enthalpy of the plenum equals the freestream stagnation enthalpy (Eq. 5.37). Because the flow from the plenum to the valve plane is modeled using a steady expansion, the stagnation enthalpy is conserved and the averaged energy equation is satisfied. The energy release in the detonation is implicitly considered in the calculation of the detonation tube impulse.

In order to calculate performance, we consider the averaged thrust equation, Eq. 5.15. The momentum and pressure contributions of the detonation tube during

the open part of the cycle (from t_{close} to τ) are calculated using the model estimates for velocity and pressure at the valve plane during the open part of the cycle. For subsonic flow at the valve plane, the velocity and pressure u_V^o and P_V^o are the post-shock values. For sonic flow, these quantities are the values at the throat c^* and P^*. The pressure contribution during the open part of the cycle is

$$\int_{t_{close}}^{\tau} A_V(P_V(t) - P_0)dt = A_V \int_{t_{close}}^{\tau} (P_V^o - P_0)dt = t_{open} A_V(P_V^o - P_0) \ . \tag{5.43}$$

The momentum contribution is estimated with

$$\int_{t_{close}}^{\tau} \dot{m}_V(t) u_V(t)dt = u_V^o \int_{t_{close}}^{\tau} \dot{m}_V(t)dt \ . \tag{5.44}$$

The averaged mass conservation equation (Eq. 5.3) yields

$$\int_{t_{close}}^{\tau} \dot{m}_V(t)dt = \tau \dot{m}_0 \ . \tag{5.45}$$

The contribution of the open part of the cycle is, therefore,

$$\int_{t_{close}}^{\tau} \left(\dot{m}_V(t)u_V(t)dt + A_V(P_V(t) - P_0)\right) dt = \tau \dot{m}_0 u_V^o + A_V(P_V^o - P_0)t_{open} \ . \tag{5.46}$$

Substituting Eq. 5.46 into Eq. 5.15, the average thrust can be expressed as follows

$$\overline{F} = \frac{1}{\tau} I_{dt} + \dot{m}_0(u_V^o - u_0) + \frac{t_{open}}{\tau} A_V(P_V^o - P_0) \ . \tag{5.47}$$

Equation 5.47 shows that the average thrust depends on the contributions of detonation tube impulse, momentum, and pressure at the valve plane. The first term is always positive. The second term is negative because of the flow losses associated with decelerating the flow through the inlet and re-accelerating it unsteadily during the filling process. The third term is positive because the air injected during the filling process is at a higher pressure than the outside air. However, the sum of the last two terms is negative and corresponds to a drag term caused by flow losses and

unsteadiness through the inlet and the plenum.

We now digress to do an analogy between Eq. 5.47 and the ramjet performance. Figure 5.13 shows the usual control volume Ω that includes the entire ramjet engine. Using this control volume, the thrust can be expressed (Hill and Peterson, 1992) as

$$F = \dot{m}_e u_e - \dot{m}_0 u_0 + A_e(P_e - P_0) \; . \tag{5.48}$$

The thrust can also be expressed by introducing the variables at the plane located just upstream of the fuel injectors, and denoted r

$$F = (\dot{m}_e u_e - \dot{m}_r u_r) + (\dot{m}_r u_r - \dot{m}_0 u_0) + (A_e P_e - A_r P_r) + (A_r P_r - A_e P_0) \; . \tag{5.49}$$

In steady flight $\dot{m}_r = \dot{m}_0$, and for the purposes of analogy with our straight-tube PDE, we consider a ramjet with a straight nozzle ($A_r = A_e$). The thrust can then be expressed as

$$F = [\dot{m}_e u_e - \dot{m}_0 u_r + A_e(P_e - P_r)] + \dot{m}_0(u_r - u_0) + A_e(P_r - P_0) \; . \tag{5.50}$$

From Eq. 5.50, the thrust of our ramjet consists of a thrust term (in brackets), a momentum term, and a pressure term. Equation 5.50 is the analog of Eq. 5.47 for the steady case where $t_{open} = \tau$. The valve plane in the PDE case corresponds to the plane upstream of the injectors in the ramjet case. Note that only the impulse terms differ between Eqs. 5.47 and 5.50, while the momentum and pressure terms correspond exactly. This analogy is helpful in understanding the origin of the terms in the PDE thrust equation.

5.7.2 Specific impulse and effect of purging time

The purging time has a strong influence on the overall engine thrust since the thrust is inversely proportional to the cycle time, and, by definition, $\tau = t_{close} + t_{purge} + t_{fill}$. Since t_{open} is determined in our model by the condition for periodicity, increasing t_{purge}

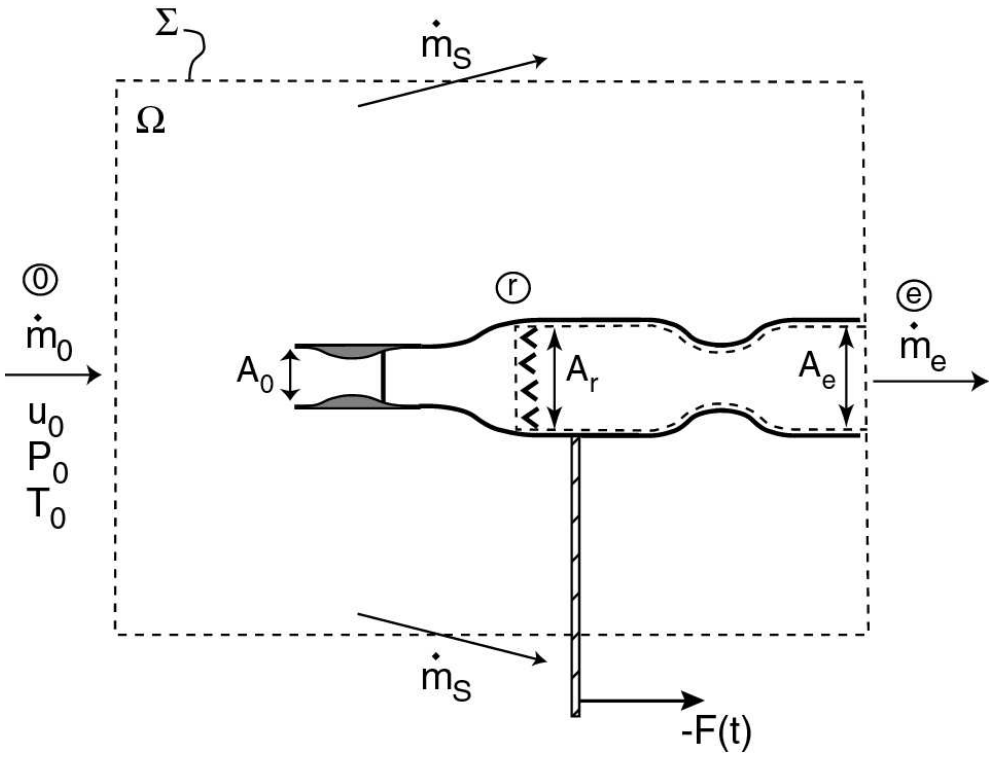

Figure 5.13: Control volume used to calculate ramjet performance.

means decreasing t_{fill} and decreasing the mass of detonable gas in the detonation tube. Decreasing the mass of detonable gas will decrease the detonation tube impulse. The other terms in the thrust equation (Eq. 5.47) are not affected by t_{fill} for a given t_{open}. Thus, we expect the specific performance of the engine to decrease with increasing purging time.

Consider the mass balance in the detonation tube when the valve is open. At the end of the purge time, fuel is injected into the detonation tube just downstream of the valve. The mixture volume is calculated assuming ideal mixing at constant pressure and temperature. We assume that the detonation tube volume equals the volume of injected gas[1]. Since fuel is injected only during a time t_{fill}, the mass of combustible mixture in the tube at the end of the filling process can be expressed two ways. From

[1]This means the length of the detonation tube is being varied with the operating conditions in this model.

the filling process, we have

$$\dot{m}_V^o t_{fill}(1+f) = \rho_i V_{dt} \tag{5.51}$$

and from mass conservation (Eq. 5.45), we have

$$\tau \dot{m}_0 = t_{open}\dot{m}_V^o = (t_{fill} + t_{purge})\dot{m}_V^o \ . \tag{5.52}$$

Define the purge coefficient as the ratio of the purging time to the fill time: $\pi = t_{purge}/t_{fill}$. Then the volume of the detonable mixture can be expressed as

$$V_{dt} = \left(\frac{1+f}{1+\pi}\right)\frac{\tau \dot{m}_0}{\rho_i} \ . \tag{5.53}$$

It is critical to make the distinction between the air mass flow rate $\dot{m}_0$ and the average detonable mixture mass flow rate $\rho_i V_{dt}/\tau$. The amount of fuel injected per cycle is equal to $\dot{m}_V^o t_{fill} f$. Using the mass balance in the detonation tube (Eq. 5.51), we calculate the average fuel mass flow rate

$$\dot{m}_f = \frac{\rho_i V_{dt} f}{(1+f)\tau} = \frac{\dot{m}_0 f}{1+\pi} \ . \tag{5.54}$$

The fuel-based specific impulse is calculated with respect to the fuel mass flow rate as

$$\begin{aligned} I_{SPF} &= \frac{\overline{F}}{\dot{m}_f g} \\ &= I_{SPFdt} - \frac{1+\pi}{fg}\left[(u_0 - u_V^o) - \frac{A_V(P_V^o - P_0)}{\dot{m}_V^o}\right] \ . \end{aligned} \tag{5.55}$$

The engine specific impulse depends on the purging time through the parameter π. Because the term in brackets in Eq. 5.55 is positive, the specific impulse decreases linearly with increasing purge coefficient.

5.7.3 Detonation tube impulse

The detonation tube impulse in the thrust equation (Eq. 5.47) needs to be evaluated for various operating conditions. The static impulse due to the detonation process only has been measured by Nicholls et al. (1958), Zhdan et al. (1994), Zitoun and Desbordes (1999), Harris et al. (2001) and Cooper et al. (2002) for single-cycle operation and several models have been proposed (Zitoun and Desbordes, 1999, Endo and Fujiwara, 2002, Wintenberger et al., 2003). However, in practice, the flow downstream of the propagating detonation wave in an air-breathing engine is not at rest because of the filling process. This is captured only in multi-cycle experiments (Zitoun and Desbordes, 1999, Schauer et al., 2001, Kasahara et al., 2002) yet the multi-cycle impulse can still be well predicted by our single-cycle estimates (Eq. 4.8) because of the low filling velocity in these tests. During supersonic flight, the average stagnation pressure in the plenum is much higher than the pressure in the tube at the end of the blowdown process. This large pressure ratio generates high filling velocities, which can significantly alter the flow field and the detonation/blowdown process so we include this effect in our model. In an idealized case, we assume the detonation wave is immediately initiated after valve closing and catches up with the expansion wave generated by the valve closing. The situation corresponds to a detonation wave propagating in a flow moving in the same direction at the filling velocity and is observed in the multi-cycle numerical simulations of an air-breathing PDE by Wu et al. (2003).

5.7.3.1 Detonation tube impulse model

The moving flow ahead of the detonation is assumed to have a velocity U_{fill}. Following the detonation is the Taylor wave, which brings the products back to rest near the closed end of the tube (see Section 1.1.4). In the moving-flow case, the energy release across the wave is identical to the no-flow case and the CJ pressure, temperature, density, and speed of sound are unchanged. However, the wave is now moving at a velocity $U_{CJ} + U_{fill}$ with respect to the tube. The flow velocity immediately following

this detonation wave is

$$u_{CJ} = U_{CJ} + U_{fill} - c_{CJ} \ . \tag{5.56}$$

The Taylor wave has to decelerate the flow from the velocity u_{CJ} to zero velocity at the upstream (closed) end of the tube. Since u_{CJ} is higher than in the no-flow case, the flow has to undergo a stronger expansion through the Taylor wave. Using the method of characteristics as described in Section 1.1.4, we can obtain the speed of sound and the pressure behind the Taylor wave

$$c_3 = c_{CJ} - \frac{\gamma_b - 1}{2} u_{CJ} = \frac{\gamma_b + 1}{2} c_{CJ} - \frac{\gamma_b - 1}{2} (U_{CJ} + U_{fill}) \ , \tag{5.57}$$

$$P_3 = P_{CJ} \left(\frac{c_3}{c_{CJ}} \right)^{\frac{2\gamma_b}{\gamma_b - 1}} \ . \tag{5.58}$$

The pressure behind the Taylor wave decreases with increasing filling velocity. For $c_3 t \leq x \leq (U_{CJ} + U_{fill})t$, the speed of sound and the pressure inside the Taylor wave are given by Eqs. 1.42 and 1.43. The Taylor wave occupies a larger region of the tube behind the detonation in the moving-flow case.

The detonation tube impulse is calculated as the integral of the pressure trace at the valve plane

$$I_{dt} = \int_0^{t_{close}} A_V (P_3(t) - P_0) dt \ . \tag{5.59}$$

Using dimensional analysis, we idealize the pressure trace at the valve plane as in Fig. 4.11 and model the pressure trace integral as described in Section 4.3.1. The pressure history is modeled by a constant pressure region followed by a decay due to gas expansion out of the tube. The pressure integral can be expressed as

$$\int_{t_{open}}^{\tau} (P_3(t) - P_0) dt = \Delta P_3 \left[\frac{L}{U_{CJ} + U_{fill}} + (\alpha + \beta) \frac{L}{c_3} \right] \ . \tag{5.60}$$

using the notations of Section 4.3.1. As in the no-flow case, it is possible to derive a similarity solution for the reflection of the first characteristic at the open end and to analytically calculate α. The reader is referred to Section 4.3.2 for the details of the

derivation in the no flow case. For the moving-flow case, the value of α is

$$\alpha = \frac{c_3}{U_{CJ} + U_{fill}} \left[2 \left(\frac{\gamma_b - 1}{\gamma_b + 1} \left(\frac{c_3 - u_{CJ}}{c_{CJ}} + \frac{2}{\gamma_b - 1} \right) \right)^{-\frac{\gamma_b + 1}{2(\gamma_b - 1)}} - 1 \right] . \tag{5.61}$$

The value of β is assumed to be independent of the filling velocity and the same value as in Section 4.3.3 is used: $\beta = 0.53$.

5.7.3.2 Comparison with numerical simulations of detonation process

In order to validate the model for the valve plane pressure integration (Eq. 5.60), the flow was simulated numerically using Amrita (Quirk, 1998). The axisymmetric computational domain consists of a tube of length L closed at the left end and open to a half-space at the right end. The moving flow was represented by an idealized inviscid pressure-matched jet profile at constant velocity U_{fill} as shown on Fig. 5.14. The modified Taylor wave similarity solution (Eqs. 5.57–5.58 and 1.42–1.43) was used as an initial condition, assuming the detonation has just reached the open end of the tube when the simulation is started. This solution was calculated using a one-γ model for detonations (Eqs. 1.15–1.19) for a non-dimensional energy release $q/RT_i = 40$ across the detonation and $\gamma = 1.2$ for reactants and products. The corresponding CJ parameters are $M_{CJ} = 5.6$ and $P_{CJ}/P_i = 17.5$, values representative of stoichiometric hydrocarbon-air mixtures. The initial refilling pressure P_i ahead of the detonation wave was taken equal to the pressure P_0 outside the detonation tube.

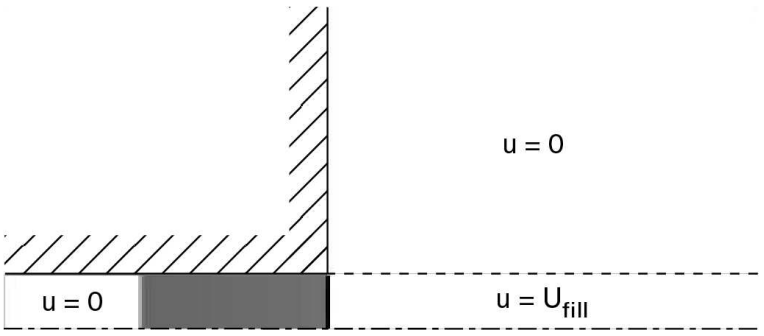

Figure 5.14: Numerical schlieren image of the initial configuration for the numerical simulations of the detonation process with moving flow. The Taylor wave is visible behind the detonation front at the tube exit.

The configuration we adopted for the moving flow is a very elementary representation of the flow at the end of the filling process. This flow will, in reality, include vortices associated with the unsteady flow and the unstable jet shear layers. However, the analysis of the numerical simulations showed that the flow in the tube is one-dimensional except for within one to two tube diameters from the open end, as observed in the no-flow case (Section 4.2.4). The flow in the tube is mainly dictated by the gas dynamic processes at the tube exit plane. Since the exit flow is choked for most of the process, the influence of our simplified jet profile on the valve plane pressure integration is minimal.

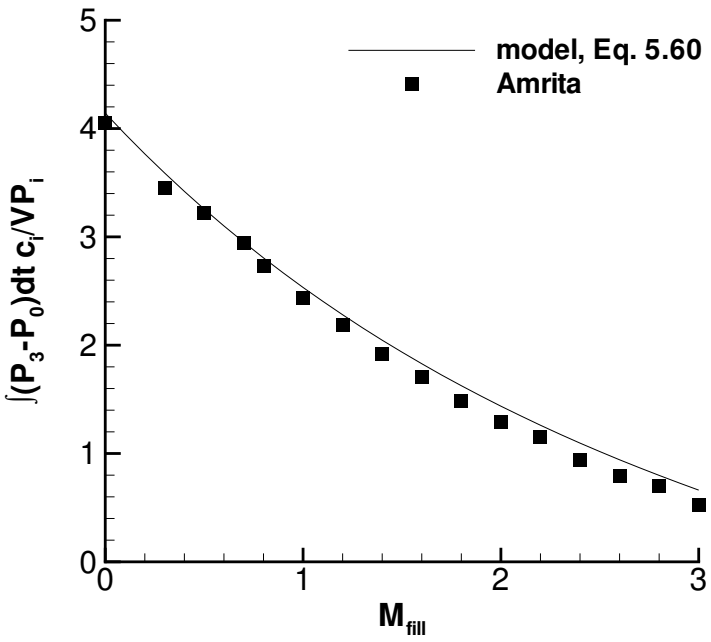

Figure 5.15: Non-dimensional detonation tube impulse as a function of the filling Mach number. Comparison of model predictions based on Eq. 5.60 and results of numerical simulations with Amrita (Quirk, 1998). $q/RT_i = 40$, $\gamma = 1.2$.

Figure 5.15 shows the comparison of the non-dimensionalized valve plane pressure integral with the predictions of our model based on Eq. 5.60 as a function of the filling Mach number. The numerical pressure integration was carried out for a time equal to $20t_1$, where $t_1 = L/U_{CJ}$. As the filling Mach number increases, the flow expansion through the Taylor wave is more severe and the plateau pressure behind the Taylor

wave P_3 decreases. Even though P_3 is lower, the blowdown process is accelerated due to the presence of the initial moving flow. The overall result is that the detonation tube impulse decreases with increasing filling Mach number, as shown in Fig. 5.15. The model agrees reasonably well with the results of the numerical simulations. It generally overpredicts the results of the numerical simulations by as much as 25% at higher filling Mach numbers. The agreement is better at lower Mach numbers (within 11% error for $M_{fill} \leq 2$ and 4% for $M_{fill} \leq 1$).

5.8 Application to hydrogen- and JP10-fueled PDEs

Performance calculations are carried out for our single-tube air-breathing PDE operating with hydrogen and JP10 fuels and compared with the ramjet performance. The performance calculations are presented for supersonic flight only because the assumptions made in the derivation of the model become invalid for subsonic flight. The results presented here do not represent the ideal performance from an optimized PDE. In particular, the addition of an exit nozzle can have a substantial influence on the engine performance, as discussed further.

5.8.1 Input parameters

The input parameters for the performance model consist of the engine geometry, the freestream conditions and flight Mach number, the fuel type and stoichiometry, the valve close time, and the purging time. In the following performance calculations, the fuel-air mixture is assumed to be stoichiometric.

The stagnation pressure loss across the inlet during supersonic flight is modeled using the military specification MIL-E-5008B (Mattingly et al., 1987), which specifies the stagnation pressure ratio across the inlet as a function of the flight Mach number, for $M_0 > 1$.

$$\frac{P_{t2}}{P_{t0}} = 1 - 0.075(M_0 - 1)^{1.35} \tag{5.62}$$

The calculation of the properties at the valve plane and the initial conditions

in the detonation tube require the knowledge of the specific heat ratio γ_b and the speed of sound c_f in the burned gases at the end of the blowdown process. γ_b and the CJ parameters are obtained by carrying out detonation equilibrium computations using realistic thermochemistry (Reynolds, 1986). The speed of sound c_f is calculated assuming that the flow is isentropically expanded from the CJ pressure to atmospheric pressure. This entire process needs to be iterated since the CJ parameters depend on the initial conditions in the tube, which are determined by γ_b and c_f. The solution was found by iteration until the prescribed values of γ_b and c_f matched the values obtained at the end of the equilibrium computations. The iterative method is described in detail in Appendix D.

5.8.2 Hydrogen-fueled PDE

5.8.2.1 Conditions inside the engine

The calculation of performance parameters first requires solving for the conditions inside the engine. Figure 5.16 shows the filling velocity, the velocity at the valve plane, and the cycle frequency for a PDE operating with stoichiometric hydrogen-air at an altitude of 10,000 m. In this case, the flow at the valve plane during the filling process is predicted to remain subsonic up to a flight Mach number of 1.36. Thus, the two curves on Fig. 5.16 match for $M_0 < 1.36$ but diverge at higher values of M_0 because $U_{fill} > u_V$. The filling velocity increases with increasing flight Mach number because of the increased stagnation pressure in the plenum, which generates a stronger shock wave at valve opening. The cycle frequency was calculated for a fixed close time of 5 ms. As shown in Fig. 5.16, it increases with increasing flight Mach number due to the increasing filling velocity and the corresponding decreasing open time (Fig. 5.8). In the case considered, the cycle frequency increases from a value of about 50 Hz at $M_0 = 1$ to about 180 Hz at $M_0 = 4$.

The model filling velocity was compared with the results of the numerical simulations of Wu et al. (2003) for an air-breathing PDE with a straight detonation tube for a PDE flying at 9.3 km altitude and at Mach 2.1. The flow observed in these sim-

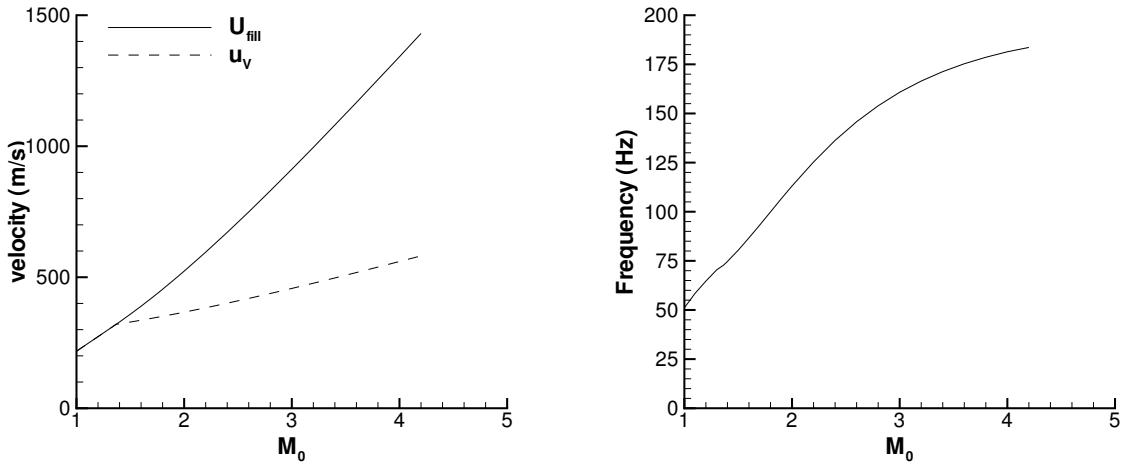

Figure 5.16: Filling velocity and velocity at the valve plane (left) and cycle frequency (right) as a function of flight Mach number for single-tube PDE operating with stoichiometric hydrogen-air. $Z = 10,000$ m, $A_0 = 0.004$ m^2, $A_2 = 0.04$ m^2, $A_V = 0.006$ m^2, $t_{close} = 0.005$ s.

ulations is qualitatively similar to the flow predicted by the model in the detonation tube and represented schematically in Fig. 5.7. The numerical simulations yielded a filling velocity of about 500 m/s, while the prediction of our model for this case is 539 m/s, within 8% error.

Figure 5.17 shows the pressure non-dimensionalized with the freestream stagnation pressure and the temperature at various locations inside the engine. The ratio of inlet stagnation pressure to freestream stagnation pressure decreases with increasing flight Mach number because of the increasing stagnation pressure losses through the inlet (Eq. 5.62). Additional losses occur in the plenum due to flow unsteadiness. The pressure at the valve plane equals the filling pressure until the flow at the valve plane becomes sonic. At higher flight Mach numbers, the filling pressure is lower because of the additional flow acceleration through the unsteady expansion. The ratio of the filling pressure to the freestream stagnation pressure decreases sharply with increasing flight Mach number because of the substantial values obtained for the filling velocity (Fig. 5.16). For example, the filling pressure represents less than 25% of P_{t0} for $M_0 > 2$ and less than 9% for $M_0 > 3$. The filling temperature increases slowly and remains low even at high flight Mach numbers. Although the freestream stagnation

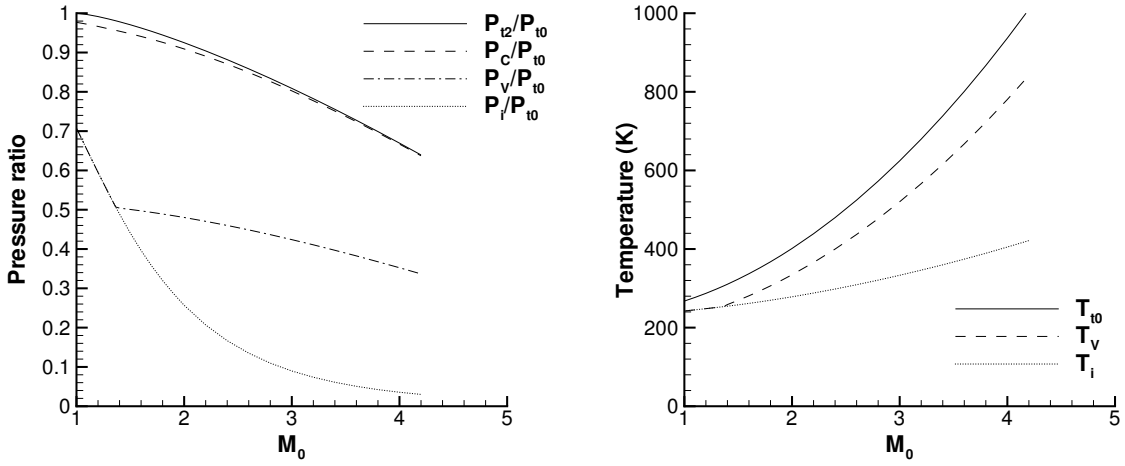

Figure 5.17: Left: inlet stagnation pressure, plenum pressure, pressure at the valve plane, and filling pressure non-dimensionalized with freestream total pressure as a function of flight Mach number. Right: freestream stagnation temperature, temperature at the valve plane and filling temperature as a function of flight Mach number. Stoichiometric hydrogen-air, $Z = 10,000$ m, $A_0 = 0.004$ m^2, $A_2 = 0.04$ m^2, $A_V = 0.006$ m^2.

temperature reaches close to 1000 K at Mach 4, the filling temperature is predicted to reach only about 400 K.

5.8.2.2 Performance variation with flight Mach number

The specific impulse for a hydrogen-air PDE is shown in Fig. 5.18 as a function of the flight Mach number for conditions at sea level and at 10,000 m altitude. The results shown in Fig. 5.18 are for $\pi = 0$, i.e., no purging, and represent the maximum values predicted by the model for a given engine geometry. Experimental static multi-cycle data from Schauer et al. (2001) and single-cycle impulse predictions (Chapter 4) are given as reference points for the specific impulse at static conditions close to sea level. Even though the model assumptions do not apply for subsonic flight, the reference values for the static case ($M_0 = 0$) apparently lie on or close to a linear extrapolation of the results obtained for supersonic flight. Our single-tube PDE generates thrust up to a flight Mach number of 3.9 at sea level and 4.2 at an altitude of 10,000 m.

The specific impulse decreases almost linearly with increasing flight Mach number

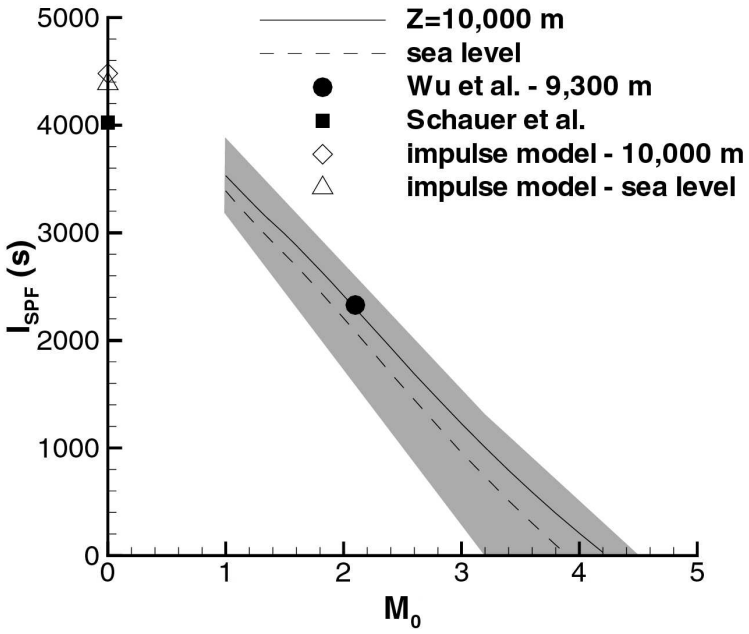

Figure 5.18: Specific impulse of a single-tube PDE operating with stoichiometric hydrogen-air as a function of flight Mach number at sea level and at an altitude of 10,000 m. $A_0 = 0.004$ m^2, $A_2 = 0.04$ m^2, $A_V = 0.006$ m^2, $\pi = 0$. Data from multi-cycle numerical simulations by Wu et al. (2003) for $M_0 = 2.1$ at 9,300 m altitude are shown. Experimental data from Schauer et al. (2001) and our single-cycle impulse model predictions are also given as a reference for the static case. The uncertainty region for the specific impulse at 10,000 m is the shaded area.

from a value at $M_0 = 1$ of about 3530 s at 10,000 m and 3390 s at sea level. In order to understand the behavior of the specific impulse with varying flight Mach number, the three terms of the specific impulse equation (Eq. 5.55) are plotted on Fig. 5.19. The detonation tube impulse decreases with increasing flight Mach number due to the increasing filling velocity (Fig. 5.16). The momentum and pressure terms are relatively constant for subsonic flow at the valve plane because of the corresponding increases in velocity, pressure and mass flow rate with increasing flight Mach number. However, for sonic flow at the valve plane, the negative momentum term decreases linearly with freestream velocity, because the speed of sound at the valve plane decreases linearly with M_0, but more slowly than u_0. Neglecting the outside pressure P_0, the pressure term is proportional to the square root of the temperature $T^* = 2T_{t0}/(\gamma + 1)$, which

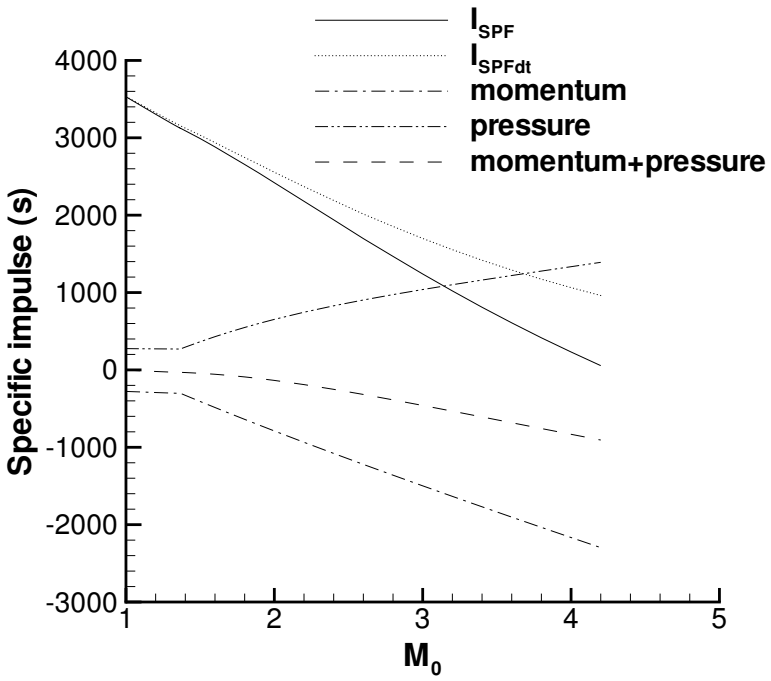

Figure 5.19: Various terms in specific impulse equation as a function of flight Mach number for hydrogen-fueled PDE. $Z = 10,000$ m, $A_0 = 0.004$ m^2, $A_2 = 0.04$ m^2, $A_V = 0.006$ m^2, $\pi = 0$.

increases almost linearly with M_0. This pressure term is positive and increases with increasing M_0 for sonic flow at the valve plane. As mentioned before, the sum of these two terms, which is displayed in Fig. 5.19, is negative.

Figure 5.18 also shows a data point from the numerical simulations by Wu et al. (2003). Their baseline case value for the specific impulse for a straight detonation tube is 2328 s. The model prediction for the same configuration and flight conditions is 2286 s, which is within 1.8% from the result of their numerical simulations.

5.8.2.3 Performance variation with altitude

The specific impulse at sea level is systematically lower than the specific impulse at 10,000 m by 150–300 s, as shown in Fig. 5.18. Both pressure and temperature change with altitude. However, the specific impulse is independent of outside pressure. At constant outside temperature, the Mach number M_S of the shock wave generated at valve opening is independent of pressure because the average plenum pressure scales

with the outside pressure (Eq. 5.30). The filling velocity and temperature are thus independent of pressure. We showed in Section 4.6.4 that the detonation tube specific impulse was independent of initial pressure in the static case. This conclusion can be extended to the moving-flow case because U_{fill} is independent of P_0. Since the momentum term and pressure terms are also independent of P_0, the engine specific impulse does not depend on the outside pressure.

However, it depends on the outside temperature T_0. At fixed outside pressure, the momentum and pressure terms vary proportionally to $\sqrt{T_0}$ for sonic flow at the valve plane. The magnitude of the drag term increases with the outside temperature, but the variation of T_0 between sea level and 10,000 m (223 K to 288 K) is not sufficient to account for the differences observed in the specific impulse. The detonation tube impulse is primarily modified because of the change in filling conditions. Increasing the outside temperature results in a stronger shock wave at valve opening, and, therefore, in a higher filling velocity. Since the detonation tube specific impulse has been shown to be insensitive to changes in initial conditions in the static case (Fig. 4.28), the variation in I_{SPFdt} observed is attributed to the effect of the filling velocity. Increasing T_0 from 223 K to 288 K causes an increase in U_{fill} consistent over the range of flight Mach numbers of about 10%. Recalculating the specific impulse at 10,000 m with U_{fill} 10% higher results in a lower I_{SPFdt} by 100–180 s. We conclude that the decrease in detonation tube specific impulse caused by the increasing outside temperature is the main contribution to the decrease in engine specific impulse observed between 10,000 m altitude and sea level. The increase in the drag term accounts for a smaller contribution to this difference.

5.8.2.4 Performance variation with purge coefficient

Figure 5.20 shows that increasing the purge coefficient results in an increase of the drag term in the specific impulse equation and a decrease of the overall specific impulse. At given flight conditions, the specific impulse decreases linearly with increasing purge coefficient. The reduction in performance due to an increase in purge coefficient increases with flight Mach number. Increasing π results in a very small

reduction in performance at low supersonic Mach numbers but results in a significant specific impulse decrease at higher Mach numbers (2.9% decrease if π is increased from 0 to 0.5 at $M_0 = 2$ but 19.3% decrease at $M_0 = 3$). Since the size of the drag term in the specific impulse equation increases significantly as M_0 increases, the purge coefficient is found to have a substantial effect on the thrust-producing range of an air-breathing PDE. Indeed, the maximum flight Mach number for a hydrogen-fueled PDE at an altitude of 10,000 m decreases from 4.2 at $\pi = 0$ to 3.8 at $\pi = 0.5$ and 3.5 at $\pi = 1$.

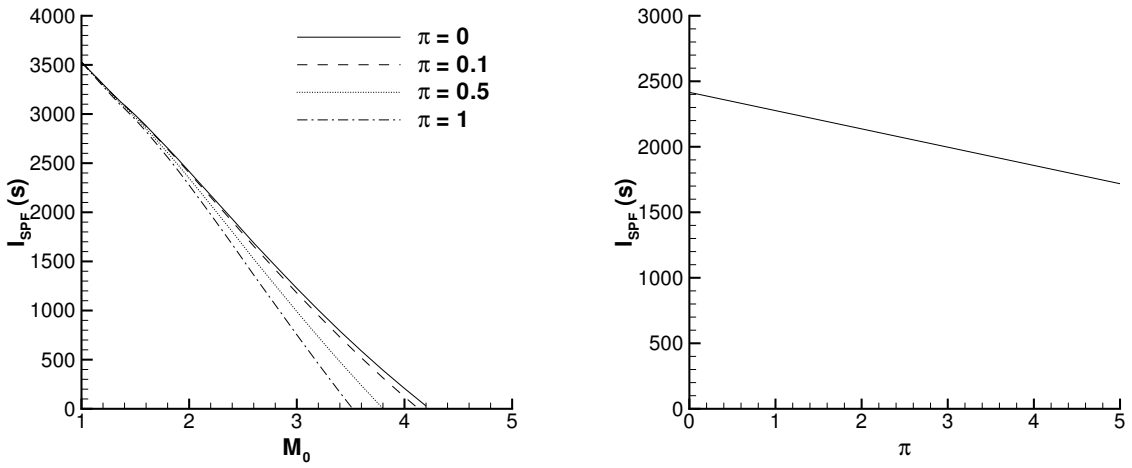

Figure 5.20: Left: specific impulse of a single-tube PDE operating with stoichiometric hydrogen-air as a function of flight Mach number varying the purge coefficient. Right: variation of specific impulse of a single-tube hydrogen-fueled PDE flying at $M_0 = 2$ with purge coefficient. $Z = 10,000$ m, $A_0 = 0.004$ m^2, $A_2 = 0.04$ m^2, $A_V = 0.006$ m^2.

5.8.3 JP10-fueled PDE

5.8.3.1 Performance parameters

The conditions inside a JP10-air PDE exhibit similar behavior to those seen for hydrogen in Fig. 5.17. The flow at the valve plane becomes sonic at $M_0 = 1.41$ for flight at 10,000 m. The filling pressure and temperature are slightly higher in the case of JP10 than in the case of hydrogen because of the lower speed of sound in the burned gases for JP10. JP10 generates a much higher detonation pressure

than hydrogen, but similar CJ temperatures. The subsequent expansion to ambient pressure is stronger and decreases the temperature of the burned gases to a lower value for JP10 than for hydrogen. Indeed, the temperature of the burned gases at the end of the blowdown process is about 120 K lower for JP10 than for hydrogen.

The specific impulse of a JP10-air PDE decreases from a value of about 1370 s at $M_0 = 1$ and vanishes for a flight Mach number of about 4, as shown in Fig. 5.21. A data point for a ballistic pendulum experiment (Wintenberger et al., 2002) for stoichiometric JP10-air at 100 kPa and 330 K and our single-cycle impulse prediction are given as references for the static case. As in the hydrogen case, the reference values for the static case apparently lie close to the extrapolation to $M_0 = 0$ of the curve obtained for supersonic flight.

5.8.3.2 Issues associated with the use of JP10

The temperature of the flow at the valve plane exceeds above $M_0 = 3$ the auto-ignition temperature (CRC, 1983) of JP10-air (518 K), which is assumed to be independent of pressure to the first order. Pre-ignition of the JP10-air mixture is expected above Mach 3 before the detonation is initiated if the fuel injection system is located at the valve plane. Pre-ignition can result in a significant decrease in detonation tube impulse due to potential expulsion of unburned reactants out of the detonation tube (Cooper et al., 2002). Moreover, combustion of the fuel while the valve is open will generate very little thrust due to a reduced thrust surface (Cooper et al., 2003). The design of the fuel injection system for high supersonic Mach numbers has to take into account this issue. An option is to move it downstream of the valve plane, where the temperature is lower due to the unsteady expansion downstream of the valve.

Another issue with the use of liquid hydrocarbon fuels is related to potential condensation of the fuel in the detonation tube due to the low filling temperature. For the case considered here with JP10, the filling temperature remains under 300 K as long as $M_0 < 2.3$. The fuel injected will vaporize completely as long as its vapor pressure is high enough at the temperature considered. In order to vaporize completely the fuel in a stoichiometric JP10-air mixture at 100 kPa, the temperature has to be

at least 330 K (Austin and Shepherd, 2003). Since both pressure and temperature in the detonation tube vary with flight Mach number, it is necessary to carry out vapor pressure calculations to verify whether all the liquid fuel injected will vaporize. It is possible that not all the fuel corresponding to stoichiometric quantity will be able to vaporize and the engine may have to be run at a leaner composition depending on the flight conditions considered. Detonations in hydrocarbon fuel sprays are undesirable because low vapor pressure liquid fuel aerosols are characterized by higher initiation energies and larger reaction zones, making it harder to establish self-sustained detonations. Papavassiliou et al. (1993) found the cell width in heterogeneous phase decane-air detonations to be twice that for decane vapor-air detonations due to the requirements for droplet breakup, heat transfer, evaporation, and mixing. In practice, during steady flight, the walls of the detonation tube will heat up due to the repetitive detonations, and heat transfer from the tube walls will contribute to fuel vaporization.

5.8.4 Uncertainty analysis

Since our performance model is based on many simplifying assumptions, we need to estimate the effect of the uncertainty on the performance parameters. Unfortunately, there is, at this time, no existing standard to which our model can be compared, due to the complexity of the unsteady reactive flow in a PDE. It is difficult to estimate the influence of our assumptions unless a numerical simulation of the entire system is conducted. At present, only Wu et al. (2003) and Ma et al. (2003) have published such computations and although our work agrees with their results at a single condition, this is far from conclusive validation of our approach.

We know from our numerical simulations of the filling process the uncertainty of the model predictions on some of the parameters, which is shown in Table 5.1. We estimated the model uncertainty for a case corresponding to a stoichiometric hydrogen-air PDE flying at 10,000 m with no purging. We evaluated how the specific impulse varies with each parameter. We carried out calculations corresponding to

Parameter	Minimum error (%)	Maximum error (%)
U_{fill}	-11.3	+23.5
u_V	0	+40
P_V	-20.5	+13.4
P_i	+5.8	+22.7
I_{SPFdt}	0	+25

Table 5.1: Uncertainty on some of the model parameters compared to the results of the numerical simulations of the filling and detonation processes.

best-case and worst-case scenarios. For example, the best-case scenario corresponds to a minimized U_{fill} and maximized u_V, P_V, P_i, and I_{SPFdt}. The value of the detonation tube impulse was first calculated with the new parameter values before being adjusted for its own uncertainty as a function of the filling Mach number (-4% for $M_{fill} < 1$, -11% for $1 < M_{fill} < 2$, and -25% for $M_{fill} > 2$). The region of uncertainty is shown in Fig. 5.18 as the grey shaded area around the predicted specific impulse curve at 10,000 m. The upper bound of the shaded region corresponds to the best-case scenario, while the lower bound is the result of the worst-case scenario. As expected, the uncertainty margin is quite large and increases with increasing flight Mach number, due to the growing uncertainty on the detonation tube impulse. The uncertainty on the specific impulse at $M_0 = 1$ is $\pm 9.9\%$ and at $M_0 = 2$, it is -36.5%/+12.7%. Since the predicted detonation tube impulse overpredicts the numerical values, the magnitude of the uncertainty in the worst-case scenario is larger than that in the best-case scenario.

5.8.5 Comparison with the ideal ramjet

The specific impulse of our air-breathing PDE is compared in Fig. 5.21 with that of the ideal ramjet at flight conditions corresponding to 10,000 m altitude for stoichiometric hydrogen- and JP10-air. The ideal ramjet performance was calculated following the ideal Brayton cycle, taking into account the stagnation pressure loss across the inlet (Eq. 5.62). Combustion at constant pressure was computed using realistic thermochemistry (Reynolds, 1986), and performance was calculated assuming

thermodynamic equilibrium at every point in the nozzle. According to our performance predictions, the single-tube air-breathing PDE in the present configuration (straight detonation tube) has a higher specific impulse than the ideal ramjet for $M_0 < 1.35$ for both hydrogen and JP10 fuels.

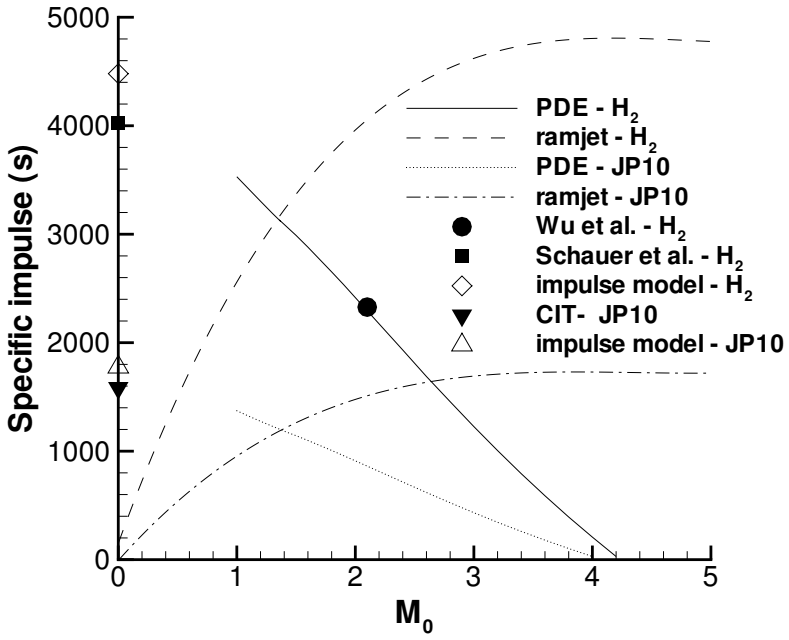

Figure 5.21: Specific impulse of a single-tube air-breathing PDE compared to the ramjet operating with stoichiometric hydrogen-air and JP10-air. $Z = 10,000$ m, $A_0 = 0.004$ m^2, $A_2 = 0.04$ m^2, $A_V = 0.006$ m^2, $\pi = 0$. Data from multi-cycle numerical simulations by Wu et al. (2003) for $M_0 = 2.1$ at 9,300 m altitude are shown. Experimental data from Schauer et al. (2001) and Wintenberger et al. (2002), referred to as CIT, and our impulse model predictions are also given as a reference for the static case.

The results of our performance calculations show that PDEs with a straight detonation tube are not competitive with the ramjet at high supersonic flight Mach numbers. The lack of performance at higher flight Mach numbers can be attributed to the decreasing detonation tube impulse. The present configuration results in very high filling velocities (higher than 500 m/s for $M_0 > 2$), which have two main consequences. First, the pressure and density of the reactants before detonation initiation are low compared to the corresponding properties in the plenum (Fig. 5.17). The

detonation tube impulse being proportional to the initial mixture density (Eq. 4.40), a low reactant density is detrimental to the specific impulse. The straight-tube PDE exhibits the same problem as the standard pulsejet, which is the inability of the engine to sustain ram pressure in the detonation tube during the filling process (Foa, 1960, p. 373). Our specific impulse predictions for the straight-tube PDE indeed display the same behavior as Foa's predictions (Fig. 1.19) for the standard pulsejet, decreasing quasi-linearly with increasing flight Mach number. Second, as shown in Fig. 5.15, the detonation tube impulse is very sensitive to the filling velocity and decreases sharply with increasing U_{fill}. For example, if the filling velocity is reduced to half of its value at $M_0 = 2$ for a hydrogen-air PDE flying at 10,000 m, our model predicts that the detonation tube impulse will increase by 36%. Adding a choked converging-diverging exit nozzle has been proposed by several researchers (Kailasanath, 2001, Wu et al., 2003) as a means to increase the chamber pressure and decrease the effective filling velocity. The strong sensitivity of the detonation tube impulse to the filling velocity suggests a potential for improving performance, provided that the filling velocity can be decreased without excessive internal flow losses. The numerical simulations of Wu et al. (2003) support this idea, showing an increase in specific impulse of up to 45% with the addition of a converging-diverging nozzle.

5.9 Conclusions

We have developed a simple analytical model for predicting the performance of a supersonic air-breathing pulse detonation engine with a single straight detonation tube. This work is the first complete system-level analysis for an air-breathing pulse detonation engine, which takes into account all components of the engine and models their respective coupling. The performance calculation methodology, which is based on gas dynamics and control volume methods, is openly described in complete detail. Performance can be easily estimated for a wide range of flight and operating conditions. We draw the following conclusions from our analysis:

a) The filling process is characterized by a shock wave generated at valve opening and propagating in the detonation tube and a combination of unsteady and steady expansions between the plenum and the detonation tube.

b) The flow in the plenum and in the detonation tube is coupled, and its unsteadiness causes average total pressure losses.

c) The flow in the plenum is characterized by density, temperature, and pressure oscillations due to the opening and closing of the valve during a cycle. The amplitude of these oscillations is critical to the study of the inlet response and was found to be proportional to the ratio of the amount of mass added to the plenum during the closed part of the cycle to the average mass of fluid in the plenum.

d) The thrust of the engine was calculated using an unsteady open-system control volume analysis. It was found to be the sum of three terms representing the detonation tube impulse, the gas momentum, and the pressure at the valve plane.

e) The detonation tube impulse was calculated by modifying our single-cycle impulse model to take into account the effect of detonation propagation into a moving flow generated by the filling process. The detonation tube impulse is found to decrease sharply with increasing filling velocity.

f) Performance calculations for hydrogen- and JP10-fueled PDEs showed that the specific impulse decreases quasi-linearly with increasing flight Mach number, and that single-tube PDEs generate thrust up to a flight Mach number of about 4.

g) PDEs with a straight detonation tube have a higher specific impulse than the ramjet below a flight Mach number of 1.35. PDE performance was found to be very sensitive to the value of the filling velocity, and potential improvements may be possible with a converging-diverging nozzle at the exit.

Chapter 6

Conclusions

The present work investigates the applications of steady and unsteady detonation waves to propulsion systems. For a fixed initial thermodynamic state and variable flow speed, detonations generate the lowest entropy rise of all physically possible combustion modes. Since thermodynamic cycle analysis shows that the thermal efficiency is maximized when the entropy generation is minimized, detonation appears as an attractive combustion mode for propulsion.

The efficiency of ideal detonation-based propulsion systems relative to conventional systems based on low-speed flames is first investigated based on thermodynamics. We observe that the conventional Hugoniot analysis for steady combustion waves, which assumes a fixed initial state and a variable inflow velocity, does not apply for steady-flow propulsion systems. Based on this observation, we reformulate this analysis to obtain a new set of solutions for a fixed initial stagnation state, which we call the stagnation Hugoniot. The implications of the stagnation Hugoniot analysis are that detonations are less desirable than deflagrations for an ideal steady air-breathing propulsion system since they entail a greater entropy rise at a given flight condition. This important result reconciles thermodynamic cycle analysis with past work on detonation-based ramjets, which has systematically concluded that these engines had poorer performance than the ramjet. This leads us to consider the situation for unsteady flow systems. We use a conceptual cycle, that we call the Fickett-Jacobs cycle, to analyze unsteady detonation waves in a purely thermodynamic fashion. At fixed conditions before combustion, detonations are found

to have the potential for generating more work than constant-pressure combustion. We also find that the thermal efficiency of cycles based on unsteady detonation and constant-volume combustion are very similar. Additional impulse calculations for a straight tube showed that constant-volume combustion and detonation result in almost identical propulsive performance, and that constant-volume combustion can be used as a convenient surrogate for detonation.

The application of steady detonation waves to propulsion is then considered, based on flow path analysis. The practical difficulties associated with stabilizing a detonation wave are highlighted. The requirement on the freesteam total enthalpy is considered in parallel with effects such as auto-ignition of the fuel-air mixture. Additional limitations associated with condensation and fuel sensitivity to detonation, which have not been considered before, are taken into account for detonation stabilization. An analytical performance model is formulated for the detonation ramjet and the detonation turbojet, which places a limitation on the total temperature at the combustor outlet, unlike previous work. The results show that steady detonation engines have a small thrust-producing range ($5.6 < M_0 < 6$ for a hydrogen-fueled detonation ramjet at 10,000 m altitude) due to the requirements for detonation stabilization. The performance of steady detonation-based engines is always lower than that of the conventional ramjet and turbojet. This result is the direct consequence of the higher entropy rise and the corresponding total pressure loss across the steady detonation wave. Additional problems associated with supersonic mixing and detonation stabilization severely limit the range of useful performance to the extent that these engines do not appear to be practical.

These conclusions lead us to consider propulsion systems based on unsteady detonations, i.e., pulse detonation engines. We first focus on the simplest version of a PDE, consisting of a straight detonation tube. An analytical model for the impulse of a single-cycle pulse detonation tube is developed based on gas dynamics, dimensional analysis, and empirical observations. The model is based on the pressure history at the thrust surface of the detonation tube. The model predictions are in reasonable agreement (within $\pm 15\%$ in most cases) with direct experimental measurements of

impulse per unit volume, specific impulse, and thrust. This model is one of the first tools available to the propulsion community to quickly and reliably estimate the impulse of a pulse detonation tube. It is used to investigate the dependence of the impulse on a wide range of initial conditions. Based on a scaling analysis, we show that the impulse of a detonation tube scales directly with the mass of explosive in the tube and the square root of the effective energy release per unit mass of the mixture. We also observe, based on equilibrium computations, that at fixed composition and sufficiently high initial pressure, the specific impulse is approximately independent of initial pressure and initial temperature. The predicted values of the mixture-based specific impulse are on the order of 155 to 165 s for hydrocarbon-oxygen mixtures, 190 s for hydrogen-oxygen, and on the order of 115 to 125 s for fuel-air mixtures at conditions of 1 bar and 300 K.

Our next step is to build on these results to develop the first complete system-level analysis for an air-breathing pulse detonation engine. Our analytical performance model for a supersonic air-breathing PDE with a single straight tube is based on gas dynamics and control volume methods. The behavior of the flow in the various components of the engine and their respective coupling is modeled for the first time. We show that the flow in the plenum oscillates due to valve opening and closing, and that this unsteadiness results in total pressure losses. We highlight the influence of the interaction between the detonation process and the filling process, which generates a moving flow into which the detonation has to initiate and propagate. Our single-cycle impulse model is extended to include the effect of filling velocity on detonation tube impulse. Based on this, the engine thrust is calculated using an open-system control volume analysis. It is found to be the sum of the contributions of detonation tube impulse, momentum, and pressure terms. Performance calculations for hydrogen- and JP10-fueled PDEs show that thrust is generated up to a flight Mach number of 4 and that the specific impulse decreases quasi-linearly with increasing flight Mach number. We find that PDEs with a straight detonation tube have a higher specific impulse than the ramjet below a flight Mach number of 1.35. PDE performance was found to be very sensitive to the value of the filling velocity, and potential improvements

may be possible with a converging-diverging nozzle at the exit if the pressure in the surrounding atmosphere is low enough so that significant conversion of chemical energy into kinetic energy in the nozzle is possible.

Bibliography

Alekseev, V. I., S. B. Dorofeev, V. P. Sidorov, and B. B. Chaivanov (1993). Experimental study of large-scale unconfined fuel spray detonations. In *Progress in Aeronautics and Astronautics*, Volume 154, pp. 95–105. AIAA. 119

Anderson, J. D. (1990). *Modern Compressible Flow*. McGraw-Hill, Second Edition. 4

Ashford, S. A. and G. Emmanuel (1996). Oblique detonation wave engine performance prediction. *Journal of Propulsion and Power 12*(2), 322–327. 111

Austin, J. M. (2003). *The Role of Instability in Gaseous Detonation*. Ph. D. thesis, California Institute of Technology, Pasadena, California. xii, 10, 12

Austin, J. M. and J. E. Shepherd (2003). Detonations in hydrocarbon fuel blends. *Combustion and Flame 132*, 73–90. xvii, 118, 123, 124, 125, 129, 255

Back, L. H., W. L. Dowler, and G. Varsi (1983). Detonation propulsion experiments and theory. *AIAA Journal 21*(10), 1418–1427. 49

Biedron, R. T. and T. C. Adamson (1988). Unsteady flow in a supercritical supersonic diffuser. *AIAA Journal 26*(11), 1336–1345. 235

Bollay, V. and D. Bitondo (1954). Preliminary program report on the experimental performance of the multi-jet engine. Project Squid Conference on Wave Engines and Pulsejets, Report AD-A952624, November 1954, Princeton University, Princeton, NJ. 44

Bratkovich, T. and T. Bussing (1995). A pulse detonation engine performance model. 31st AIAA/ASME/SAE/ASEE Joint Propulsion Conference and Exhibit, July 10–12, 1995, San Diego, CA, AIAA 95–3155. 49, 207

Bratkovich, T. E., M. J. Aarnio, J. T. Williams, and T. R. A. Bussing (1997). An introduction to pulse detonation rocket engines (PDREs). 33rd AIAA/ASME/SAE/ASEE Joint Propulsion Conference and Exhibit, July 6–9, 1997, Seattle, WA, AIAA 97–2742. 49

Brophy, C. M., J. O. Sinibaldi, and P. Damphousse (2002). Initiator performance for liquid-fueled pulse detonation engines. 40th Aerospace Sciences Meeting and Exhibit, January 14–17, 2002, Reno, NV, AIAA 2002–0472. 50

Brophy, C. M., L. S. Werner, and J. O. Sinibaldi (2003). Performance characterization of a valveless pulse detonation engine. 41st AIAA Aerospace Sciences Meeting and Exhibit, January 6–9, 2003, Reno, NV, AIAA 2003-1344. 50, 206, 209

Bussing, T. R. A. (1995). A rotary valve multiple pulse detonation engine (RVMPDE). AIAA Paper 95-2577, 1995. 49, 50

Bussing, T. R. A., T. E. Bratkovich, and J. B. Hinkey (1997). Practical implementation of pulse detonation engines. 33rd AIAA/ASME/SAE/ASEE Joint Propulsion Conference and Exhibit, July 6–9, 1997, Seattle, WA, AIAA 97-2748. 153, 155, 156, 187

Bussing, T. R. A. and G. Pappas (1996). Pulse detonation engine theory and concepts. In *Progress in Aeronautics and Astronautics*, Volume 165, pp. 421–472. AIAA. 43, 48, 49, 50, 84, 153, 154, 208, 209

Cambier, J.-L., H. Adelman, and G. Menees (1988). Numerical simulations of an oblique detonation wave engine. AIAA Paper 88-0063, 1988. 111

Cambier, J. L. and J. K. Tegner (1998). Strategies for pulsed detonation engine performance optimization. *Journal of Propulsion and Power 14*(4), 489–498. 49, 153, 187, 206

Chao, T., E. Wintenberger, and J. E. Shepherd (2001). On the design of pulse detonation engines. Technical Report FM00-7, GALCIT. 186

Chapman, D. L. (1899). On the rate of explosion in gases. *Philos. Mag. 47*, 90–104. 1, 3

Ciccarelli, G., T. Ginsberg, J. Boccio, C. Economos, K. Sato, and M. Kinashita (1994). Detonation cell size measurements and predictions in hydrogen-air-steam mixtures at elevated temperatures. *Combustion and Flame 99*, 212–220. xvii, 123, 125

Clarke, J. M. and J. H. Horlock (1975). Availability and propulsion. *Journal of Mechanical Engineering Science 17*(4), 223–232. 56

Cooper, M., S. Jackson, J. Austin, E. Wintenberger, and J. E. Shepherd (2002). Direct experimental impulse measurements for deflagrations and detonations. *Journal of Propulsion and Power 18*(5), 1033–1041. xx, 155, 168, 169, 178, 179, 180, 182, 183, 184, 185, 204, 242, 254

Cooper, M., J. Jewell, and J. E. Shepherd (2003). Effect of a porous thrust surface on detonation tube impulse. 39th AIAA/ASME/SAE/ASEE Joint Propulsion Conference and Exhibit, July 20–23, Huntsville, AL, AIAA 2003-4822. 254

Cooper, M. and J. E. Shepherd (2002). The effect of nozzles and extensions on detonation tube performance. 38th AIAA/ASME/SAE/ASEE Joint Propulsion Conference and Exhibit, July 7-10, 2002, Indianapolis, IN, AIAA 2002-3628. 51, 71

Courant, R. and K. O. Friedrichs (1967). *Supersonic Flow and Shock Waves*. Interscience Publishers, Inc., New York. 4, 5

Coy, E. (2003). Pulse combustion rockets for space propulsion applications. 41st Aerospace Sciences Meeting and Exhibit, January 6–9, 2003, Reno, NV, AIAA 2003–1174. 49

CRC (1983). Aviation fuel properties. Technical report, Coordinating Research Council. No. 530. xxv, 119, 254

Culick, F. E. C. and T. Rogers (1983). The response of normal shocks in diffusers. *AIAA Journal 21*(10), 1382–1390. 234, 236

Curran, E. T., W. H. Heiser, and D. T. Pratt (1996). Fluid phenomena in scramjet combustion systems. *Annual Review of Fluid Mechanics 28*, 323–360. 140

Dabora, E. K. (1994). Status of gaseous detonation waves and their role in propulsion. In *Fall Technical Meeting of the Eastern States Section of the Combustion Institute*, Pittsburgh, PA, pp. 11–18. 110

Dabora, E. K. and J. C. Broda (1993). Standing normal detonations and oblique detonations for propulsion. AIAA Paper 93-2325, 1993. 113, 127

Dabora, E. K., D. Desbordes, C. Guerraud, and H. G. Wagner (1991). Oblique detonations at hypersonic velocities. In *Progress in Aeronautics and Astronautics*, Volume 133, pp. 187–204. AIAA. 122

Daniau, E. (2001). *Contribution à l'Etude des Performances d'un Moteur à Détonation Pulsée*. Ph. D. thesis, ENSMA et Faculté des Sciences Fondamentales et Appliquées, Poitiers, France. 181

Davidson, D. F., D. C. Horning, J. T. Herbon, and R. K. Hanson (2000). Shock tube measurements of JP-10 ignition. In *Proceedings of the 28th Symposium on Combustion*, pp. 1687–1692. xvii, xxv, 123, 124, 125, 126, 130, 141

Dean, A. J. (2003). Recent developments in approaches to pulsed detonation propulsion. 39th AIAA/ASME/SAE/ASEE Joint Propulsion Conference and Exhibit, July 21–23, 2003, Huntsville, AL, AIAA 2003–4510. 49, 50, 51

Döring, W. (1943). On detonation processes in gases. *Ann. Phys. 43*, 421–436. 7

Dorofeev, S., M. Kuznetsov, V. Alekseev, A. Efimenko, and W. Breitung (2001). Evaluation of limits for effective flame acceleration in hydrogen mixtures. *Journal of Loss Prevention in the Process Industries 14*(6), 583–589. 183, 184

Dorofeev, S., V. P. Sidorov, M. S. Kuznetzov, I. D. Matsukov, and V. I. Alekseev (2000). Effect of scale on the onset of detonations. *Shock Waves 10*, 137–149. 184

Dudebout, R., J. P. Sislian, and R. Oppitz (1998). Numerical simulation of hypersonic shock-induced combustion ramjets. *Journal of Propulsion and Power 14*(6), 869–879. 111

Dunlap, R., R. L. Brehm, and J. A. Nicholls (1958). A preliminary study of the application of steady-state detonative combustion to a reaction engine. *Jet Propulsion 28*(7), 451–456. 56, 107, 109, 127, 140

Dupre, G., J. Joannon, R. Knystautas, and J. H. Lee (1990). Unstable detonations in the near-limit regime in tubes. In *Proceedings of the 23rd Symposium on Combustion*, pp. 1813–1820. 127

Dupre, G., R. Knystautas, and J. H. Lee (1986). Near-limit propagation of detonation in tubes. *Progress in Aeronautics and Astronautics 106*, 244–259. 126

Dyer, R. S. and T. A. Kaemming (2002). The thermodynamic basis of pulsed detonation engine thrust production. 38th AIAA/ASME/SAE/ASEE Joint Propulsion Conference and Exhibit, July 7–10, 2002, Indianapolis, IN, AIAA 2002–4072. 51

Edelman, L. B. (1947). The pulsating jet engine—its evolution and future prospects. *SAE Quarterly Transactions 1*(2), 204–216. 43

Edwards, D. H., A. T. Jones, and D. E. Phillips (1976). The location of the Chapman-Jouguet surface in a multi-headed detonation wave. *Journal of Physics D: Applied Physics 9*, 1331–1342. 128

Eidelman, S., W. Grossmann, and I. Lottati (1991). Review of propulsion applications

and numerical simulations of the pulsed detonation engine concept. *Journal of Propulsion and Power 7*(6), 857–865. 43, 48, 49, 84

Endo, T. and T. Fujiwara (2002). A simplified analysis on a pulse detonation engine. *Trans. Japan Soc. Aero. Space Sci. 44*(146), 217–222. 155, 242

Falempin, F., D. Bouchaud, B. Forrat, D. Desbordes, and E. Daniau (2001). Pulsed detonation engine possible application to low-cost tactical missile and to space launcher. 37th AIAA/ASME/SAE/ASEE Joint Propulsion Conference and Exhibit, July 8-11, 2001, Salt Lake City, UT, AIAA 2001-3815. 51

Fickett, W. and W. C. Davis (2001). *Detonation Theory and Experiment*. Dover Publications Inc. 6, 7, 9, 10, 67, 70, 158, 161, 175

Foa, J. V. (1951). Single flow jet engines—a generalized treatment. *Journal of the American Rocket Society 21*, 115–126. 32, 39, 40, 41, 44, 66

Foa, J. V. (1959). Intermittent jets. In O. E. Lancaster (Ed.), *Jet Propulsion Engines*, Volume 12, pp. 377–438. Princeton University Press. xiii, 32, 34, 37, 39, 43, 44, 45, 46

Foa, J. V. (1960). *Elements of Flight Propulsion*. John Wiley & Sons, Inc. xiii, 31, 32, 34, 36, 39, 40, 41, 42, 43, 44, 45, 46, 80, 111, 209, 258

Fuller, E. J., R. B. Mays, R. H. Thomas, and J. A. Schetz (1992). Mixing studies of helium in air at high supersonic speeds. *AIAA Journal 30*, 2234–2243. 140

Gavrikov, A. I., A. A. Efimenko, and S. B. Dorofeev (2000). A model for detonation cell size prediction from chemical kinetics. *Combustion and Flame 120*, 19–33. 12, 122

Glass, I. I. and J. P. Sislian (1994). *Nonstationary Flows and Shock Waves*. Clarendon Press, Oxford Science Publications. 158, 159, 222, 224, 225

Gross, R. A. and W. Chinitz (1960). A study of supersonic combustion. *Journal of the Aero/Space Sciences 27*(7), 517–524. 112, 113

Guirao, C. M., R. Knystautas, J. Lee, W. Benedick, and M. Berman (1982). Hydrogen-air detonations. In *Proceedings of the 19th Symposium on Combustion*, pp. 583–590. xvii, 123, 125

Harris, P. G., R. Farinaccio, and R. A. Stowe (2001). The effect of DDT distance on impulse in a detonation tube. 37th AIAA/ASME/SAE/ASEE Joint Propulsion Conference and Exhibit, July 8–11, 2001, Salt Lake City, UT, AIAA 2001-3467. 155, 242

Harris, P. G., S. Guzik, R. Farinaccio, R. A. Stowe, D. Whitehouse, T. Josey, D. Hawkin, R. Ripley, R. Link, A. J. Higgins, and P. A. Thibault (2002). Comparative evaluation of performance models of pulse detonation engines. 38th AIAA/ASME/SAE/ASEE Joint Propulsion Conference and Exhibit, July 7–10, 2002, Indianapolis, IN, AIAA 2002-3912. 208

Heiser, W. H. and D. T. Pratt (2002). Thermodynamic cycle analysis of pulse detonation engines. *Journal of Propulsion and Power 18*(1), 68–76. 51, 82, 83, 86, 148, 149, 154, 155, 207, 208

Helman, D., R. P. Shreeve, and S. Eidelman (1986). Detonation pulse engine. AIAA 86–1683. 49

Hertzberg, A. and A. Russo (1954). The investigation of a resonant wave engine. Project Squid Conference on Wave Engines and Pulsejets, Report AD-A952624, November 1954, Princeton University, Princeton, NJ. 44

Hill, P. G. and C. R. Peterson (1992). *Mechanics and Thermodynamics of Propulsion*. Addison-Wesley, Second Edition. 17, 22, 23, 24, 25, 26, 27, 35, 111, 120, 205, 211, 239, 283

Hoffmann, N. (1940). Reaction propulsion by intermittent detonative combustion. German Ministry of Supply, AI152365 Volkenrode Translation. 48

Hornung, H. (2000). Computations carried out at GALCIT, Pasadena, CA. 161

Jackson, S. I. and J. E. Shepherd (2002). Initiation systems for pulse detonation engines. 38th AIAA/ASME/SAE/ASEE Joint Propulsion Conference and Exhibit, July 7–10, 2002, Indianapolis, IN, AIAA 2002–3627. 50

Jacobs, S. J. (1956). The energy of detonation. NAVORD Report 4366, U.S. Naval Ordnance Laboratory, White Oak, MD. Available as NTIS AD113271 – Old Series. 67, 92, 93

Jouguet, E. (1905). On the propagation of chemical reactions in gases. *Journal de Mathématiques Pures et Appliquées 1*, 347. 1, 3

Kaemming, T. (2001). Integrated vehicle comparison of turbo-ramjet engine and pulsed detonation engine (pde). International Gas Turbine & Aeroengine Congress and Exhibition, June 4–7, 2001, New Orleans, LA. 207

Kailasanath, K. (2000). Review of propulsion applications of detonation waves. *AIAA Journal 38*(9), 1698–1708. 48, 49, 67, 153, 156, 187

Kailasanath, K. (2001). A review of research on pulse detonation engine nozzles. 37th AIAA/ASME/SAE/ASEE Joint Propulsion Conference and Exhibit, July 8–11, 2001, Salt Lake City, UT, AIAA 2001-3932. 51, 207, 258

Kailasanath, K. (2002). Recent developments in the research on pulse detonation engines. 40th AIAA Aerospace Sciences Meeting and Exhibit, January 14–17, 2002, Reno, NV, AIAA 2002-0470. 49, 50, 51, 156, 206

Kailasanath, K., G. Patnaik, and C. Li (2001). Computational studies of pulse detonation engines: a status report. 35th AIAA/ASME/SAE/ASEE Joint Propulsion Conference and Exhibit, 20-24 June, 1999, Los Angeles, CA, AIAA 1999-2634. 156

Kaneshige, M. K. and J. E. Shepherd (1996). Oblique detonation stabilized on a hypervelocity projectile. In *Proceedings of the 26th Symposium on Combustion*, pp. 3015–3022. 121

Kasahara, J., K. Takazawa, T. Arai, and A. Matsuo (2002). Experimental study of impulse and heat transfer on pulse detonation engines. 38th AIAA/ASME/SAE/ASEE Joint Propulsion Conference and Exhibit, July 7–10, 2002, Indianapolis, IN, AIAA 2002-4071. 206, 242

Kee, R., F. Rupley, and J. Miller (1989). Chemkin II: A Fortran chemical kinetics package for the analysis of gas-phase chemical kinetics. Technical Report SAND89-8009, Sandia National Laboratory. xvii, xxv, 9, 122, 124, 125, 126, 130, 141

Kentfield, J. A. C. (2002). Fundamentals of idealized airbreathing pulse-detonation engines. *Journal of Propulsion and Power 18*(1), 77–83. 51, 84, 86, 208

Konnov, A. A. (1998). Detailed reaction mechanism for small hydrocarbons combustion. Release 0.4. http://www.homepages.vub.ac.be/∼akonnov. xii, 9, 122

Krzycki, L. J. (1962). Performance characteristics of an intermittent detonation device. U.S. Naval Ordnance Test Station, U.S. Naval Weapons Report 7655, China Lake, CA. 49

Kuchta, J. M. (1985). Investigation of fire and explosion accidents in the chemical, mining, and fuel-related industries—a manual. Technical report, Bureau of Mines, United States Department of the Interior. Bulletin 680. xxv, 117, 119

Lasheras, J., B. Varatharajan, C. Varga, and F. Williams (2001). Studies of fuel distribution and detonation chemistry for pulse detonation engines. ISABE 2001-1174, Bangalore, India. 50

Lawrence, H. R. and R. Weatherston (1954). The capabilities of the shrouded wave engine. Project Squid Conference on Wave Engines and Pulsejets, Report AD-A952624, November 1954, Princeton University, Princeton, NJ. 44, 47

Lee, J. H. S. (1984). Dynamic parameters of gaseous detonations. *Annual Review of Fluid Mechanics 16*, 311–336. 12, 13, 126, 183

Lee, J. J., G. Dupre, R. Knystautas, and J. H. Lee (1995). Doppler interferometry study of unstable detonations. *Shock Waves 5*, 175–181. 128, 129

Lewis, B. and G. von Elbe (1961). *Combustion, Flames and Explosions of Gases*. Academic Press, Second Edition. 5, 124

Li, C. and K. Kailasanath (2001). A numerical study of reactive flows in pulse detonation engines. 37th AIAA/ASME/SAE/ASEE Joint Propulsion Conference and Exhibit, July 8-11, 2001, Salt Lake City, UT, AIAA 2001-3933. 51

Lide, D. R. (Ed.) (2001). *CRC Handbook of Chemistry and Physics*. 82nd Edition. xxv, 119

Lockwood, R. M. (1954). Ducted pulsejets for high subsonic speed, high altitude propulsion. Project Squid Conference on Wave Engines and Pulsejets, Report AD-A952624, November 1954, Princeton University, Princeton, NJ. 46, 47

Logan, J. G. (1954). Valveless intermittent engines for subsonic propulsion applications. Project Squid Conference on Wave Engines and Pulsejets, Report AD-A952624, November 1954, Princeton University, Princeton, NJ. 44

Lynch, E. D. and R. B. Edelman (1996). Analysis of the pulse detonation wave engine. In *Progress in Aeronautics and Astronautics*, Volume 165, pp. 473–516. AIAA. 43, 48, 49, 209

Ma, F., Y. Wu, J. Y. Choi, and V. Yang (2003). Thrust chamber dynamics of multi-tube pulse detonation engines. 41st AIAA Aerospace Sciences Meeting and Exhibit, January 6–9, 2003, Reno, NV, AIAA 2003-1168. 207, 255

Manzhalei, V. I. (1999). Low-velocity detonation limits of gaseous mixtures. *Combustion, Explosion and Shock Waves 35*, 296–302. 127, 128, 129

Mattingly, J. D., W. H. Heiser, and D. H. Daley (1987). *Aircraft Engine Design*. AIAA Education Series. 246

Menees, G. P., H. G. Adelman, J.-L. Cambier, and J. V. Bowles (1992). Wave combustors for trans-atmospheric vehicles. *Journal of Propulsion and Power 8*(3), 709–713. 111

Morris, C. (2003). Quasi-one-dimensional modeling of pulse detonation rocket engines. 39th AIAA/ASME/SAE/ASEE Joint Propulsion Conference and Exhibit, July 20-23, 2003, Huntsville, AL, AIAA 2003-5204. 51

Mullagiri, S., C. Segal, and P. J. Hubner (2003). Oscillating flows in a model pulse detonation engine. *AIAA Journal 41*(2), 324–326. 35, 50, 235

Nicholls, J. A. and E. K. Dabora (1962). Recent results on standing detonation waves. In *Proceedings of the 8th Symposium on Combustion*, pp. 644–655. 112, 113

Nicholls, J. A., E. K. Dabora, and R. L. Gealer (1959). Studies in connection with stabilized gaseous detonation waves. In *Proceedings of the 7th Symposium on Combustion*, pp. 766–772. 112, 114, 117

Nicholls, J. A., H. R. Wilkinson, and R. B. Morrison (1958). Intermittent detonation as a thrust-producing mechanism. *Jet Propulsion 27*(5), 534–541. 48, 49, 155, 242

Nori, V., N. Lerma, and C. Segal (2003). Oscillating flows in inlets for pulse detonation engines. 41st AIAA Aerospace Sciences Meeting and Exhibit, January 6–9, 2003, Reno, NV, AIAA 2003-0886. 35, 50, 236

Oates, G. C. (1984). *Aerothermodynamics of Gas Turbines and Rocket Propulsion*. AIAA Education Series. 22, 25, 27, 34, 57, 84

Papamoschou, D. (1994). Thrust loss due to supersonic mixing. *Journal of Propulsion and Power 10*, 804–809. 140

Papavassiliou, J., A. Makris, R. Knystautas, J. H. S. Lee, C. K. Westbrook, and W. J. Pitz (1993). Measurements of cellular structure in spray detonation. In *Progress in Aeronautics and Astronautics*, Volume 154, pp. 148–169. AIAA. 118, 119, 255

Peraldi, O., R. Knystautas, and J. H. Lee (1986). Criteria for transition to detonation in tubes. In *Proceedings of the 21st Symposium on Combustion*, pp. 1629–1637. 126

Pratt, D. T., J. W. Humphrey, and D. E. Glenn (1991). Morphology of standing oblique detonation waves. *Journal of Propulsion and Power 7*(5), 837–845. 111, 121

Quirk, J. J. (1998). AMRITA—a computational facility (for CFD modelling). VKI 29th CFD Lecture Series, ISSN 0377-8312, 1998. xxii, xxiii, 90, 95, 161, 218, 228, 231, 244, 245

Radulescu, M. I. and R. K. Hanson (2004). Comment on "Analytical model for the impulse of single-cycle pulse detonation tube" by E. Wintenberger, et al. *Submitted to Journal of Propulsion and Power*. 176, 287

Rasheed, A., V. Tangirala, P. F. Pinard, and A. J. Dean (2003). Experimental and numerical investigations of ejectors for PDE applications. 39th AIAA/ASME/SAE/ASEE Joint Propulsion Conference and Exhibit, July 21–23, 2003, Huntsville, AL, AIAA 2003–4971. 51

Reynolds, W. (1986). The element potential method for chemical equilibrium analysis: Implementation in the interactive program stanjan. Technical report, Mechanical Engineering Department, Stanford University. 4, 21, 77, 83, 85, 86, 90, 104, 120, 123, 138, 158, 174, 192, 193, 247, 256, 282, 288, 303

Riggins, D. W., C. R. McClinton, and P. H. Vitt (1997). Thrust losses in hypersonic engines part 1: Methodology. *Journal of Propulsion and Power 13*(2), 281–287. 56, 66

Rubins, P. M. and R. C. Bauer (1994). Review of shock-induced supersonic combustion research and hypersonic applications. *Journal of Propulsion and Power 10*(5), 593–601. 110, 113, 116

Rudinger, G. (1951). On the performance analysis of the ducted pulsejet. Project Squid Technical Memorandum, ATI-122295, Cornell Aeronautical Laboratory. 46

Sajben, M., T. J. Bogar, and J. C. Kroutil (1984). Forced oscillation experiments in supercritical diffuser flows. *AIAA Journal 22*(4), 465–474. 235

Saretto, S., S. Lee, C. Conrad, J. Brumberg, S. Pal, and R. Santoro (2003). Predetonator to thrust tube detonation transition studies for multi-cycle PDE applications. 39th AIAA/ASME/SAE/ASEE Joint Propulsion Conference and Exhibit, July 21–23, 2003, Huntsville, AL, AIAA 2003–4825. 50

Sargent, W. H. and R. A. Gross (1960). Detonation wave hypersonic ramjet. *ARS Journal 30*(6), 543–549. 56, 107, 109, 127

Schauer, F., J. Stutrud, and R. Bradley (2001). Detonation initiation studies and performance results for pulsed detonation engines. 39th AIAA Aerospace Sciences Meeting and Exhibit, January 8–11, 2001, Reno, NV, AIAA 2001-1129. xx, xxiv, 51, 182, 183, 184, 185, 186, 187, 204, 206, 242, 249, 250, 257

Schauer, F., J. Stutrud, R. Bradley, V. Katta, and J. Hoke (2001). Detonation initiation and performance in complex hydrocarbon fueled pulsed detonation engines. 50th JANNAF Propulsion Meeting, Paper I-05, July 11–13, 2001, Salt Lake City, UT. xx, 184

Schultz, E. and J. E. Shepherd (2000). Validation of detailed reaction mechanisms for detonation simulation. Technical Report FM 99-5, GALCIT. 123

Schultz-Grunow, F. (1947). Gas-dynamic investigation of the pulse-jet tube. NACA Technical Memorandum 1131. 43, 44

Shchelkin, K. I. and Y. K. Troshin (1965). *Gasdynamics of Combustion*. Mono Book. Corp., Baltimore, MD. 12

Shepherd, J. (1986). Chemical kinetics of hydrogen-air-diluent detonations. In *Progress in Aeronautics and Astronautics*, Volume 106, pp. 263–293. AIAA. xvii, xxv, 9, 12, 122, 124, 125, 126, 130, 141

Shepherd, J. E. (1994). Detonation waves and propulsion. In *Combustion in High Speed Flows*, pp. 373–420. Kluwer Academic Publishers. 109, 113

Shepherd, J. E. and M. Kaneshige (1997). Detonation database. Technical Report FM97-8, GALCIT. Revised 2001 - see www.galcit.caltech.edu/detn_db/html for the most recent version. 183

Shepherd, J. E. and J. H. S. Lee (1992). On the transition from deflagration to detonation. In *Major Topics in Combustion*, pp. 439–487. Springer Verlag. 50

Sislian, J. P., H. Schirmer, R. Dudebout, and J. Schumacher (2001). Propulsive performance of hypersonic oblique detonation wave and shock-induced combustion ramjets. *Journal of Propulsion and Power 17*(3), 599–604. 111

Stamps, D. W. and S. R. Tieszen (1991). The influence of initial pressure and temperature on hydrogen-air-diluent detonations. *Combustion and Flame 83*, 353–364. xvii, 123, 124, 126

Stanyukovich, K. P. (1960). *Unsteady Motion of Continuous Media*, pp. 142–196. Pergamon Press. 155

Sterling, J., K. Ghorbanian, J. Humphrey, T. Sobota, and D. Pratt (1995). Numerical investigations of pulse detonation wave engines. 31st AIAA/ASME/SAE/ASEE Joint Propulsion Conference and Exhibit, July 10–12, 1995. San Diego, CA. AIAA 95–2479. 153, 186

Sutton, G. P. (1986). *Rocket Propulsion Elements*. Wiley-Interscience, Fifth Edition. 205

Talley, D. and E. Coy (2002). Constant volume limit of pulsed propulsion for a constant gamma ideal gas. *Journal of Propulsion and Power 18*(2), 400–406. 85, 87, 90, 97, 98, 101, 105, 208

Taylor, G. I. (1950). The dynamics of the combustion products behind plane and

spherical detonation fronts in explosives. *Proc. Roy. Soc. A200*, 235–247. 13, 95, 157, 161

Thompson, P. A. (1988). *Compressible Fluid Dynamics*. Advanced Engineering Series, Rensselaer Polytechnic Institute, pp. 347–359. 6, 14, 158, 161

Tsien, H. S. (Ed.) (1946). *Jet Propulsion*, pp. 404–424. Air Technical Service Command. 97

Urtiew, P. A. and A. K. Oppenheim (1966). Experimental observations of transition to detonation in an explosive gas. *Proceedings of the Royal Society A 295*, 13. 11

Vasiliev, A. A., T. P. Gavrilenko, and M. E. Topchian (1972). On the Chapman-Jouguet surface in multi-headed gaseous detonations. *Astronautica Acta 17*, 499–502. 127, 128

von Neumann, J. (1942). *John von Neumann, Collected Works*, Volume 6. Editions A. J. Taub, New York: Macmillan. 7

Weber, M., H. Olivier, H. Grönig, and J. Biegling (2001). On the location of the Chapman-Jouguet surface in gaseous detonations close to the limit of propagation. In *Proceedings of the 18th ICDERS*. 128

Westbrook, C. K. and P. A. Urtiew (1982). Chemical kinetic prediction of critical parameters in gaseous detonations. In *Proceedings of the 19th Symposium on Combustion*, pp. 615–623. 12, 122, 124

Wintenberger, E., J. M. Austin, M. Cooper, S. Jackson, and J. E. Shepherd (2002). Impulse of a single-pulse detonation tube. Technical report, Graduate Aeronautical Laboratories, California Institute of Technology. Report FM00-8, revised January 2004. xxiv, 175, 177, 254, 257

Wintenberger, E., J. M. Austin, M. Cooper, S. Jackson, and J. E. Shepherd (2003). Analytical model for the impulse of single-cycle pulse detonation tube. *Journal of Propulsion and Power 19*(1), 22–38. 153, 208, 242, 287

Wintenberger, E., J. M. Austin, M. Cooper, S. Jackson, and J. E. Shepherd (2004). Reply to comment on "Analytical model for the impulse of single-cycle pulse detonation tube" by W. H. Heiser and D. T. Pratt. *Journal of Propulsion and Power 20*(1), 189–191. 34, 149, 155

Wintenberger, E. and J. E. Shepherd (2003a). A model for the performance of air-breathing pulse detonation engines. *Submitted to Journal of Propulsion and Power*. also AIAA 2003-4511. 67, 87, 206

Wintenberger, E. and J. E. Shepherd (2003b). The performance of steady detonation engines. 41st Aerospace Sciences Meeting and Exhibit, January 6–9, 2003, Reno, NV, AIAA 2003-0714. 56, 107, 109

Wintenberger, E. and J. E. Shepherd (2004). Thermodynamic analysis of combustion processes for propulsion systems. *To be submitted to Journal of Propulsion and Power*. also AIAA 2004-1033. 53

Wu, Y., F. Ma, and V. Yang (2003). System performance and thermodynamic cycle analysis of airbreathing pulse detonation engines. *Journal of Propulsion and Power 19*(4), 556–567. xxiv, 51, 67, 83, 207, 227, 242, 247, 250, 251, 255, 257, 258

Yang, V. and F. E. C. Culick (1985). Analysis of unsteady inviscid diffuser flow with a shock wave. *Journal of Propulsion and Power 1*(3), 222–228. 235, 236

Zabetakis, M. G. (1965). Flammability characteristics of combustible gases and vapors. Technical report, Bureau of Mines, United States Department of the Interior. Bulletin 627. xxv, 119

Zel'dovich, Y., S. Kogarko, and N. Simonov (1956). An experimental investigation of spherical detonation. *Soviet Phys. Tech. Phys. 1*(8), 1689–1713. 183

Zel'dovich, Y. B. (1940a). On the theory of the propagation of detonations in gaseous systems. *Journal of Experimental and Theoretical Physics 10*, 542–568. Available in translation as NACA TM 1261 (1950). 7, 13, 95, 157, 161

Zel'dovich, Y. B. (1940b). On the use of detonative combustion in power engineering. *Journal of Technical Physics 10*(17), 1453–1461. In Russian. 67

Zhang, F., R. S. Chue, D. L. Frost, J. H. S. Lee, P. Thibault, and C. Yee (1995). Effects of area change and friction on detonation stability in supersonic ducts. *Proceedings of the Royal Society of London - Series A 449*, 31–49. 121, 139

Zhdan, S. A., V. V. Mitrofanov, and A. I. Sychev (1994). Reactive impulse from the explosion of a gas mixture in a semi-infinite space. *Combustion, Explosion and Shock Waves 30*(5), 657–663. 153, 155, 242

Zipkin, M. A. and G. W. Lewis (1948). Analytical and experimental performance of an explosion-cycle combustion chamber for a jet-propulsion engine. NACA Technical Note 1702. 43, 44

Zitoun, R. and D. Desbordes (1999). Propulsive performances of pulsed detonations. *Comb. Sci. Tech. 144*, 93–114. 155, 174, 178, 181, 204, 206, 208, 215, 242

Appendix A

Steady detonation engine performance computation

A.1 Formulas for steady detonation engine performance

The performance of ideal steady detonation engines can be expressed as a function of key non-dimensional parameters: γ, M_0, q_f/RT_{t0}, T_{max}/T_{t0}. The main performance parameters for the dramjet are given subsequently.

$$f = \frac{\gamma}{\gamma - 1}\left(\frac{RT_{t0}}{q_f}\right)\left(\frac{T_{max}}{T_{t0}} - 1\right) \tag{A.1}$$

$$\frac{T_4}{T_{t0}} = 2\frac{\gamma - 1}{\gamma + 1}\left[\frac{1}{\gamma - 1} - \left(\frac{T_{max}}{T_{t0}} - 1\right) - \sqrt{\left(\frac{T_{max}}{T_{t0}} - 1\right)\frac{T_{max}}{T_{t0}}}\right] \tag{A.2}$$

$$\frac{F}{\dot{m}c_0} = \sqrt{\frac{2}{\gamma - 1}\frac{T_{max}}{T_0}\left(1 - \frac{2}{\gamma + 1}\frac{T_0}{T_4}\left(\frac{\gamma + 1}{1 + \frac{2\gamma}{\gamma - 1}\left(\frac{T_{t0}}{T_4} - 1\right)}\right)^{\frac{\gamma - 1}{\gamma}}\right)} - M_0 \tag{A.3}$$

$$\eta_0 = \frac{(\gamma - 1)M_0}{\left(\frac{T_{max}}{T_{t0}} - 1\right)\left(1 + \frac{\gamma - 1}{2}M_0^2\right)}\left(\frac{F}{\dot{m}c_0}\right) \tag{A.4}$$

The performance parameters for the turbodet are the following.

$$f = \frac{\gamma}{\gamma - 1}\left(\frac{RT_{t0}}{q_f}\right)\left(\frac{T_{max}}{T_{t0}} - \pi_c^{\frac{\gamma-1}{\gamma}}\right) \tag{A.5}$$

$$\frac{T_4}{T_{t0}} = 2\frac{\gamma-1}{\gamma+1}\left[\frac{\pi_c^{\frac{\gamma-1}{\gamma}}}{\gamma-1} - \left(\frac{T_{max}}{T_{t0}} - \pi_c^{\frac{\gamma-1}{\gamma}}\right) - \sqrt{\left(\frac{T_{max}}{T_{t0}} - \pi_c^{\frac{\gamma-1}{\gamma}}\right)\frac{T_{max}}{T_{t0}}}\right] \tag{A.6}$$

$$\frac{F}{\dot{m}c_0} = \sqrt{\frac{2}{\gamma-1}\left(\frac{T_{max}}{T_{t0}} - (\pi_c^{\frac{\gamma-1}{\gamma}} - 1)\right)\left(1 + \frac{\gamma-1}{2}M_0^2\right)} \times \sqrt{\left[1 - \frac{2}{\gamma+1}\frac{T_0}{T_4}\left(\frac{\gamma+1}{1 + \frac{2\gamma}{\gamma-1}\left(\frac{T_{t0}}{T_4}\pi_c^{\frac{\gamma-1}{\gamma}} - 1\right)}\right)^{\frac{\gamma-1}{\gamma}} \frac{\frac{T_{max}}{T_{t0}}}{\frac{T_{max}}{T_{t0}} - (\pi_c^{\frac{\gamma-1}{\gamma}} - 1)}\right]} - M_0 \tag{A.7}$$

$$\eta_0 = \frac{(\gamma-1)M_0}{\left(\frac{T_{max}}{T_{t0}} - \pi_c^{\frac{\gamma-1}{\gamma}}\right)\left(1 + \frac{\gamma-1}{2}M_0^2\right)}\left(\frac{F}{\dot{m}c_0}\right) \tag{A.8}$$

A.2 Realistic thermodynamic cycle

The performance study of the steady detonation engines has been carried out so far considering ideal models for the detonation. It is, however, possible to calculate the thermodynamic cycle for these devices using state variables with a general equation of state and using realistic thermochemical properties. The following set of equations present, in a general way, the conservation equations required to analyze the cycle, assuming that all the processes are adiabatic. The conditions across the detonation wave can be evaluated by doing equilibrium computations based on realistic thermochemical properties using a code such as STANJAN (Reynolds, 1986), for example. The calculation for the stabilized detonation wave then has to be iterated before the appropriate solution for T_4 is found. Realistic thermochemical calculations will include the effects of endothermic dissociation reactions that will increase the fuel

consumption necessary to maintain the combustor outlet temperature at the given value T_{max}. The enthalpy per unit mass of the flow at a given station i in the engine depends on the mass fractions and respective enthalpies of the species j at the corresponding conditions.

$$h_i = \sum_{j=1}^{k} Y_j h(T_i) \tag{A.9}$$

If the components (inlet, compressor, turbine, nozzle) are assumed to be ideal, the corresponding thermodynamic processes are isentropic, and the entropy $s = s(T, P)$ is assumed to be constant. The equation of state and the constant entropy conditions can then be used to obtain a relationship between the pressure and temperature ratios. However, aerodynamic losses also occur in realistic engine components. The compression and expansion processes are not isentropic and the stagnation pressure at the end of the process is lower than for an isentropic process. The typical approach to model aerodynamic losses (Hill and Peterson, 1992, Chap. 5) is to define empirical adiabatic efficiencies for diffusers, compressors, and nozzles. The adiabatic efficiency of an engine component is defined as the ratio of the ideal (isentropic) to the actual enthalpy change during the process across the engine component for the same given pressure ratio (Hill and Peterson, 1992, p. 170). A more specific study of each engine component at the given conditions enables the determination of these coefficients. Finally, the exit plane assumption is that the flow be pressure-matched, i.e. $P_9 = P_0$. If the exit is not pressure-matched, the thrust equation, Eq. 5.47, has to be rewritten taking into account the pressure differential terms in the control volume analysis. The set of equations for the dramjet are given below. The specified parameters are P_0, T_0, M_0, T_{max}, ϵ_d, and ϵ_n. The solution for state 4 is found by iterating steps a. and b.

a. freestream (0) - combustor inlet (4):

$$h_0 + u_0^2/2 = h_4 + u_4^2/2 \ ; \ s_0 = s_4 \ ; \ \epsilon_d = (h_{t4is} - h_0)/(h_{t4} - h_0)$$

b. combustor inlet (4) - combustor outlet (5):

$$h_4 + u_4^2/2 + f h_{tf} = (1 + f)(h_5 + c_5^2/2) \ ; \ T_{t5} = T_{max}$$

c. combustor outlet (5) - nozzle exit (9):

$$h_5 + c_5^2/2 = h_9 + u_9^2/2 \; ; \; s_5 = s_9 \; ; \; \epsilon_n = (h_{t5} - h_9)/(h_{t5} - h_{9is}) \; ; \; P_9 = P_0$$

The set of equations for the turbodet has to include the work supplied by the compressor and the energy balance across the turbine. The specified parameters are P_0, T_0, M_0, π_c, T_{max}, ϵ_d, ϵ_c, ϵ_{n1}, ϵ_{n2}, ϵ_t, and ϵ_n. The solution for state 4 is found by iterating steps c. and d.

a. freestream (0) - compressor inlet (2):

$$h_0 + u_0^2/2 = h_2 \; ; \; s_0 = s_2 \; ; \; \epsilon_d = (h_{t2is} - h_0)/(h_{t2} - h_0)$$

b. compressor inlet (2) - compressor outlet (3):

$$h_2 + \dot{w} = h_3 \; ; \; P_3/P_2 = \pi_c \; ; \; s_2 = s_3 \; ; \; \epsilon_c = (h_{3is} - h_2)/(h_3 - h_2)$$

c. compressor outlet (3) - combustor inlet (4):

$$h_3 = h_4 + u_4^2/2 \; ; \; s_3 = s_4 \; ; \; \epsilon_{n1} = (h_3 - h_{t4})/(h_3 - h_{t4is})$$

d. combustor inlet (4) - combustor outlet (5):

$$h_4 + u_4^2/2 + f h_{tf} = (1 + f)(h_5 + c_5^2/2) \; ; \; T_{t5} = T_{max}$$

e. combustor outlet (5) - turbine inlet (6):

$$h_5 + c_5^2/2 = h_6 \; ; \; s_5 = s_6 \; ; \; \epsilon_{n2} = (h_{6is} - h_{t5})/(h_6 - h_{t5})$$

f. turbine inlet (6) - turbine outlet (8):

$$(1 + f)(h_8 - h_6) = h_3 - h_2 = \dot{w} \; ; \; s_6 = s_8 \; ; \; \epsilon_t = (h_6 - h_8)/(h_6 - h_{8is})$$

g. turbine outlet (8) - nozzle exit (9):

$$h_8 = h_9 + u_9^2/2 \; ; \; s_8 = s_9 \; ; \; \epsilon_n = (h_8 - h_9)/(h_8 - h_{9is}) \; ; \; P_9 = P_0$$

Appendix B

Influence of non-equilibrium flow on detonation tube impulse

The competition between the rate of pressure change along a particle path in the Taylor wave and the chemical reaction rates in the dissociating gases has a strong influence on the properties in the stagnant region behind the Taylor wave (state 3) and the specific impulse generated by the detonation of the gaseous mixture. The self-similarity of the flow in the Taylor wave (Section 1.1.4) implies that the rate of pressure change along a particle path depends on the initial location of this particle. A fluid particle located near the closed end of the tube spends a very short time in the Taylor wave, whereas another particle located further downstream from the closed end will spend more time in the Taylor wave. This means that particles located near the closed end of the tube will undergo a more rapid expansion than particles located further away. Hence, fluid particles located very close to the closed end of the tube will expand along the frozen isentrope, since the rate of pressure change is much higher than the chemical reaction rates. On the other hand, fluid particles located very far downstream of the closed end expand along the equilibrium isentrope, since the expansion is slower than the chemical reaction rates. These limiting cases bound the range of possible behaviors for the dissociating gas.

The chemical reaction rates for dissociation and recombination reactions strongly depend on temperature. Dissociation reactions are favored in the detonation products of fuel-oxygen mixtures, which are characterized by high CJ temperatures (on

the order of 3800 K). The degree of dissociation is lower in the products of fuel-air mixtures, which are characterized by much lower CJ temperatures, on the order of 2900 K. Thus, the difference between the frozen and the equilibrium isentropes is much larger in the case of fuel-oxygen mixtures than for fuel-air mixtures. In practice, a fluid particle expanding behind a CJ detonation will initially be in chemical equilibrium, because of the fast chemical reaction rates caused by the high CJ temperature. However, as the particle expands, its temperature drops and the chemical reaction rates slow down. Below a certain temperature, the particle cannot be considered in chemical equilibrium any more, and the effect of chemical kinetics becomes dominant. If the particle expands even further, as for example would be the case in an exit nozzle, its temperature will drop below a critical temperature under which its composition can essentially be considered as frozen, because the chemical reaction rates are too slow to compete with the expansion process.

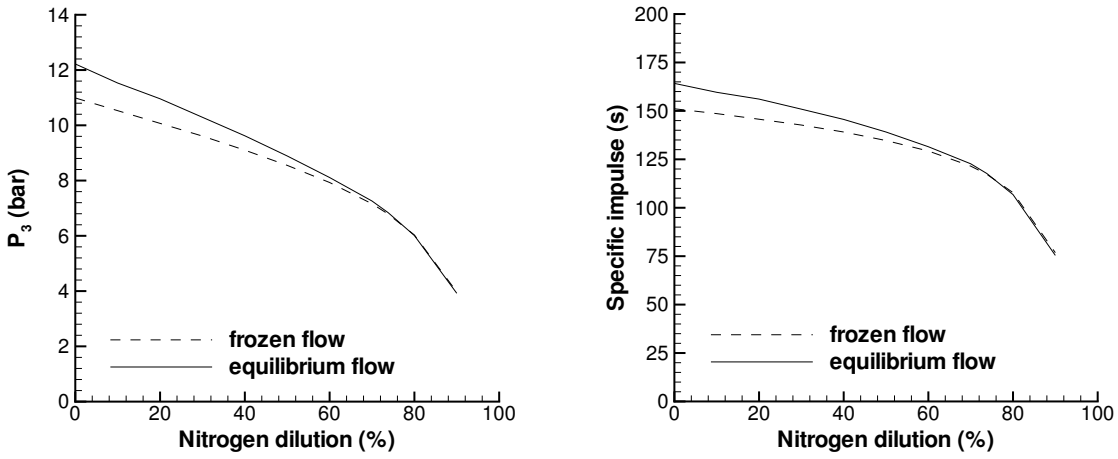

Figure B.1: Influence of non-equilibrium flow in the Taylor wave on the plateau pressure P_3 and the specific impulse for stoichiometric ethylene-oxygen mixtures diluted with nitrogen at 1 bar and 300 K initial conditions.

The influence of non-equilibrium flow on the pressure behind the Taylor wave and the specific impulse is illustrated in Fig. B.1 for ethylene-oxygen mixtures diluted with nitrogen. The frozen flow calculation fits the frozen isentrope with a constant value of γ_{fr} calculated at the CJ point. The equilibrium flow calculation numerically inte-

grates the equilibrium isentrope to solve the Riemann invariant equation (Eq. 4.20). The equilibrium calculation yields higher pressure values than the frozen calculation because of the additional energy released by exothermic recombination reactions during the expansion process. The difference increases with decreasing nitrogen dilution, due to the increasing CJ temperature and the corresponding increased dissociation. In particular, the pressure P_3 for stoichiometric ethylene-oxygen is 10% lower when assuming frozen flow rather than equilibrium flow. This translates into a predicted specific impulse being about 8% lower for frozen flow than for equilibrium flow. Figure B.1 shows that as the amount of nitrogen dilution increases, the pressure values get closer because of the decreasing CJ temperatures and chemical reaction rates. For ethylene-air mixtures, the pressure P_3 obtained from the frozen calculation is within 0.7% of that obtained from the equilibrium calculation and the specific impulse values are within 0.4%. As discussed in Section 4.3.4, the equilibrium calculation is more representative of typical detonation tube laboratory experiments. In conclusion, for fuel-air mixtures at standard conditions, the assumption made for the behavior of the dissociating gas during the expansion in the Taylor wave has little influence on the specific impulse. However, for fuel-oxygen mixtures, this assumption can result in significant differences for the specific impulse. I am grateful to Radulescu and Hanson (2004) for initially pointing out this issue and commenting on the incorrect value of the isentropic exponent used in Wintenberger et al. (2003).

Appendix C

Impulse model prediction tables

The following tables give the CJ properties and the predicted values for the impulse per unit volume, the mixture-based and the fuel-based specific impulse, calculated with the impulse model described in Chapter 4. The calculations cover a range of fuels including ethylene, propane, acetylene, hydrogen, Jet A and JP10. The CJ properties were calculated using thermochemical equilibrium computations with STANJAN (Reynolds, 1986). The speed of sound c_2 and the value of γ reported in the tables are those corresponding to equilibrium flow. The properties at state 3 were calculated by numerically integrating Eq. 4.20 along the equilibrium isentrope. The impulse is calculated based on Eqs. 4.8 and 4.16 with $\beta = 0.53$.

Table C.1: Impulse model predictions for C_2H_4-O_2 mixtures

P_1 (bar)	T_1 (K)	Mixture	U_{CJ} (m/s)	P_2 (bar)	c_2 (m/s)	γ	c_3 (m/s)	P_3 (bar)	α	I_V (kg/m^{2}s)	I_{SP} (s)	I_{SPF} (s)
0.2	300	C2H4+3O2	2298.1	6.26	1237.3	1.1291	1165.7	2.30	1.117	238.0	97.5	431.2
0.4	300	C2H4+3O2	2331.3	12.86	1256.8	1.1332	1182	4.72	1.117	676.1	138.5	612.6
0.6	300	C2H4+3O2	2350.9	19.59	1268.4	1.1358	1191.6	7.20	1.116	1117.1	152.6	674.7
0.8	300	C2H4+3O2	2364.9	26.4	1276.8	1.1378	1198.5	9.70	1.116	1560.1	159.8	706.7
1	300	C2H4+3O2	2375.8	33.27	1283.5	1.1397	1203.9	12.22	1.116	2004.2	164.3	726.3
1.2	300	C2H4+3O2	2384.7	40.2	1288.7	1.1407	1208.2	14.77	1.116	2450.5	167.4	740.0
1.4	300	C2H4+3O2	2392.2	47.2	1292.8	1.1410	1212	17.34	1.116	2898.9	169.6	750.0
1.6	300	C2H4+3O2	2398.8	54.2	1296.5	1.1415	1215.2	19.91	1.116	3347.5	171.6	759.0
1.8	300	C2H4+3O2	2404.5	61.25	1299.9	1.1422	1218	22.50	1.116	3796.9	173.0	765.0
2	300	C2H4+3O2	2409.6	68.32	1303	1.1429	1220.5	25.10	1.116	4246.8	174.0	769.5
1	300	0.2C2H4+3O2	1719	17.85	948.9	1.1631	890.4	6.69	1.109	1375.0	110.0	1992.6
1	300	0.4C2H4+3O2	1974	23.55	1070.4	1.1342	1008.2	8.75	1.115	1654.0	133.4	1274.3
1	300	0.6C2H4+3O2	2137.6	27.38	1155.5	1.1335	1087.7	10.17	1.116	1814.2	147.2	986.7
1	300	0.8C2H4+3O2	2267.5	30.55	1224.7	1.1360	1150.6	11.22	1.116	1910.6	155.8	822.3
1	300	1C2H4+3O2	2375.8	33.27	1283.5	1.1397	1203.9	12.22	1.116	2004.2	164.3	726.3
1	300	1.2C2H4+3O2	2467	35.62	1333.2	1.1429	1248.9	13.09	1.116	2080.4	171.4	660.0
1	300	1.4C2H4+3O2	2542.9	37.61	1374.9	1.1458	1285.9	13.70	1.116	2121.7	175.4	604.1
1	300	1.6C2H4+3O2	2604	39.17	1410.2	1.1511	1316.7	14.27	1.115	2164.8	179.6	563.8
1	300	1.8C2H4+3O2	2650.3	40.3	1438.4	1.1576	1340.7	14.68	1.115	2191.7	182.5	529.5
1	300	2C2H4+3O2	2681.8	40.98	1459.6	1.1651	1358	14.89	1.114	2197.4	183.7	497.9
1	300	2.2C2H4+3O2	2699.3	41.2	1474.5	1.1747	1367.9	14.84	1.113	2172.9	182.1	465.3
1	300	2.4C2H4+3O2	2704.2	41.03	1483.5	1.1857	1372.6	14.78	1.112	2155.2	181.2	439.7
1	300	2.6C2H4+3O2	2698.5	40.54	1487.1	1.1974	1372.5	14.60	1.110	2127.5	179.3	415.4
1	300	C2H4+3O2	2375.8	33.27	1283.5	1.1397	1203.9	12.22	1.116	2003.9	164.2	726.2
1	300	C2H4+3O2+0.44N2	2316.2	31.38	1251.2	1.1373	1175	11.53	1.116	1927.6	159.6	776.3
1	300	C2H4+3O2+N2	2258.3	29.57	1220.7	1.1366	1147.2	10.96	1.116	1867.0	156.1	845.9
1	300	C2H4+3O2+1.71N2	2197.8	27.77	1189.3	1.1367	1117.7	10.29	1.115	1787.4	150.9	924.7
1	300	C2H4+3O2+2.67N2	2131.9	25.89	1155.3	1.1372	1085.9	9.62	1.115	1706.6	145.6	1032.1
1	300	C2H4+3O2+4N2	2059.9	23.94	1118.7	1.1389	1051.2	8.89	1.114	1614.9	139.1	1170.7
1	300	C2H4+3O2+6N2	1976.8	21.82	1077.4	1.1430	1011.5	8.11	1.113	1511.0	131.5	1369.7
1	300	C2H4+3O2+9.33N2	1873.8	19.37	1028.3	1.1534	964.1	7.26	1.110	1395.3	122.7	1686.4
1	300	C2H4+3O2+11.28N2	1824.6	18.25	1005.8	1.1610	941.8	6.84	1.109	1333.0	117.7	1845.8
1	300	C2H4+3O2+16N2	1722.7	16.04	961.8	1.1851	896.7	6.01	1.105	1201.3	106.8	2178.2
1	300	C2H4+3O2+36N2	1404.2	10.27	823	1.2780	744.1	3.92	1.086	839.2	75.4	3042.5

Table C.2: Impulse model predictions for C_3H_8-O_2 mixtures

P_1 (bar)	T_1 (K)	Mixture	U_{CJ} (m/s)	P_2 (bar)	c_2 (m/s)	γ	c_3 (m/s)	P_3 (bar)	α	I_V (kg/m^{2}s)	I_{SP} (s)	I_{SPF} (s)
0.2	300	C3H8+5O2	2287.1	6.81	1227.9	1.1252	1158.9	2.50	1.119	276.6	103.2	477.6
0.4	300	C3H8+5O2	2318.2	13.96	1246.3	1.1294	1174.2	5.13	1.118	754.7	141.0	652.6
0.6	300	C3H8+5O2	2336.5	21.24	1257	1.1315	1183.2	7.80	1.118	1235.9	154.0	712.5
0.8	300	C3H8+5O2	2349.5	28.61	1264.7	1.1332	1189.6	10.51	1.118	1719.2	160.7	743.8
1	300	C3H8+5O2	2359.6	36.04	1270.7	1.1345	1194.6	13.24	1.117	2204.2	164.7	762.2
1.2	300	C3H8+5O2	2367.9	43.53	1275.6	1.1356	1198.7	15.99	1.117	2690.6	167.6	775.6
1.4	300	C3H8+5O2	2374.9	51.05	1279.8	1.1366	1202.1	18.76	1.117	3178.0	169.8	785.6
1.6	300	C3H8+5O2	2380.9	58.61	1283.7	1.1380	1205.1	21.53	1.117	3665.5	171.1	792.0
1.8	300	C3H8+5O2	2386.3	66.21	1286.9	1.1387	1207.8	24.32	1.117	4154.7	172.4	797.8
2	300	C3H8+5O2	2391.1	73.84	1289.7	1.1392	1210.1	27.12	1.117	4645.2	173.8	804.3
1	300	0.2C3H8+5O2	1692.1	17.62	937.4	1.1716	877.4	6.55	1.108	1360.4	106.6	2041.2
1	300	0.4C3H8+5O2	1956.7	24.13	1060.4	1.1340	999.3	8.96	1.115	1715.2	132.5	1334.7
1	300	0.6C3H8+5O2	2122.3	28.68	1145.3	1.1313	1079.1	10.63	1.116	1920.5	146.6	1033.3
1	300	0.8C3H8+5O2	2252.4	32.59	1213.6	1.1324	1142.1	11.97	1.117	2066.7	156.1	864.1
1	300	1C3H8+5O2	2359.6	36.04	1270.7	1.1345	1194.6	13.24	1.117	2204.2	164.7	762.2
1	300	1.2C3H8+5O2	2448.1	39.07	1318.6	1.1375	1237.5	14.23	1.117	2298.8	170.1	684.5
1	300	1.4C3H8+5O2	2518.6	41.62	1357.7	1.1414	1272.7	15.16	1.117	2391.8	175.5	630.5
1	300	1.6C3H8+5O2	2570.2	43.54	1388.3	1.1476	1299.5	15.86	1.117	2458.9	179.0	584.8
1	300	1.8C3H8+5O2	2601.4	44.73	1410.3	1.1576	1317.1	16.25	1.116	2490.3	179.7	542.0
1	300	2C3H8+5O2	2611.8	45.13	1423.2	1.1709	1324.4	16.25	1.114	2475.6	177.4	499.2
1	300	2.2C3H8+5O2	2602.7	44.77	1427.6	1.1877	1322.3	15.98	1.112	2434.5	173.5	459.6
1	300	2.4C3H8+5O2	2575.7	43.75	1423.3	1.2068	1311.6	15.62	1.110	2393.3	169.3	425.3
1	300	2.6C3H8+5O2	2531.7	42.11	1411.1	1.2293	1290.7	15.01	1.107	2327.2	163.7	392.1
1	300	C3H8+5O2	2359.6	36.04	1270.7	1.1345	1194.6	13.24	1.117	2204.2	164.7	762.2
1	300	C3H8+5O2+0.67N2	2305.2	33.84	1241.8	1.1331	1168	12.43	1.117	2105.2	160.1	808.7
1	300	C3H8+5O2+1.5N2	2251.3	31.73	1213.8	1.1330	1142	11.66	1.117	2008.0	155.6	868.2
1	300	C3H8+5O2+2.57N2	2194	29.61	1184.4	1.1335	1114.8	10.97	1.116	1924.6	151.9	950.7
1	300	C3H8+5O2+4N2	2131.4	27.45	1152.4	1.1342	1084.6	10.17	1.116	1819.4	146.3	1049.1
1	300	C3H8+5O2+6N2	2061.4	25.2	1117.3	1.1365	1051.2	9.36	1.115	1711.5	140.3	1183.8
1	300	C3H8+5O2+9N2	1979.9	22.79	1077.3	1.1411	1012.4	8.47	1.113	1586.7	132.6	1372.1
1	300	C3H8+5O2+14N2	1878	20.06	1029.2	1.1520	965.1	7.45	1.111	1437.3	122.5	1656.3
1	300	C3H8+5O2+18.8N2	1800.6	18.15	994.4	1.1655	930.9	6.80	1.109	1340.4	115.6	1915.6
1	300	C3H8+5O2+24N2	1728.2	16.48	963.7	1.1840	898.9	6.17	1.106	1237.5	107.7	2141.0
1	300	C3H8+5O2+54N2	1413.7	10.52	827	1.2754	748.3	4.02	1.087	862.1	76.6	2983.4

Table C.3: Impulse model predictions for C_2H_2-O_2 mixtures

P_1 (bar)	T_1 (K)	Mixture	U_{CJ} (m/s)	P_2 (bar)	c_2 (m/s)	γ	c_3 (m/s)	P_3 (bar)	α	I_V (kg/m^{2}s)	I_{SP} (s)	I_{SPF} (s)
0.2	300	C2H2+2.5O2	2335.9	6.29	1263.4	1.1405	1184.3	2.31	1.115	236.0	99.0	403.2
0.4	300	C2H2+2.5O2	2373.5	12.94	1285.9	1.1458	1202.8	4.76	1.115	670.1	140.6	572.5
0.6	300	C2H2+2.5O2	2395.8	19.75	1299	1.1483	1213.7	7.26	1.114	1107.7	154.9	630.9
0.8	300	C2H2+2.5O2	2411.8	26.65	1308.7	1.1509	1221.6	9.80	1.114	1547.1	162.3	660.9
1	300	C2H2+2.5O2	2424.2	33.63	1316.3	1.1527	1227.7	12.37	1.114	1988.4	166.8	679.3
1.2	300	C2H2+2.5O2	2434.4	40.66	1322.4	1.1542	1232.8	14.95	1.114	2431.1	170.0	692.3
1.4	300	C2H2+2.5O2	2443.1	47.74	1327.7	1.1554	1237.2	17.56	1.114	2874.9	172.3	701.7
1.6	300	C2H2+2.5O2	2450.6	54.87	1332.2	1.1563	1240.9	20.18	1.113	3320.2	174.0	708.4
1.8	300	C2H2+2.5O2	2457.3	62.03	1336.2	1.1573	1244.1	22.81	1.113	3766.7	175.5	714.6
2	300	C2H2+2.5O2	2463.2	69.23	1339.7	1.1579	1247	25.46	1.113	4214.0	177.0	720.7
1	300	0.2C2H2+2.5O2	1763.5	18.74	968.6	1.1535	909.9	7.02	1.111	1423.7	114.7	1875.9
1	300	0.4C2H2+2.5O2	2008.3	24.06	1090	1.1375	1024.6	8.94	1.114	1665.7	135.8	1179.1
1	300	0.6C2H2+2.5O2	2173.7	27.75	1178.4	1.1414	1105.1	10.27	1.114	1803.9	148.6	909.4
1	300	0.8C2H2+2.5O2	2308.5	30.89	1251.8	1.1462	1170.8	11.35	1.114	1898.6	157.9	764.4
1	300	1C2H2+2.5O2	2424.2	33.63	1316.3	1.1527	1227.7	12.37	1.114	1988.4	166.8	679.3
1	300	1.2C2H2+2.5O2	2525.5	36.08	1373.3	1.1588	1277	13.14	1.113	2039.9	172.4	613.7
1	300	1.4C2H2+2.5O2	2614.9	38.27	1424.3	1.1650	1321	13.94	1.113	2101.4	178.9	571.4
1	300	1.6C2H2+2.5O2	2693.8	40.22	1469.9	1.1711	1359.7	14.65	1.112	2153.3	184.6	539.1
1	300	1.8C2H2+2.5O2	2763.2	41.93	1511.1	1.1780	1394.2	15.28	1.111	2195.1	189.1	511.8
1	300	2C2H2+2.5O2	2823.7	43.38	1548.4	1.1860	1424.2	15.75	1.110	2219.0	192.3	487.6
1	300	2.2C2H2+2.5O2	2875.6	44.57	1581.8	1.1951	1449.6	16.05	1.109	2222.2	193.5	463.6
1	300	2.4C2H2+2.5O2	2918.8	45.49	1611.6	1.2057	1471.6	16.40	1.107	2238.8	195.8	446.5
1	300	2.6C2H2+2.5O2	2902.2	44.75	1603.8	1.2076	1464.1	16.11	1.107	2208.1	193.8	422.8
1	300	C2H2+2.5O2	2424.2	33.63	1316.3	1.1527	1227.7	12.37	1.114	1988.4	166.8	679.3
1	300	C2H2+2.5O2+0.39N2	2368.9	31.91	1286.7	1.1516	1200.5	11.71	1.114	1915.2	161.8	726.8
1	300	C2H2+2.5O2+0.88N2	2310.5	30.17	1255.4	1.1503	1171.9	11.08	1.113	1846.5	157.4	788.9
1	300	C2H2+2.5O2+1.5N2	2248.2	28.37	1222.8	1.1504	1142.3	10.53	1.113	1791.7	153.8	874.4
1	300	C2H2+2.5O2+2.33N2	2180.7	26.53	1187.1	1.1497	1109.6	9.82	1.113	1707.4	147.8	972.6
1	300	C2H2+2.5O2+3.5N2	2106.1	24.58	1148.4	1.1503	1073.5	9.13	1.112	1627.0	141.8	1111.4
1	300	C2H2+2.5O2+5.25N2	2020.5	22.46	1104.6	1.1523	1032.3	8.34	1.111	1528.4	134.3	1305.5
1	300	C2H2+2.5O2+8.17N2	1915.3	20.01	1052.5	1.1590	983	7.50	1.110	1420.0	125.8	1617.5
1	300	C2H2+2.5N2+9.4N2	1878.8	19.2	1035.2	1.1631	966.4	7.19	1.109	1376.9	122.2	1734.1
1	300	C2H2+2.5O2+14N2	1764.3	16.73	983.1	1.1832	915.2	6.27	1.106	1237.4	110.5	2114.2
1	300	C2H2+2.5O2+31.5N2	1446.6	10.86	844.7	1.2741	764.6	4.15	1.088	880.8	79.3	3009.7

Table C.4: Impulse model predictions for H_2-O_2 mixtures

P_1 (bar)	T_1 (K)	Mixture	U_{CJ} (m/s)	P_2 (bar)	c_2 (m/s)	γ	c_3 (m/s)	P_3 (bar)	α	I_V (kg/m^{2}s)	I_{SP} (s)	I_{SPF} (s)
0.2	300	2H2+O2	2751.6	3.53	1493.8	1.1204	1415.5	1.34	1.114	49.7	52.6	469.6
0.4	300	2H2+O2	2789.7	7.25	1515.7	1.1240	1434.1	2.75	1.113	260.6	137.9	1232.3
0.6	300	2H2+O2	2812.1	11.03	1528.7	1.1263	1445.2	4.18	1.113	472.6	166.7	1489.5
0.8	300	2H2+O2	2828.1	14.86	1538	1.1279	1452.7	5.61	1.113	683.0	180.3	1611.4
1	300	2H2+O2	2840.4	18.72	1545.2	1.1292	1458.8	7.07	1.113	895.8	189.0	1689.2
1.2	300	2H2+O2	2850.5	22.61	1551	1.1301	1463.7	8.54	1.113	1109.3	195.6	1748.2
1.4	300	2H2+O2	2859.2	26.58	1556	1.1309	1467.9	10.02	1.113	1323.2	199.6	1783.9
1.6	300	2H2+O2	2866.5	30.45	1560.2	1.1316	1471.5	11.51	1.113	1537.5	203.7	1820.7
1.8	300	2H2+O2	2873	34.4	1564	1.1323	1474.7	13.00	1.113	1752.2	205.4	1835.6
2	300	2H2+O2	2878.8	38.36	1567.3	1.1327	1477.6	14.50	1.113	1967.4	208.6	1864.0
1	300	0.4H2+O2	1825.3	14.94	1012.1	1.1613	950.9	5.66	1.107	1055.5	114.0	4639.6
1	300	0.8H2+O2	2185.9	17.24	1193.6	1.1331	1126.8	6.53	1.112	1056.7	144.3	3008.3
1	300	1.2H2+O2	2446	18.1	1331.9	1.1294	1258	6.86	1.113	1001.9	162.4	2310.3
1	300	1.6H2+O2	2659.9	18.52	1447.2	1.1289	1366.6	7.00	1.113	944.8	177.2	1935.1
1	300	2H2+O2	2840.4	18.72	1545.2	1.1292	1458.8	7.07	1.113	895.8	189.0	1689.2
1	300	2.4H2+O2	2993.5	18.74	1629.2	1.1305	1537.5	7.08	1.113	851.2	199.6	1519.4
1	300	2.8H2+O2	3123.2	18.63	1701.7	1.1329	1605	7.04	1.113	810.0	208.1	1387.6
1	300	3.2H2+O2	3233.4	18.43	1764.6	1.1361	1663.1	6.97	1.112	771.7	214.0	1275.4
1	300	3.6H2+O2	3327.2	18.16	1819.6	1.1405	1713.3	6.86	1.111	736.3	219.2	1185.5
1	300	4H2+O2	3407.4	17.85	1868	1.1454	1756	6.69	1.111	696.8	220.9	1097.4
1	300	4.4H2+O2	3476.1	17.51	1910.9	1.1510	1794.2	6.56	1.110	666.6	224.2	1033.2
1	300	4.8H2+O2	3535.2	17.16	1948.7	1.1566	1827.8	6.43	1.109	638.9	226.0	973.2
1	300	5.2H2+O2	3586.2	16.8	1982.5	1.1627	1857.3	6.29	1.108	613.1	227.5	921.8
1	300	2H2+O2	2840.4	18.72	1545.2	1.1292	1458.8	7.07	1.113	895.8	189.0	1689.2
1	300	2H2+O2+0.33N2	2641.8	18.35	1438	1.1293	1358.4	6.94	1.113	940.6	175.5	1973.9
1	300	2H2+O2+0.75N2	2474	17.98	1348.4	1.1313	1272.7	6.82	1.112	983.2	164.4	2325.4
1	300	2H2+O2+1.29N2	2324.9	17.53	1269.8	1.1348	1197	6.64	1.112	1014.3	153.0	2734.7
1	300	2H2+O2+2N2	2186.5	16.95	1198.3	1.1410	1128.5	6.42	1.111	1034.1	142.3	3249.0
1	300	2H2+O2+3N2	2050.5	16.14	1130.5	1.1526	1062.4	6.10	1.109	1032.5	131.6	3917.7
1	300	2H2+O2+3.76N2	1970.7	15.51	1092.3	1.1633	1024.1	5.86	1.107	1021.4	123.9	4343.7
1	300	2H2+O2+4.5N2	1904.3	14.91	1061.5	1.1750	992.9	5.63	1.106	1003.7	117.7	4730.3
1	300	2H2+O2+7N2	1722.9	12.88	981.4	1.2209	905.3	4.87	1.098	917.4	100.1	5760.8
1	300	2H2+O2+12N2	1469.7	9.88	862.3	1.2759	780.9	3.81	1.086	768.5	78.3	7231.7
1	300	2H2+O2+27N2	1119.4	6.15	685	1.3204	617.7	2.52	1.072	526.6	50.5	9917.0

Table C.5: Impulse model predictions for Jet A-O_2 mixtures

P_1 (bar)	T_1 (K)	Mixture	U_{CJ} (m/s)	P_2 (bar)	c_2 (m/s)	γ	c_3 (m/s)	P_3 (bar)	α	I_V (kg/m^{2}s)	I_{SP} (s)	I_{SPF} (s)
0.2	300	JetA+13O2	2163.4	6.91	1160.5	1.1236	1096	2.54	1.119	300.1	98.9	430.7
0.4	300	JetA+13O2	2191.9	14.16	1177.3	1.1275	1110.1	5.20	1.118	813.2	134.0	583.3
0.6	300	JetA+13O2	2208.8	21.54	1187.2	1.1297	1118.3	7.91	1.118	1329.3	146.1	636.1
0.8	300	JetA+13O2	2220.7	29	1194.2	1.1312	1124.2	10.66	1.118	1847.9	152.2	662.8
1	300	JetA+13O2	2230	36.53	1199.7	1.1325	1128.8	13.42	1.118	2368.2	156.2	680.1
1.2	300	JetA+13O2	2237.6	44.11	1204.1	1.1334	1132.6	16.21	1.118	2889.8	158.8	691.4
1.4	300	JetA+13O2	2244	51.74	1207.9	1.1343	1135.7	19.01	1.118	3412.8	160.7	699.9
1.6	300	JetA+13O2	2249.5	59.39	1211.2	1.1350	1138.4	21.82	1.117	3936.7	162.1	706.0
1.8	300	JetA+13O2	2254.4	67.08	1214.2	1.1359	1140.8	24.65	1.117	4461.4	163.3	711.0
2	300	JetA+13O2	2258.8	74.8	1216.8	1.1365	1143	27.48	1.117	4986.8	164.2	715.0
1	300	0.2JetA+13O2	1640.1	16.97	912.8	1.1810	852	6.31	1.107	1339.2	102.4	1819.8
1	300	0.4JetA+13O2	1888.3	23.74	1023.8	1.1343	965	8.82	1.115	1744.1	127.7	1198.3
1	300	0.6JetA+13O2	2031.9	28.5	1095.9	1.1297	1033.4	10.56	1.117	1991.4	140.5	925.9
1	300	0.8JetA+13O2	2141.4	32.69	1152.9	1.1306	1085.8	12.01	1.117	2181.6	148.6	771.5
1	300	1JetA+13O2	2230	36.53	1199.7	1.1325	1128.8	13.42	1.118	2368.2	156.2	680.1
1	300	1.2JetA+13O2	2301.3	40.01	1238.1	1.1356	1163.1	14.60	1.118	2514.8	160.7	610.1
1	300	1.4JetA+13O2	2354.6	42.99	1268.4	1.1406	1189.7	15.63	1.117	2644.3	164.2	557.5
1	300	1.6JetA+13O2	2385.5	45.11	1289.5	1.1504	1206.9	16.42	1.117	2748.5	166.1	514.5
1	300	1.8JetA+13O2	2386.5	45.94	1299	1.1685	1210.6	16.54	1.115	2759.4	162.6	465.6
1	300	2JetA+13O2	2352.7	45.22	1293.8	1.1947	1196.1	16.15	1.111	2720.7	156.1	418.1
1	300	2.2JetA+13O2	2283.8	43.01	1271.5	1.2268	1162.7	15.32	1.107	2640.1	148.0	373.7
1	300	2.4JetA+13O2	2180.7	39.55	1229.2	1.2592	1109.2	14.01	1.102	2507.3	137.5	329.7
1	300	2.6JetA+13O2	2046.5	35.18	1166.4	1.2877	1041.4	12.42	1.097	2340.0	125.7	287.9
1	300	JetA+13O2	2230	36.53	1199.7	1.1325	1128.8	13.42	1.118	2368.2	156.2	680.1
1	300	JetA+13O2+1.56N2	2188.1	34.26	1177.5	1.1312	1108.6	12.57	1.118	2246.1	152.3	716.6
1	300	JetA+13O2+3.5N2	2146.8	32.09	1156.3	1.1309	1088.8	11.79	1.117	2131.5	148.6	764.7
1	300	JetA+13O2+6N2	2102.2	29.9	1133.6	1.1312	1068	11.08	1.117	2031.7	145.8	832.5
1	300	JetA+13O2+9.33N2	2052.5	27.68	1108.7	1.1322	1044.4	10.26	1.116	1907.5	141.2	912.4
1	300	JetA+13O2+14N2	1995.7	25.38	1080.6	1.1343	1017.5	9.43	1.115	1781.7	136.0	1022.7
1	300	JetA+13O2+21N2	1927.7	22.92	1047.8	1.1389	985.5	8.52	1.114	1640.6	129.4	1177.8
1	300	JetA+13O2+32.7N2	1839.9	20.15	1007.1	1.1494	945.7	7.55	1.112	1489.4	121.5	1425.3
1	300	JetA+13O2+48.9N2	1743.3	17.51	965.3	1.1698	903.2	6.56	1.108	1324.2	110.8	1706.4
1	300	JetA+13O2+56N2	1705.7	16.58	949.7	1.1804	886.8	6.21	1.106	1263.7	106.7	1813.9
1	300	JetA+13O2+126N2	1409.6	10.63	823.5	1.2728	745.8	4.06	1.088	877.5	76.7	2518.9

Table C.6: Impulse model predictions for JP10-O_2 mixtures

P_1 (bar)	T_1 (K)	Mixture	U_{CJ} (m/s)	P_2 (bar)	c_2 (m/s)	γ	c_3 (m/s)	P_3 (bar)	α	I_V (kg/m^{2}s)	I_{SP} (s)	I_{SPF} (s)
0.2	300	JP10+14O2	2221.3	7.34	1192.7	1.1279	1124.3	2.70	1.119	322.4	105.2	451.2
0.4	300	JP10+14O2	2252.2	15.05	1210.9	1.1319	1139.5	5.53	1.118	853.6	139.2	597.0
0.6	300	JP10+14O2	2270.5	22.91	1221.7	1.1343	1148.5	8.42	1.118	1388.4	151.0	647.6
0.8	300	JP10+14O2	2283.5	30.87	1229.5	1.1363	1154.9	11.34	1.117	1925.5	157.0	673.4
1	300	JP10+14O2	2293.6	38.89	1235.6	1.1378	1159.9	14.29	1.117	2464.4	160.8	689.5
1.2	300	JP10+14O2	2301.9	46.98	1240.7	1.1392	1164	17.26	1.117	3004.5	163.5	701.4
1.4	300	JP10+14O2	2308.9	55.12	1244.8	1.1400	1166.8	20.07	1.117	3515.7	163.8	702.3
1.6	300	JP10+14O2	2315	63.3	1248.2	1.1405	1169.8	23.06	1.117	4055.2	165.3	709.1
1.8	300	JP10+14O2	2320.3	71.54	1251.1	1.1406	1172.4	26.06	1.117	4596.6	166.8	715.3
2	300	JP10+14O2	2325.1	79.79	1253.8	1.1410	1174.8	29.06	1.117	5137.7	167.6	718.7
1	300	0.2JP10+14O2	1681.6	17.95	930.7	1.1703	871.5	6.67	1.109	1399.1	106.3	1853.3
1	300	0.4JP10+14O2	1928.1	24.84	1044.5	1.1345	983.9	9.23	1.115	1799.3	131.1	1209.3
1	300	0.6JP10+14O2	2078.8	29.95	1121.6	1.1326	1056.1	11.10	1.117	2057.3	144.1	933.7
1	300	0.8JP10+14O2	2196.4	34.57	1183.4	1.1343	1112.6	12.70	1.117	2262.4	152.9	781.4
1	300	1JP10+14O2	2293.6	38.89	1235.6	1.1378	1159.9	14.29	1.117	2464.4	160.8	689.5
1	300	1.2JP10+14O2	2374.5	42.93	1279.7	1.1416	1198.8	15.64	1.117	2625.0	165.9	620.5
1	300	1.4JP10+14O2	2440.2	46.61	1316.2	1.1459	1231.1	16.97	1.117	2789.0	170.9	572.2
1	300	1.6JP10+14O2	2489.5	49.75	1345.4	1.1523	1256	18.08	1.116	2923.0	174.0	531.6
1	300	1.8JP10+14O2	2520.1	52.15	1366.2	1.1612	1272.4	18.78	1.116	3003.2	173.9	491.6
1	300	2JP10+14O2	2530	53.59	1378.6	1.1749	1279.9	19.31	1.114	3072.8	173.5	458.9
1	300	2.2JP10+14O2	2519	54.02	1381.6	1.1922	1276.6	19.28	1.112	3075.7	169.3	422.4
1	300	2.4JP10+14O2	2488.8	53.5	1375.4	1.2122	1263	18.89	1.110	3039.3	163.6	387.7
1	300	2.6JP10+14O2	2440.8	52.09	1360.5	1.2351	1241	18.40	1.107	3004.9	158.1	358.0
1	300	JP10+14O2	2293.6	38.89	1235.6	1.1378	1159.9	14.29	1.117	2464.4	160.8	689.5
1	300	JP10+14O2+1.67N2	2248.4	36.39	1211.2	1.1357	1138	13.37	1.117	2338.2	157.1	727.4
1	300	JP10+14O2+3.75N2	2203.9	34	1188.1	1.1351	1116.7	12.49	1.117	2213.7	153.0	774.1
1	300	JP10+14O2+6.43N2	2156	31.6	1163.4	1.1350	1093.6	11.61	1.116	2087.0	148.7	834.3
1	300	JP10+14O2+10N2	2103	29.18	1136.4	1.1353	1068.8	10.81	1.116	1975.4	145.2	921.1
1	300	JP10+14O2+15N2	2042.8	26.69	1106.1	1.1366	1040.2	9.91	1.115	1843.2	140.0	1032.1
1	300	JP10+14O2+22.5N2	1971.5	24.06	1071	1.1398	1006.5	8.94	1.114	1695.8	133.1	1186.6
1	300	JP10+14O2+35N2	1881.2	21.14	1028	1.1478	964.6	7.85	1.112	1528.0	124.1	1425.8
1	300	JP10+14O2+52.64N2	1783.5	18.4	983.9	1.1637	921.3	6.90	1.109	1376.3	114.9	1736.5
1	300	JP10+14O2+60N2	1748	17.49	968.9	1.1725	905.9	6.55	1.108	1318.5	111.0	1845.8
1	300	JP10+14O2+135N2	1458.5	11.4	847.4	1.2649	769	4.32	1.090	923.6	80.7	2585.9

Table C.7: Impulse model predictions for C_2H_4-air mixtures

P_1 (bar)	T_1 (K)	Mixture	U_{CJ} (m/s)	P_2 (bar)	c_2 (m/s)	γ	c_3 (m/s)	P_3 (bar)	α	I_V (kg/m^{2}s)	I_{SP} (s)	I_{SPF} (s)
0.2	300	C2H4+3O2+11.28N2	1791.6	3.54	984	1.1495	924.8	1.33	1.110	73.1	32.3	506.3
0.4	300	C2H4+3O2+11.28N2	1806.2	7.18	993.5	1.1543	932.3	2.69	1.110	387.8	85.6	1342.3
0.6	300	C2H4+3O2+11.28N2	1814.5	10.85	998.9	1.1570	936.5	4.07	1.110	702.6	103.4	1621.1
0.8	300	C2H4+3O2+11.28N2	1820.2	14.54	1002.8	1.1593	939.5	5.45	1.109	1017.7	112.3	1762.2
1	300	C2H4+3O2+11.28N2	1824.6	18.25	1005.8	1.1610	941.8	6.84	1.109	1333.0	117.7	1845.8
1.2	300	C2H4+3O2+11.28N2	1828.2	21.97	1008.2	1.1623	943.6	8.23	1.109	1648.7	121.3	1903.4
1.4	300	C2H4+3O2+11.28N2	1831.2	25.7	1010.2	1.1634	945.1	9.63	1.109	1964.7	124.0	1944.5
1.6	300	C2H4+3O2+11.28N2	1833.7	29.44	1011.9	1.1644	946.5	11.03	1.109	2280.6	125.8	1972.8
1.8	300	C2H4+3O2+11.28N2	1835.9	33.19	1013.4	1.1652	947.6	12.43	1.109	2597.1	127.3	1997.4
2	300	C2H4+3O2+11.28N2	1837.9	36.94	1014.7	1.1658	948.6	13.84	1.109	2913.4	128.6	2017.1
1	300	0.4C2H4+3O2+11.28N2	1424.6	10.8	829.6	1.2651	753.3	4.13	1.089	887.6	78.3	2951.7
1	300	0.6C2H4+3O2+11.28N2	1623.8	14.16	922.2	1.2216	849.4	5.31	1.099	1087.8	95.9	2443.6
1	300	0.8C2H4+3O2+11.28N2	1749.7	16.7	973.1	1.1779	910	6.20	1.107	1230.2	108.6	2102.1
1	300	1C2H4+3O2+11.28N2	1824.6	18.25	1005.8	1.1610	941.8	6.84	1.109	1333.0	117.7	1845.8
1	300	1.2C2H4+3O2+11.28N2	1868.1	19.04	1031.6	1.1684	968.5	7.07	1.110	1350.5	119.2	1578.2
1	300	1.4C2H4+3O2+11.28N2	1887.2	19.2	1051.3	1.1922	979.8	7.05	1.107	1329.6	117.4	1348.6
1	300	1.6C2H4+3O2+11.28N2	1888	18.99	1062.1	1.2182	978.5	6.98	1.103	1310.8	115.8	1179.1
1	300	1.8C2H4+3O2+11.28N2	1878.7	18.64	1064.7	1.2378	972.8	6.85	1.100	1287.6	113.8	1042.2
1	300	2C2H4+3O2+11.28N2	1864.2	18.24	1062.3	1.2520	965.1	6.70	1.097	1263.8	111.7	931.9
1	300	2.2C2H4+3O2+11.28N2	1846.3	17.8	1056.9	1.2636	956.2	6.54	1.096	1238.6	109.6	841.1
1	300	2.4C2H4+3O2+11.28N2	1825.8	17.33	1049.5	1.2739	945.8	6.37	1.094	1212.2	107.3	763.5
1	300	2.6C2H4+3O2+11.28N2	1802.8	16.83	1040.4	1.2835	934.6	6.18	1.092	1184.2	104.8	696.6

Table C.8: Impulse model predictions for C_3H_8-air mixtures

P_1 (bar)	T_1 (K)	Mixture	U_{CJ} (m/s)	P_2 (bar)	c_2 (m/s)	γ	c_3 (m/s)	P_3 (bar)	α	I_V (kg/m^{2}s)	I_{SP} (s)	I_{SPF} (s)
0.2	300	C3H8+5O2+18.8N2	1771.1	3.53	974.4	1.1538	915.6	1.32	1.110	73.3	31.6	523.6
0.4	300	C3H8+5O2+18.8N2	1784.2	7.15	983.3	1.1591	922.4	2.68	1.109	389.8	84.1	1393.2
0.6	300	C3H8+5O2+18.8N2	1791.6	10.8	988.3	1.1620	926.3	4.05	1.109	706.4	101.5	1682.4
0.8	300	C3H8+5O2+18.8N2	1796.7	14.47	991.7	1.1638	928.9	5.42	1.109	1023.3	110.4	1828.8
1	300	C3H8+5O2+18.8N2	1800.6	18.15	994.4	1.1655	930.9	6.80	1.109	1340.4	115.6	1915.6
1.2	300	C3H8+5O2+18.8N2	1803.7	21.84	996.6	1.1669	932	8.11	1.109	1642.1	118.0	1955.6
1.4	300	C3H8+5O2+18.8N2	1806.3	25.54	998.4	1.1680	933.4	9.49	1.108	1956.9	120.7	1999.9
1.6	300	C3H8+5O2+18.8N2	1808.5	29.24	999.9	1.1689	934.6	10.87	1.108	2271.7	122.5	2030.0
1.8	300	C3H8+5O2+18.8N2	1810.5	32.95	1001.3	1.1698	935.6	12.24	1.108	2586.8	123.9	2053.8
2	300	C3H8+5O2+18.8N2	1812.2	36.67	1002.5	1.1706	936.5	13.63	1.108	2902.0	125.1	2073.6
1	300	0.4C3H8+5O2+18.8N2	1388.9	10.35	811.7	1.2704	735.8	3.96	1.088	859.1	75.1	2996.6
1	300	0.6C3H8+5O2+18.8N2	1587.7	13.68	906.2	1.2324	831	5.13	1.097	1064.0	92.5	2493.4
1	300	0.8C3H8+5O2+18.8N2	1721.5	16.39	961.7	1.1884	896.8	6.09	1.106	1220.5	105.8	2164.2
1	300	1C3H8+5O2+18.8N2	1800.6	18.15	994.4	1.1655	930.9	6.80	1.109	1340.4	115.6	1915.6
1	300	1.2C3H8+5O2+18.8N2	1835.6	18.78	1018.8	1.1809	954.3	6.90	1.109	1331.6	114.4	1599.3
1	300	1.4C3H8+5O2+18.8N2	1834.1	18.52	1032	1.2172	950.9	6.80	1.103	1309.8	112.2	1359.5
1	300	1.6C3H8+5O2+18.8N2	1813.5	17.99	1029.9	1.2412	938.8	6.61	1.099	1278.8	109.0	1169.6
1	300	1.8C3H8+5O2+18.8N2	1785.3	17.39	1020.1	1.2565	924.1	6.39	1.096	1246.6	105.8	1021.5
1	300	2C3H8+5O2+18.8N2	1752.5	16.74	1006.4	1.2683	907.6	6.15	1.094	1212.3	102.6	901.2
1	300	2.2C3H8+5O2+18.8N2	1716.1	16.06	989.8	1.2779	890.6	5.95	1.092	1187.5	100.1	808.6
1	300	2.4C3H8+5O2+18.8N2	1676.4	15.34	971	1.2868	871.3	5.68	1.091	1147.5	96.5	722.6
1	300	2.6C3H8+5O2+18.8N2	1633.3	14.58	950	1.2949	850.6	5.42	1.089	1107.9	92.8	648.8

Table C.9: Impulse model predictions for C_2H_2-air mixtures

P_1 (bar)	T_1 (K)	Mixture	U_{CJ} (m/s)	P_2 (bar)	c_2 (m/s)	γ	c_3 (m/s)	P_3 (bar)	α	I_V (kg/m^{2}s)	I_{SP} (s)	I_{SPF} (s)
0.2	300	C2H2+2.5O2+9.4N2	1838	3.7	1009.1	1.1516	945.7	1.39	1.110	84.8	37.7	534.2
0.4	300	C2H2+2.5O2+9.4N2	1855.8	7.52	1020.4	1.1564	954.8	2.82	1.109	407.0	90.4	1281.9
0.6	300	C2H2+2.5O2+9.4N2	1866.1	11.39	1027	1.1594	960	4.27	1.109	729.7	108.0	1532.1
0.8	300	C2H2+2.5O2+9.4N2	1873.3	15.28	1031.6	1.1614	963.6	5.73	1.109	1053.1	116.9	1658.4
1	300	C2H2+2.5O2+9.4N2	1878.8	19.2	1035.2	1.1631	966.4	7.19	1.109	1376.9	122.2	1734.1
1.2	300	C2H2+2.5O2+9.4N2	1883.3	23.13	1038.1	1.1645	968.6	8.67	1.109	1701.2	125.9	1785.9
1.4	300	C2H2+2.5O2+9.4N2	1887.1	27.08	1040.5	1.1655	970.5	10.15	1.109	2025.6	128.4	1821.9
1.6	300	C2H2+2.5O2+9.4N2	1890.3	31.03	1042.6	1.1665	972.1	11.63	1.108	2350.6	130.3	1849.0
1.8	300	C2H2+2.5O2+9.4N2	1893.1	35	1044.4	1.1672	973	13.00	1.108	2652.2	130.9	1856.2
2	300	C2H2+2.5O2+9.4N2	1895.6	38.98	1046.1	1.1681	974.2	14.48	1.108	2975.0	131.9	1871.3
1	300	0.4C2H2+2.5O2+9.4N2	1497.1	11.84	869.3	1.2677	787.3	4.49	1.090	946.4	83.6	2840.8
1	300	0.6C2H2+2.5O2+9.4N2	1696.9	15.47	956.4	1.2081	885.9	5.75	1.102	1151.0	102.0	2342.5
1	300	0.8C2H2+2.5O2+9.4N2	1807.8	17.76	1001.4	1.1718	935.6	6.65	1.108	1299.3	115.2	2014.5
1	300	1C2H2+2.5O2+9.4N2	1878.8	19.2	1035.2	1.1631	966.4	7.19	1.109	1376.9	122.2	1734.1
1	300	1.2C2H2+2.5O2+9.4N2	1930.9	20.2	1063.6	1.1656	992.6	7.50	1.109	1407.9	125.1	1500.2
1	300	1.4C2H2+2.5O2+9.4N2	1970.3	20.9	1088.3	1.1748	1016.5	7.75	1.109	1427.4	127.0	1323.4
1	300	1.6C2H2+2.5O2+9.4N2	1999.1	21.33	1109.7	1.1892	1033	7.84	1.108	1423.4	127.0	1173.3
1	300	1.8C2H2+2.5O2+9.4N2	2018.6	21.56	1126.9	1.2050	1042.2	7.85	1.106	1411.8	126.1	1049.5
1	300	2C2H2+2.5O2+9.4N2	2031.6	21.66	1139.8	1.2191	1048.2	7.89	1.104	1409.8	126.0	957.0
1	300	2.2C2H2+2.5O2+9.4N2	2040.4	21.71	1149.3	1.2303	1052.6	7.91	1.102	1407.9	126.0	881.3
1	300	2.4C2H2+2.5O2+9.4N2	2046.7	21.73	1156.4	1.2390	1055.9	7.91	1.101	1403.3	125.7	816.5
1	300	2.6C2H2+2.5O2+9.4N2	2037.7	21.48	1153.2	1.2432	1051.5	7.83	1.100	1391.8	124.9	758.0

Table C.10: Impulse model predictions for H_2-air mixtures

P_1 (bar)	T_1 (K)	Mixture	U_{CJ} (m/s)	P_2 (bar)	c_2 (m/s)	γ	c_3 (m/s)	P_3 (bar)	α	I_V (kg/m^{2}s)	I_{SP} (s)	I_{SPF} (s)
0.2	300	2H2+O2+3.76N2	1934.2	3.01	1067.1	1.1489	1005.4	1.14	1.109	27.5	16.7	586.5
0.4	300	2H2+O2+3.76N2	1950.5	6.11	1078	1.1546	1013.9	2.31	1.108	276.9	84.1	2949.3
0.6	300	2H2+O2+3.76N2	1959.6	9.23	1084.5	1.1587	1018.6	3.50	1.108	526.0	106.7	3741.0
0.8	300	2H2+O2+3.76N2	1965.9	12.36	1089	1.1614	1021.7	4.67	1.107	772.6	117.3	4113.9
1	300	2H2+O2+3.76N2	1970.7	15.51	1092.3	1.1633	1024.1	5.86	1.107	1021.4	123.9	4343.7
1.2	300	2H2+O2+3.76N2	1974.6	18.67	1095	1.1649	1026.1	7.06	1.107	1270.3	128.2	4494.5
1.4	300	2H2+O2+3.76N2	1977.8	21.89	1097.3	1.1663	1027.7	8.25	1.107	1519.3	131.6	4615.4
1.6	300	2H2+O2+3.76N2	1980.5	25.01	1099.2	1.1674	1029.1	9.45	1.107	1768.4	135.2	4740.1
1.8	300	2H2+O2+3.76N2	1982.9	28.19	1100.9	1.1685	1030.3	10.65	1.107	2017.7	135.7	4759.2
2	300	2H2+O2+3.76N2	1985	31.38	1102.4	1.1694	1031.4	11.86	1.107	2267.0	137.7	4828.7
1	300	0.8H2+O2+3.76N2	1491.3	10.31	868.6	1.2595	791.3	3.97	1.089	803.6	81.1	6985.9
1	300	1.2H2+O2+3.76N2	1709.6	12.83	973.5	1.2194	897.8	4.85	1.098	919.8	99.4	5741.0
1	300	1.6H2+O2+3.76N2	1865.3	14.56	1044.5	1.1852	974.2	5.46	1.104	983.7	113.3	4937.3
1	300	2H2+O2+3.76N2	1970.7	15.51	1092.3	1.1633	1024.1	5.86	1.107	1021.4	123.9	4343.7
1	300	2.4H2+O2+3.76N2	2033	15.63	1129	1.1689	1060.2	5.86	1.108	986.4	126.7	3722.9
1	300	2.8H2+O2+3.76N2	2072.3	15.38	1157.5	1.1830	1082.2	5.76	1.106	946.6	127.4	3226.2
1	300	3.2H2+O2+3.76N2	2101.5	15.02	1180.1	1.1955	1098.2	5.63	1.104	906.3	127.5	2841.4
1	300	3.6H2+O2+3.76N2	2125.3	14.65	1199	1.2060	1111.2	5.49	1.102	867.9	127.4	2538.1
1	300	4H2+O2+3.76N2	2146.4	14.29	1215.7	1.2148	1123	5.36	1.100	832.6	127.3	2295.3
1	300	4.4H2+O2+3.76N2	2165	13.95	1230.6	1.2225	1133.5	5.23	1.099	799.7	127.2	2096.1
1	300	4.8H2+O2+3.76N2	2181.5	13.61	1244	1.2295	1142.9	5.10	1.097	769.0	127.0	1929.3
1	300	5.2H2+O2+3.76N2	2196.4	13.28	1256.4	1.2360	1151.5	4.98	1.096	740.2	126.8	1787.5

Table C.11: Impulse model predictions for Jet A-air mixtures

P_1 (bar)	T_1 (K)	Mixture	U_{CJ} (m/s)	P_2 (bar)	c_2 (m/s)	γ	c_3 (m/s)	P_3 (bar)	α	I_V (kg/m^{2}s)	I_{SP} (s)	I_{SPF} (s)
0.2	300	JetA+13O2+48.9N2	1717.2	3.42	946.8	1.1572	889.6	1.28	1.109	65.1	27.2	419.5
0.4	300	JetA+13O2+48.9N2	1728.8	6.92	954.9	1.1626	895.7	2.59	1.109	379.9	79.5	1224.1
0.6	300	JetA+13O2+48.9N2	1735.3	10.43	959.5	1.1657	899.1	3.91	1.109	694.6	96.9	1492.6
0.8	300	JetA+13O2+48.9N2	1739.8	13.97	962.8	1.1682	901.5	5.23	1.108	1009.3	105.7	1626.9
1	300	JetA+13O2+48.9N2	1743.3	17.51	965.3	1.1698	903.2	6.56	1.108	1324.2	110.8	1706.4
1.2	300	JetA+13O2+48.9N2	1746	21.06	967.3	1.1713	904.7	7.89	1.108	1639.2	114.3	1759.8
1.4	300	JetA+13O2+48.9N2	1748.3	24.62	968.9	1.1726	905.9	9.23	1.108	1954.4	116.9	1800.6
1.6	300	JetA+13O2+48.9N2	1750.2	28.19	970.3	1.1736	906.3	10.47	1.108	2249.3	117.6	1811.1
1.8	300	JetA+13O2+48.9N2	1752	31.76	971.6	1.1744	907.2	11.80	1.107	2561.9	119.1	1833.6
2	300	JetA+13O2+48.9N2	1753.5	35.34	972.7	1.1752	908	13.13	1.107	2874.7	120.4	1854.5
1	300	0.4JetA+13O2+48.9N2	1341.1	9.78	787.1	1.2753	713.2	3.78	1.086	832.7	71.9	2659.7
1	300	0.6JetA+13O2+48.9N2	1533.6	12.97	879.7	1.2418	804.3	4.90	1.095	1038.4	88.7	2217.1
1	300	0.8JetA+13O2+48.9N2	1667.1	15.69	935.9	1.1986	869.5	5.83	1.104	1193.8	101.0	1918.7
1	300	1JetA+13O2+48.9N2	1743.3	17.51	965.3	1.1698	903.2	6.56	1.108	1324.2	110.8	1706.4
1	300	1.2JetA+13O2+48.9N2	1761.3	17.81	985.2	1.1980	916.4	6.54	1.106	1300.3	107.8	1400.7
1	300	1.4JetA+13O2+48.9N2	1729.5	17.01	983.4	1.2408	896.3	6.25	1.098	1253.5	103.0	1162.1
1	300	1.6JetA+13O2+48.9N2	1679.2	16.07	962.8	1.2602	870.9	5.96	1.094	1216.0	98.9	989.0
1	300	1.8JetA+13O2+48.9N2	1621.9	15.08	935.6	1.2728	842.8	5.60	1.092	1165.3	94.0	845.5
1	300	2JetA+13O2+48.9N2	1558.8	14.02	904.1	1.2824	812	5.21	1.090	1105.8	88.4	724.5
1	300	2.2JetA+13O2+48.9N2	1489.4	12.9	869.2	1.2927	779	4.83	1.088	1049.1	83.0	626.1
1	300	2.4JetA+13O2+48.9N2	1412.6	11.69	830.3	1.3038	742.7	4.43	1.085	984.5	77.3	540.8
1	300	2.6JetA+13O2+48.9N2	1326.1	10.38	786.6	1.3178	702.1	3.96	1.082	900.2	70.0	457.7

Table C.12: Impulse model predictions for JP10-air mixtures

P_1 (bar)	T_1 (K)	Mixture	U_{CJ} (m/s)	P_2 (bar)	c_2 (m/s)	γ	c_3 (m/s)	P_3 (bar)	α	I_V (kg/m^{2}s)	I_{SP} (s)	I_{SPF} (s)
0.2	300	JP10+14O2+52.64N2	1753.5	3.58	963.9	1.1525	905.7	1.34	1.110	78.1	32.6	492.9
0.4	300	JP10+14O2+52.64N2	1766.7	7.25	972.7	1.1573	912.6	2.72	1.110	402.3	84.0	1269.2
0.6	300	JP10+14O2+52.64N2	1774.3	10.95	977.7	1.1601	916.5	4.10	1.109	726.7	101.2	1529.3
0.8	300	JP10+14O2+52.64N2	1779.5	14.67	981.2	1.1621	919.2	5.50	1.109	1051.4	109.7	1658.6
1	300	JP10+14O2+52.64N2	1783.5	18.4	983.9	1.1637	921.3	6.90	1.109	1376.3	114.9	1736.5
1.2	300	JP10+14O2+52.64N2	1786.7	22.15	986.1	1.1650	922.4	8.23	1.109	1685.5	117.2	1770.9
1.4	300	JP10+14O2+52.64N2	1789.3	25.9	987.9	1.1660	923.8	9.62	1.109	2008.2	119.8	1809.8
1.6	300	JP10+14O2+52.64N2	1791.6	29.66	989.5	1.1670	925	11.02	1.109	2331.0	121.7	1838.6
1.8	300	JP10+14O2+52.64N2	1793.6	33.43	990.9	1.1679	926.1	12.42	1.109	2653.7	123.1	1860.1
2	300	JP10+14O2+52.64N2	1795.4	37.2	992.1	1.1686	927	13.82	1.108	2976.9	124.4	1880.3
1	300	0.4JP10+14O2+52.64N2	1385.5	10.44	809.3	1.2699	733.7	3.99	1.088	871.1	75.1	2725.5
1	300	0.6JP10+14O2+52.64N2	1581.8	13.85	902	1.2311	827.5	5.19	1.097	1085.3	92.6	2270.6
1	300	0.8JP10+14O2+52.64N2	1710.1	16.62	953.8	1.1852	890.5	6.18	1.106	1250.3	105.5	1967.2
1	300	1JP10+14O2+52.64N2	1783.5	18.4	983.9	1.1637	921.3	6.90	1.109	1376.3	114.9	1736.5
1	300	1.2JP10+14O2+52.64N2	1817.2	19.16	1006.5	1.1767	944.4	7.04	1.110	1378.0	113.9	1453.7
1	300	1.4JP10+14O2+52.64N2	1816.6	19.01	1020.4	1.2142	941.9	6.98	1.104	1364.3	111.7	1237.5
1	300	1.6JP10+14O2+52.64N2	1794	18.5	1018.5	1.2423	928.1	6.79	1.099	1336.9	108.3	1063.9
1	300	1.8JP10+14O2+52.64N2	1762	17.89	1007.1	1.2595	911.4	6.57	1.096	1307.6	104.9	927.3
1	300	2JP10+14O2+52.64N2	1725.1	17.23	991.1	1.2719	892.8	6.33	1.094	1275.4	101.4	817.0
1	300	2.2JP10+14O2+52.64N2	1684.3	16.52	972.2	1.2826	872.7	6.07	1.092	1240.3	97.7	724.7
1	300	2.4JP10+14O2+52.64N2	1639.8	15.76	950.8	1.2924	851.1	5.79	1.090	1200.5	93.6	644.1
1	300	2.6JP10+14O2+52.64N2	1591.3	14.94	927	1.3019	828.5	5.54	1.089	1167.6	90.2	579.9

Appendix D

Iterative method for air-breathing PDE performance model

The general equations and iterative method used in the air-breathing PDE model of Chapter 5 to calculate performance are described in this section.

1. Input parameters: M_0, T_{t0}, P_{t0}, γ, R, C_p, A_0, A_2, A_V, t_{close}.

2. Inlet

$$T_{t2} = T_{t0}$$

$$P_{t2} = P_{t0}\left(1 - 0.075(M_0 - 1)^{1.35}\right)$$

3. Plenum

$$\overline{T_C} = T_{t2}$$

Guess the value of c_f and γ_b. Solve the following system of equations for M_S:

$$\overline{P_C} = P_{t2} - \frac{\dot{m}_0 u_V^o}{A_2} + \frac{\dot{m}_0 R\overline{T_C}}{A_2 u_V^o}\left(1 - \frac{{u_V^o}^2}{2C_p\overline{T_C}}\right)^{-\frac{1}{\gamma-1}}\left[1 - \left(1 - \frac{{u_V^o}^2}{2C_p\overline{T_C}}\right)^{\frac{\gamma}{\gamma-1}}\right]$$

$$\overline{P_C} = P_0 \frac{1 + \frac{2\gamma_b}{\gamma_b+1}(M_S^2 - 1)}{\left[1 - \frac{2(\gamma-1)}{(\gamma_b+1)^2}\left(\frac{c_f}{\overline{c_C}}\right)^2 (M_S - 1/M_S)^2\right]^{\frac{\gamma_b}{\gamma_b-1}}}$$

$$U_{fill} = u_V^o = \frac{2c_f}{\gamma_b + 1}\left(M_S - \frac{1}{M_S}\right)$$

Calculate the Mach number of the flow at the valve plane: $M_V = u_V^o/c_V = u_V^o/\sqrt{\gamma R T_V}$. If $M_V < 1$, go to step 5. If $M_V \geq 1$, go to step 4.

4. If the flow at the valve plane is choked ($M_V = 1$), the previous system of equations (step 3) is not valid. Start by calculating the velocity at the valve plane:

$$u_V^o = c^* = \sqrt{\frac{2\gamma}{\gamma+1} R \overline{T_C}}$$

Deduce the average plenum pressure:

$$\overline{P_C} = P_{t2} - \frac{\dot{m}_0 c^*}{\gamma A_2}\left[\gamma + 1 - \left(\frac{\gamma+1}{2}\right)^{\frac{\gamma}{\gamma-1}}\right]$$

Knowing $\overline{P_C}$, solve the following equation implicitly for M_S:

$$\frac{\overline{P_C}}{P_0} = \frac{1 + \frac{2\gamma_b}{\gamma_b+1}(M_S^2 - 1)}{\left[\sqrt{\frac{\gamma+1}{2}} - \frac{\gamma-1}{\gamma_b+1}\frac{c_f}{\overline{c_C}}\left(M_S - 1/M_S\right)\right]^{\frac{2\gamma}{\gamma-1}}}$$

Once M_S is known, calculate the filling velocity:

$$U_{fill} = \frac{2c_f}{\gamma_b + 1}\left(M_S - \frac{1}{M_S}\right)$$

5. Valve plane

Calculate the properties at the valve plane during the open part of the cycle:

$$T_V^o = \overline{T_C} - \frac{{u_V^o}^2}{2C_p}$$

$$P_V^o = \overline{P_C}\left(\frac{T_V^o}{\overline{T_C}}\right)^{\frac{\gamma}{\gamma-1}}$$

6. Calculate the value of the open time and the cycle time:

$$t_{open} = \frac{t_{close}}{\frac{\dot{m}_V^o}{\dot{m}_0} - 1}$$

$$\tau = t_{close} + t_{open} = t_{close} + t_{fill} + t_{purge} = t_{close} + t_{fill}(1+\pi)$$

7. Detonation tube

   Calculate the initial conditions before detonation as those just behind the contact surface:

$$P_i = \left(1 + \frac{2\gamma_b}{\gamma_b + 1}(M_S^2 - 1)\right) P_0$$

$$T_i = \left(\frac{P_i}{\overline{P_C}}\right)^{\frac{\gamma-1}{\gamma}} \overline{T_C}$$

   Calculate CJ detonation parameters, including γ_b, using realistic thermochemistry (Reynolds, 1986). Calculate state 3 parameters using the modified Taylor wave solution and c_f using isentropic expansion to atmospheric pressure.

8. Iterate steps 3-7 until the assumed values of c_f and γ_b match those obtained from the detonation properties. Once these values match, go to step 9.

9. Detonation tube impulse

$$I_{dt} = V_{dt}\Delta P_3 \left[\frac{1}{U_{CJ} + U_{fill}} + (\alpha + \beta)\frac{1}{c_3}\right]$$

$$V_{dt} = \left(\frac{1+f}{1+\pi}\right)\frac{\tau \dot{m}_0}{\rho_i}$$

$$\alpha = \frac{c_3}{U_{CJ} + U_{fill}}\left[2\left(\frac{\gamma_b - 1}{\gamma_b + 1}\left(\frac{c_3 - u_{CJ}}{c_{CJ}} + \frac{2}{\gamma_b - 1}\right)\right)^{-\frac{\gamma_b+1}{2(\gamma_b-1)}} - 1\right]$$

$$\beta = 0.53$$

10. Thrust

$$\overline{F} = \frac{1}{\tau} I_{dt} + \dot{m}_0(u_V^o - u_0) + \frac{t_{open}}{\tau} A_V(P_V^o - P_0)$$

11. Specific impulse

$$I_{SPF} = I_{SPFdt} - \frac{1+\pi}{fg}\left[(u_0 - u_V^o) - \frac{A_V(P_V^o - P_0)}{\dot{m}_V^o}\right]$$